Parametrically-driven nonlinear optical resonators and their networks for sensing and computing

Thesis by
Arkadev Roy

In Partial Fulfillment of the Requirements for the
Degree of
Doctor of Philosophy

CALIFORNIA INSTITUTE OF TECHNOLOGY
Pasadena, California

2023
Defended April 7, 2023

Arkadev Roy
ORCID: 0000-0001-5659-8388

To my grandmother

Revered Basanti Lata Roy

and my parents

Shri Benimadhab Roy

Shrimati Kakali Roy

Satyameva Jayate

ACKNOWLEDGEMENTS

First and foremost, I would like to express gratitude to my advisor, Prof. Alireza Marandi, for his support and guidance. His thoughtful evaluations provided a lot of crucial input, and I have learned invaluable lessons in planning and managing research projects along with appreciating the practical implications of any research problem. His knowledge of a wide breadth of scientific domains is inspiring. After working with him for ~ 4.5 years, I am convinced that chi2 is useful. Although I entered the group as a chi3 person, I now consider chi2 > chi3 in most scenarios, with a caveat that in some cases, chi3 is superior.

I want to thank Prof. Kerry Vahala, Prof. Lihong Wang, and Prof. Andrei Faraon for their service as my graduate committee and for their insightful inputs to this thesis.

The graduate studies at Caltech have been transformative for me. I am very fortunate to have been able to learn from faculty/instructors who are leading researchers/academicians in their own fields. It was highly inspiring to be in association with some of the greatest scientific minds of our times which was also instrumental in instilling confidence in me. The academic ambiance at Caltech really makes it a very special place, and I think it will impart a lasting impact on my journey ahead.

I would like to acknowledge the fruitful collaboration with the group of Prof. Martin Fejer from Stanford. His insights and feedback on my work have been extremely useful. The initial experiments were made possible by using the hero devices provided by Carsten.

I am extremely grateful to the postdocs of our group for their research mentorship and valuable career advice. I am extremely indebted for the help I received from Saman, Qiushi, Midya, and Myoung-Gyun. The interactions with them shaped my scientific approach and helped develop a broader perspective of the field beyond the narrow confines of my own projects. The several valuable lessons I learned include the ability to put my work into a more general framework, the possibility of finding something interesting and worthy even if something appears dumb, the importance of presenting the work with the aid of illustrations, and the capability to criticize my own work. I also enjoyed working and having discussions with Raj, Luis (C), and Joong-Hwan. I would like to acknowledge the mentorship and countless pieces

of advice I have received from Avik Da over the course of years dating back to my undergraduate days. Despite his busy schedule, he always managed to find spare time to talk to me and answer my doubts.

My appreciation also goes to my colleagues. I enjoyed a productive collaboration with (in no particular order) Mingchen, Luis (L), Robby, Ryoto, and other members of the nonlinear photonics group. The number of things I learned over the course of years from countless discussions and project meetings with the group members is remarkable.

I would like to thank my undergraduate advisor, Prof. Shailendra Kumar Varshney. I was fortunate to start research under his guidance, which has played a formative role in my academic career. During this period, I received mentorship from his Ph.D. students including Raktim Da and Partha Da which has been invaluable. The foundation in theoretical and numerical approaches that got laid during this period at IIT KGP got consolidated later during my Ph.D. I would like to express my gratitude to Prof. Shankar Kumar Selvaraja for giving me the opportunity to work with him during the summer of my sophomore year. This was my first initiation to research and I got addicted to it.

I am forever grateful to my teachers since childhood. I cannot mention the names of many, even though I want to, for the sake of brevity. But this acknowledgment would not have been complete without mentioning the contributions of Tamonash Da whose role has been pivotal for my growth as a human being and who was also responsible for instilling in me the purpose of life.

I would like to thank all my friends for providing the company and much-needed help whenever I asked for. I would like to thank my elder brother and his family for their support. I would like to thank all my well-wishers including those who were not directly associated with my academic pursuits but have been integral to this journey.

I would like to pay my regards to my grandmother whose life is an inspiration to me. Her intelligence and skills are unmatched, and she was the embodiment of Goddess Saraswati to us. Her way of life will be the constant guiding light in the pursuit of fulfilling my dreams. My parents are a perennial source of encouragement, enthusiasm, and endeavor in my life. Their sacrifices and hard work formed the bedrock of whatever I have demonstrated so far. Any collection of words to describe their contribution will be an understatement. I hope that I can make them proud.

Finally but most importantly I would like to pay salutations to my personal God (Joy Bhaba). The constant Witness of my successes and failures, the Companion in my happy days and sorrowful moments, the Protector of me from all evils, the Guide who shows the light whenever I deviate and directs me at crossroads, the Insurer who assured me of coming to my rescue in the event of anything unwarranted as long as I am on the path of truth, not once or twice but an indefinite number of times, I pay my homage to you. I pray to you: *Lead me from the unreal to the real, Lead me from darkness to light, Lead me from ephemeral to eternal*.

ABSTRACT

New physics and novel applications in various fields ranging from biology and spectroscopy, to manipulation of quantum systems are driven by the availability of coherent light sources including frequency combs in the visible and mid-infrared spectral regimes. Nonlinear optical systems, that are parametrically driven by technologically mature near-infrared lasers, are leveraged in this regard to access challenging wavelengths where conventional lasers may be unavailable. It is of paramount importance to miniaturize these systems and replace the traditional bulky setups thereby paving the way for a plethora of applications. Optical parametric oscillators are among the most prominent examples of such nonlinear systems and beyond their indispensable usage as light sources (both classical and quantum) their unique non-equilibrium dynamics can endow a wealth of functionalities absent in their linear counterparts. These properties can be engineered and utilized for realizing highly sensitive sensors as well as special-purpose computing hardware that may outperform conventional digital computers. A network of these coupled parametric oscillators can be made to interact leading to emergent behaviors that are not expected from the individual constituents.

In this work, we experimentally and theoretically study the dynamics of individual and coupled optical parametric oscillators towards sensing and computing applications. We explore a previously avoided regime of operation for generating ultra-short pulses from these parametrically driven nonlinear resonators that lead to extreme pulse compression. We engineer the nonlinear dynamics of these systems to realize all-optical spectral phase transitions (both first-order and second-order) that behave as highly-sensitive sensors. We show how these critical phenomena can be utilized to enhance the solution accuracy of physics-based solvers in finding optimum solutions to combinatorial optimization problems in the context of coherent Ising machines. We also realize optical parametric oscillators in integrated lithium-niobate nanophotonic platform and demonstrate a mid-infrared frequency comb source that is widely tunable over an octave accompanied by visible frequency comb generation. We develop a comprehensive description to investigate the noise properties of optical parametric oscillators that provide new insights into the phase noise behavior of optical parametric oscillators in their various operating regimes. Finally, we propose a system of parametrically driven resonators as a synthetic medium with highly reconfigurable interactions

that can host a plethora of emergent phenomena ranging from topological behaviors to non-Hermitian dynamics. These networks of nonlinear resonators display intriguing dynamical properties in contrast to their static counterparts in condensed-matter physics with implications in quantum sensing and robust device functionality.

PUBLISHED CONTENT AND CONTRIBUTIONS

[1] **Roy, Arkadev**, Saman Jahani, Qiushi Guo, Avik Dutt, Shanhui Fan, Mohammad-Ali Miri, and Alireza Marandi. Nondissipative non-Hermitian dynamics and exceptional points in coupled optical parametric oscillators. ***Optica***, 8(3):415–421, 2021. doi: https://doi.org/10.1364/OPTICA.415569.
A.R. contributed to the conception of the project, developed the modeling, performed numerical simulations, and participated in the writing of the manuscript.

[2] **Roy, Arkadev**, Saman Jahani, Carsten Langrock, Martin Fejer, and Alireza Marandi. Spectral phase transitions in optical parametric oscillators. ***Nature Communications***, 12(1):835, 2021. doi: https://doi.org/10.1038/s41467-021-21048-z.
A.R. contributed to the conception of the project, executed the experiments, performed numerical simulations, and participated in the writing of the manuscript.

[3] **Roy, Arkadev***, Luis Ledezma*, Luis Costa, Robert Gray, Ryoto Sekine, Qiushi Guo, Mingchen Liu, Ryan M. Briggs, and Alireza Marandi. Visible-to-mid-IR tunable frequency comb in nanophotonics. *arXiv preprint arXiv:2212.08723*, 2022. doi: https://doi.org/10.48550/arXiv.2212.08723.
* denotes equal contribution. Parts of this work appeared as post-deadline presentations at the following conferences: CLEO 2022 and Advanced Photonics Congress 2022. **A.R.** contributed to the experiments, performed numerical simulations, and participated in the writing of the manuscript.

[4] **Roy, Arkadev**, Rajveer Nehra, Saman Jahani, Luis Ledezma, Carsten Langrock, Martin Fejer, and Alireza Marandi. Temporal walk-off induced dissipative quadratic solitons. ***Nature Photonics***, 16(2):162–168, 2022. doi: https://doi.org/10.1038/s41566-021-00942-4.
A.R. performed the experiments, executed numerical simulations alongside associated formulations, and participated in the writing of the manuscript.

[5] **Roy, Arkadev**, Midya Parto, Rajveer Nehra, Christian Leefmans, and Alireza Marandi. Topological optical parametric oscillation. ***Nanophotonics***, 11(8): 1611–1618, 2022. doi: https://doi.org/10.1515/nanoph-2021-0765.
A.R. contributed to the conception of the project, developed the analytical modeling, performed numerical simulations, and participated in the writing of the manuscript.

[6] **Roy, Arkadev**, Rajveer Nehra, Carsten Langrock, Martin Fejer, and Alireza Marandi. Non-equilibrium spectral phase transitions in coupled nonlinear optical resonators. ***Nature Physics***, pages 1–8, 2023. doi: https://doi.org/10.1038/s41567-022-01874-8.

A.R. contributed to the conception of the project, executed the experiments, performed numerical simulations alongside associated analytical results, and participated in the writing of the manuscript.

[1] Qiushi Guo, Ryoto Sekine, Luis Ledezma, Rajveer Nehra, Devin J. Dean, **Roy, Arkadev**, Robert M. Gray, Saman Jahani, and Alireza Marandi. Femtojoule femtosecond all-optical switching in lithium niobate nanophotonics. ***Nature Photonics***, 16(9):625–631, 2022. doi: https://doi.org/10.1038/s41566-022-01044-5.
A.R. contributed to the numerical simulations.

[2] Saman Jahani, **Roy, Arkadev**, and Alireza Marandi. Wavelength-scale optical parametric oscillators. ***Optica***, 8(2):262–268, 2021. doi: https://doi.org/10.1364/OPTICA.411708.
A.R. participated in the development of the theory.

[3] Luis Ledezma, **Roy, Arkadev**, Luis Costa, Ryoto Sekine, Robert Gray, Qiushi Guo, Ryan M. Briggs, and Alireza Marandi. Widely-tunable optical parametric oscillator in lithium niobate nanophotonics. *arXiv preprint arXiv:2203.11482*, 2022. doi: https://doi.org/10.48550/arXiv.2203.11482.
A.R. participated in the experiments.

[4] Mingchen Liu, Robert M. Gray, **Roy, Arkadev**, Kirk A. Ingold, Evgeni Sorokin, Irina Sorokina, Peter G. Schunemann, and Alireza Marandi. High-power mid-ir few-cycle frequency comb from quadratic solitons in an optical parametric oscillator. ***Laser & Photonics Reviews***, 16(11):2200453, 2022. doi: https://doi.org/10.1002/lpor.202200453.
A.R. contributed to the numerical simulations.

[5] Mingchen Liu, Robert Gray, Luis Costa, Charles Markus, **Roy, Arkadev**, and Alireza Marandi. Mid-infrared cross-comb spectroscopy. ***Nature Communications***, 14(1044), 2023. doi: https://doi.org/10.1038/s41467-023-36811-7.
A.R. participated in the conception of the project.

[6] Rajveer Nehra, Ryoto Sekine, Luis Ledezma, Qiushi Guo, Robert M. Gray, **Roy, Arkadev**, and Alireza Marandi. Few-cycle vacuum squeezing in nanophotonics. ***Science***, 377(6612):1333–1337, 2022. doi: DOI:10.1126/science.abo6213.
A.R. contributed to data analysis.

TABLE OF CONTENTS

LIST OF ILLUSTRATIONS

NOMENCLATURE

CW. Continuous Wave.

EP. Exceptional Point.

FSR. Free Spectral Range.

GDD. Group Delay Dispersion.

GVD. Group Velocity Dispersion.

GVM. Group Velocity Mismatch.

IR. Infrared.

OPA. Optical Parametric Amplification.

OPO. Optical Parametric Oscillators.

PIA. Phase Insensitive Amplification.

PPLN. Periodically Poled Lithium Niobate.

PSA. Phase Sensitive Amplification.

Q. Quality Factor.

QPM. Quasi Phase Matching.

RF. Radio Frequency.

SFG. Sum Frequency Generation.

SHG. Second Harmonic Generation.

SNR. Signal to Noise Ratio.

TOD. Third Order Dispersion.

$\mathbf{F_{CEO}}$**.** Carrier Envelope Offset frequency.

$\mathbf{F_{REP}}$**.** Repetition rate frequency.

Chapter 1

INTRODUCTION

In this age of artificial intelligence and intelligent cyber-physical systems, there is an ever-increasing demand for the acquisition and processing of multi-dimensional data. The key constituents of these cyber-physical systems involve sensors, actuators, controllers, and computing units. There exist several sensing modalities leveraging multi-physical effects originating from the interplay of electrical, thermal, mechanical, and chemical processes. Optical technology based approaches enjoy several advantages in terms of specificity (spectroscopy), resolution (diffraction limit in the order of wavelength), remote sensing capability (label-free and non-invasive), low-latency signal acquisition, and so on. Thus the exploration of sensitivity enhancement of these optics-based sensing mechanisms and exploring means of new regimes of sensing and their fundamental limits is of paramount importance.

Laser is the enabling technology that is powering most optics-based applications. Lasers are sources of coherent radiation that have over the course of years ushered in unprecedented possibilities ranging from long-distance communications to spectroscopy and imaging. However, lasers are available at selected wavelength ranges corresponding to the transition energy levels of the material constituting the gain medium. In order to access coherent radiation at arbitrary wavelengths one has to use nonlinear optical processes to either up-convert or down-convert existing laser frequencies. One of the most ubiquitous devices used in this regard is the optical parametric oscillator (OPO). Although immensely successful these OPOs traditionally have been very bulky and power-hungry. It is extremely valuable to miniaturize these devices in line with the nanophotonic revolution. This can open possibilities for countless consumer applications relying on OPOs requiring widely tunable coherent radiation sources in the technologically important visible and mid-infrared frequency regimes. We are going to witness the rapid incorporation of lasers and LEDs in smart devices for continuous health monitoring and one can envision the integration of OPOs in these devices as well to increase the gamut of possible applications. Apart from the miniaturization focus, we are also interested in making these OPOs more efficient, and one can exploit the rich nonlinear dynamics to choose a suitable operating point to achieve the same. A continuing

pursuit has been to generate ultra-short pulses (orders of several 10s of femtoseconds) from these OPOs. Ultra-short pulses will enable resolving light-matter interactions at ultra-fast time scales thereby informing the design of next-generation detectors and modulators enabling peta-Hertz scale electronics in the future. An ultra-short pulse train also corresponds to a broadband frequency comb source which has found a plethora of applications ranging from precision measurements to microwave synthesis, massively-parallel coherent communication, and so on. There is an outstanding demand to be able to generate a stable-phase locked optical frequency comb at arbitrary wavelengths which can unveil a host of applications.

Next, we introduce the various themes central to our work.

1.1 $\chi^{(2)}$ based nonlinear optics

When an intense laser field is incident on a medium the induced polarization of the medium on account of the dipole reorientation no longer responds linearly [1, 4]. The linear response is due to the linear susceptibility ($\chi^{(1)}$) which is responsible for the linear polarization component ($P^{(1)}$), where $P^{(1)}(\omega) = \epsilon_0 \chi^{(1)}(\omega) E(\omega)$. In addition to the induced linear polarization component, there will be nonlinear contributions of higher orders, and the net polarization of the medium can be expressed as: $P(\omega) = P^{(1)}(\omega) + P^{(2}(\omega) + P^{(3)}(\omega) + \ldots$. The higher order terms arise due to nonlinear susceptibility that is associated with the underlying phenomena of distortion of electronic cloud among others. The second-order susceptibility ($\chi^{(2)}$) represents the coupling of three waves. One of these second-order effects (alternatively quadratic nonlinear effects) can be expressed by the following induced polarization component at the sum-frequency: $P^{(2)}(\omega = \omega_1 + \omega_2) = \epsilon_0 \chi^{(2)}(\omega_1, \omega_2) E(\omega_1) E(\omega_2)$. Similarly, the third-order susceptibility ($\chi^{(3)}$) represents the coupling of four waves. One of these third-order effects (alternatively Kerr nonlinear effects) can be expressed by the following induced polarization component at the sum-frequency: $P^{(3)}(\omega = \omega_1 + \omega_2 + \omega_3) = \epsilon_0 \chi^{(3)}(\omega_1, \omega_2, \omega_3) E(\omega_1) E(\omega_2) E(\omega_3)$.

These nonlinearities involve virtual transitions instead of real resonant light-matter interactions. Inevitably they are weak in nature and require intense fields (dependent on the peak electric field) to produce any substantial nonlinear phase shift. The higher the order of this nonlinearity in the perturbative expansion the weaker it is and approximately follows the scaling: $\frac{|\chi^{(n)}|}{|\chi^{(n-1)}|} \sim \frac{1}{E_0}$, where $|E_0|$ is of the order of

magnitude of the average electric field strength in an atom. However, the effect of nonlinearity is dictated by the induced polarization instead of the susceptibilities themselves. Even in terms of induced polarization, the ratio of polarizations of successive orders can be given by: $\frac{P^{(n)}}{P^{(n-1)}} \sim \frac{|E|}{|E_0|}$, which is typically « 1 for laser intensities that can be realized in chip-scale integrated platforms. Thus it is of great interest to realize nonlinear processes with quadratic nonlinearities which promise to be less power-hungry than their Kerr counterpart.

In a centro-symmetric medium (no surface/interface effects considered) all even order nonlinear coefficients $\chi^{(2n)}$ vanishes. Therefore, a non-centrosymmetric medium is required to display second-order nonlinear phenomena. The material we are interested in this work is lithium niobate. However, other materials that can also be used include lithium tantalate, Potassium titanyl phosphate, aluminum gallium arsenide, beta-barium borate, gallium phosphide, gallium arsenide, and so on.

1.2 Parametric devices

Parametric devices refer to systems where the device parameters are temporally modulated by a driving source. The energy is transferred from the driving agent to the system of interest. It typically involves a resonant system with a characteristic frequency (ω_0), and is driven periodically at a different frequency. The canonical example of a parametric device is a parametrically driven mechanical pendulum where the point of suspension is periodically modulated. Such devices are ubiquitous in several domains ranging from piezo-electric devices to micro-electro-mechanical devices, and high-frequency electrical circuits. In the context of electrical circuits, they appear as resonant circuits constituting a varactor where the capacitance of the varactor is parametrically modulated. These parametric devices are now used routinely in superconducting quantum circuits as parametric amplifiers [26]. For the purpose of this work, we are interested in optical parametric devices.

1.3 Optical parametric amplification and oscillation

Optical parametric devices involve the parametric modulation of the refractive index of the constituting nonlinear medium. The induced nonlinear polarization of the medium is responsible for the modulation of the refractive index. A consequence of parametric driving is the possibility to do frequency conversion. Thus, the frequency of the input radiations can be combined to create output photons with higher frequencies leveraging the nonlinear up-conversion processes

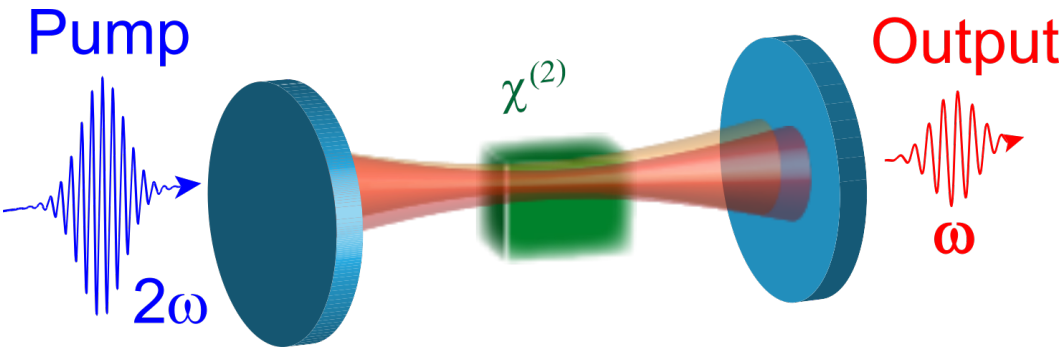

Figure 1.1: **Schematic of an optical parametric oscillator.**

like sum-frequency generation, second-harmonic generation, high-harmonic generation, etc. Similarly, the frequency of the input radiations can be combined to create output photons with lower frequencies leveraging the nonlinear down-conversion processes like difference frequency generation, optical rectification, etc.

These can also be employed as amplifiers useful for amplifying the signal by transferring the energy from the pump. This constitutes the class of phase-sensitive amplifiers whereby the amplification is phase-sensitive. If the phase relations are not set correctly then instead of amplification one obtains de-amplification. The phase-sensitive amplification process has markedly different characteristics compared to its phase-insensitive counterpart which is ubiquitously used in conventional optical amplifiers. Phase-insensitive amplifiers inherently add extra noise in the due process of amplification (dictated by quantum mechanical principles) and the noise figure of such amplifiers can be at best 3 dB in the limit of large amplification [12]. On the other hand, parametric amplifiers can be made to operate below the 3 dB noise figure limit and are indispensable for quantum applications [6]. Ideally, the amplification process can be shown to be noiseless.

The parametric amplifier in combination with a cavity can constitute an oscillator also known as an optical parametric oscillator (OPO). This will be the central device under consideration in our work. A schematic representation of it is shown in Fig. 1.1. Here, the vacuum fluctuations can be amplified by the driving pump to produce a coherent signal.

1.4 Degenerate and non-degenerate optical parametric oscillators

Optical parametric oscillators operating in the down-conversion regime can be classified into two categories, namely the degenerate and the non-degenerate OPOs.

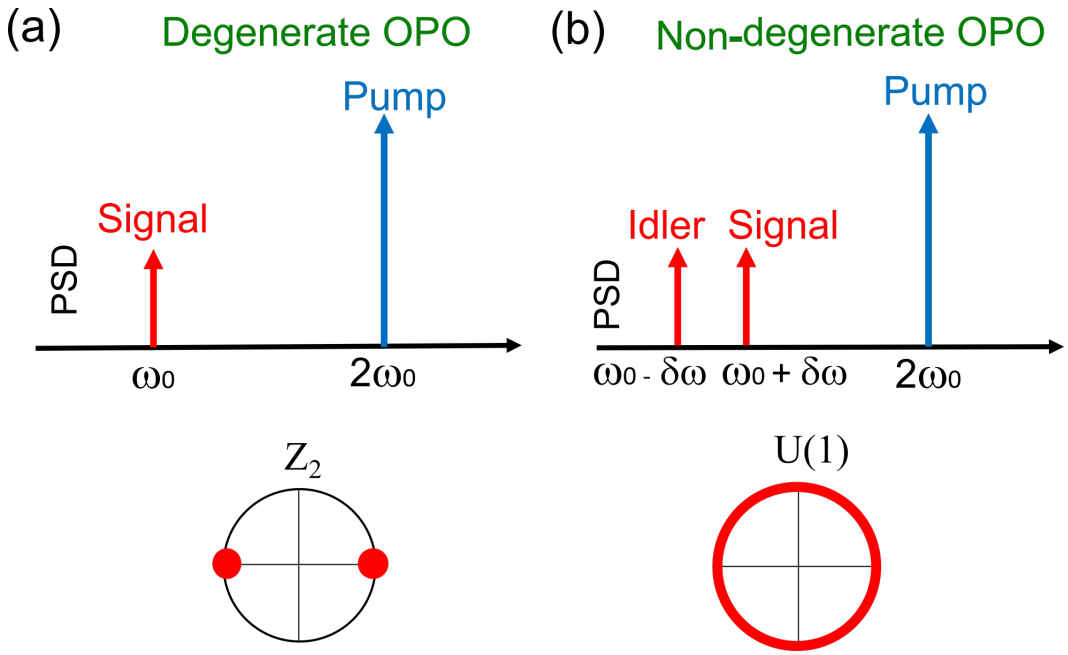

Figure 1.2: **Degenerate and non-degenerate oscillation regimes of an OPO.** a) The degenerate regime is characterized by the binary phase states, while b) in the non-degenerate regime the OPO signal is free to occupy any phase, as long as the idler phase is its conjugate.

In a degenerate OPO, a single pump photon ($2\omega_0$) is converted into two degenerate signal photons (ω_0). Degenerate OPO is associated with phase and frequency locking which is detailed further in the next section. While in a non-degenerate OPO, a single pump photon ($2\omega_0$) is converted into a signal photon ($\omega_0 + \Delta\omega$) and an idler photon ($\omega_0 - \Delta\omega$). Non-degenerate OPOs in general do not inherit the phase and frequency locking properties from the pump (except in special circumstances like divide by 3 OPOs [8]) and are mostly useful to generate tunable sources of coherent radiation that can extend into the mid-infrared starting from a near-infrared pump. The phase and frequency relations for OPOs operating in the degenerate and non-degenerate regimes are illustrated in Fig. 1.2.

1.5 Binary phase states and degenerate optical parametric oscillators

Degenerate OPOs exhibit several unique properties owing to their phase and frequency locking with respect to the pump. This can be understood by analyzing the following set of simplified equations for an OPO only considering the parametric amplifier region.

$$\frac{dE_s}{dz} = \kappa E_p E_s^* \tag{1.1a}$$

$$\frac{dE_p}{dz} = -\kappa E_s^2 \tag{1.1b}$$

where, we assume the pump (E_p) phase as a reference, and the signal complex electric field (E_s) is denoted in the magnitude phase representation as $E_s = |E_s|e^{i\theta_s}$. Here, κ is the effective nonlinear coefficient and z denotes the propagation axis along the parametric interaction length.

In the undepleted pump approximation, the dynamics can be approximated as:

$$\frac{d|E_s|}{dz} = \kappa E_p |E_s| \cos(2\theta_s) \tag{1.2a}$$

$$\frac{d\theta_s}{dz} = -\kappa E_p \sin(2\theta_s). \tag{1.2b}$$

The above equations reveal that the two binary phases 0 and π experience the maximum gain and both these phase solutions are stable.

They exhibit binary phase states which are π phase shifted with respect to each other and of equal intensity. This property of degenerate OPOs has been used for random number generation [20] since an OPO randomly selects one of the two phases as it transitions from below to above threshold. These binary phase states are the fixed points of a degenerate OPO and can be mapped to behave as classical analogs of Ising spins. Thus, a network of coupled OPOs has been utilized to realize a coherent Ising machine where the ground state of the system corresponds to the solution of the combinatorial optimization problem (like MAXCUT) [21, 22]. The behavior of degenerate OPOs below and above the oscillation threshold is depicted in Fig. 1.3.

However, in the non-degenerate regime, the signal phase is unconstrained as long as it is conjugate to the idler phase. This phase degree of freedom is denoted as U(1) symmetry which is reduced to being Z_2 symmetry in the degenerate oscillation regime.

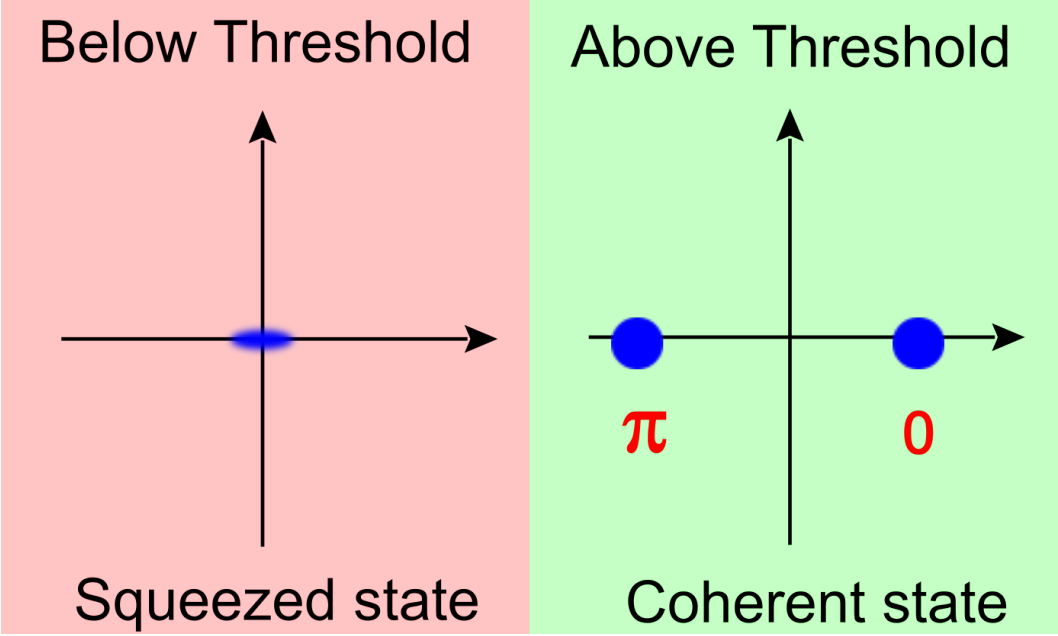

Figure 1.3: **Binary phase states of a degenerate OPO above the threshold.** Below the threshold the OPO exists in a squeezed state. Spontaneous symmetry breaking occurs at the threshold followed by the OPO occupying one of the two binary phase states (coherent states).

1.6 Triply, doubly, and singly resonant optical parametric oscillators

Resonant systems are associated with resonant phenomena that correspond to particular frequencies. A detuning from the exact resonance frequency will weaken the resonant enhancement. Thus mechanisms that critically depend on resonant interactions are inherently narrowband. In order to realize widely tunable devices one has to resort to non-resonant architectures. However, the trade-off is incurred in terms of increased power requirement (reflected in terms of the threshold).

OPOs can be realized in different configurations ranging from being completely resonant to being partially so. Triply-resonant configurations require all the signal, idler, and pump waves to be resonant. These configurations enjoy the minimum thresholds/ power requirements, but at the same time suffer from strict resonance constraints [2]. They are generally narrowly tunable and face stability issues. Tunability requires multiple degrees of freedom such that the simultaneous resonance condition is satisfied.

Doubly-resonant configurations only require the signal and the idler to be resonant. This class of OPOs has intermediate thresholds and higher tunability [11, 24, 25]. Degenerate and near-degenerate OPO tend to be doubly resonant by nature. On the

other hand, singly-resonant conditions only involve either the signal or the idler to be resonant. They have the highest threshold requirement and at the same time the maximum tunability [9, 18]. We are mainly interested in the dynamics of doubly and singly resonant OPOs and the ensuing applications for the purpose of this work.

1.7 Phase-matching and optical parametric oscillation bandwidth

The parametric interaction involves waves of disparate frequencies which has to satisfy the energy conservation relation. Additionally, it has to satisfy the momentum conservation condition as well for efficient parametric energy transfer. The momentum of the waves is related to the propagation constant and is given by $k_{(\omega)} = \frac{n_{\text{eff}}(\omega)\omega}{c}$, where ω is the frequency, c is the velocity of light in free space, and n_{eff} is the effective index of the medium at that frequency. The vector sum of the momentum of the input waves has to be equal to the corresponding sum for the output waves, otherwise, a phase accumulation happens which beyond a propagation distance exceeding the coherence length (inversely proportional to the residual momentum mismatch) leads to energy back conversion. The coherence length here refers to the mutual coherence between the waves participating in the parametric process. The residual momentum mismatch in the case of QPM is canceled by the periodic poling and is given as:

$$k_p(\omega_p) - k_s(\omega_s) - k_i(\omega_i) = K = \frac{2\pi}{\Lambda} \tag{1.3}$$

where we considered the parametric interaction between the input pump (p), and the output signal (s) and idler (i) waves.

To realize phase-matching, i.e., to cancel the residual phase mismatch we resort to periodic poling. The periodic poling periodically inverts the ferroelectric domains of lithium niobate thereby altering the sign of the nonlinearity coefficient periodically. This is known as quasi-phase-matching (QPM). Lithium niobate can sustain the poling pattern as long as the operating temperature is below the Curie temperature. QPM allows very efficient nonlinear interaction while the nonlinear conversion efficiency is limited by the coherence length in a phase-mismatched scenario. Perfect phase matching can only be satisfied at particular frequencies and modal geometries and leads to constraints that may not allow the independent tuning of dispersion engineering. QPM decouples the dispersion engineering from the phase-matching criterion only at the cost of a reduction of the effective nonlinear coefficient by a factor of $\frac{2}{\pi}$.

The periodic-poling-induced QPM can ensure phase-matching at a particular set of frequencies (unless it is chirped), and hence there is a finite phase-matching bandwidth imposed by the dispersion. This dispersion is contributed both by the inherent material dispersion (frequency-dependent refractive index which can be modeled by Sellmeier equation) as well as the geometric dispersion that is imposed by the waveguide boundary conditions. Away from the quasi-phase-matched frequency (ω), the momentum mismatch accrued as a function of frequency deviation (Ω) is given by:

$$\Delta k(\Omega) = k(2\omega + 2\Omega) - 2k(\omega + \Omega) - \frac{2\pi}{\Lambda} \tag{1.4}$$

which can be approximated by a Taylor series expansion as:

$$\Delta k(\Omega) = \Delta k_0 + 2\Delta k^{'}\Omega + (2k^{''}_{2\omega} - k^{''}_{\omega})\Omega^2 + \dots \tag{1.5}$$

Here we have considered the simplified situation of a degenerate frequency conversion where only the pump (2ω) and signal ω are involved. Δk_0 is the zeroth order mismatch which can be completely nullified by the appropriate poling period. The first-order correction is related to the first derivative $\Delta k^{'}$ also referred to as the walk-off parameter/ group-velocity-mismatch (GVM) parameter and can also be expressed as the difference of the inverse of group-velocity of the participating waves $\Delta k^{'} = \frac{1}{v_{g,2\omega}} - \frac{1}{v_{g,\omega}}$. In the next order appears the second derivative which is also termed the group-velocity dispersion (GVD) parameter. Higher-order correction involves third-order dispersion (TOD) and so on.

To ensure a broad bandwidth for the parametric interaction, small dispersion coefficients (GVM, GVD, TOD, etc) are desired. The ability to perform dispersion engineering by varying the geometric parameters of the waveguide can allow one to operate in a small dispersion regime characterized by near-zero GVM and near-zero GVD. This regime is known also referred to as the stationary regime or the quasi-static regime [14, 15, 19]. Traditionally, the stationary regime has been sought after especially in the context of femtosecond optical parametric oscillators. In contrast, the non-stationary regime is characterized by a large GVM parameter. Counter-intuitively, we show in Chapter 2 that we can leverage the unique nonlinear dynamics in this regime to obtain extreme pulse compression.

1.8 Modeling of synchronously pumped optical parametric oscillators

Synchronously pumped OPOs represent a class of OPOs that is driven by a pulsed pump [16]. The pulsed nature of the pump enables the utilization of the temporal confinement of the pulses to access the peak intensities required for nonlinear interactions. The peak power to average power ratio of a pulsed source is much higher than a continuous wave source and is related to the ratio between the repetition time period and the pulse width. The nonlinear interactions rely on the peak value of the electric fields (correspondingly the peak power), while the damaging effects (material breakdown, thermal damage), etc. are related to the average power.

The modeling of dynamics of a sync-pumped OPO is described below. The nonlinear interaction inside the periodically-poled lithium niobate (PPLN) waveguide is governed by:

$$\frac{\partial a}{\partial z} = \left[-\frac{\alpha^{(a)}}{2} - i\frac{\beta_2^{(a)}}{2!}\frac{\partial^2}{\partial t^2} + \dots \right] a + \epsilon a^* b \tag{1.6a}$$

$$\frac{\partial b}{\partial z} = \left[-\frac{\alpha^{(b)}}{2} - u\frac{\partial}{\partial t} - i\frac{\beta_2^{(b)}}{2!}\frac{\partial^2}{\partial t^2} + \dots \right] b - \frac{\epsilon a^2}{2}. \tag{1.6b}$$

The evolution of the signal(a) and the pump(b) envelopes in the slowly varying envelope approximation are dictated by equations 1.6a and 1.6b, respectively [11]. The effects of higher-order group velocity dispersions (GVD) β_2, β_3, group velocity mismatch (GVM) (u), and the back-conversion from the signal to the pump is included. The round-trip feedback is given by:

$$a^{(n+1)}(0,t) = \mathcal{F}^{-1}\left\{ G_0^{-\frac{1}{2}} e^{i\bar{\phi}} \mathcal{F}\left\{ a^{(n)}(L,t) \right\} \right\} \tag{1.7a}$$

$$\bar{\phi} = \Delta\phi + \frac{l\lambda^{(a)}}{2c}(\omega - \omega_0) + \frac{\phi_2}{2!}(\omega - \omega_0)^2 + \dots \tag{1.7b}$$

Eq. 1.7 takes into consideration the round-trip loss which is lumped into an aggregated out-coupling loss factor G_0, the GVD (ϕ_2) of the feedback path, and the detuning ($\Delta\phi$) ($\Delta\phi = \pi l + \phi_0$, l is the cavity length detuning in units of signal half-wavelengths in vacuum) of the circulating signal from the exact synchrony with respect to the pump. The effective second-order nonlinearity co-efficient (ϵ) is related to the SHG efficiency [11]. The round-trip number is denoted by n and

the cavity length by L. The equations are numerically solved by adopting the split-step Fourier algorithm [1].

Other modeling techniques include nonlinear envelope equation, where a single envelope is solved instead of coupled wave equations as mention in eq. 1.6 [7]. For analytical studies one can resort to investigating the Mathieu equation [27] and soliton perturbation equations [1].

1.9 Reverse proton exchange waveguide based optical parametric oscillators with fiber feedback

This platform is characterized by guided modes possessing low confinement. The mode area is of the order of $\sim 10\mu m^2$. Thus it is difficult to realize sharp bends in this platform. However, we can realize directional couplers that are capable of wavelength filtering, thereby separating the signal and the pump wavelengths in distinct ports. Since the mode area of the waveguides matches closely with the fiber modes, a very low-loss interface is realizable without resorting to tapering or multi-layered structuring. Typical second-harmonic generation efficiency expected in these waveguides are of the order of $\sim 100\%W^{-1}cm^{-2}$ [23]. Details of the fabrication process can be obtained from [17]. An image of the reverse proton exchange waveguide used in our experiments is shown in Fig. 1.4. The name "reverse proton exchange" refers to the fabrication process which involves doping followed by the reverse-proton-exchange step in order to realize buried waveguides for reduced propagation loss.

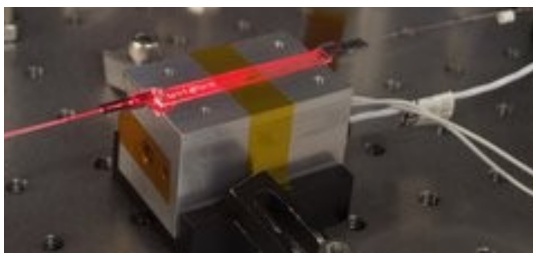

Figure 1.4: **Fiber-coupled reverse proton exchange periodically poled lithium niobate waveguide.** Credits: Dr. Carsten Langorck, and Prof. Martin Fejer.

1.10 Thin-film lithium niobate based integrated optical parametric oscillators

Thin-film lithium niobate on insulator platform provides access to waveguides with a much smaller mode area ($\sim 1\mu m^2$), thanks to the high confinement provided by ridge waveguides [5, 10, 13, 19]. Typical second-harmonic generation efficiency expected in these waveguides are of the order of $\sim 1000\%W^{-1}cm^{-2}$ [29]. Now, it is possible to realize very sharp waveguide bends (limited by bending loss) and one can envision implementing large-scale integrated circuits on lithium niobate. We use X-cut LNOI (lithium niobate on insulator) wafer where silica forms the cladding underneath. Other possible variations include Z-cut lithium niobate and/or using sapphire as the oxide layer. A sapphire-based cladding layer will have a wider transparency window extending into the mid-infrared thereby allowing the operation of integrated devices over the entire transparency range of lithium niobate which extends from approximately 400 nm to 4.5 μm [3, 25]. Lithium niobate is an anisotropic medium with uniaxial anisotropy featuring ordinary and extraordinary refractive indices. Thus an X-cut wafer allows the utilization of the strongest electro-optic co-efficient with TE (transverse electric) mode. However, a Z-cut crystal will potentially allow a continuous poling region along the circumference of the ring which is only constrained to be oriented linearly in an X-cut configuration. Apart from strong second-order nonlinearity ($\sim$ 27 pm/V which is also frequency-dependent), Lithium niobate exhibits various other useful properties namely the electro-optic effect, the piezoelectric, and the ferroelectric effects. This opens up the possibility of realizing active photonic devices that can be tuned at fast time scales (exceeding 100s of GHz) [28, 30]. At the same time, lithium niobate can potentially suffer from pyroelectric and/or photo-refractive effects. To alleviate some of these issues we resort to MgO-doped lithium niobate wafers. Figure 1.5 shows images for etched waveguides and poling profiles used in our integrated nanophotonics experiment.

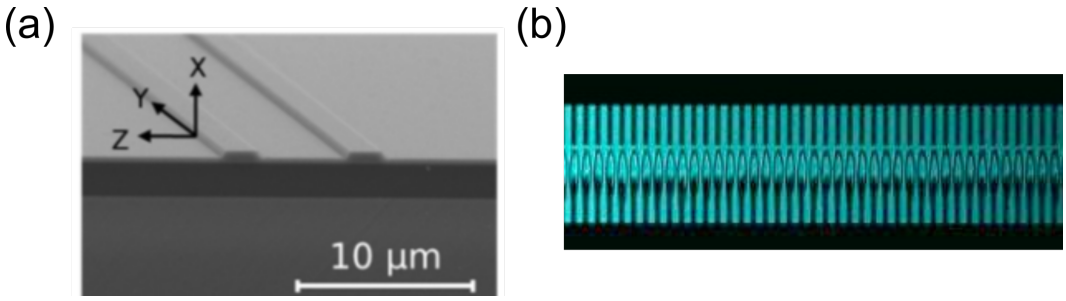

Figure 1.5: **Thin-film lithium niobate nanophotonics platform.** a) SEM image of a ridge waveguide, b) second harmonic microscope image of the poled region showing the periodic poling. Credits: Nonlinear Photonics Group, Caltech.

1.11 Overview of chapters

In this dissertation, we will explore several applications of nonlinear optics in the context of sensing and computing. The overarching goal of the thesis is to investigate how nonlinear dynamics can be engineered to endow photonic devices with enhanced functionalities. These functionalities can be further amplified by enhancing the nonlinear interactions underlying these dynamics. Parametric nonlinear interactions rely on the peak electric field magnitudes and therefore the generation of ultra-short pulses is of paramount importance. **Chapter 2** discusses the generation of ultra-short pulses ($\sim$ 100 of fs) from picosecond long pulses, representing an efficient mechanism of extreme pulse compression. To achieve the same, we operated the degenerate OPO in an unconventional dispersion regime characterized by a large value of the walk-off parameter.

In **Chapter 3**, we discuss the first realization of synchronously pumped OPOs in an integrated lithium niobate nanophotonic platform. This represents a promising mechanism to generate ultra-short pulses (alternatively broadband frequency combs) at arbitrary wavelengths ranging from the visible to the mid-IR. We demonstrate the widely tunable source of coherent radiation that can pave the way for the realization of a universal frequency comb source for interfacing with molecules in the mid-infrared for spectroscopy as well as with atoms in the visible for their applications related to precision measurements.

Chapters 4 and 5 deal with leveraging nonlinear dynamics for sensing applications requiring very high sensitivity. We resort to critical phenomena related to spectral phase transitions in OPOs in this regard. We note that sensing protocols should optimize the overall signal-to-noise ratio that is concerned with measurement precision and not merely sensitivity. We explore the class of

parametrically driven critical phenomena in this regard. We discuss the occurrence of second-order spectral phase transitions in OPOs in **Chapter 4**. We demonstrate the enhanced sensitivity (akin to exceptional points in terms of scaling) to perturbations (reflected in terms of detunings) when the OPO is biased at the critical point by leveraging the continuous spectral splitting corresponding to a degenerate to non-degenerate transition. **Chapter 5** is concerned with its discontinuous counterpart the first-order spectral phase transition that emerges when two OPOs are coupled to each other dispersively. We show how these spectral transitions can be exploited to endow high sensitivity to the underlying linear system which otherwise features low-Q properties associated with low sensitivities. This can potentially allow us to relax the strict fabrication requirements of linear photonic devices and instead utilize nonlinear enhancement.

Chapter 6 describes how we can utilize the second-order spectral phase transition for improving the accuracy of physics-based optimization solvers in the context of finding optimal solutions to hard combinatorial optimization problems. Here we leverage the symmetry unbroken phase of non-degenerate OPOs (XY phase) to explore the optimization energy landscape via the Kuramoto synchronization mechanism. The subsequent steps involve spontaneous symmetry breaking by traversing the spectral phase transition and collapsing into the Ising Hamiltonian adiabatically. Our method represents a distinct protocol in the context of coherent Ising machines consisting of a network of coupled OPOs with potential advantages in terms of solution accuracy for certain problem classes.

Chapter 7 is concerned with the investigation of noise characteristics in OPOs. We provide a comprehensive description of noise behavior in OPOs operating in various regimes (ranging from degenerate to non-degenerate on one hand, and doubly-resonant to singly-resonant on the other). In stark contrast to the rich literature involving phase-noise in lasers, a comprehensive model for OPOs encompassing these various operating regimes is lacking. Our results highlight among others the potential to generate a highly coherent signal from a noisy pump in a singly-resonant OPO. We also bring forth the concept of linewidth enhancement in OPOs associated with phase-mismatched operation. Our formalism provides important insights into the use of optical parametric oscillators as frequency dividers that can inform the design and operation of next-generation OPOs.

Next in **Chapter 8**, we explore the possibility of replacing the gain/loss dynamics exhibited by the conventional gain medium which amounts to phase-insensitive

gain by phase-sensitive amplification/de-amplification that arises in parametrically driven systems. Our motivation is to get rid of the unavoidable fluctuations that accompany phase-insensitive gain in the measurement quadrature of interest. In particular, we explore the interplay of squeezing dynamics and exceptional points for enhancing sensitivity without accompanying noise amplification. In **Chapter 9** we discuss the prospects of topological phenomena in a network of coupled OPOs. We show that these systems exhibit dynamics compared to their linear topological photonic counterparts with important implications in the quantum regime as well. Finally, we conclude by envisioning some of the important research directions that can be pursued in near future.

References

[1] Govind P. Agrawal. Nonlinear fiber optics. In *Nonlinear Science at the Dawn of the 21st Century*, pages 195–211. Springer, 2000.

[2] Nicolas Amiune, Kevin T. Zawilski, Peter G. Schunemann, Karsten Buse, and Ingo Breunig. Pump tuning of a mid-infrared whispering gallery optical parametric oscillator. *Optics Express*, 30(23):41084–41091, 2022.

[3] Andreas Boes, Lin Chang, Carsten Langrock, Mengjie Yu, Mian Zhang, Qiang Lin, Marko Lončar, Martin Fejer, John Bowers, and Arnan Mitchell. Lithium niobate photonics: Unlocking the electromagnetic spectrum. *Science*, 379 (6627):eabj4396, 2023.

[4] Robert W. Boyd. *Nonlinear optics*. Academic Press, 2020.

[5] Alexander W. Bruch, Xianwen Liu, Zheng Gong, Joshua B. Surya, Ming Li, Chang-Ling Zou, and Hong X. Tang. Pockels soliton microcomb. *Nature Photonics*, 15(1):21–27, 2021.

[6] Carlton M. Caves. Quantum limits on noise in linear amplifiers. *Physical Review D*, 26(8):1817, 1982.

[7] Matteo Conforti, Fabio Baronio, and Costantino De Angelis. Nonlinear envelope equation for broadband optical pulses in quadratic media. *Physical Review A*, 81(5):053841, 2010.

[8] Alban Douillet, Jean-jacques Zondy, Giorgio Santarelli, Ala'a Makdissi, and André Clairon. A phase-locked frequency divide-by-3 optical parametric oscillator. *IEEE Transactions on Instrumentation and Measurement*, 50(2): 548–551, 2001.

[9] Robert C. Eckardt, CD Nabors, William J. Kozlovsky, and Robert L. Byer. Optical parametric oscillator frequency tuning and control. *Journal of the Optical Society of America B*, 8(3):646–667, 1991.

[10] Qiushi Guo, Ryoto Sekine, Luis Ledezma, Rajveer Nehra, Devin J. Dean, Arkadev Roy, Robert M. Gray, Saman Jahani, and Alireza Marandi. Femtojoule femtosecond all-optical switching in lithium niobate nanophotonics. *Nature Photonics*, 16(9):625–631, 2022.

[11] Ryan Hamerly, Alireza Marandi, Marc Jankowski, Martin M Fejer, Yoshihisa Yamamoto, and Hideo Mabuchi. Reduced models and design principles for half-harmonic generation in synchronously pumped optical parametric oscillators. *Physical Review A*, 94(6):063809, 2016.

[12] Hubert Heffner. The fundamental noise limit of linear amplifiers. *Proceedings of the IRE*, 50(7):1604–1608, 1962.

[13] Marc Jankowski, Carsten Langrock, Boris Desiatov, Alireza Marandi, Cheng Wang, Mian Zhang, Christopher R. Phillips, Marko Lončar, and Martin M. Fejer. Ultrabroadband nonlinear optics in nanophotonic periodically poled lithium niobate waveguides. *Optica*, 7(1):40–46, 2020.

[14] Marc Jankowski, Jatadhari Mishra, and Martin M. Fejer. Dispersion-engineered nanophotonics: A flexible tool for nonclassical light. *Journal of Physics: Photonics*, 3(4):042005, 2021.

[15] Marc Jankowski, Nayara Jornod, Carsten Langrock, Boris Desiatov, Alireza Marandi, Marko Lončar, and Martin M. Fejer. Quasi-static optical parametric amplification. *Optica*, 9(3):273–279, 2022.

[16] Yohei Kobayashi, Kenji Torizuka, Alireza Marandi, Robert L. Byer, Richard A. McCracken, Zhaowei Zhang, and Derryck T. Reid. Femtosecond optical parametric oscillator frequency combs. *Journal of Optics*, 17(9):094010, 2015.

[17] Carsten Langrock, Martin M. Fejer, Ingmar Hartl, and Martin E. Fermann. Generation of octave-spanning spectra inside reverse-proton-exchanged periodically poled lithium niobate waveguides. *Optics Letters*, 32(17):2478–2480, 2007.

[18] Luis Ledezma, Arkadev Roy, Luis Costa, Ryoto Sekine, Robert Gray, Qiushi Guo, Ryan M. Briggs, and Alireza Marandi. Widely-tunable optical parametric oscillator in lithium niobate nanophotonics. *arXiv preprint arXiv:2203.11482*, 2022.

[19] Luis Ledezma, Ryoto Sekine, Qiushi Guo, Rajveer Nehra, Saman Jahani, and Alireza Marandi. Intense optical parametric amplification in dispersion-engineered nanophotonic lithium niobate waveguides. *Optica*, 9(3):303–308, 2022.

[20] Alireza Marandi, Nick C. Leindecker, Konstantin L. Vodopyanov, and Robert L. Byer. All-optical quantum random bit generation from intrinsically binary phase of parametric oscillators. *Optics express*, 20(17):19322–19330, 2012.

[21] Alireza Marandi, Zhe Wang, Kenta Takata, Robert L. Byer, and Yoshihisa Yamamoto. Network of time-multiplexed optical parametric oscillators as a coherent ising machine. *Nature Photonics*, 8(12):937–942, 2014.

[22] Peter L McMahon, Alireza Marandi, Yoshitaka Haribara, Ryan Hamerly, Carsten Langrock, Shuhei Tamate, Takahiro Inagaki, Hiroki Takesue, Shoko Utsunomiya, Kazuyuki Aihara, et al. A fully programmable 100-spin coherent ising machine with all-to-all connections. *Science*, 354(6312):614–617, 2016.

[23] Chris R. Phillips, Carsten Langrock, Jason S. Pelc, Martin M. Fejer, Ingmar Hartl, and Martin E. Fermann. Supercontinuum generation in quasi-phasematched waveguides. *Optics Express*, 19(20):18754–18773, 2011.

[24] Arkadev Roy, Saman Jahani, Carsten Langrock, Martin Fejer, and Alireza Marandi. Spectral phase transitions in optical parametric oscillators. *Nature Communications*, 12(1):835, 2021.

[25] Arkadev Roy, Luis Ledezma, Luis Costa, Robert Gray, Ryoto Sekine, Qiushi Guo, Mingchen Liu, Ryan M. Briggs, and Alireza Marandi. Visible-to-mid-ir tunable frequency comb in nanophotonics. *arXiv preprint arXiv:2212.08723*, 2022.

[26] Tanay Roy, Suman Kundu, Madhavi Chand, A. M. Vadiraj, Arpit Ranadive, N. Nehra, Meghan P. Patankar, José Aumentado, Aashish A. Clerk, and Rajamani Vijay. Broadband parametric amplification with impedance engineering: Beyond the gain-bandwidth product. *Applied Physics Letters*, 107(26):262601, 2015.

[27] Marcello Calvanese Strinati, Leon Bello, Avi Pe'er, and Emanuele G. Dalla Torre. Theory of coupled parametric oscillators beyond coupled ising spins. *Physical Review A*, 100(2):023835, 2019.

[28] Forrest Valdez, Viphretuo Mere, Xiaoxi Wang, Nicholas Boynton, Thomas A. Friedmann, Shawn Arterburn, Christina Dallo, Andrew T. Pomerene, Andrew L. Starbuck, Douglas C. Trotter, et al. 110 GHz, 110 mW hybrid silicon-lithium niobate Mach-Zehnder modulator. *Scientific Reports*, 12(1): 18611, 2022.

[29] Cheng Wang, Carsten Langrock, Alireza Marandi, Marc Jankowski, Mian Zhang, Boris Desiatov, Martin M. Fejer, and Marko Lončar. Ultrahigh-efficiency wavelength conversion in nanophotonic periodically poled lithium niobate waveguides. *Optica*, 5(11):1438–1441, 2018.

[30] Cheng Wang, Mian Zhang, Xi Chen, Maxime Bertrand, Amirhassan Shams-Ansari, Sethumadhavan Chandrasekhar, Peter Winzer, and Marko Lončar. Integrated lithium niobate electro-optic modulators operating at cmos-compatible voltages. *Nature*, 562(7725):101–104, 2018.

Chapter 2

TEMPORAL WALK-OFF INDUCED DISSIPATIVE QUADRATIC SOLITONS IN OPTICAL PARAMETRIC OSCILLATORS

Roy, Arkadev, Rajveer Nehra, Saman Jahani, Luis Ledezma, Carsten Langrock, Martin Fejer, and Alireza Marandi. Temporal walk-off induced dissipative quadratic solitons. ***Nature Photonics***, 16(2):162–168, 2022. doi: https://doi.org/10.1038/s41566-021-00942-4.
A.R. performed the experiments, executed numerical simulations alongside associated formulations, and participated in the writing of the manuscript.

2.1 Abstract

A plethora of applications has recently motivated extensive efforts on the generation of Kerr solitons and coherent frequency combs. However, the Kerr (cubic) nonlinearity is inherently weak, and in contrast, strong quadratic nonlinearity in optical resonators is expected to provide a promising alternative means for soliton formation. Here, we demonstrate dissipative quadratic soliton formation via non-stationary optical parametric amplification in the presence of significant temporal walk-off between pump and signal leading to half-harmonic generation accompanied by a substantial pulse compression (exceeding a factor of 40) supported at low pump pulse energies ($\sim$ 4 picojoules). The quadratic soliton forms in a low-finesse cavity in both normal and anomalous dispersion regimes. We present a route to significantly improve the performance of the demonstrated quadratic soliton when extended to an integrated platform to realize highly-efficient extreme pulse compression leading to the formation of few-cycle soliton pulses starting from ultra-low energy picosecond scale pump pulses.

2.2 Introduction

Formation of dissipative solitons in nonlinear resonators has become a versatile mechanism for stable femtosecond sources [15, 22]. In the frequency domain it corresponds to a broadband frequency comb which, when self-referenced, leads to a myriad of applications in precision measurements spanning from spectroscopy [10, 37], astro-combs [41, 50], atomic clocks [48], ranging [49, 52], and imaging [20], to name a few. Recently, the ambit of frequency combs has expanded to cover promising avenues including massively parallel data communication [33],

and the realization of machine learning accelerators [54]. To cater to this increasing list of technologically important applications there lies the outstanding challenges of attaining low-power operation [30], high pump to soliton conversion efficiency [3, 4, 40, 55, 56], broadband (octave-spanning and widely tunable) comb formation in a compact platform [46, 47], reliable fabrication and operation of high-Q resonators which need to be addressed.

In the past decade, there has been extensive research on Kerr-based frequency combs where a $\chi^{(3)}$ nonlinear resonator is coherently driven by a continuous wave (CW) laser to excite temporal solitons [15]. However, the Kerr nonlinearity, being a cubic nonlinearity, is inherently weak, and so requires the use of high Q resonators to reach the threshold of parametric oscillation with reasonable pump power. The frequency comb forms around the driving CW laser, and it requires precise dispersion engineering and in some cases, the use of multiple pump lasers [34] to extend the comb to its harmonics and sub-harmonics. These issues can be alleviated by operating with quadratic nonlinearity which can typically cause significant nonlinear mixing at power levels that are orders of magnitude lower than its cubic counterpart [5]. With the ability to perform harmonic conversion through properly phase-matched quadratic nonlinear interactions, $\chi^{(2)}$ nonlinear media promise an ideal platform to realize widely tunable self-referenced frequency combs. Although frequency comb generation through quadratic nonlinearity [28, 35, 36, 38, 39, 42] and femtosecond optical parametric oscillators [27] have been the subject of several theoretical and experimental investigations, demonstration of quadratic soliton formation remains sparse [5, 17].

Fundamental limits on the efficiency (pump to soliton conversion) of CW-pumped Kerr solitons [3, 55] have motivated the study of their pulsed-pump driven arrangements [40, 41]. Modulated pumps also provide additional control on the dynamics of the temporal solitons [7, 12, 16]. Another route to achieve high conversion efficiency is to use low finesse cavities with large outcoupling, where the round-trip loss is compensated by proportionate amplification [11]. Thus soliton formation in a synchronously pumped low-finesse quadratic nonlinear resonator represents a viable route to realize highly efficient widely tunable broadband frequency combs [17].

We demonstrate walk-off induced temporal solitons in a degenerate optical parametric oscillator (OPO) based on pure quadratic nonlinearity. We follow the notion of the dissipative solitons as defined in [2]. We show that the quadratic

soliton can be supported in both normal and anomalous group-velocity dispersion regimes. We also show that this quadratic soliton exists in a low-finesse optical cavity which can lead to high conversion efficiency. We achieved giant pulse compression exceeding a factor of 40 at picojoule level pump energy. We investigate the dynamics of this quadratic soliton and characterize its different regimes of operation. Furthermore, we define a figure of merit that can act as the design guideline for achieving extreme pulse compression and optimum soliton formation in a dispersion-engineered cavity that can be accessed through integrated platforms. Our results pave the way for the generation of energy-efficient dissipative quadratic solitons breaking some of the barriers for the generation of Kerr solitons which demand high Q cavities, feature limited conversion efficiency, require anomalous dispersion for bright soliton formation, and possess limited wavelength tunability.

2.3 Results

We consider a degenerate OPO [14] as illustrated in Fig. 2.1(a) (see Supplementary Section 2.5.1 for a detailed schematic). The OPO is driven synchronously by a pump pulse with a temporal width of several picoseconds. The quadratic nonlinear interaction takes place in a periodically poled lithium niobate waveguide [24, 32] providing parametric interactions between the pump at the fundamental frequency and the signal at the half-harmonic frequency. The cavity is completed with a combination of polarization-maintaining fibers and a suitable free-space section to ensure that the pump repetition rate is approximately equal to multiples of the cavity free-spectral range.

The walk-off induced quadratic soliton formation is supported by a non-stationary optical parametric amplification (OPA) process [1, 21]. The temporal soliton at the half-harmonic (1550 nm) walks through the pump (775 nm) due to the group velocity mismatch (GVM) (see Supplementary Section 2.5.2). This allows a signal pulse that is much shorter than the pump pulse to extract most of the pump energy. In contrast, in a stationary OPA process (with negligible temporal walk-off between the pump and signal), the signal gets amplified without considerable pulse compression as shown in Fig. 2.1(a) [25]. Figure 2.1(b) shows the mechanisms contributing to the nonlinear dynamics of the OPO which are responsible for this quadratic soliton formation. The dissipative soliton loses energy via different dissipation pathways of the low-finesse cavity which include intrinsic cavity round-trip loss and the

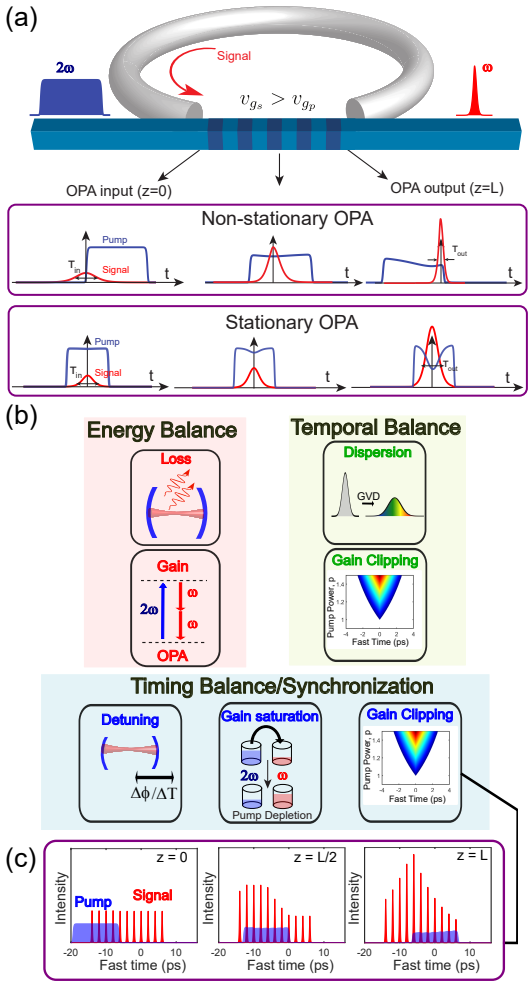

Figure 2.1: **Walk-off induced quadratic soliton formation process.** a) Schematic of the doubly-resonant half-harmonic synchronously pumped OPO with resonant signal and non-resonant pump. The quadratic nonlinear interaction happens in the periodically poled region and, owing to the large GVM between the signal and the pump, significant pulse compression occurs due to the non-stationary OPA process as the signal walks off through the pump. This is contrasted with the stationary OPA case which features negligible temporal walk-off, where the signal amplification is not accompanied by considerable pulse compression. b) The dissipative soliton is sustained in the OPO by a triple balance of energy, temporal broadening, and timing. The energy loss through dissipation is balanced by the parametric gain through the OPA process, while the temporal broadening due to the group-velocity dispersion is arrested by the temporal gain-clipping mechanism. Finally, timing synchronization is achieved by the delicate balance between linear cavity detuning, nonlinear acceleration due to gain saturation, and gain-clipping mechanism. c) Illustration of the temporal gain-gating mechanism, i.e., the dependence of gain on the relative delay between the pump and signal pulses, which is responsible for the gain-clipping. The signal pulse that experiences maximum temporal overlap with the pump pulse throughout the non-stationary OPA process extracts the highest gain.

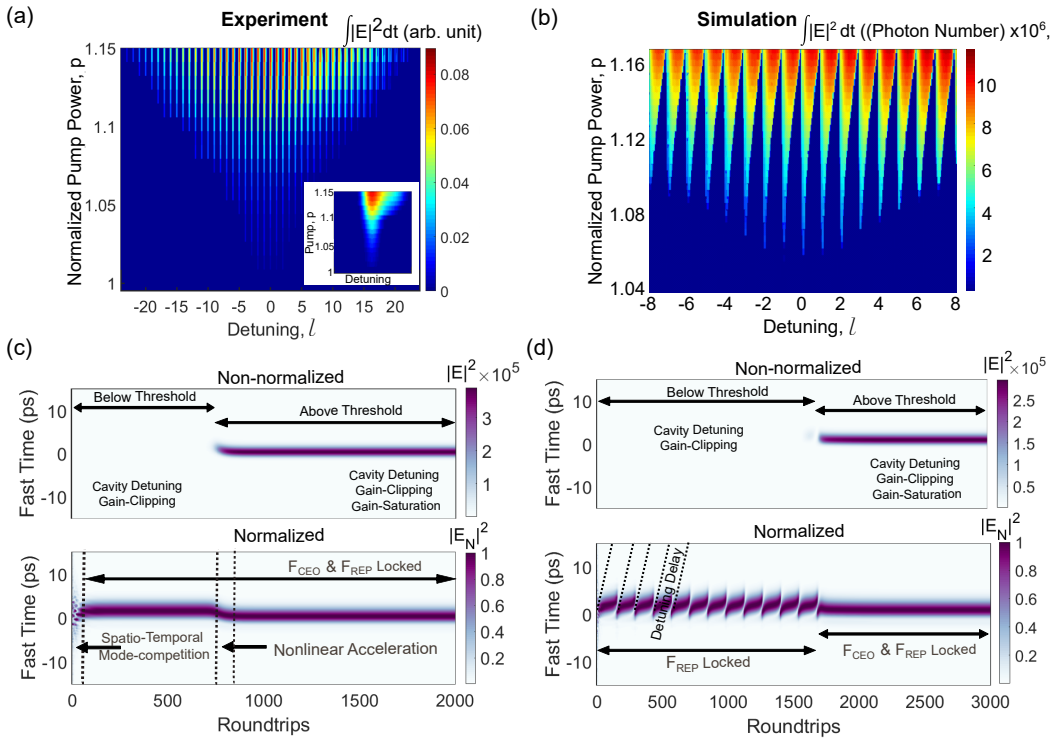

Figure 2.2: **Cavity detuning dependence of doubly-resonant OPO and its impact on synchronization.** Mode-locking range of doubly-resonant sync pumped OPO as a function of cavity detuning obtained a) experimentally and b) via numerical simulation. OPO oscillation occurs around discrete peaks centered at integer values of detuning parameter l. The zoomed-in view of a single peak is shown in the inset. c) Evolution of the intra-cavity OPO field from random noise to the approximate sech-shaped signal soliton pulses in the steady state. (top panel: Non-normalized intensity; bottom panel: Normalized intensity to highlight different dynamical regimes). d) Evolution of the intra-cavity OPO field in the case of large cavity detuning (l = 50) highlighting the importance of gain-saturation and gain-clipping in timing balance/ synchronization (top panel: Non-normalized intensity; bottom panel: Normalized intensity to highlight different synchronization regimes in the large detuning scenario).

out-coupling. This energy loss is counterbalanced by the parametric amplification process. The OPO oscillation threshold occurs when the parametric gain overcomes the loss, and the quadratic soliton is supported near the threshold.

The group-velocity dispersion (GVD) of the medium (waveguide + cavity) leads to temporal pulse broadening. This GVD-induced broadening is prevented by the temporal gain-clipping mechanism (see Supplementary Section 2.5.2) [14]. The pulsed pumping scheme in the synchronously driven OPO leads to a temporal gain window which is responsible for the time gating of the parametric gain and is

expressed by the gain-clipping effect. In Fig. 2.1(c) we consider the unsaturated amplification of several signal pulses with different temporal positions on the fast time scale with respect to the pump pulse. The signal pulse which undergoes the maximal overlap with the pump in the entire non-stationary OPA process experiences the maximum gain. This gain gradually decreases on either side of this optimal temporal position on the fast-time axis, thereby enforcing a temporal gating of the gain. This gain window progressively broadens as the pump power is increased above the threshold. A signal pulse that experiences GVD-induced temporal broadening and extends beyond this temporal gain window will experience a less net gain. This competition between GVD and this gain-clipping mechanism gives rise to the temporal balance.

Finally, the timing balance (synchronization) is determined by the mutual interplay between the linear cavity detuning, gain saturation, and gain clipping. The cavity detuning causes a timing mismatch from exact synchrony with the pump repetition rate. Doubly-resonant OPOs can only oscillate around cavity detunings where the round-trip phase accumulation are integer multiples of π [14]. The cavity detuning phase can be expressed as $\Delta\phi = \pi l$, where integer values of l represent the center of these discrete OPO peaks as shown in Fig. 2.2(a,b). A zoomed-in view of a single peak structure is shown in the inset of Fig. 2.2(a). Within a peak, the OPO can oscillate in degenerate or non-degenerate regimes [44]. We operate at the cavity detuning which corresponds to the degenerate mode of operation in order to access the dissipative quadratic soliton. The timing mismatch (detuning induced delay with respect to the synchronous pumping) can be expressed as $\Delta T = \frac{\lambda l}{2c}$, where c is the group velocity of the half-harmonic signal with wavelength λ in the cavity.

The gain saturation arises due to pump depletion. As the signal walks through the pump (due to the group velocity mismatch) the leading edge of the soliton experiences a larger gain than the trailing edge since the trailing edge experiences the depleted pump. This causes a pulse centroid shift in response to this underlying nonlinear acceleration [17]. The gain-clipping on the other hand is aligned with the pump's temporal position on the fast-time scale and also contributes to the timing balance. The synchronization of the quadratic soliton supported in the synchronously pumped OPO can be expressed in terms of F_{CEO} (Carrier Envelope Offset Frequency) locking, and F_{REP} (Repetition Frequency) locking to the pump. While the doubly-resonant OPO can have multiple modes of operation (see Supplementary Section 2.5.8), the quadratic soliton in the steady state exists in the

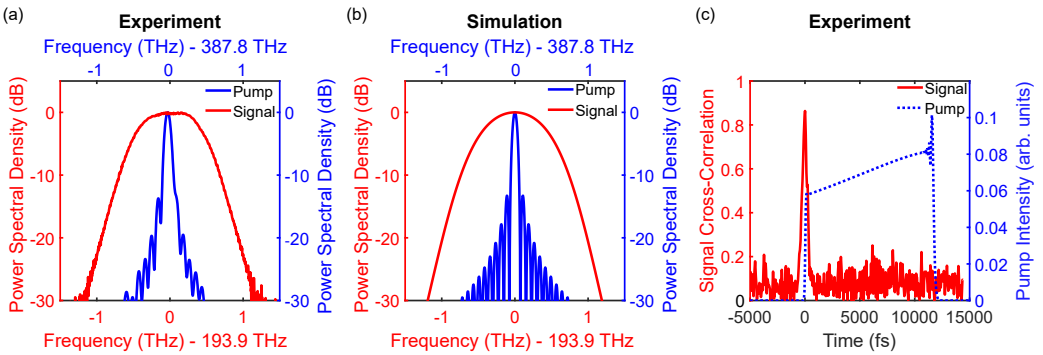

Figure 2.3: **Spectral and temporal characteristics of the quadratic soliton**. The spectrum of the soliton (signal at half-harmonic centered around 193.9 THz represented by red solid line) obtained a) experimentally and b) through numerical simulation. The pump spectrum is represented in blue solid lines centered around 387.8 THz. c) The degenerate half-harmonic quadratic soliton formation is accompanied by significant temporal pulse compression as can be visualized from the intensity cross-correlation trace. The flat-top pump temporal profile ($\sim$ 13.2ps) is shown as the blue dotted line and is obtained by numerical simulation.

F_{REP} and F_{CEO} locked synchronized state. Thus the demonstrated quadratic soliton is capable of transferring the frequency comb stability properties of the pump in addition to the coherent spectral broadening (i.e., the pulse shortening) mechanism. The spontaneous evolution of these solitonic pulses from background noise obtained via numerical simulation is shown in Fig. 2.2(c). The non-normalized version (top panel of Fig. 2.2(c)) and normalized version (bottom panel of Fig. 2.2(c), where the intra-cavity intensity of each round-trip is normalized to itself) of the round-trip evolution highlights the several dynamical regimes of the quadratic soliton formation. The nonlinear dynamics is initiated by spatio-temporal gain competition, followed by gradual building up of the signal/soliton pulse which eventually becomes intense enough to undergo gain-saturation leading to pulse centroid shift/nonlinear acceleration. Finally, the soliton reaches the steady state and maintains synchronization with the pump. Figure 2.2(d) shows the time evolution of the OPO in the case of large cavity detuning. This exemplifies the role of gain-saturation and gain-clipping in timing balance/synchronization. Large cavity detuning is also associated with timing mismatch (from exact synchrony) which results in a pulse delay/ advance each round-trip, as shown in the initial evolution cycles in the bottom panel of Fig. 2.2(d). The slope of this pulse delay is represented by the dotted lines and corresponds to the cavity detuning-induced timing delay (ΔT). Below the

threshold, this large timing mismatch cannot be completely compensated by the gain-clipping mechanism leading to an F_{CEO} unlocked state, where the signal still maintains F_{REP} locking. Above the threshold, the onset of gain-saturation takes place, and the combined effect of gain-saturation and gain-clipping leads to the timing balance resulting in the soliton maintaining synchronization (F_{CEO} and F_{REP} locked) with the pump. The combination of these balancing effects can be elucidated using the semi-analytical variational formalism which expresses the pulse parameters (energy, temporal width, and centroid) in terms of the cavity and driving parameters (see Supplementary Section 2.5.2) [14].

Figure 2.3 shows the measured and simulated spectral and temporal characteristics of the quadratic soliton. Significant spectral broadening of the signal compared to the pump is shown in Fig. 2.3(a,b). The soliton pulse is characterized using an intensity cross-correlation technique as shown in Fig. 2.3(c) overlaid with the pump pulses at the output of the waveguide. The OPO operation at degeneracy is confirmed by the radio-frequency (RF) beat-note measurement (see Supplementary Section 2.5.4).

The quadratic soliton is formed near the oscillation threshold of the OPO. The OPO threshold is associated with a phase transition in the spatiotemporal correlation properties of the quadrature fluctuations and the accompanying symmetry breaking [13]. As the pump power (expressed in the normalized form p denoting the number of times above the threshold) increases further above the threshold, the temporal width of the gain-clipping region increases, and the soliton transitions into the box-pulse regime (see Supplementary Section 2.5.3) [14]. In the box-pulse regime, gain-clipping dominates over the cavity GVD, and the pulse assumes a box-pulse shape, deviating from the approximate sech profile in the near-threshold soliton regime. In the soliton regime, the effect of group-velocity dispersion is counterbalanced by the gain-clipping, and the soliton exhibits characteristic pulse-width variation with a power law dependence on the total cavity dispersion (GDD, group delay dispersion) (scale to the 2/5 power of the GDD, see Supplementary Section 2.5.2), while in the box pulse regime, the pulse length is almost invariant with GDD. This distinct pulse-width scaling is shown in Fig. 2.4(a). Figure 2.4(b) shows an illustrative diagram of the region of existence of different pulse regimes in the parameter space of pump power and dispersion. The soliton regime is accessed close to the threshold. When the pump power is far above the threshold, the system enters the box-pulse regime for large values of dispersion, while multi-pulsing occurs for small values of

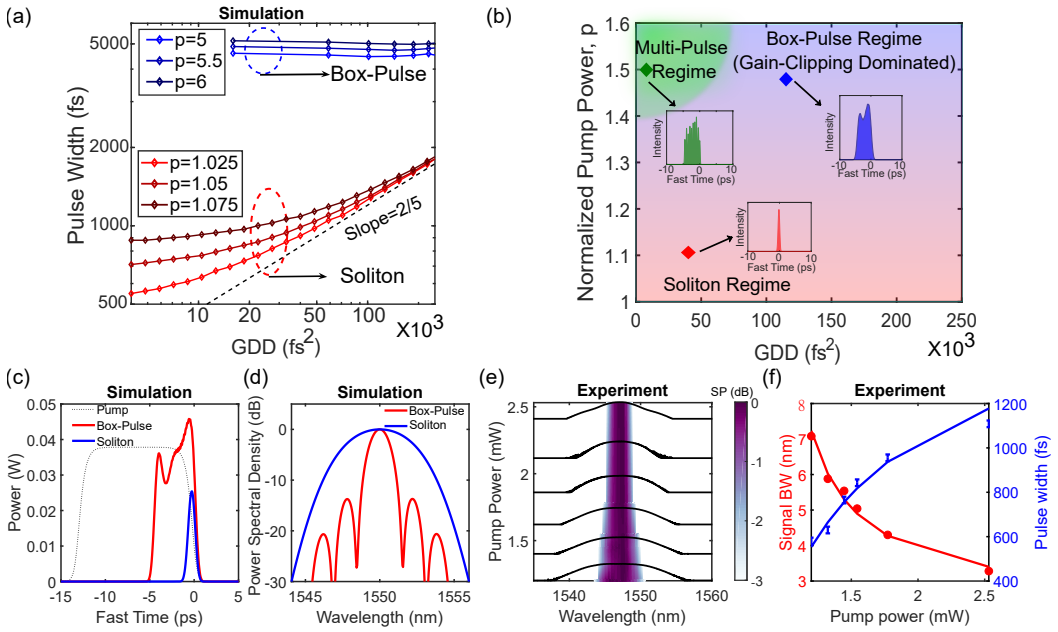

Figure 2.4: **Soliton and Box-pulse regimes.** a) Pulse width scaling as a function of dispersion in the soliton and box-pulse regimes. The soliton pulse width scales linearly (in log-scale) with dispersion, while the pulse width in the box-pulse regime, which is dominated by gain-clipping, is almost independent of dispersion. b) Illustrative phase diagram in the parameter space of pump power and dispersion indicating the region of existence of various pulse regimes (soliton, box-pulse, multi-pulse). c) Temporal profiles and d) spectrum of the OPO in the soliton and box-pulse regimes, respectively. The doubly-resonant OPO supports quadratic soliton near the threshold, and it transits to box-pulse-shaped pulses as the pump power is raised above the threshold. e) Spectral narrowing as the OPO enters further in the box-pulse regime as is evident by the decreasing OPO 3 dB bandwidth. The shading represents the 3dB portion of the spectra. f) The associated temporal broadening reflected in terms of temporal full-width half maximum obtained from the intensity cross-correlation data as the pump power is increased above the threshold. The solid curves represent fit according to the gain-clipping variation. The error bars represent uncertainty associated with the intensity cross-correlation technique.

dispersion. Typical spectral and temporal characteristics of the OPO in the solitonic and box-pulse regimes are shown in Fig. 2.4(c,d). The 3 dB spectral bandwidth of the OPO decreases with increasing pump power as shown in Fig. 2.4(e), and the corresponding variation of the measured full-width at half-maximum of the pulses in the time domain is shown in Fig. 2.4(f). This scaling of the pulse width is distinct from the temporal simultons, which are bright/dark soliton pairs in a quadratic media (see Supplementary Section 2.5.7) [51].

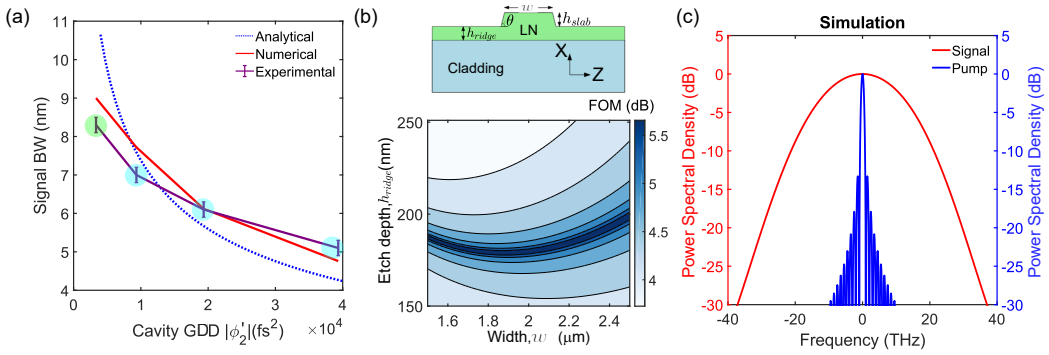

Figure 2.5: **Dispersion engineering and efficient half-harmonic soliton pulse-compression.** a) Variation of the soliton bandwidth as a function of cavity dispersion. Different dispersion configurations are realized in the experiment by altering the combinations of normal (dispersion compensating polarization maintaining fibers) and anomalous dispersion (polarization maintaining fibers) fibers. The blue and green circles refer to the scenarios corresponding to net normal and anomalous cavity dispersion, respectively. The error bars represent variations due to the uncertainty in the number of times above threshold operation in different GDD scenarios. b) Fine control in dispersion engineering is possible in thin-film integrated waveguide-based devices by choosing appropriate etch depth and waveguide width. The FOM defined in (Eq. 2.1) is plotted, where high values of FOM indicate large attainable pulse compression. Here, L is assumed to be 6 mm. c) Numerical simulation corresponding to the optimum FOM showing significant spectral broadening in the soliton formation, corresponding to a pulse compression by a factor of ~ 60.

The soliton pulse width can be obtained from the semi-analytical variational calculations (see Supplementary Section 2.5.2), and its dependence on the cavity parameters can be expressed as: $\tau_{sech} = \left(\frac{7}{15} \frac{\left(\phi_2'\right)^2 T_p}{\ln(G_0)\ln(2)} \right)^{\frac{1}{5}}$, where ϕ_2' is the cavity GDD, $(1 - G_0^{-1})$ represents the round-trip loss, and T_p is the pump pulse width. We have assumed the optimum pump pulse width ($T_p = Lu$, where L is the waveguide length and u is the walk-off parameter) where the pulse width matches

the walk-off length in the waveguide. Also, the contribution of higher-order dispersions has been neglected in deriving this expression. In the limit of GDD $\rightarrow$ 0, the above GDD-dependent approximation of the pulse width breaks down, and the pulse width is instead determined by the higher-order dispersion coefficients (see Supplementary Section 2.5.2). The pulse compression factor can then be expressed as T_p/τ_{sech}. We define a figure of merit (FOM) which is indicative of the amount of pulse compression attained and can serve as the design guidelines for achieving optimum soliton compression. The FOM in a non-zero GDD scenario for a given length (L) of the phase-matched quadratically nonlinear region is defined as (see Supplementary Section 2.5.2):

$$FOM = \left| \frac{u^2 L}{\beta_2} \right|. \tag{2.1}$$

A large value of GVM and a small value of GVD (β_2) (either normal or anomalous) favors efficient soliton compression. Figure 2.5(a) shows the experimental results of variation of soliton spectral bandwidth with changing cavity dispersion that has been realized by combining different lengths of normal and anomalous GVD fibers. Some of these fiber combinations yield net normal cavity GVD (blue circles in Fig. 2.5(a)), and the rest experiences net anomalous cavity GVD (green circles in Fig. 2.5(a)). The quadratic soliton can exist irrespective of the sign of the cavity second order GVD coefficient. Extensive dispersion engineering capability can be accessed through an integrated nanophotonics platform which can be designed to maximize the FOM [18, 19, 25]. Fig 2.5(b) shows the plot of the FOM as the width and etch depth of a typical lithium niobate ridge waveguide are varied (see Supplementary Section 2.5.5). If we now consider a point corresponding to a large value of the FOM, we predict (using numerical simulation) a pulse compression in excess of a factor of 60 for a 6-mm-long parametric gain section (dispersion parameters are reported in Supplementary Section 2.5.5), leading to the generation of few optical cycles pulses starting from picosecond pump pulses as shown in Fig. 2.5(c). Further improvement can be obtained by utilizing longer gain sections and engineering a flat dispersion profile while taking higher-order GVD coefficients into consideration [9].

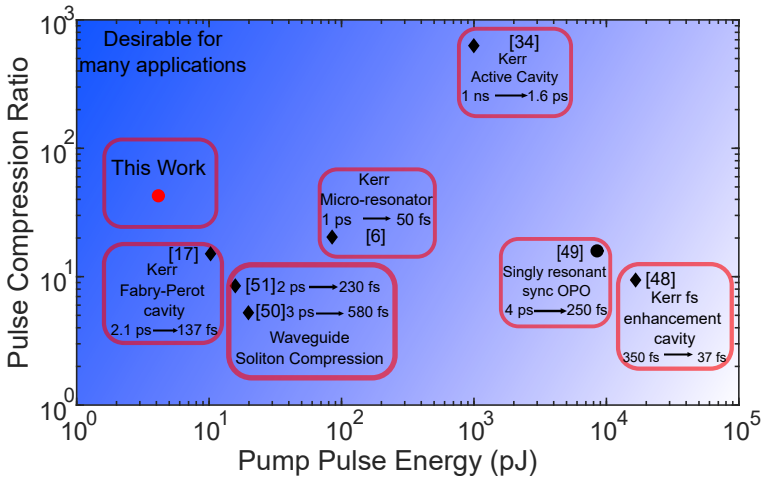

Figure 2.6: **Comparison of existing approaches of quadratic and cubic nonlinearity mediated pulse compression.** The ♦ (Kerr nonlinearity driven) and • (quadratic nonlinearity driven) refer to the data points in the space of the amount of pulse compression attained against the average pump power used as obtained from the corresponding references. A desirable operating condition is the top-left corner of the plot. Here only pulse-driven systems have been considered and the CW-driven soliton generation process has not been included in this comparison.

2.4 Discussion

Figure 2.6 presents an overview of the existing approaches of pulse compression in the parameter space of compression factor and pump pulse energy utilized. Prevailing popular approaches include, but are not limited to, pulse-pumped Kerr solitons [40, 41], Kerr solitons in enhancement cavities [29], Kerr solitons in active cavities [11], singly resonant synchronously pumped OPOs [26], and soliton compression in waveguides [6, 8]. It is highly desirable to attain large compression factors with low pump pulse energy (top-left corner of the landscape in Fig. 2.6). In our work, we have achieved a pump-to-signal pulse-compression factor of ~ 42 which compressed a ~ 13.2 ps flat-top pulse at 775 nm, to ~ 316 fs at 1550 nm corresponding to a 3 dB spectral bandwidth of 8.3 nm. The pump average power was close to 1 mW, which amounts to 4 picojoules of pulse energy. This presents our work as a significant advancement over the existing approaches and elucidates the opportunities associated with soliton generation in quadratic nonlinear resonators. The experimental conversion efficiency is estimated to be near 10% (after considering the effect of insertion losses in the interfaces of the setup), which is consistent with our numerical simulation (see Supplementary Section 2.5.6). Additionally, an extension of the demonstrated concept to integrated nano-photonic

platforms will allow ultra-low power operation with soliton formation possible at several femtojoules of pump pulse energy [18, 25, 30]. The low-finesse operation relaxes fabrication requirements for the on-chip realization of quadratic solitons, and the picosecond pump pulses can be generated using integrated electro-optic modulators [53], thereby paving the way for the complete system integration.

The dissipative quadratic soliton under consideration is reliant on pump pulses, which is unlike CW-driven Kerr solitons but shares similarities to other variants of solitons where a trigger pulse is required [11]. However, the soliton exhibits only a weak dependence on the exact temporal structure of the pump pulse because of the importance of all the balancing mechanisms for the soliton formation.

We should also note that the presented soliton formation is in stark contrast with previous demonstrations of pulse compression in bulk OPOs, where only the non-degenerate signal oscillates [21, 26]. While non-stationary OPA is a common element, the presented soliton formation in doubly-resonant OPOs is rooted in the interplay between phase-sensitive amplification and degenerate signal resonant condition, which is absent in their singly resonant counterparts. This demarcation is further accentuated by the synchronization of both the CEO frequency and the repetition rate to the pump, fixed output wavelength, and low-power operation.

Various modes of operation of degenerate OPOs (DOPO) provide a rich landscape that can cater to the diverse requirements in ultra-short pulse sources in different wavelength ranges [17, 45]. The walk-off induced soliton represents the giant pulse-compression regime of operation of DOPO. In this solitonic regime, the pulse width scales with GDD, and good conversion efficiencies can be achieved on account of low finesse cavity operation. However, due to the gain-clipping dominated box-pulse scaling behavior, the bandwidth decreases with increasing pump power, which prevents it to achieve even higher conversion efficiencies. The simulton regime represents another solitonic mode of operation of DOPOs [17]. In this regime, GVD-free scaling of pulse width is observed, and thanks to the favorable trend of increasing bandwidth with pump power, higher conversion efficiency can be attained. However, the simulton regime requires that the detuning-induced timing mismatch and gain-clipping window are of comparable timescale along with some minimum third-order dispersion for its existence. This leads to a trade-off in terms of the attainable pulse compression and pump power (threshold requirement) (see Supplementary Section 2.5.7). Proper dispersion engineering of an OPO can lead to the formation of simultons in a dispersion

regime where large pulse compression is expected to be accompanied by high ($> 50\%$) conversion efficiencies, (see Supplementary Section 2.5.7).

2.5 Supplementary

2.5.1 Experimental Details

The detailed schematic of the experimental setup is shown in Fig. 2.7. Here, red solid lines (with glows) refer to the free space optical path, blue/orange/red solid lines represent polarization maintaining (PM) fiber-guided optical path (1550 nm/ 780nm/ PM-DCF), and black solid lines represent electrical connections. The wavelength of the light is represented as 775 (775 nm) or 1550 (1550 nm) at various places in the schematic.

The pump at 775 nm which is approximately 13 ps long is prepared by Second Harmonic Generation (SHG) of 1550 nm light coming from mode-locked Menlo optical frequency comb via a 40 mm long Periodically Poled Lithium Niobate (PPLN) bulk crystal. The pump power is controlled by a combination of a Half-wave plate and a polarizer which acts as a Variable Optical Attenuator (VOA). The pump wavelength is controlled by temperature tuning of the PPLN SHG crystal.

The OPO consists of a 40 mm long PPLN reverse-proton exchange waveguide with fiber pigtails [24]. The rest of the cavity is composed of various lengths of polarization-maintaining single-mode fibers and polarization-maintaining dispersion compensating fibers (DCF) to engineer the cavity dispersion. A free-space portion terminated by fiber collimators is incorporated in order to ensure the cavity round-trip time is approximately equal to an integer multiple of the inverse of the mode-locked laser pulse repetition rate (4ns/ 250 MHz). A fiber phase shifter (FBS) is used to lock the cavity via the Pound-Drever-Hall (PDH) locking technique, and a Piezo Transducer (PZT) is used to dither the cavity for the locking purpose. The OPO is sampled using a Pellicle Beam Splitter (BS) having 45% reflectivity. The round-trip loss of the cavity is ~ 12 dB.

The OPO output is filtered by a long pass filter ensuring that there is no residual 775 nm light. The OPO spectrum is characterized by an Optical Spectrum Analyser (OSA). Beat-note measurement (green dashed rectangle) with Local Oscillator (LO) has been performed to monitor the OPO operation at degeneracy/ non-degeneracy. Here the LO is delayed by a suitable amount to ensure temporal overlap between the LO pulses and OPO pulses at the PM fiber coupler. An Electrical Spectrum Analyzer

(ESA) measures the beat-note from the signal received using a fast photo-detector (FPD). Temporal characterization of the OPO pulses has been performed using the intensity non-collinear cross-correlation measurement technique. The OPO output power was not high enough to perform auto-correlation. Instead, we performed SHG cross-correlation on a 0.5 mm thick BBO crystal (angle phase-matched) using an ultra-short (much shorter than the OPO pulses) auxiliary pulse/LO (Menlo Comb output). To enhance the Signal to Noise ratio a lock-in detection scheme was employed using a mechanical chopper and the SHG up-converted signal was detected using an avalanche silicon photo-detector. The LO was scanned using a motorized delay stage.

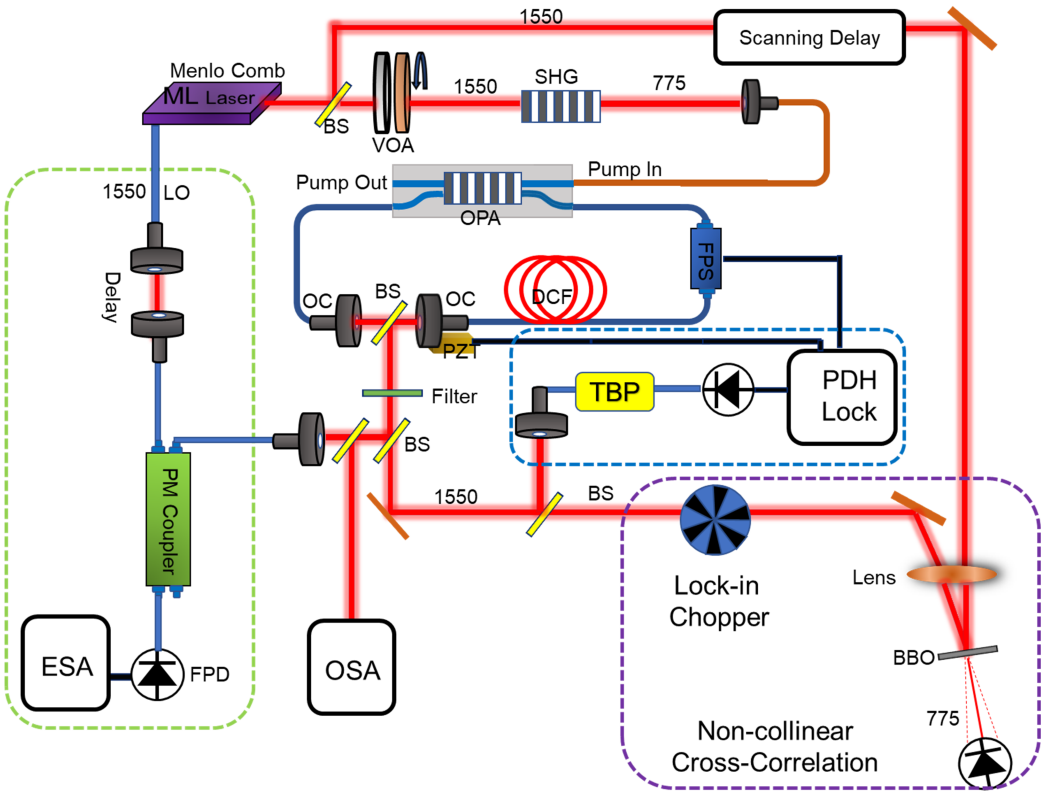

Figure 2.7: **Detailed schematic of the experimental setup.** Abbreviations used are: OPA- Optical Parametric Amplification, SHG- Second Harmonic Generation, VOA- Variable Optical Attenuator, LO- Local Oscillator, OC- Optical Collimator, BS- Beam Splitter, TBP- Tunable Band-pass Filter, ESA- Electrical Spectrum Analyser, OSA- Optical Spectrum Analyser, BBO- Beta-Barium Borate Crystal, FPS- Fiber Phase Shifter, PZT- Piezo Transducer, PDH-Pound Drever Hall, DCF- Dispersion Compensating Fiber, PM- Polarization Maintaining.

2.5.2 Analytical Expression for Soliton Pulse Parameters

Governing Equations

Here, we show the derivation of the dependence of the pulse parameters on the OPO dynamics. The formalism follows the approach in [14]. The evolution of the signal and pump envelopes in the $\chi^{(2)}$ nonlinear waveguide is given by:

$$\frac{\partial a(z,t)}{\partial z} = \left[-\frac{1}{2}\alpha_a - \mathrm{i}\frac{\beta_2^a}{2}\frac{\partial^2}{\partial t^2} + \frac{\beta_3^a}{6}\frac{\partial^3}{\partial t^3} + \dots\right] + \epsilon a^* b \tag{2.2a}$$

$$\frac{\partial b(z,t)}{\partial z} = \left[-\frac{1}{2}\alpha_b - u\frac{\partial}{\partial t} - \mathrm{i}\frac{\beta_2^b}{2}\frac{\partial^2}{\partial t^2} + \frac{\beta_3^b}{6}\frac{\partial^3}{\partial t^3} + \dots\right] - \frac{1}{2}\epsilon a^2 \tag{2.2b}$$

where, a and b represents the signal and pump envelopes, with $\int |a|^2 dt$, $\int |b|^2 dt$ represents the corresponding photon number in the pulse. α_a, α_b are the attenuation co-efficient which we neglect henceforth, since we will be dealing with low Q cavities, and the cavity loss (outside the waveguide) is much higher than the loss in the waveguide propagation. β_2, β_3 denotes the second-order and third-order group velocity dispersion parameters. u represents the walk-off parameter and is given by: $u = \frac{1}{v_g^b} - \frac{1}{v_g^a}$ as the difference of the inverse of the group-velocities. The effective nonlinear coupling is given by ϵ which is expressed as $\epsilon = \frac{2\omega_a \varepsilon_b d_{eff} \int\int E_{T,a}^2 E_{T,b} dx dy}{n_a c}$, with $\varepsilon = \sqrt{\frac{\hbar\omega_b}{2n_n\epsilon_0 c}}$, and E_T are the normalized transverse mode-profile. We assume a flat-top pump profile and will neglect the pump dispersion terms henceforth. The dynamics of the signal outside the waveguide (feedback path) are given by:

$$a_w^{n+1}(0,t) = \mathcal{F}^{-1}\left[G_0^{-\frac{1}{2}} \exp^{-\mathrm{i}\phi} \mathcal{F}\left[a_\omega^n(L,t)\right]\right]. \tag{2.3}$$

Here, $(1 - G_0^{-1})$ is the round-trip cavity loss (including the out-coupling loss and propagation loss/ insertion loss of components), and L is the length of the PPLN waveguide. ϕ is given by: $\phi = \Delta\phi + \frac{l\omega\lambda_a}{2c} + \frac{\phi_2}{2}\omega^2$, where $\Delta\phi = \pi l$ is the cavity detuning, with l when changed in integers results in the cavity being detuned by $\lambda_a/2$ and denotes the peak number in the doubly-resonant OPO scanning peak structure. ϕ_2 represents the cavity group-velocity dispersion contribution. The pump is non-resonant, so no feedback contribution.

The CW threshold of the OPO is given by the pump amplitude $b_0 = \frac{1}{2\epsilon L}\ln(G_0)$. The applied pump amplitude is expressed as $b = pb_0$, where p is the number of

times above the threshold. The pump is a flat-top pulse with amplitude b and width T_p. The optimum pulse width is given by $T_p = Lu$, i.e., when the pump pulse length matches the walk-off length.

The OPO dynamics in each round-trip can be divided into two steps akin to the split-step approach. The first is the **Dispersion step** where the effect of dispersion is included and the pump is assumed to be CW, and the other step is the **Dispersion-less step** where the finite extent of the pump is considered, but the effect of dispersions are neglected.

In the **Dispersion step** the round-trip pulse evolution can be expressed as: $a(\omega; n+1) = \Delta(\omega)a(\omega; n)$, where n is the round-trip number. We define, $D(\delta\omega) = \ln\left(\frac{\Delta(\delta\omega)}{\Delta_{max}}\right)$.

In the **Dispersion-less step** the round-trip pulse evolution can be expressed as: $a(t; n+1) = \Gamma a(t; n)$. We define, $G(t) = \ln(\Gamma)$.

Combining we get: $a(t; n+1) = \Gamma(t)\Delta(\mathrm{i}\frac{d}{dt})a(t; n)$. We can approximate $\Delta \simeq \Delta_{max}(1+D)$ and $\Gamma \simeq 1+G$. This leads to the following OPO master equation:

$$a(t; n+1) = \Delta_{max}\left[1 + G(t) + D(\mathrm{i}\frac{d}{dt})\right]a(t; n). \tag{2.4}$$

Dispersion step: We assume the signal is located at frequency $\omega_a + \delta\omega$ and its counterpart idler is located at $\omega_a - \delta\omega$. We can write the coupled evolution of the signal and the idler in the nonlinear waveguide in the frequency domain as:

$$\begin{bmatrix} a_s(L) \\ a_i(L)^* \end{bmatrix} = \exp\left(\begin{bmatrix} \mathrm{i}\frac{\beta_2^a}{2}(\delta\omega)^2 + \mathrm{i}\frac{\beta_3^a}{6}(\delta\omega)^3 & \epsilon b \\ \epsilon b & -\mathrm{i}\frac{\beta_2^a}{2}(\delta\omega)^2 + \mathrm{i}\frac{\beta_3^a}{6}(\delta\omega)^3 \end{bmatrix} L\right)\begin{bmatrix} a_s(0) \\ a_i(0)^* \end{bmatrix}. \tag{2.5}$$

Including the cavity feedback path we get:

$$\begin{bmatrix} a_s^{n+1} \\ a_i^{*n+1} \end{bmatrix} = G_0^{-\frac{1}{2}}\exp^{\mathrm{i}\left(\frac{\beta_3^a L}{6}(\delta\omega)^3 + \frac{\phi_3}{6}(\delta\omega)^3 + \frac{l\delta\omega\lambda_a}{2c}\right)}\begin{bmatrix} \exp^{\mathrm{i}\left(\frac{\phi_2}{2}(\delta\omega)^2 + \pi l\right)} & 0 \\ 0 & \exp^{-\mathrm{i}\left(\frac{\phi_2}{2}(\delta\omega)^2 + \pi l\right)} \end{bmatrix}$$
$$\exp\left(\begin{bmatrix} \mathrm{i}\frac{\beta_2^a}{2}(\delta\omega)^2 & \epsilon b \\ \epsilon b & -\mathrm{i}\frac{\beta_2^a}{2}(\delta\omega)^2 \end{bmatrix} L\right)\begin{bmatrix} a_s^n \\ a_i^{*n} \end{bmatrix}. \tag{2.6}$$

The gain is given by the larger eigenvalue which is given by:

$$\Delta(\delta\omega) \simeq \Delta_{max}\cos\left(\pi l + \frac{\phi_2^{'}}{2}(\delta\omega)^2\right) \tag{2.7}$$

where, $\phi_2^{'} = \phi_2 + \beta_2^a L$ and $\Delta_{max} = G_0^{\frac{p-1}{2}}$. Thus we get:

$$D(\delta\omega) = \ln\left(\frac{\Delta(\delta\omega)}{\Delta_{max}}\right) \simeq -\frac{\phi_2^{'}}{2}\tan(\pi l)(\delta\omega)^2 - \frac{(\phi_2^{'}\sec(\pi l))^2}{8}(\delta\omega)^4. \tag{2.8}$$

Dispersion-less step: Eq. 2.2(b) (neglecting the dispersions and propagation loss) can be solved using the method of characteristics which gives:

$$b(z,t) = b_{in}(t-uz) - \frac{\epsilon}{2}\int_0^z a(z^{'}, t+u(z^{'}-z))^2 dz^{'}. \tag{2.9}$$

We invoke the gain-without-distortion ansatz. This implies we assume: $a(z^{'},t) = \exp^{\frac{g(z^{'}-z)}{2}} a(z,t)$, where $gL = \ln(G_0)$. Substituting $t^{'} = t + u(z^{'}-z)$ and in the limit, where the walk-off length is much greater than signal pulse width (regime of pulse compression) ($Lu \gg \tau$), we can replace the lower limit $t - uz$ to $-\infty$.

$$b(z,t) = b_{in}(t-uz) - \frac{\epsilon}{2u}\int_{-\infty}^{t} \exp^{\frac{g(t^{'}-t)}{u}} a(z,t^{'})^2 dt^{'} \tag{2.10}$$

This when substituted in Eq. 2.2(a) eliminates the pump in the dispersion-less step:

$$\frac{\partial a(z,t)}{\partial z} = \epsilon a^* b_{in}(t-uz) - \frac{\epsilon^2}{2u}a^*(z,t)\int_{-\infty}^{t} \exp^{\frac{g(t^{'}-t)}{u}} a(z,t^{'})^2 dt^{'}. \tag{2.11}$$

Now removing the DC component of the pump to prevent double-counting in both steps we get:

$$\frac{\partial a(z,t)}{\partial z} = \epsilon a^*\left(b_{in}(t-uz) - b_{max}\right) - \frac{\epsilon^2}{2u}a^*(z,t)\int_{-\infty}^{t} \exp^{\frac{g(t^{'}-t)}{u}} a(z,t^{'})^2 dt^{'}. \tag{2.12}$$

First, we consider the dispersion-less step without gain saturation. We have:

$$\frac{\partial a(z,t)}{\partial z} = \epsilon a^*\left(b_{in}(t-uz) - b_{max}\right). \tag{2.13}$$

This leads to:

$$a^{n+1}(t) \rightarrow a^n(t)\exp^{\int_0^L \epsilon(b_{in}(t-uz)-b_{max})} dz. \tag{2.14}$$

Here, we have assumed $a(t)$ is real resulting from the phase-sensitive amplification. Thus, we get: $G(t) = \int_0^L \epsilon\left(b_{in}(t-uz) - b_{max}\right) dz$. For a flat-top pulse with pulse

width, $T_p = Lu$, we have: $G(t) \simeq -\frac{\epsilon b_{max}|t|}{u} = -\frac{p\ln(G_0)|t|}{2T_p}$. $G(t)$ is known as the **gain-clipping** function.

Now, we consider the dispersion-less step with gain saturation. Near the threshold, we can approximate Eq. 2.10 as:

$$b(z,t) = b_{in}(t-uz) - \frac{\epsilon}{2u}\int_{-\infty}^{t} a(z,t^{'})^2 dt^{'}. \tag{2.15}$$

This leads to:

$$\frac{\partial a(z,t)}{\partial z} = \epsilon a^{*}\left(b_{in}(t-uz) - b_{max}\right) - \frac{\epsilon^2}{2u}a^{*}(z,t)\int_{-\infty}^{t} a(z,t^{'})^2 dt^{'}. \tag{2.16}$$

Sech Ansatz

We assume that the quadratic soliton near the threshold can be expressed as a sech pulse assuming the form:

$$a(z,t) = \frac{A(z)}{\sqrt{2\tau}}\text{sech}\left(\frac{t-T(z)}{\tau(z)}\right). \tag{2.17}$$

Here, the pulse parameters are: $|A|^2$ represents the photon number in the pulse, T represents the centroid of the pulse, and τ represents the width of the pulse. We obtain the evolution of the pulse parameters using the manifold projection method, where the equation of motion given by Eq. 2.16 is projected on the space of sech-shaped pulses of the form given by Eq. 2.17. According to the projection method, the evolution of the pulse parameters $\xi, \xi \in \{A, T, \tau\}$ is given by:

$$\frac{d\xi}{dz} = \frac{\int \frac{\partial a}{\partial \xi}\frac{\partial a}{\partial z}dt}{\int \frac{\partial a}{\partial \xi}\frac{\partial a}{\partial \xi}dt} \tag{2.18}$$

where, $\frac{\partial a}{\partial \xi}$ is calculated using Eq. 2.17 and $\frac{\partial a}{\partial z}$ is calculated using Eq. 2.16.

Along with the evolution governed by Eq. 2.16, perturbations are incorporated due to dispersion and detuning. In the near-threshold limit, this leads to the following equations for the pulse parameters:

$$\frac{dA}{dn} = \left[\frac{p-1}{2}\ln(G_0) - \frac{\ln(G_0)}{2T_p}\ln\left[2\cosh\left(\frac{T}{\tau}\right)\right]\tau - \frac{1}{3}\frac{\phi_2^{'}\tan(\pi l)}{2\tau^2}\right]A - \frac{7}{15}\frac{\left(\phi_2^{'}\sec(\pi l)\right)^2}{8\tau^4}A - \beta A^3 \tag{2.19a}$$

$$\frac{dT}{dn} = \frac{\lambda_a l}{2c} - \tau\beta A^2 - \frac{3\tau^2}{4T_p}\ln(G_0)\tanh\left(\frac{T}{\tau}\right) \tag{2.19b}$$

$$\begin{aligned}\frac{d\tau}{dn} =& \frac{18}{3+\pi^2}\frac{\ln(G_0)}{2T_p}\left[\frac{T}{\tau}\tanh\left(\frac{T}{\tau}\right) - \ln\left[2\cosh\left(\frac{T}{\tau}\right)\right]\right]\tau^2 \\ &+ \frac{12}{3+\pi^2}\frac{\phi_2^{'}\tan(\pi l)}{2\tau} + \frac{168}{5(3+\pi^2)}\frac{\left(\phi_2^{'}\sec(\pi l)\right)^2}{8\tau^3}\end{aligned} \tag{2.19c}$$

where, $\beta = \frac{G_0-1}{8N_{b,0}}$.

In Eq. 2.19(a), the first term on the right represents the CW gain, the $O(\tau)$ represents gain-clipping, while $O(\tau^{-1}), O(\tau^{-3})$ represents dispersion terms. The pulse width at zero detuning ($\Delta\phi$=0), can be calculated by balancing the gain-clipping and dispersion terms. Also, at threshold $T \simeq 0$. We get:

$$\tau_{\text{sech}} = \left(\frac{7}{15}\frac{\left(\phi_2^{'}\right)^2 T_p}{\ln(G_0)\ln(2)}\right)^{\frac{1}{5}}. \tag{2.20}$$

This leads to the characteristic slope of $\frac{2}{5}$ in the log scale plot of pulse width with respect to GDD. Note that, while deriving Eq. 2.20 we have neglected the effect of third-order group-velocity dispersion. When $\phi_2^{'} \to 0$, the contributions from third-order dispersion should be included.

For, $l \neq 0$, (in the degenerate regime), the τ^{-1} term in Eq. 2.19(c) dominates and the pulse width in steady state is given by:

$$\tau_{\text{sech}} = \left(\frac{2}{3}\frac{\phi_2^{'} T_p \tan(\pi l)}{\ln(G_0)\ln(2)}\right)^{\frac{1}{3}}. \tag{2.21}$$

This will lead to the characteristic slope of $\frac{1}{3}$ in the log scale plot of pulse width with respect to GDD.

The agreement between the semi-analytical method described here and the full numerical simulations are shown in Fig. 2.8.

Effect of higher-order dispersion

When the second-order dispersion (GVD) goes to zero, the effect of higher-order dispersions has to be accounted for. The total third order dispersion (TOD) can be expressed as $\phi_3^{'} = \phi_3 + \beta_3 L$, where ϕ_3 is the total TOD of the feedback path, and β_3

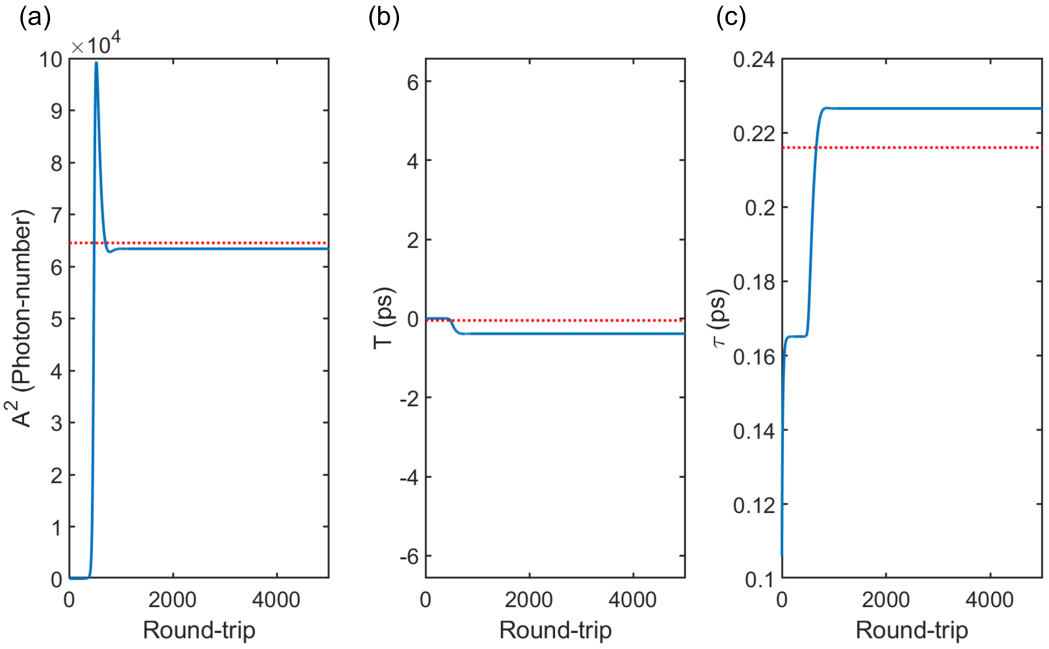

Figure 2.8: **Comparison of semi-analytical calculation and numerical results**. a) Photon-number, b) Centroid, and c) Pulse-width. The red dotted lines represent the steady-state values obtained using numerical simulations. Parameters used are: $p = 1.05, G_0 = 3.3$. The cavity detuning is zero and zero cavity dispersion ($\phi_2 = 0$). The two approaches agree closely in the near-threshold regime.

is the TOD co-efficient of the waveguide in the OPA region. The TOD influences the pulse centroid. In the presence of TOD, Eq. 2.8 is modified as:

$$D(\delta\omega) = \ln\left(\frac{\Delta(\delta\omega)}{\Delta_{max}}\right) \simeq -\frac{\phi_2^{'}}{2}\tan(\pi l)(\delta\omega)^2 - \frac{(\phi_2^{'}\sec(\pi l))^2}{8}(\delta\omega)^4 + \mathrm{i}\frac{\phi_3^{'}}{6}(\delta\omega)^3. \tag{2.22}$$

With this modification, Eq. 2.19(b) is re-written as:

$$\frac{dT}{dn} = \frac{\lambda_a l}{2c} - \tau\beta A^2 - \frac{3\tau^2}{4T_p}\ln(G_0)\tanh\left(\frac{T}{\tau}\right) + \frac{7\phi_3^{'}}{30\tau^2}. \tag{2.23}$$

Assuming, the GDD approaches zero, and the operation close to zero detuning, the governing equations for the soliton parameters can be expressed as:

$$\frac{dA}{dn} = \left[\frac{p-1}{2}\ln(G_0) - \frac{\ln(G_0)}{2T_p}\ln\left[2\cosh\left(\frac{T}{\tau}\right)\right]\tau\right]A - \beta A^3 \tag{2.24a}$$

$$\frac{dT}{dn} = -\tau\beta A^2 - \frac{3\tau^2}{4T_p}\ln(G_0)\tanh\left(\frac{T}{\tau}\right) + \frac{7\phi_3^{'}}{30\tau^2} \tag{2.24b}$$

$$\frac{d\tau}{dn} = \frac{18}{3+\pi^2}\frac{\ln(G_0)}{2T_p}\left[\frac{T}{\tau}\tanh\left(\frac{T}{\tau}\right) - \ln\left[2\cosh\left(\frac{T}{\tau}\right)\right]\right]\tau^2. \tag{2.24c}$$

In this case, close to the threshold, the pulse width will approximately vary as:

$$\tau_{\text{sech}} \propto \left(\frac{\phi_3^{'}T_p}{\ln(G_0)}\right)^{\frac{1}{4}}. \tag{2.25}$$

Thus, near zero GDD the effect of TOD has to be taken into consideration. The simplified formula for FOM defined previously breaks down and one has to consider the effect of higher-order dispersions. The design can then be aided by solving the semi-analytical dynamical equations or resorting to full numerical simulations.

2.5.3 Soliton to Box-pulse transition

In Section 3, we have shown the behavior of the OPO in the soliton regime near the threshold i.e., $p \sim 1$. Here, we study the behavior of the OPO in the box-pulse regime, i.e., $p > 1$. The formalism follows the approach in [14].

In this regime, the pulse dynamics is dominated by the gain-clipping and gain saturation. The effects of dispersion are negligible. We ignore the dispersion and only have to analyze the dispersion-less step to obtain the pulse properties in the box-pulse regime. We consider the signal envelope to be slowly varying and decompose it as: $a(z,t) = \exp^{\frac{gz}{2}}\bar{a}(z,t)$. The evolution of $\bar{a}(z,t)$ can be obtained from Eq. 2.12 as:

$$\frac{\partial\bar{a}(z,t)}{\partial z} = \epsilon\bar{a}\left(b_{in}(t-uz) - b_0\right) - \frac{\epsilon^2}{2u}\exp^{gz}\bar{a}(z,t)\int_{-\infty}^{t}\exp^{\frac{g(t^{'}-t)}{u}}\bar{a}(z,t^{'})^2dt^{'}. \tag{2.26}$$

The solution of Eq. 2.26 can be written as:

$$\bar{a}^{n+1} = \bar{a}^n\exp^{\left[F(t) - \frac{\epsilon^2\left(\exp^{gL}-1\right)}{2gu}\int_{-\infty}^{t}\exp^{\frac{g(t^{'}-t)}{u}}\bar{a}(t^{'})^2dt^{'}\right]} \tag{2.27}$$

where $F(t) = G(t) + \frac{p-1}{2}\ln(G_0)$. $G(t)$ is the usual gain-clipping function. Now, at a steady state, the argument of the exponential should vanish. Clearly, the second term is negative. So, for non-trivial solution $F(t) > 0$. Also, $F(t)$ should be increasing.

This leads to: $\bar{a}(t) \neq 0$, when$-T_p(1-p^{-1}) < t < 0$, and $\bar{a}(t) = 0$, elsewhere. Now, at steady state we can put the argument of the exponent as well as its derivative (Eq. 2.27) to zero yielding:

$$\begin{aligned}\bar{a}(t)^2 =& \frac{2gu}{\epsilon^2\left(\exp^{gL}-1\right)}\left[F^{'}(t)+\frac{g}{u}F(t)\right] \\ =& \frac{2gu}{\epsilon^2\left(\exp^{gL}-1\right)}\left[\frac{\ln(G_0)}{2T_p}p+\frac{\ln^2(G_0)}{2T_p}\left((p-1)-p\frac{|t|}{T_p}\right)\right] \\ =& \frac{4N_{b,0}}{(G_0-1)T_p}\left[p+\ln(G_0)\left(p-1-p\frac{|t|}{T_p}\right)\right].\end{aligned} \tag{2.28}$$

Eq. 2.24 gives $\bar{a}(t)$ for $-T_p(1-p^{-1}) < t < 0$, and $\bar{a}(t) = 0$ elsewhere.

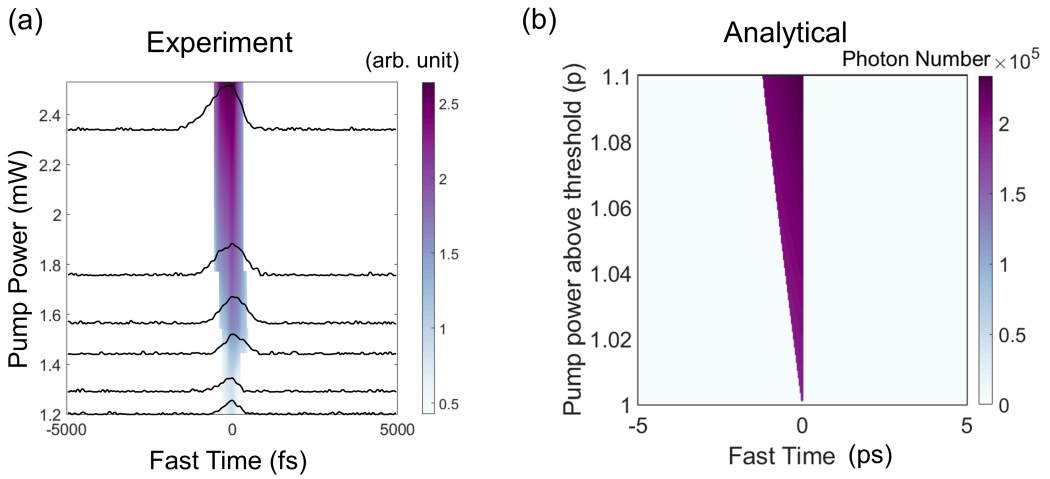

Figure 2.9: **Variation of pulse-width with pump power**. a) Experimentally obtained cross-correlation traces, with the color plot representing the FWHM variation with increasing pump power. b) Pulse shapes obtained from the box-pulse theory using Eq. 2.23.

2.5.4 Beat-note measurement, degenerate and non-degenerate oscillation

Beat-note measurement helps to identify the OPO oscillation regime: degenerate/ non-degenerate. Doubly resonant OPO can oscillate both in degenerate/ non-degenerate regimes, which is a function of the cavity detuning and the cavity dispersion [43]. When the OPO oscillates at degeneracy then the OPO consists of a single signal frequency comb which is phase-locked to the pump. If the OPO oscillates in the non-degenerate regime, then the OPO output consists of both a signal and idler frequency comb having different carrier envelope offset

frequencies. This will give rise to two beat-notes when the OPO output beats with an LO frequency comb.

Degenerate doubly resonant OPO oscillates in a bi-phase state, with a phase that can be denoted as 0 and π. This bi-phase solution is the basis for the operation of coherent Ising machine [31]. Synchronously pumped degenerate OPO can undergo oscillation around different cavity detunings that are separated by pump wavelength [14]. This leads to the well-known doubly resonant degenerate OPO peak structure centered around peak number l, where the cavity detuning is given by $\Delta\phi = \pi l$. l can be odd or even. In a usual synchronously pumped degenerate OPO, where the cavity Free Spectral Range (FSR) is set close to the pump repetition rate, the signal frequency comb can assume two possible comb structures [23]. They are $f_n = \frac{f_{ceo,p}}{2} + nf_{rep}$, or $f_n = \frac{f_{ceo,p}}{2} + \frac{f_{rep}}{2} + nf_{rep}$, where the former is associated with peaks corresponding to even l, whereas the later is associated with peaks corresponding to odd l. Here, f_{rep} is the pump repetition frequency of the mode-locked laser, and $f_{ceo,p}$ is the carrier envelope frequency of the pump frequency comb. This implies that in the degenerate regime, the half-harmonic OPO frequency comb is phase-locked to the pump frequency comb. When $f_n = \frac{f_{ceo,p}}{2} + nf_{rep}$ i.e., l is even, the signal envelope assumes a phase of either 0 or π in successive round-trips. When l is odd, the signal envelope assumes a phase of 0 and π that alternates every other round-trip.

In our experimental configurations, the cavity FSR is a sub-multiple of the repetition rate. Here we consider the case where $FSR = \frac{f_{rep}}{3}$. In the degenerate regime, we observe beat-notes as shown in Fig. 2.10(a,b). In Fig. 2.10(a), the signal envelope can acquire phase: for example 0, 0, π every $\frac{f_{rep}}{3}$. While in the case of Fig. 2.10(b) the signal envelope can assume a phase of 0, π, 0, π, 0, π every $\frac{f_{rep}}{6}$. Clearly, these two cases correspond to odd and even l.

However, in the non-degenerate regime, the OPO doesn't operate in the phase-locked regime and shows a typical beat-note like that shown in Fig. 2.10(c). A typical optical spectrum of non-degenerate OPO is shown in Fig. 2.10(d).

2.5.5 Dispersion engineering

The quadratic soliton bandwidth is a function of cavity dispersion. Here, we present the optical spectrum for different cavity Group Velocity Dispersion (GVD) corresponding to data points in Fig. 2.44(a). These spectra are acquired close to the threshold where the OPO is in the soliton regime and displayed in Fig. 2.11. Different cavity GVD was realized by combining varying lengths of anomalous

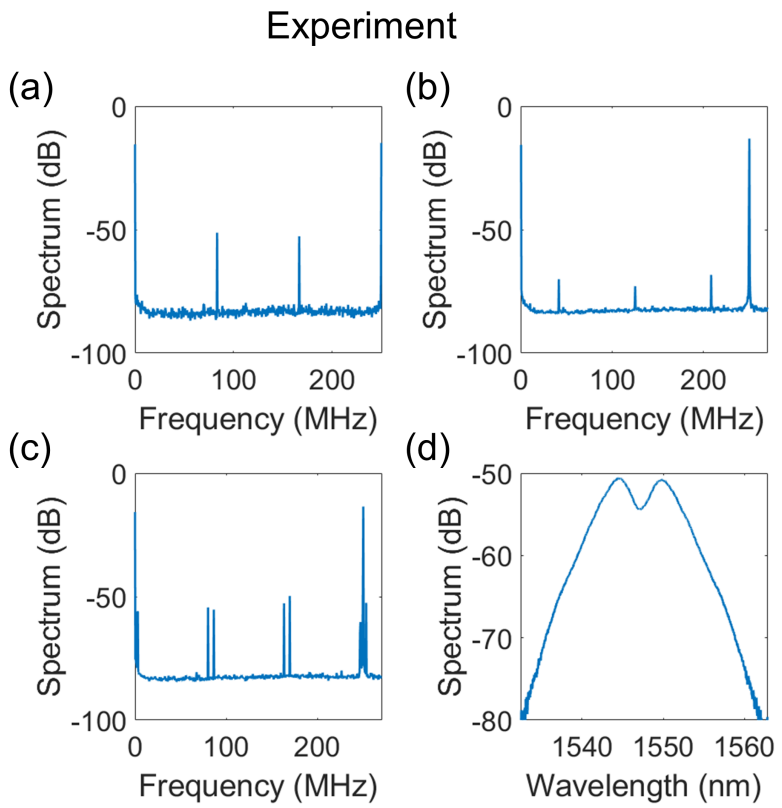

Figure 2.10: **Beat-note characterization of the degenerate and non-degenerate oscillation regime of the OPO**. a) Beat-note spectrum for degenerate OPO for a particular family of l, b) Beat-note spectrum for degenerate OPO for a different family of l, c) Beat-note spectrum for non-degenerate OPO, d) A typical optical spectrum corresponding to a doubly resonant OPO oscillating in non-degeneracy.

PM fiber (GVD $\sim -25 * 10^{-3}\text{ps}^2/\text{mm}$) and normal PM-DCF fiber (GVD $\sim +128 * 10^{-3}$ ps^2/mm).

As we have already seen, the temporal walk-off induced soliton's bandwidth can be increased by deploying larger values of temporal walk-off (GVM) and smaller values of group velocity dispersion (GVD), thereby maximizing the Figure of Merit (FOM). Thin film Lithium niobate platform provides such dispersion engineering capability. Fig. 2.12 shows the dispersion engineering landscape.

The dispersion parameters for the case studied in Fig. 2.5(c) are presented here. The parameters at the pump wavelength (775 nm) are: second-order group velocity dispersion ($\beta_2^b = 40.6$ fs^2/mm), third order dispersion ($\beta_3^b = 25.1$ fs^3/mm). The parameters at the signal wavelength (1550 nm) are: second-order group velocity dispersion ($\beta_2^a = 0.5$ fs^2/mm), third order dispersion ($\beta_3^a = 3.09$ fs^3/mm). The

group velocity mismatch between the pump and the signal is $u = 170$ fs/mm.

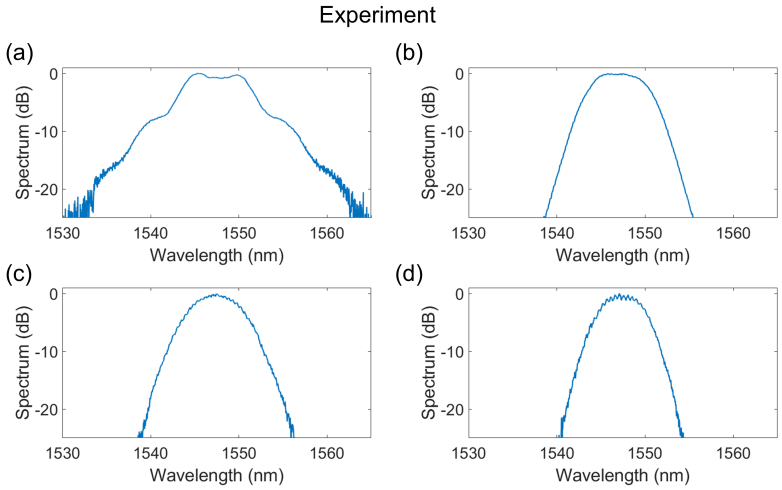

Figure 2.11: **Soiton spectrum as a function of cavity dispersion**. a) Optical spectrum with a 3dB bandwidth of 8.3 nm for cavity GVD $\sim -4 * 10^{-3}$ ps^2/mm b) Optical spectrum with a 3dB bandwidth of 7 nm for cavity GVD $\sim 10 * 10^{-3}$ ps^2/mm c) Optical spectrum with a 3dB bandwidth of 6.1 nm for cavity GVD $\sim 20 * 10^{-3}$ ps^2/mm d) Optical spectrum with a 3dB bandwidth of 5.1 nm for cavity GVD $\sim 40 * 10^{-3}$ ps^2/mm.

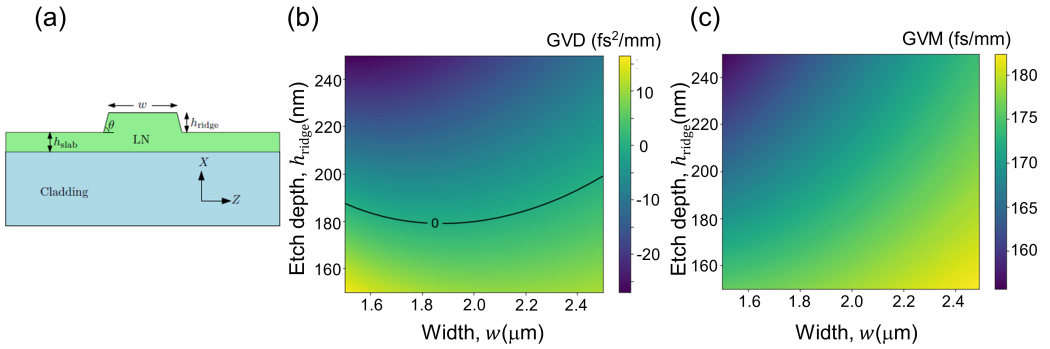

Figure 2.12: **Dispersion engineering possibility on integrated thin film lithium niobate platform**. a) cross-section of a waveguide with the varying width (w), varying etch depth (h_{ridge}), and a thin-film thickness of $h_{ridge} + h_{slab} = 700$ nm of X-cut Lithium niobate. The cladding underneath is SiO_2. b) GVD calculated at 1550 nm for TE_{00} mode for varying parameters c) GVM calculated between the signal at 1550 nm and pump at 775 nm for varying parameters.

2.5.6 Route to high conversion efficiency

Quadratic soliton formation can be supported in the low-finesse cavity. The round-trip loss is to be compensated with parametric gain from the optical parametric

amplification process. When the round-trip loss is dominated by the out-coupling, it is possible to extract high pump-to-soliton conversion efficiency. In the current experiment, however, the roundtrip loss (15 dB) is dominated by coupling losses at the interfaces of the waveguides and fibers while the output coupling is only ~45%. The measured output power at this output coupler is about 1%. When considering the power lost at the interfaces, the total conversion efficiency in the experiment is estimated to be 10%. In numerical simulations, 15 dB of output coupling leads to nearly 10% of conversion efficiency as shown in Fig. 2.13. Note, that even higher parametric gain is achievable in the integrated platform.

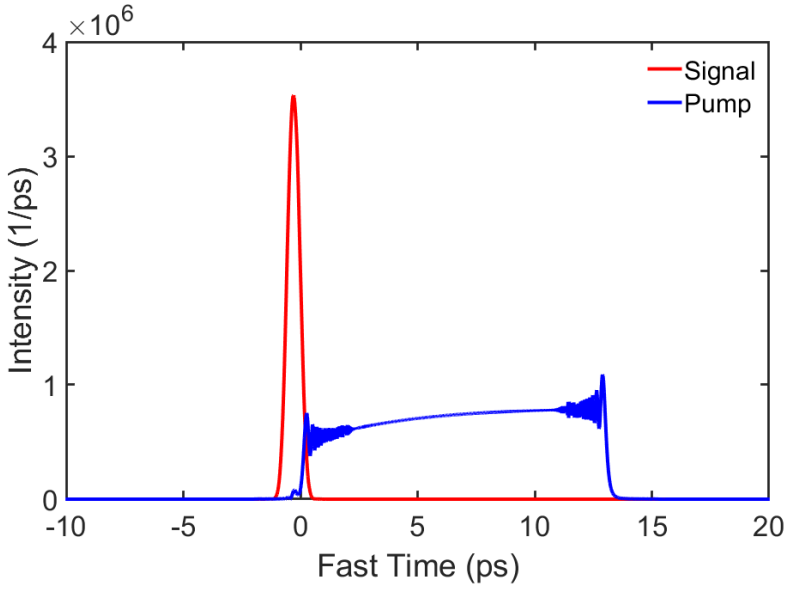

Figure 2.13: **High pump to half-harmonic soliton conversion efficiency achieved with 15 dB round-trip out-coupling**. The plots show the steady state signal and pump temporal profiles at the end of the round-trip. The pump pulse was assumed to be flat-top.

2.5.7 Operating in the simulton regime

Reference [17] has demonstrated the simulton regime of operation, where the timing mismatch (cavity detuning induced delay) is balanced by the gain saturation induced nonlinear acceleration. This regime is accessed when the timing mismatch is in the same order of magnitude as the width of the gain-clipping region. Under this condition, the increase in pump power causes a broadening of the gain-clipping window as well as the amount of nonlinear acceleration which are comparable in magnitude. The amount of nonlinear acceleration should compensate for the timing mismatch for timing balance/ synchronization. If the nonlinear acceleration is very

small as compared to the width of the gain-clipping window, then the gain-clipping dominates, and the OPO follows the box-pulse scaling with the increase in pump power. On the other hand, when the nonlinear acceleration is significant, it leads to an increase in OPO bandwidth with pump power, which is the simulton scaling. Nonlinear acceleration is enhanced with increased pump power and larger OPO pulse width. Thus, to maintain the timing synchronization, the OPO pulse width decreases with increasing pump power. However, this scaling does not continue for ever-increasing pump power. After some point, the gain-clipping contribution will dominate over the nonlinear acceleration component, and this simulton scaling will cease.

In our case, we have been considering a small timing mismatch (several fs), while the gain-clipping window temporal width rapidly grows to picoseconds. This is due to the large pump pulse width ($\sim 13ps$) and large gain per round-trip. In order to access the simulton regime where the timing mismatch is in the order of picoseconds or fraction thereof, we have to operate at large cavity detuning ($l \sim 100$) or more. At the same time, we have to operate at low GVD values. There is another requirement in terms of the minimum amount of third-order dispersion (TOD) required to support simulton operation [9]. For simulton operation, we need to operate in the long detuned cavity region ($l > 0$), so that the nonlinear acceleration can compensate for it. This can be attained by ensuring a minimum amount of positive TOD in the cavity. In this scenario, we can access the simulton regime, as shown in Fig. 2.14. Here, the bandwidth increases with pump power, as opposed to the case of Fig. 2.4(e,f).

Operation in the simulton regime can give access to even higher conversion efficiency. Conversion efficiency exceeding 50% can be achieved. A typical soliton formation in simulton regime is shown in Fig. 2.15. However, the amount of pulse compression will be limited due to the stringent requirement of the TOD.

In the walk-off-induced soliton discussed in this work, the pump depletion is not significant near the threshold. As the soliton walks through the pump, it continuously depletes it. However, in the simulton regime, there is significant pump deletion. Moreover, the signal induces a π phase-shifted pump through second harmonic generation. This creates a bright-dark simulton pair that propagates simultaneously. This is illustrated in Fig. 2.16.

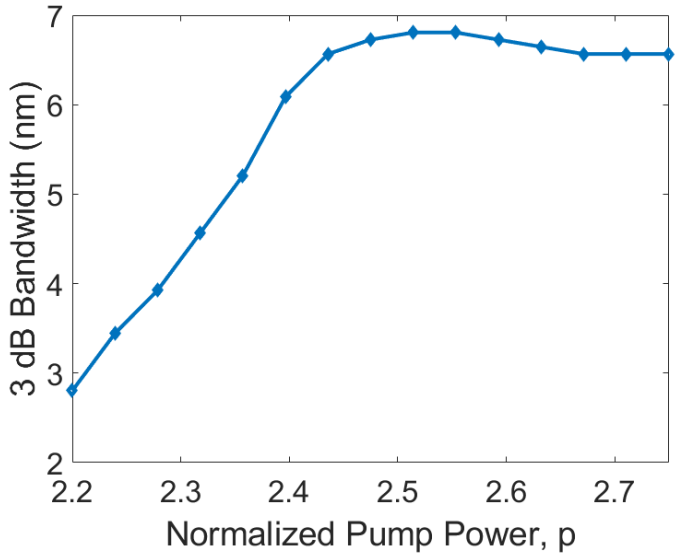

Figure 2.14: **Bandwidth scaling when operated in the simulton regime obtained via numerical simulation**. Here, with an increase in pump power, the OPO bandwidth increases. Parameters used in the simulation are: l = 80, GDD = 0.0045 ps^2, TOD= 0.0091ps^3. Other parameters are kept unchanged.

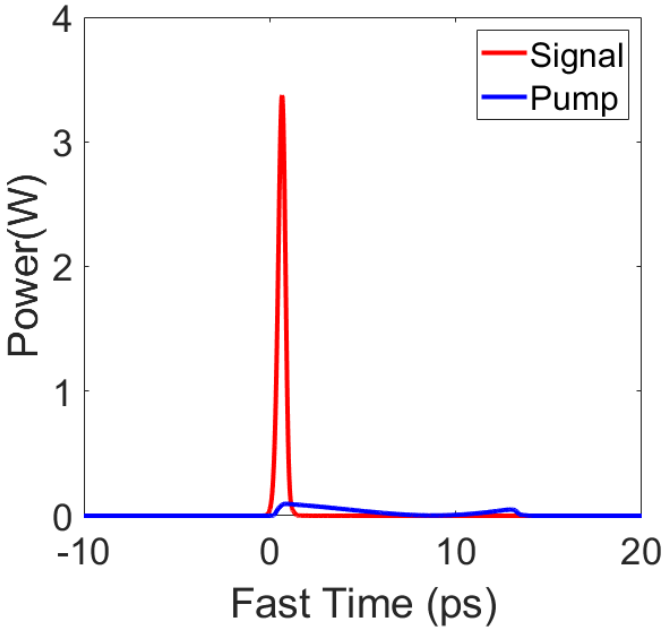

Figure 2.15: **Soliton pulse in simulton regime.** It is characterized by high conversion efficiency. Parameters are the same as in Fig. 2.14.

2.5.8 Effect of Cavity Detuning

Doubly resonant OPO when operating at degeneracy is phase-locked to the pump, and thus its F_{CEO} and F_{REP} are locked with respect to the pump. However, there

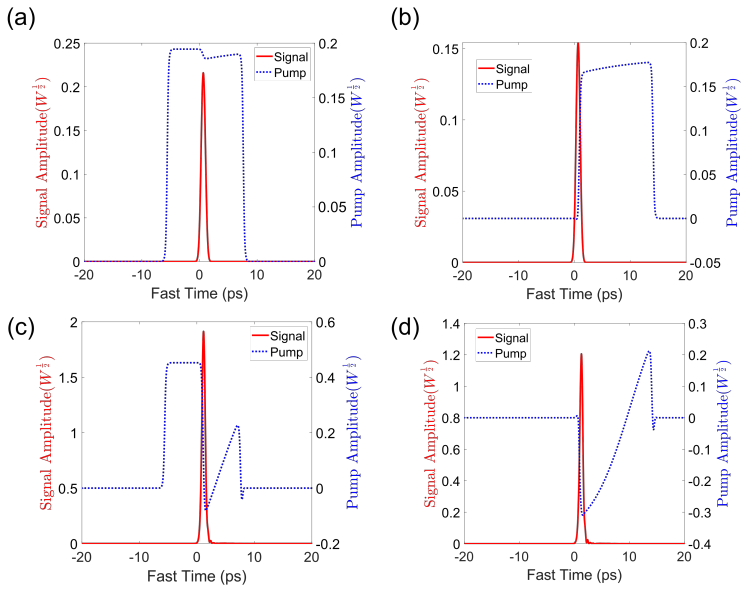

Figure 2.16: **Pump depletion in near-threshold walk-off induced soliton (a,b) and simulton (c,d) regimes.** (a,c) corresponds to the field profiles in the middle of the waveguide, while (b,d) corresponds to the field profiles at the end of the waveguide. The real part of the field profiles for the signal and the pump are plotted.

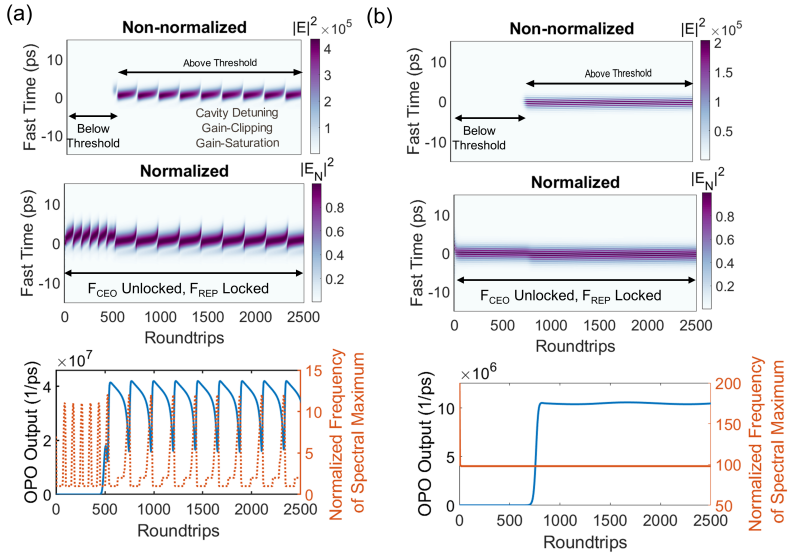

Figure 2.17: **Different modes of synchronization in doubly resonant OPO.** a) via a limit cycle, when the detuning is large. b) operation at non-degeneracy.

are other modes of operation, where the OPO synchronization is enabled by a limit cycle as shown in Fig. 2.17(a). Here, the F_{REP} is locked, while the F_{CEO} is unlocked. This occurs when the OPO operates at large detuning, and the combined

effect of gain saturation and gain-clipping is not enough to counterbalance the effect of cavity detuning-induced drift. Thus the OPO's phase rotates as its spectral components periodically switch between degeneracy and non-degeneracy to maintain synchronization. Similar behavior is also expected for OPO operating at near degeneracy. OPO operating at non-degeneracy also features locked F_{REP} and unlocked F_{CEO} as shown in Fig. 2.17(b).

References

[1] S. Akhmanov, A. Chirkin, K. Drabovich, A. Kovrigin, R. Khokhlov, and Anatoly Sukhorukov. Nonstationary nonlinear optical effects and ultrashort light pulse formation. *IEEE Journal of Quantum Electronics*, 4(10):598–605, 1968.

[2] Nail Akhmediev and Adrian Ankiewicz. *Dissipative solitons: From optics to biology and medicine*, volume 751. Springer Science & Business Media, 2008.

[3] Changjing Bao, Lin Zhang, Andrey Matsko, Yan Yan, Zhe Zhao, Guodong Xie, Anuradha M Agarwal, Lionel C. Kimerling, Jurgen Michel, Lute Maleki, et al. Nonlinear conversion efficiency in Kerr frequency comb generation. *Optics Letters*, 39(21):6126–6129, 2014.

[4] Hualong Bao, Andrew Cooper, Maxwell Rowley, Luigi Di Lauro, Juan Sebastian Totero Gongora, Sai T. Chu, Brent E. Little, Gian-Luca Oppo, Roberto Morandotti, David J. Moss, et al. Laser cavity-soliton microcombs. *Nature Photonics*, 13(6):384–389, 2019.

[5] Alexander W. Bruch, Xianwen Liu, Zheng Gong, Joshua B. Surya, Ming Li, Chang-Ling Zou, Hong Tang, et al. Pockels soliton microcomb. *Nature Photonics*, 15(1):53–58, 2021.

[6] Ju Won Choi, Byoung-Uk Sohn, George F. R. Chen, Doris K. T. Ng, and Dawn T. H. Tan. Soliton-effect optical pulse compression in cmos-compatible ultra-silicon-rich nitride waveguides. *APL Photonics*, 4(11):110804, 2019.

[7] Daniel C. Cole, Jordan R. Stone, Miro Erkintalo, Ki Youl Yang, Xu Yi, Kerry J. Vahala, and Scott B. Papp. Kerr-microresonator solitons from a chirped background. *Optica*, 5(10):1304–1310, 2018.

[8] Pierre Colman, Chad Husko, Sylvain Combrié, Isabelle Sagnes, Chee Wei Wong, and Alfredo De Rossi. Temporal solitons and pulse compression in photonic crystal waveguides. *Nature Photonics*, 4(12):862, 2010.

[9] Christian M. Dietrich, Ihar Babushkin, José R Cardoso de Andrade, Han Rao, Ayhan Demircan, and Uwe Morgner. Higher-order dispersion and the spectral behavior in a doubly resonant optical parametric oscillator. *Optics Letters*, 45 (20):5644–5647, 2020.

[10] Avik Dutt, Chaitanya Joshi, Xingchen Ji, Jaime Cardenas, Yoshitomo Okawachi, Kevin Luke, Alexander L. Gaeta, and Michal Lipson. On-chip dual-comb source for spectroscopy. *Science Advances*, 4(3):e1701858, 2018.

[11] Nicolas Englebert, Carlos Mas Arabí, Pedro Parra-Rivas, Simon-Pierre Gorza, and François Leo. Temporal solitons in a coherently driven active resonator. *Nature Photonics*, pages 1–6, 2021.

[12] Miro Erkintalo, Stuart G. Murdoch, and Stéphane Coen. Phase and intensity control of dissipative Kerr cavity solitons. *Journal of the Royal Society of New Zealand*, pages 1–19, 2021.

[13] Alessandra Gatti and Luigi Lugiato. Quantum images and critical fluctuations in the optical parametric oscillator below threshold. *Physical Review A*, 52(2): 1675, 1995.

[14] Ryan Hamerly, Alireza Marandi, Marc Jankowski, Martin M. Fejer, Yoshihisa Yamamoto, and Hideo Mabuchi. Reduced models and design principles for half-harmonic generation in synchronously pumped optical parametric oscillators. *Physical Review A*, 94(6):063809, 2016.

[15] Tobias Herr, Victor Brasch, John D. Jost, Christine Y. Wang, Nikita M. Kondratiev, Michael L. Gorodetsky, and Tobias J. Kippenberg. Temporal solitons in optical microresonators. *Nature Photonics*, 8(2):145–152, 2014.

[16] Jae K. Jang, Miro Erkintalo, Stephane Coen, and Stuart G. Murdoch. Temporal tweezing of light through the trapping and manipulation of temporal cavity solitons. *Nature Communications*, 6(1):1–7, 2015.

[17] Marc Jankowski, Alireza Marandi, Chris R. Phillips, Ryan Hamerly, Kirk A. Ingold, Robert L. Byer, and Martin M. Fejer. Temporal simultons in optical parametric oscillators. *Physical Review Letters*, 120(5):053904, 2018.

[18] Marc Jankowski, Carsten Langrock, Boris Desiatov, Alireza Marandi, Cheng Wang, Mian Zhang, Christopher R. Phillips, Marko Lončar, and Martin M. Fejer. Ultrabroadband nonlinear optics in nanophotonic periodically poled lithium niobate waveguides. *Optica*, 7(1):40–46, 2020.

[19] Marc Jankowski, Nayara Jornod, Carsten Langrock, Boris Desiatov, Alireza Marandi, Marko Lončar, and Martin M. Fejer. Efficient octave-spanning parametric down-conversion at the picojoule level. *arXiv preprint arXiv:2104.07928*, 2021.

[20] Xingchen Ji, Xinwen Yao, Alexander Klenner, Yu Gan, Alexander L. Gaeta, Christine P. Hendon, and Michal Lipson. Chip-based frequency comb sources for optical coherence tomography. *Optics Express*, 27(14):19896–19905, 2019.

[21] John D. V. Khaydarov, James H. Andrews, and Kenneth D. Singer. Pulse-compression mechanism in a synchronously pumped optical parametric oscillator. *Journal of the Optical Society of America B*, 12(11):2199–2208, 1995.

[22] Tobias J. Kippenberg, Alexander L. Gaeta, Michal Lipson, and Michael L. Gorodetsky. Dissipative Kerr solitons in optical microresonators. *Science*, 361(6402), 2018.

[23] Yohei Kobayashi, Kenji Torizuka, Alireza Marandi, Robert L. Byer, Richard A. McCracken, Zhaowei Zhang, and Derryck T. Reid. Femtosecond optical parametric oscillator frequency combs. *Journal of Optics*, 17(9):094010, 2015.

[24] Carsten Langrock and Martin M. Fejer. Fiber-feedback continuous-wave and synchronously-pumped singly-resonant ring optical parametric oscillators using reverse-proton-exchanged periodically-poled lithium niobate waveguides. *Optics Letters*, 32(15):2263–2265, 2007.

[25] Luis Ledezma, Ryoto Sekine, Qiushi Guo, Rajveer Nehra, Saman Jahani, and Alireza Marandi. Intense optical parametric amplification in dispersion engineered nanophotonic lithium niobate waveguides. *arXiv preprint arXiv:2104.08262*, 2021.

[26] L. Lefort, K. Puech, S. D. Butterworth, Y. P. Svirko, and David C. Hanna. Generation of femtosecond pulses from order-of-magnitude pulse compression in a synchronously pumped optical parametric oscillator based on periodically poled lithium niobate. *Optics Letters*, 24(1):28–30, 1999.

[27] Nick Leindecker, Alireza Marandi, Robert L. Byer, Konstantin L. Vodopyanov, Jie Jiang, Ingmar Hartl, Martin Fermann, and Peter G. Schunemann. Octave-spanning ultrafast OPO with 2.6-6.1 μm instantaneous bandwidth pumped by femtosecond Tm-fiber laser. *Optics Express*, 20(7):7046–7053, 2012.

[28] François Leo, Tobias Hansson, Iolanda Ricciardi, Maurizio De Rosa, Stéphane Coen, Stefan Wabnitz, and Miro Erkintalo. Walk-off-induced modulation instability, temporal pattern formation, and frequency comb generation in cavity-enhanced second-harmonic generation. *Physical Review Letters*, 116 (3):033901, 2016.

[29] Nikolai Lilienfein, Christina Hofer, Maximilian Högner, Tobias Saule, Michael Trubetskov, Volodymyr Pervak, Ernst Fill, Claudius Riek, Alfred Leitenstorfer, Jens Limpert, et al. Temporal solitons in free-space femtosecond enhancement cavities. *Nature Photonics*, 13(3):214–218, 2019.

[30] Juanjuan Lu, Ayed Al Sayem, Zheng Gong, Joshua B. Surya, Chang-Ling Zou, and Hong X. Tang. Ultralow-threshold thin-film lithium niobate optical parametric oscillator. *Optica*, 8(4):539–544, Apr 2021. doi: 10.1364/OPTICA.418984. URL http://www.osapublishing.org/optica/abstract.cfm?URI=optica-8-4-539.

[31] Alireza Marandi, Zhe Wang, Kenta Takata, Robert L. Byer, and Yoshihisa Yamamoto. Network of time-multiplexed optical parametric oscillators as a coherent Ising machine. *Nature Photonics*, 8(12):937, 2014.

[32] Alireza Marandi, Carsten Langrock, Martin M. Fejer, and Robert L. Byer. Guided-wave half-harmonic generation of frequency combs with 75-fold spectral broadening. In *Nonlinear Optics*, pages NM1A–2. Optical Society of America, 2015.

[33] Pablo Marin-Palomo, Juned N. Kemal, Maxim Karpov, Arne Kordts, Joerg Pfeifle, Martin H. P. Pfeiffer, Philipp Trocha, Stefan Wolf, Victor Brasch, Miles H. Anderson, et al. Microresonator-based solitons for massively parallel coherent optical communications. *Nature*, 546(7657):274–279, 2017.

[34] Gregory Moille, Edgar F. Perez, Ashutosh Rao, Xiyuan Lu, Yanne Chembo, and Kartik Srinivasan. Ultra-broadband soliton microcomb through synthetic dispersion. *arXiv preprint arXiv:2102.00301*, 2021.

[35] Simona Mosca, Iolanda Ricciardi, Maria Parisi, Pasquale Maddaloni, Luigi Santamaria, Paolo De Natale, and Maurizio De Rosa. Direct generation of optical frequency combs in χ (2) nonlinear cavities. *Nanophotonics*, 5(2): 316–331, 2016.

[36] Simona Mosca, Melissa Parisi, Iolanda Ricciardi, François Leo, Tobias Hansson, Miro Erkintalo, Pasquale Maddaloni, Paolo De Natale, Stefan Wabnitz, and Maurizio De Rosa. Modulation instability induced frequency comb generation in a continuously pumped optical parametric oscillator. *Physical Review Letters*, 121(9):093903, 2018.

[37] Andrey V. Muraviev, Viktor O. Smolski, Zachary E. Loparo, and Konstantin L. Vodopyanov. Massively parallel sensing of trace molecules and their isotopologues with broadband subharmonic mid-infrared frequency combs. *Nature Photonics*, 12(4):209–214, 2018.

[38] Mingming Nie and Shu-Wei Huang. Quadratic soliton mode-locked degenerate optical parametric oscillator. *Optics Letters*, 45(8):2311–2314, 2020.

[39] Mingming Nie, Yijun Xie, and Shu-Wei Huang. Deterministic generation of parametrically driven dissipative Kerr soliton. *Nanophotonics*, 10(6):1691–1699, 2021.

[40] Ewelina Obrzud, Steve Lecomte, and Tobias Herr. Temporal solitons in microresonators driven by optical pulses. *Nature Photonics*, 11(9):600, 2017.

[41] Ewelina Obrzud, Monica Rainer, Avet Harutyunyan, Miles H. Anderson, Junqiu Liu, Michael Geiselmann, Bruno Chazelas, Stefan Kundermann, Steve Lecomte, Massimo Cecconi, et al. A microphotonic astrocomb. *Nature Photonics*, 13(1):31–35, 2019.

[42] Pedro Parra-Rivas, Lendert Gelens, Tobias Hansson, Stefan Wabnitz, and François Leo. Frequency comb generation through the locking of domain walls in doubly resonant dispersive optical parametric oscillators. *Optics Letters*, 44 (8):2004–2007, 2019.

[43] Arkadev Roy, Saman Jahani, Carsten Langrock, Martin Fejer, and Alireza Marandi. Spectral phase transitions in optical parametric oscillators. *arXiv preprint arXiv:2009.00930*, 2020.

[44] Arkadev Roy, Saman Jahani, Carsten Langrock, Martin Fejer, and Alireza Marandi. Spectral phase transitions in optical parametric oscillators. *Nature Communications*, 12(1):1–9, 2021.

[45] Qitian Ru, Zachary E. Loparo, XiaoSheng Zhang, Sean Crystal, Subith Vasu, Peter G. Schunemann, and Konstantin L. Vodopyanov. Self-referenced octave-wide subharmonic GaP optical parametric oscillator centered at 3 μm and pumped by an Er-fiber laser. *Optics Letters*, 42(22):4756–4759, 2017.

[46] Boqiang Shen, Lin Chang, Junqiu Liu, Heming Wang, Qi-Fan Yang, Chao Xiang, Rui Ning Wang, Jijun He, Tianyi Liu, Weiqiang Xie, et al. Integrated turnkey soliton microcombs. *Nature*, 582(7812):365–369, 2020.

[47] Brian Stern, Xingchen Ji, Yoshitomo Okawachi, Alexander L. Gaeta, and Michal Lipson. Battery-operated integrated frequency comb generator. *Nature*, 562(7727):401–405, 2018.

[48] Liron Stern, Jordan R. Stone, Songbai Kang, Daniel C. Cole, Myoung-Gyun Suh, Connor Fredrick, Zachary Newman, Kerry Vahala, John Kitching, Scott A. Diddams, et al. Direct Kerr frequency comb atomic spectroscopy and stabilization. *Science Advances*, 6(9):eaax6230, 2020.

[49] Myoung-Gyun Suh and Kerry J. Vahala. Soliton microcomb range measurement. *Science*, 359(6378):884–887, 2018.

[50] Myoung-Gyun Suh, Xu Yi, Yu-Hung Lai, Stephanie Leifer, Ivan S. Grudinin, Gautam Vasisht, Emily C. Martin, Michael P. Fitzgerald, et al. Searching for exoplanets using a microresonator astrocomb. *Nature Photonics*, 13(1):25–30, 2019.

[51] Stefano Trillo. Bright and dark simultons in second-harmonic generation. *Optics Letters*, 21(15):1111–1113, 1996.

[52] Philipp Trocha, Maxim Karpov, D Ganin, Martin HP Pfeiffer, Arne Kordts, S Wolf, J Krockenberger, Pablo Marin-Palomo, Claudius Weimann, Sebastian Randel, et al. Ultrafast optical ranging using microresonator soliton frequency combs. *Science*, 359(6378):887–891, 2018.

[53] Cheng Wang, Mian Zhang, Brian Stern, Michal Lipson, and Marko Lončar. Nanophotonic lithium niobate electro-optic modulators. *Optics Express*, 26 (2):1547–1555, 2018.

[54] Xingyuan Xu, Mengxi Tan, Bill Corcoran, Jiayang Wu, Andreas Boes, Thach G Nguyen, Sai T. Chu, Brent E. Little, Damien G. Hicks, Roberto Morandotti, et al. 11 TOPS photonic convolutional accelerator for optical neural networks. *Nature*, 589(7840):44–51, 2021.

[55] Xiaoxiao Xue, Pei-Hsun Wang, Yi Xuan, Minghao Qi, and Andrew M Weiner. Microresonator Kerr frequency combs with high conversion efficiency. *Laser & Photonics Reviews*, 11(1):1600276, 2017.

[56] Xiaoxiao Xue, Xiaoping Zheng, and Bingkun Zhou. Super-efficient temporal solitons in mutually coupled optical cavities. *Nature Photonics*, 13(9):616–622, 2019.

Chapter 3

VISIBLE-TO-MID-IR TUNABLE VISIBLE COMBS FROM NANOPHOTONIC OPTICAL PARAMETRIC OSCILLATORS

Roy, Arkadev[*], Luis Ledezma[*], Luis Costa, Robert Gray, Ryoto Sekine, Qiushi Guo, Mingchen Liu, Ryan M. Briggs, and Alireza Marandi. Visible-to-mid-IR tunable frequency comb in nanophotonics. *arXiv preprint arXiv:2212.08723*, 2022. doi: https://doi.org/10.48550/arXiv.2212.08723.
[*] denotes equal contribution. Parts of this work appeared as post-deadline presentations at the following conferences: CLEO 2022 and Advanced Photonics Congress 2022. **A.R.** contributed to the experiments, performed numerical simulations, and participated in the writing of the manuscript.

3.1 Abstract

Optical frequency comb is an enabling technology for a multitude of applications from metrology to ranging and communications. The tremendous progress in sources of optical frequency combs has mostly been centered around the near-infrared spectral region while many applications demand sources in the visible and mid-infrared, which have so far been challenging to achieve, especially in nanophotonics. Here, we report frequency combs tunable from visible to mid-infrared on a single chip based on ultra-widely tunable optical parametric oscillators in lithium niobate nanophotonics. Using picosecond-long pump pulses around 1 μm and tuning of the quasi-phase matching, we show sub-picosecond frequency combs tunable beyond an octave extending from 1.5 μm up to 3.3 μm with femtojoule-level thresholds. We utilize the up-conversion of the infrared combs to generate visible frequency combs reaching 620 nm on the same chip. The ultra-broadband tunability and visible-to-mid-infrared spectral coverage of our nanophotonic source can be combined with an on-chip picosecond source as its pump, as well as pulse shortening and spectral broadening mechanisms at its output, all of which are readily available in lithium niobate nanophotonics. Our results highlight a practical and universal path for the realization of efficient frequency comb sources in nanophotonics overcoming their spectral sparsity.

3.2 Introduction

Optical frequency combs consisting of several spectral lines with accurate frequencies are at the core of a plethora of modern-day applications [7, 22], including spectroscopy [4], optical communication [32], optical computing [53], atomic clocks [45], ranging [46, 49], and imaging [21]. Many of these applications demand optical frequency combs in the technologically important mid-infrared [8, 43] and visible [37, 47] spectral regimes. Accessing optical frequency comb sources in integrated photonic platforms is of paramount importance for the translation of many of these technologies to real-world applications and devices [44]. Despite outstanding progress in that direction in the near-infrared, there is a dearth of widely tunable frequency comb sources, especially in the highly desired mid-infrared and visible spectral regimes.

Notable efforts on miniaturized mid-IR comb sources typically rely on supercontinuum generation, and/or intra-pulse difference frequency generation [12, 23]. Not only do these nonlinear processes usually require a femtosecond pump as an input (which has its own challenges for efficient on-chip manifestation), but their power is also distributed over a wide frequency range including undesired spectral bands. Engineered semiconductor devices like quantum cascade lasers have successfully been demonstrated as mid-infrared frequency comb sources [19], however, they are not tunable over a broad wavelength range and are still difficult to operate in the ultrashort pulse regime [52, 55]. The situation is exacerbated by the lack of a suitable laser gain medium that is amenable to room temperature operation in the mid-IR. Kerr nonlinearity can lead to tunable broadband radiation [11, 42, 57] but is contingent on satisfying demanding resonator quality factor requirements and typically relies on a mid-IR pump to begin with for subsequent mid-infrared frequency comb generation. Similar challenges exist for Raman-based mid-IR frequency comb generation [48].

On the other hand, optical parametric oscillators (OPOs) based on quadratic nonlinearity have been the predominant way of accessing tunable coherent radiation in the mid-IR spectral region enjoying broadband tunability through appropriate phase matching of the three-wave mixing [8]. However, their impressive generation of tunable frequency combs in the mid-infrared have been limited to bulky free-space configurations pumped by femtosecond lasers [1, 31]. Recently, integrated quadratic OPOs are realized in the near-IR, using high-Q resonators with pump-resonant designs [3, 16, 29], which have not been able to

access the broad tunability of phase matching and mid-IR frequency comb generation.

We demonstrate ultra-widely tunable frequency comb generation from on-chip OPOs in lithium niobate nanophotonics. Leveraging the ability to control the phase-matching via periodic poling combined with dispersion engineering, we show an on-chip tuning range that exceeds an octave. We pump the OPOs with picosecond pulses from an electro-optic frequency comb source in the near-IR, which is already demonstrated to be compatible with nanophotonic lithium niobate [18, 58, 59]. The demonstrated frequency combs cover the typical communication bands and extend into the mid-infrared spectral region beyond 3 μm with instantaneous bandwidths supporting sub-picosecond pulse durations. Additionally, the same chip produces tunable frequency combs in the visible resulting from up-conversion processes. Tunable visible frequency comb realization has been challenging owing to the absence of a suitable broadband gain medium and the typical large normal dispersion at these wavelengths in most integrated photonic platforms [14, 30].

3.3 Results

To achieve broadband and widely-tunable frequency combs, we design a doubly-resonant OPO [15, 24, 40] based on nano-waveguides etched on X-cut 700-nm-thick MgO-doped lithium niobate, which is illustrated in Fig. 3.1(a). Unlike the previous triply-resonant designs [3, 16, 29], our design provides access to the wide tunability of quasi-phase-matching (QPM) and avoids stringent requirements such as ensuring the resonance of the pump [9]. Doubly resonant operation is achieved by controlling the precise spectral response of the OPO resonator using two spectrally selective adiabatic couplers (highlighted in Fig. 3.1(a)) that only let the long wavelengths (signal and idler) to resonate in the OPO while allowing the short wavelengths (pump and up-converted light) to leave the cavity (see Supplementary Section 3.6.2). This is not only important for achieving a broad tuning range for the signal and the idler, but it also enables non-resonant broadband and widely tunable up-conversion into the visible, which is in stark contrast with previous parametric sources in that range [14, 30]. Another important aspect of the on-chip OPO design is the dispersion engineering of the main interaction waveguide of the OPO, which in combination with periodic poling leads to broad spectral coverage of the QPM tuning. Engineering the dispersion of the remainder of the resonator is another important design degree of

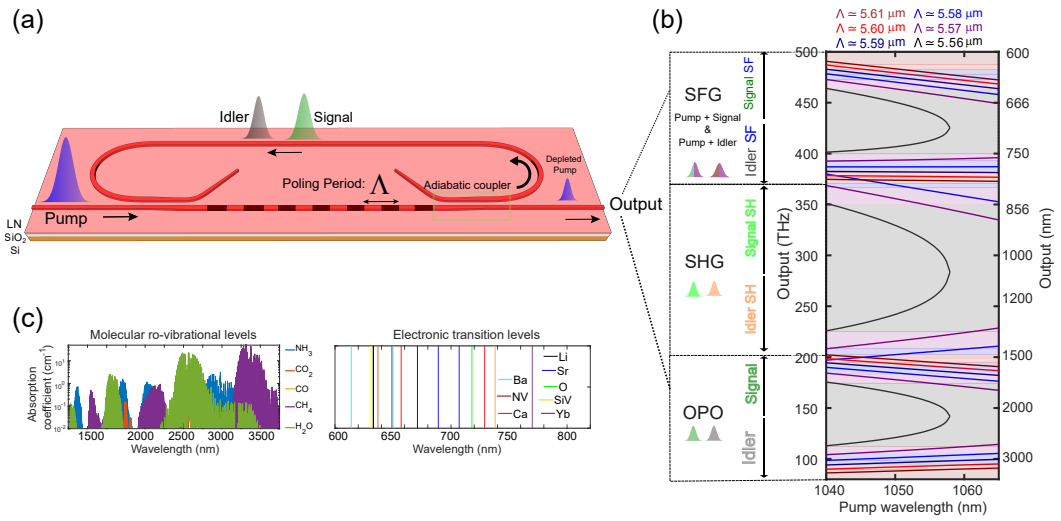

Figure 3.1: **Ultra-widely tunable frequency combs from nanophotonic parametric oscillators.** a) Schematic of a doubly resonant optical parametric oscillator fabricated on an X-cut thin-film lithium niobate consisting of a periodically poled region for efficient parametric nonlinear interaction. The waveguides (dimensions: width of 2.5 μm, etch depth of 250 nm) support guided modes in the mid-infrared corresponding to the idler wave. b) Quasi-phase matched parametric gain tuning from visible-to-mid-IR. Phase-matching curves leading to tunable mid-infrared idler emission enabled by optical parametric oscillator devices with slightly different poling periods (Λ) integrated on the same chip. The same chip is capable of producing tunable visible frequency combs thanks to the sum frequency generation (SFG) process between the pump with the signal and idler waves. Other accompanying up-conversion processes include the second-harmonic (SH) of the signal and the idler. Some second-harmonic phase-matching curves have been omitted for better clarity. c) The emission from the chip overlaps with strong molecular absorption lines in the mid-infrared covering a spectral window important for molecular spectroscopy. The spectral coverage in the visible includes atomic transition wavelengths corresponding to commonly used trapped ions/ neutral atoms/ color centers.

freedom that can be further utilized for achieving quadratic solitons and pulse compression mechanisms [41].

Quadratic parametric nonlinear interactions take place in a 5-mm-long poled waveguide region, which has a fixed poling period (Λ) for each OPO on the chip. The periodic poling phase matches parametric nonlinear interaction between the pump, the signal, and the idler waves which can be tuned from degeneracy to far non-degeneracy. The chip consists of multiple OPOs with poling periods for type-0 phase matching of down-conversion of a non-resonant pump at around 1 um

to an octave-spanning range of resonant signal and idler wavelengths, i.e., the OPO output. The QPM tuning curves are shown in Fig. 3.1(b). In addition to these OPO outputs, the poled waveguide also provides additional parametric up-conversion processes, notably the second-harmonic of the signal/idler, and the sum-frequency generation from the pump and signal/idler. The overall tuning range of the chip overlaps with many molecular and atomic transitions as illustrated in Fig. 3.1(c). The strong spatiotemporal confinement of the interacting waves in the waveguide guarantees substantial up-conversion efficiencies which can be further enhanced with the addition of proper poling periods and tailoring to specific applications (see Supplementary Section 3.6.1).

As shown in Fig. 3.1(b), to continuously cover the visible to the mid-infrared, we focus on tuning the QPM by coarsely switching the poling period as well as fine-tuning the pump wavelength over ~25 nm. It is worth noting that this tuning range for the pump is compatible with the existing semiconductor lasers [50]. Moreover, the coarse switching of the poling period can be achieved without mechanical movements for instance by means of electro-optic routing (see Supplementary Section 3.6.8). In addition, temperature tuning of the poled region can provide another substantial tuning mechanism (see Supplementary Section 3.6.9). The emission from the OPO chip covers important wavelengths corresponding to atomic transitions in the visible as well as molecular absorption lines in the mid-infrared (Fig. 3.1(c)).

The OPO is synchronously pumped [27, 36, 40] by ~ 1-ps-long pulses operating at a repetition rate of approximately 19 GHz. The repetition rate was tuned close to the OPO cavity free spectral range or its harmonics (see Supplementary Section 3.6.5). The octave-wide tunability of the parametric oscillation from the OPO chip is obtained by tuning the pump central wavelength between 1040 nm and 1065 nm only. The pump is generated from an electro-optic frequency comb [39] (see Supplementary Section 3.6.3). The schematic of the experimental setup is shown in Fig. 3.2(a). The spectral and temporal characteristics of the near-infrared pump are shown in Fig. 3.2(b).

Figure 3.2(c) shows the broad spectral coverage of the OPO output extending up to 3.3 μm in the mid-infrared obtained from a single chip. The comb lines can be resolved by the optical spectrum analyzer (OSA) and can be seen in the inset, where the separation of the peaks corresponds to the pump repetition rate. The on-chip threshold amounts to approximately 1 mW of average power (~ 50 mW of

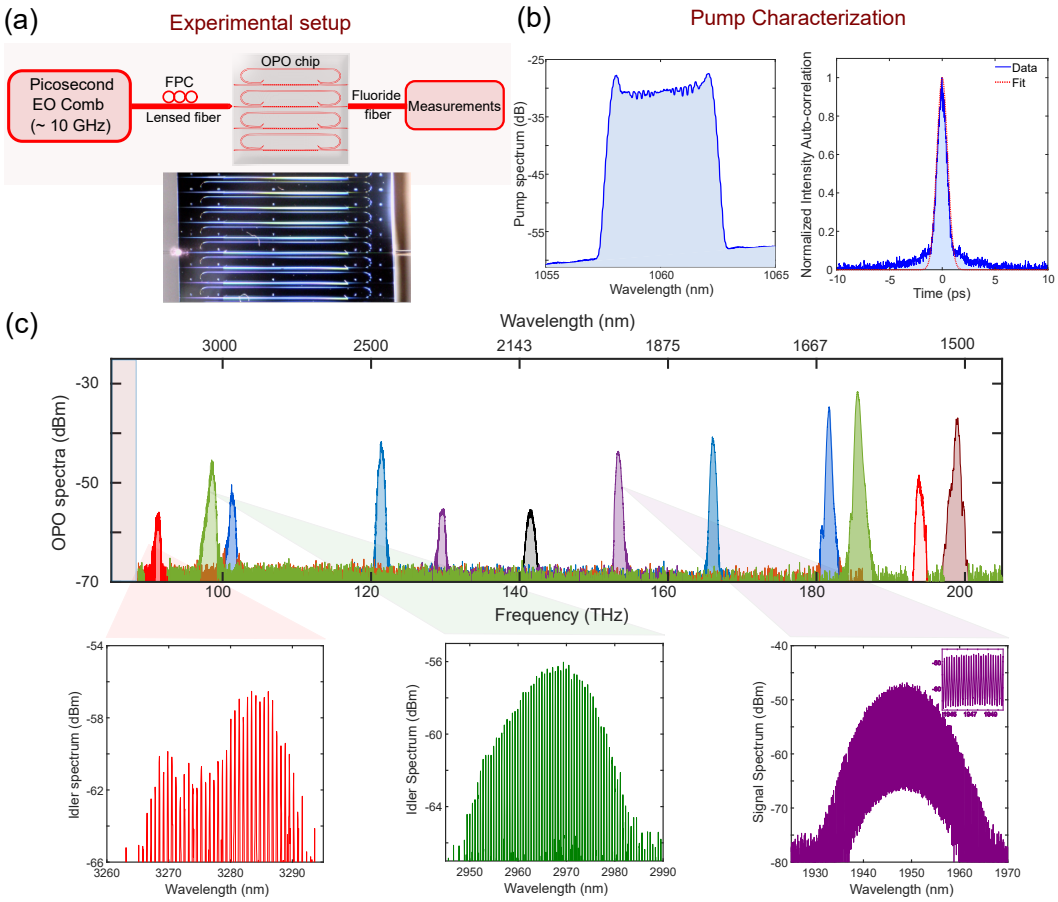

Figure 3.2: **Near-IR to mid-IR frequency combs from nanophotonic OPOs on a single chip.** a) Schematic of the experimental setup used to pump and measure the synchronously pumped optical parametric oscillator chip. The image of the OPO chip is shown alongside, b) Experimental measurements of the spectral and temporal characteristics (intensity auto-correlation trace) of the electro-optic pulsed pump showing a pulse-width of ~ 1 ps, c) Broadband infrared spectral coverage of the OPO chip showing the signal and the idler spectrum as its operation is tuned from degeneracy to far non-degeneracy. Separate colors represent outputs from different OPO devices on the same chip with distinct poling periods. Zoomed-in versions display the comb line structure.

peak power, and ~ 100 femtojoules of pulse energy) for the near-degenerate OPOs. The signal conversion efficiency approaches ~ 5% for the near-degenerate OPOs, while the mid-infrared (3.3 μm) idler conversion efficiency exceeds 1% for the far non-degenerate OPOs (see Supplementary Section 3.6.2). This corresponds to an estimated ~ 25 mW of peak power and ~ 5 μW of power per comb line in the mid-infrared.

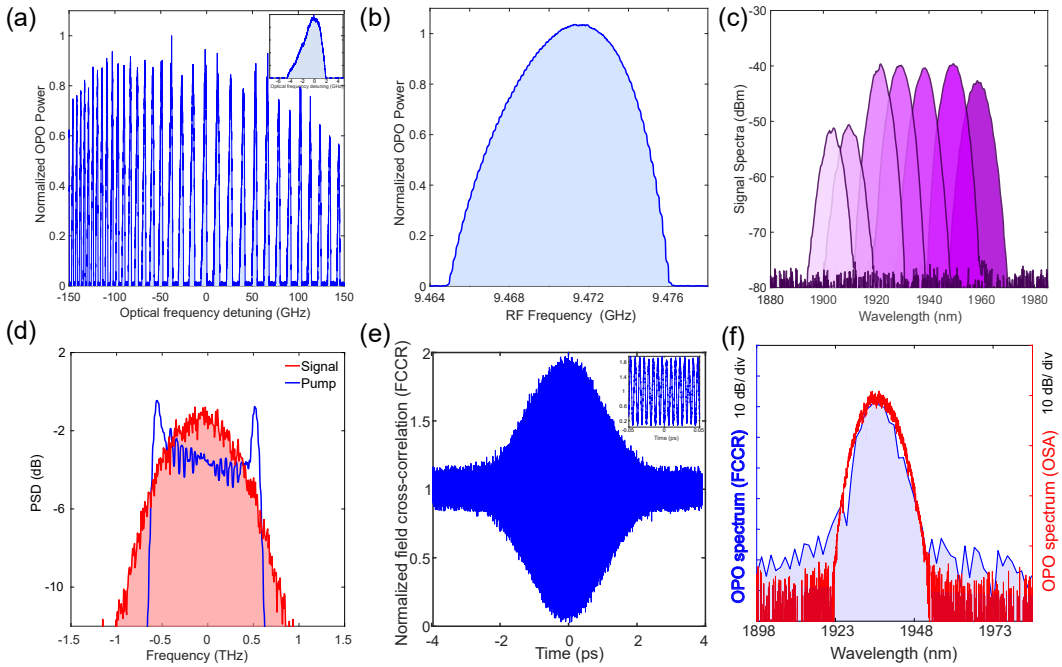

Figure 3.3: **Characteristics of the frequency comb generated from the synchronously pumped on-chip OPOs**. a) Resonance peak structure obtained by sweeping the pump central wavelength which is typical of doubly-resonant OPO operation. A zoomed-in view of a single peak is shown in the inset, b) Range of existence of the synchronously pumped OPO for a fixed pump power as the pump repetition rate is varied, c) Fine tuning of the OPO frequency comb output enabled by tuning the pump central wavelength, d) Spectral broadening of the OPO operating at degeneracy corresponding to a sub-picosecond transform-limited duration of ~ 400 fs, e) Verification of the coherence of the OPO output as evident from the existence of interference fringes (see inset) in the electric-field cross-correlation trace, f) The close agreement between the spectra obtained from an optical spectrum analyzer measurement and that obtained by Fourier transforming the field cross-correlation corroborates the coherence of the OPO output.

The doubly-resonant operation of the OPO is also confirmed by the appearance of the resonance peak structure with the variation of the pump central wavelength as shown in Fig. 3.3(a). Figure 3.3(b) shows the tolerance of the synchronous pumping repetition rate mismatch with respect to the optimum OPO operating point. The fine tunability of the OPO output spectra as offered by tuning the pump wavelength is depicted in Fig. 3.3(c). The combination of fine tunability and course tunability potentially enables continuous spectral coverage across the accessible spectral region. The OPO output at degeneracy (Fig. 3.3(d)) corresponds to a sub-picosecond transform-limited temporal duration (~ 400 fs), representing a pulse compression factor exceeding 2 with respect to the pump (see Supplementary

section 3.6.6). We further evaluate the coherence of the output frequency comb by performing a linear field cross-correlation of the output signal light as shown in Fig. 3.3(e), where each OPO pulse is interfered with another pulse delayed by 10 roundtrips. The presence of the interference fringes (see inset of Fig. 3.3(e)), combined with the consistency of the Fourier transform of the cross-correlation trace and the signal spectrum obtained using an OSA, serve as evidence for the coherence of the output frequency comb over the entire spectrum (see Fig. 3.3(f)).

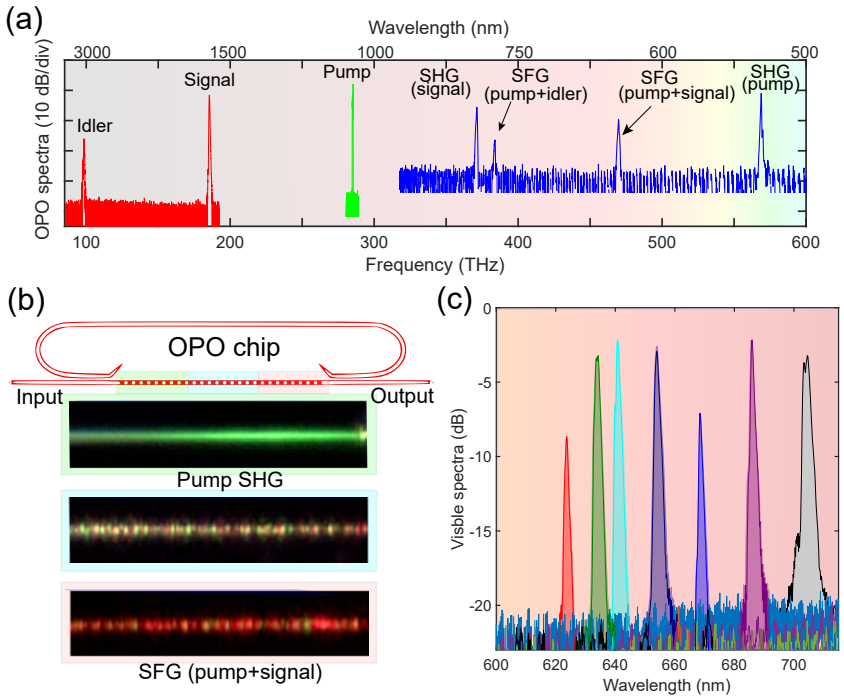

Figure 3.4: **Visible frequency comb generation from the integrated optical parametric oscillator chip.** a) The complete emission spectrum of an OPO (Spectra obtained from different optical spectrum analyzers/ spectrometers are stitched together). Apart from the emission of the signal and the idler waves, the OPO also produces output in the visible spectra owing to the auxiliary nonlinear processes namely the second-harmonic generation (SHG) and the sum-frequency generation (SFG). b) Optical microscope image capturing the visible light emission from various regions of the periodically poled section of the OPO device, c) Tunable visible frequency comb generation from the integrated OPO chip, where different colors indicate spectra obtained from OPOs with distinct poling periods.

The occurrence of other quadratic nonlinear processes, namely second harmonic generation (SHG) and sum-frequency generation (SFG), leads to frequency comb formation in the visible spectral region. The complete emission spectrum of an OPO consisting of the second harmonic of the pump and the signal waves, the sum

frequency components between the pump and the signal/idler waves along with the usual signal/idler is shown in Fig. 3.4(a). The scattered visible light emanating from the chip is captured by the optical microscope image (see Fig. 3.4(b)) showing the emission of the pump second harmonic (green) and the sum frequency components (red). Note that in the poling region, green dominates at the input side, which progressively is overpowered by the sum-frequency red component. The SFG between the pump and the signal waves leads to tunable visible frequency comb generation between 600 nm and 700 nm as shown in Fig. 3.4(c). Tuning the OPO farther from degeneracy leads to idler emission further into the mid-IR as well as the SFG component that lies to the bluer side of the visible spectrum.

3.4 Discussion

The pump, which is a near-IR electro-optic comb, can be incorporated into the lithium niobate chip in the future [6, 59]. With proper dispersion engineering, our OPO design can additionally achieve large instantaneous bandwidth accompanied by significant pulse compression [41], enabling the generation of femtosecond mid-infrared frequency combs in nanophotonics. Efficient supercontinuum generation requiring only a couple of picojoules of pulse energy can then be performed using periodically-poled lithium niobate waveguides on these femtosecond pulses for subsequent f-2f self-referencing/comb stabilization [20]. Future work will involve the integration of electro-optic modulators for active locking of the OPO frequency comb. The on-chip OPO threshold can be reduced further by improving waveguide losses and enhancing the effective nonlinear co-efficient by separately optimizing the modal overlap between the pump and the signal/idler fields for each OPO device catering to dedicated spectral bands. We estimate that an on-chip threshold for operation near degeneracy with an average power less than 500 μW (for 10 GHz repetition rate operation) is feasible. The low power requirement combined with the need for a relatively narrow pump tunability range opens the door for pumping the OPO chip with butt-coupled near-infrared diode lasers. This paves the way for a fully integrated solution for mid-IR frequency comb generation based on lithium niobate nanophotonics [13, 18, 25, 58] (see supplementary section 3.6.8).

Optimizing the coupler design can enable OPO operation with lower thresholds and higher mid-infrared comb conversion efficiency. Advanced coupler designs like the ones inspired by inverse design [35] can satisfy the simultaneous

requirements of low coupling for the pump, high coupling for the signal, and optimum coupling for the idler waves, leading to conversion efficiencies even exceeding 30 %. Realizing OPO devices in lithium niobate on sapphire will give access to a wider transparency window, leading to frequency comb generation deeper into the mid-infrared [34]. Thanks to the strong parametric nonlinear interaction, it is possible to realize frequency combs with lower repetition rates ($\sim$ 1 GHz) using spiral waveguides [26] in the feedback arm of the OPO resonator which will be useful for on-chip dual-comb spectroscopy applications. The emission in the mid-infrared overlaps with important molecular rovibrational absorption lines and paves the way for novel integrated spectroscopic solutions.

3.5 Methods

The devices are fabricated on a 700 nm thick X-cut MgO-doped lithium niobate on silica die (NANOLN). Periodic poling is performed by first patterning electrodes using e-beam lithography, followed by e-beam evaporation of Cr/ Au, and subsequently metal lift-off. Ferroelectric domain inversion is undergone by applying high voltage pulses, and the poling quality is inspected using second-harmonic microscopy. The waveguides are patterned by e-beam lithography and dry-etched with Ar^+ plasma. The waveguide facets are polished using fiber polishing films. The OPO-chip consists of multiple devices with poling periods ranging from 5.55 μm to 5.7 μm (in 10-nm increments) that provides parametric gain spanning over an octave.

Optical spectra were recorded using a combination of a near-infrared optical spectrum analyzer (OSA) (Yokogawa AQ6374), mid-infrared OSAs (Yokogawa AQ6375B, AQ6376E), and a CCD spectrometer (Thorlabs CCS200). The OPOs are synchronously driven at either the fundamental repetition rate ($\sim$ 9.5 GHz) or its harmonic ($\sim$ 19 GHz). The optical spectrum results are obtained with the harmonic repetition rate operation as it leads to wider instantaneous bandwidth owing to shorter electro-optic pump pulses. The OPOs operating at longer wavelengths have higher thresholds (because of increased effective area, increased coupler loss corresponding to the signal wave, and larger mismatch between the relative walk-off parameters of the signal and the idler wave) and therefore, we operate them intermittently in what we call “quasi-synchronous” operation, as a way to reduce the average power and avoid thermal damage (see Supplementary Section 3.6.4). This limitation is mainly attributed to the avoidable input insertion loss ($\sim$ 12 dB) of our current setup. With the aid of better fiber-to-chip coupling

design/mechanisms (insertion loss of the order of 1 dB has been reported in the context of thin-film lithium niobate) the mid-IR OPOs can be operated in a steady state sync-pumped configuration [17].

3.6 Supplementary

3.6.1 Single-envelope simulation and visible frequency comb

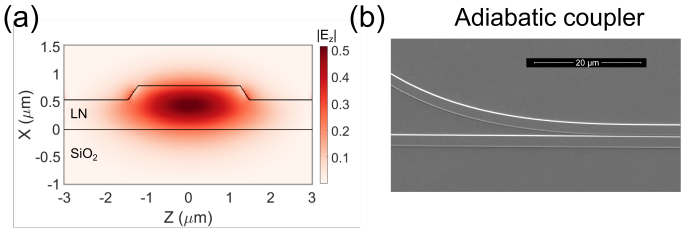

Figure 3.5: **SEM image of the adiabatic coupler region.** a) The waveguides (dimensions: width of 2.5 μm, etch depth of 250 nm) support guided-modes in the mid-infrared corresponding to the idler wave, the electric field distribution (fundamental TE mode) of which is shown. b) The SEM image of the fabricated device showing the coupler region.

To capture the process of the generation of the second-harmonic and sum-frequency generation signals (responsible for the generation of the visible frequency comb), we resort to single nonlinear envelope simulation [5]. The numerically obtained results are shown in Fig. 3.6(a), which alludes to the existence of the visible frequency comb components. We have assumed the presence of non-idealities in the poling period in our simulation. We note that these second-harmonic and sum-frequency generation components are generated due to parasitic phase-matching owing to duty-cycle errors and/or higher-order phase-matching for the visible components.

In order to enhance the efficiency of the visible frequency comb generation process one can add an additional phase matching section at the output waveguide of the OPO. This would boost the conversion efficiency for the phase-matched component, and can also be designed to be broadband using chirped poling periods. Such a scenario where the efficiency of the SFG component between the pump and the signal is boosted is simulated in Fig. 3.6(b). Similarly, it can also be designed for the other components, namely the SFG of the idler and the pump, or the second harmonic frequency combs. We note that these visible frequency combs are single-pass due to the long-pass nature of the spectral response of the adiabatic couplers. The visible components inherit their wide tunability for their parent signal/idler frequency combs.

The fine tunability of the visible frequency comb (sum frequency generation between the signal and the pump) can also be performed using pump wavelength control as shown in Fig. 3.6(c). The up-conversion resulting from the second-harmonic generation of the signal also leads to near-infrared frequency comb generation. The phase-matching curves are shown in Fig. 3.7(a). The coarse tuning and fine-tuning of the second-harmonic signal comb as obtained experimentally are shown in Fig. 3.7(b) and Fig. 3.7(c), respectively.

3.6.2 Signal/Idler conversion efficiency

We plot the signal power as a function of the pump power as shown in Fig. 3.8(a). The OPO conversion efficiency is a function of the escape efficiency, number of times above threshold operation, etc.. [2].

The escape efficiency is determined by the OPO-cavity output coupling, which is given by the frequency response of our adiabatic coupler. The schematic of the geometry of our coupler is shown in Fig. 3.8(b). The geometrical parameters are mentioned in the caption of figure 4. The simulated performance from the coupler is shown in Fig. 3.8(c). The coupler response is also characterized experimentally by illuminating with a super-continuum source. The results are overlaid in Fig. 3.8(d).

We measure an off-chip mid-infrared power of $\sim$ 300 nW. The spectrum is shown in Fig. 3.9. The corresponding on-chip average power is $\sim$ 3 μW. The estimated pulse width for the idler is $\sim$ 500 fs (transform-limited). This indicates a peak power of $\sim$ of 25 mW. The power per comb line is $\sim$ 5 μW. Note that we have multiplied the power levels with the quasi-pulse duty cycle of 100. The threshold of the extreme mid-infrared OPO is estimated to be approximately 10 times that of the near-degenerate OPO (possessing a threshold of $\sim$ 1 mW of average power).

3.6.3 Pump preparation/ Electro-optic frequency comb generation

The OPO is pumped by an electro-optic frequency comb whose repetition rate is tuned close to the cavity FSR. The pump pulse width is approximately 1 ps long and based on the available electronics in our current version the repetition rate can be tuned from 5 GHz to 20 GHz (the upper limit is dictated by the bandwidth of the RF amplifiers). The electro-optic frequency comb generation scheme closely follows the approach demonstrated in [33, 39]. The center frequency can be tuned from 1040 nm to 1065 nm (the upper limit is determined by the operating range of the waveshaper, while the lower limit is chosen to ensure the safe operation of the YDFA).

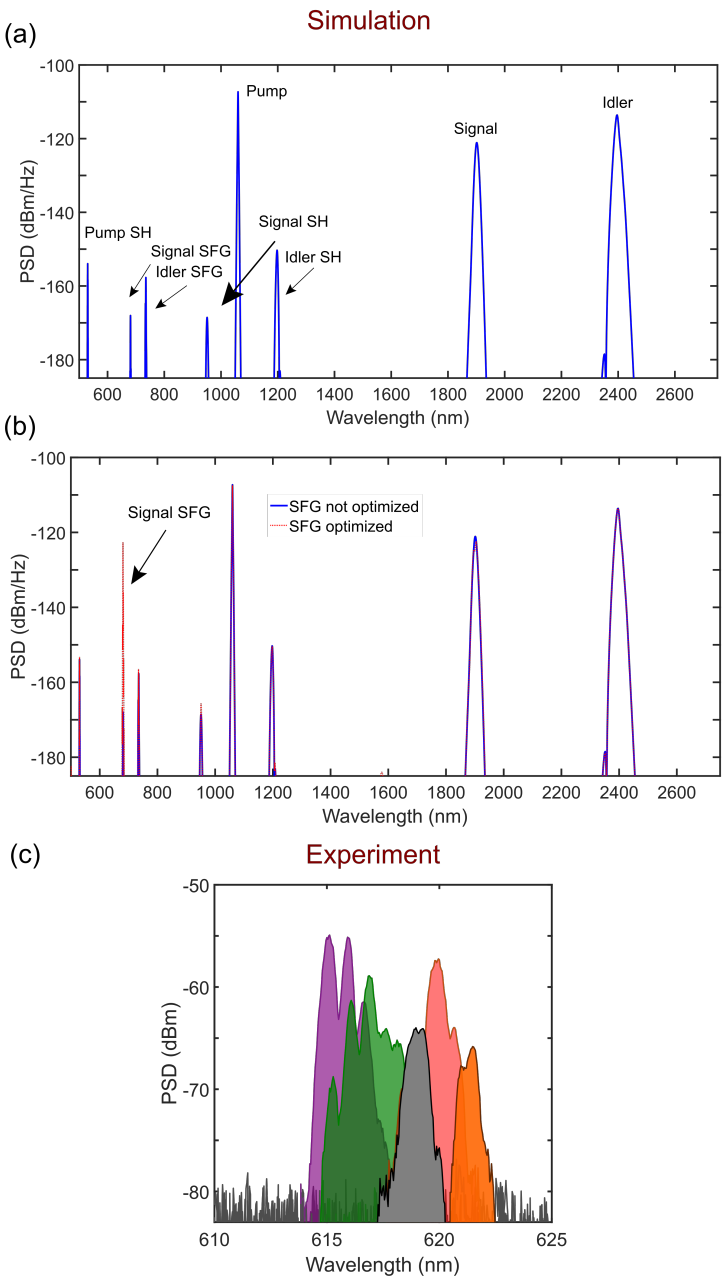

Figure 3.6: **Visible frequency comb generation.** a), b), c) Experimentally obtained tunable visible frequency comb (sum frequency generation between the signal and the pump) via pump frequency tuning.

The schematic of the pump preparation setup is shown in Fig. 3.10(a). The output of the CW laser is modulated by a series of modulators. The modulators are driven by an RF signal generator followed by an RF amplifier. The Intensity modulator (IM) bias is chosen such that pulses can be carved out from the continuous wave. At this stage (Stage 1) the time domain output resembles the simulated waveform

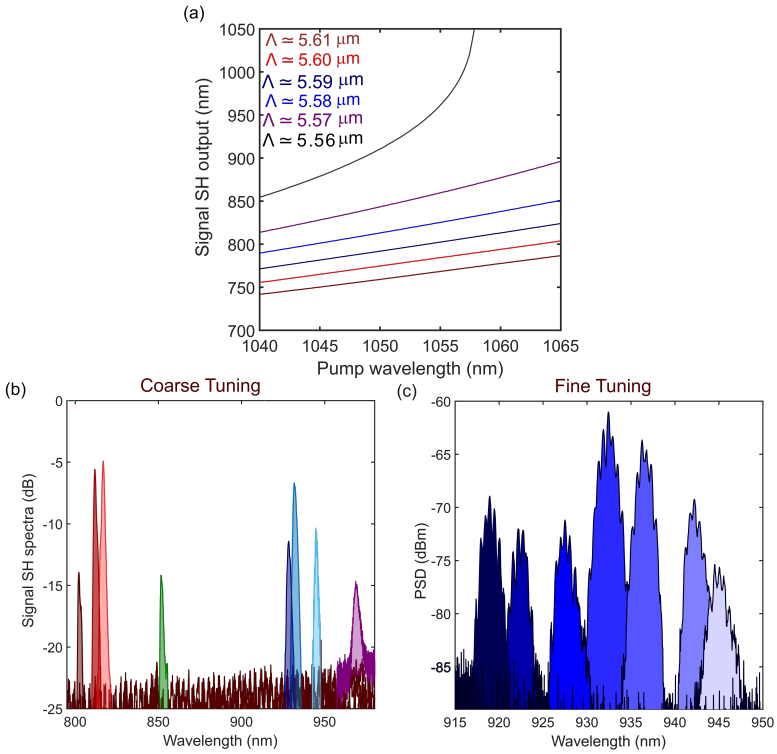

Figure 3.7: **Second harmonic generation of the signal frequency comb.** a) Phase matching curves for different poling periods corresponding to the second-harmonic generation of the signal frequency comb. b) Coarse tuning of the second harmonic of the signal frequency combs as obtained from the OPO chip. c) Fine tuning of the second harmonic of the signal frequency combs as obtained from a single OPO via pump wavelength tuning.

shown in Fig. 3.10(b). Next, a cascade of 3 Phase modulators (PM) enables the addition of spectral sidebands which are separated by the repetition rate. The Phase modulators are driven in sync by adjusting the electronic delay lines. At this stage (Stage 2) the spectrum will be similar to the one shown in Fig. 3.10(c). The resultant signal is amplified with the help of a semiconductor optical amplifier (SOA) and then sent to a waveshaper. The programmable waveshaper allows the compression of the pulses by de-chirping the input temporal waveform through the application of suitable dispersion. At this stage (Stage 3), the time domain waveform will look like the one shown in Fig. 3.10(d), where both the compressed pulses as well as the pre-compressed chirped pulses are shown. Finally, the electro-optic frequency comb is characterized in the frequency domain using an optical spectrum analyzer (OSA), and in the time domain using an intensity auto-correlator.

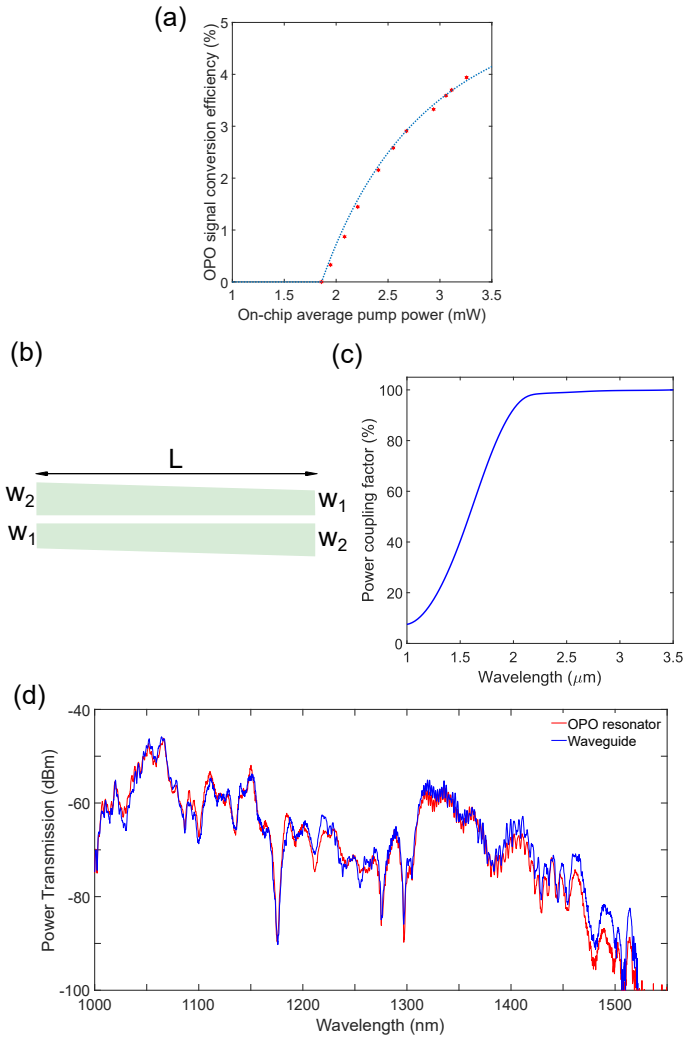

Figure 3.8: **Coupler response and OPO conversion efficiency.** a) Signal conversion efficiency as a function of on-chip pump power. The experimental data fit well with the analytically expected scaling of $\frac{\sqrt{N}-1}{N}$, where N, is the number of times above threshold operation. b) Schematic of the adiabatic coupler with the following parameters: $w_1 = 2.3\mu$m, $w_2 = 2.5\mu$m, gap $= 1\mu$m, and length $L = 500\mu$m. c) Simulated Response of the adiabatic coupler, showing that it transmits most of the pump wavelengths (around $1\mu m$) while coupling the majority of the power contained in the longer wavelengths ($> 2\mu m$) d) Measured transmission of a supercontinuum source through the OPO resonators containing the couplers (red curve). The response for the case of transmission through a straight waveguide is shown for reference (blue curve). It can be seen that at longer wavelengths the transmission through the OPO resonators dips on account of the coupling response of the couplers.

3.6.4 Quasi-sync pumping

The thresholds of the far non-degenerate OPOs are higher owing to a combination of multiple reasons. The adiabatic coupler is not tailor-designed for each OPO,

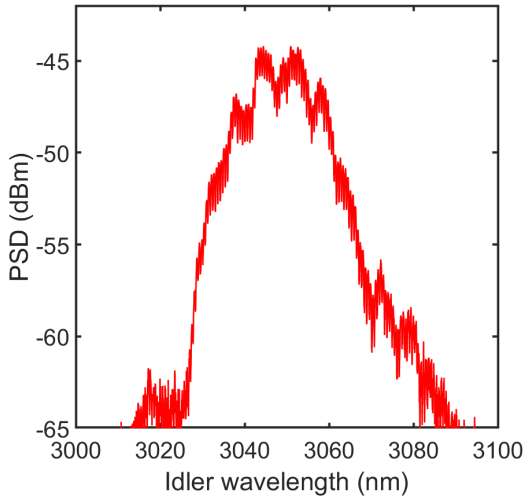

Figure 3.9: **Measurement data for average power per comb line.** Mid-infrared frequency comb (Idler frequency comb) spectrum obtained using optical spectrum analyzer that is used for the calculation of power per comb line. Optical spectrum analyzer settings: Resolution bandwidth 1 nm, sampling interval 0.05 nm, and frequency comb repetition rate ~ 19 GHz.

instead, a uniform coupler has been implemented in this first-generation chip design. As a result, the far non-degenerate operation of the OPOs leads to signals experiencing higher round-trip losses (due to progressively larger out-coupling for smaller wavelengths). Moreover, the effective nonlinear coefficient which takes into consideration the effective area of the modes, and the field overlap between the pump, signal, and idler modes also degrades.

The higher threshold requirement demands more pump power which is currently on the higher side due to the rather high input coupling loss/ insertion loss (approximately between 10 to 12 dB). There have been several proposals and demonstrations to bring this number down to a few dBs [54, 56]. In the scenario of the availability of low insertion loss, the required external pump power can be dramatically reduced by approximately 10 dB. Under these circumstances, the threshold requirement for far non-degenerate operations can be easily accessible even with sub-optimum design.

However, in our present implementation, we, unfortunately, do suffer from excess insertion loss, which results in the required off-chip average power exceeding 60 mW. At these power levels, we are prone to burning/ damaging the connectors and affecting the YDFA in the presence of undesired back-reflected power. To ensure safe operation we resort to quasi-sync pumping, whereby the average power is

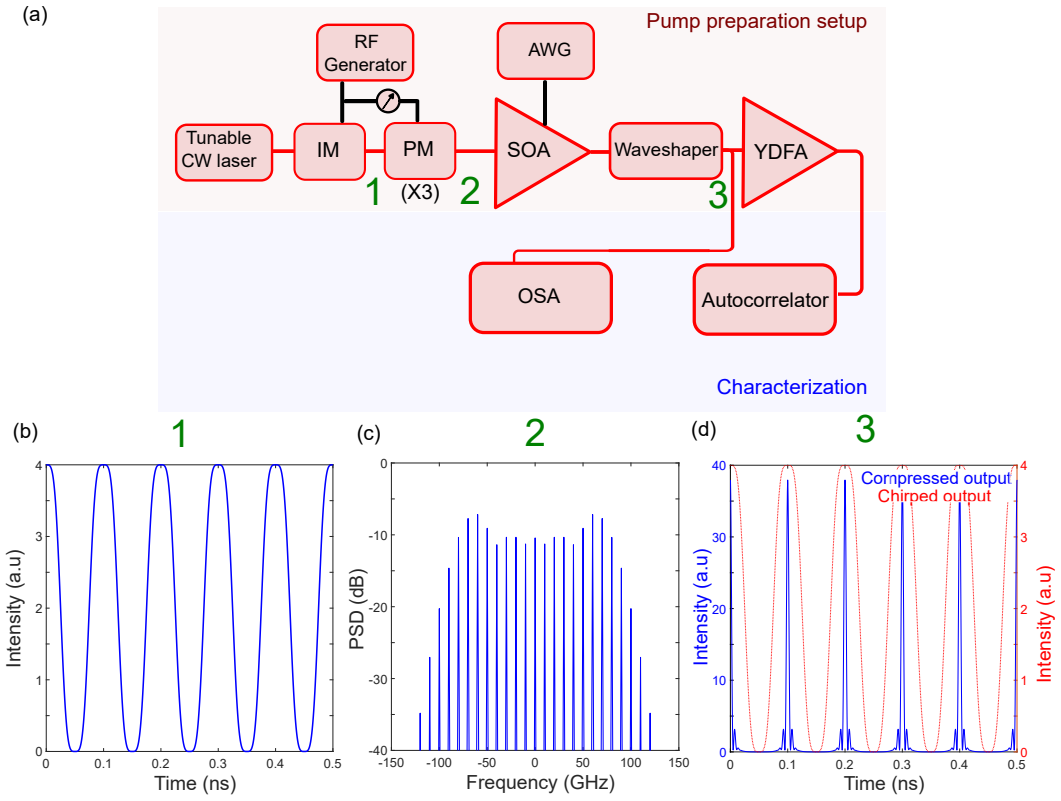

Figure 3.10: **Electro-optic comb generation setup.** a) Schematic of the setup for electro-optic comb generation that is used for the sync-pumping of the OPO. Arbitrary Waveform Generator (AWG), Semiconductor Optical Amplifier (SOA), Intensity Modulator (IM), Phase Modulator (PM), Ytterbium Doped Fiber Amplifier (YDFA), Optical Spectrum Analyzer (OSA). b,c,d) Simulated waveforms in the time and frequency domain at different stages of the pump preparation setup.

reduced by pulsing the pump. This can be achieved by driving the semiconductor optical amplifier (SOA) using an arbitrary waveform generator (AWG) leading to microsecond scale pulses at a repetition rate varying from 1 to 20 KHz (Duty cycle of 1000 to 50). The schematic is shown in Fig. 3.11(a), which is the same as the pump preparation setup with the addition of an AWG-driven SOA. The time domain traces captured using a slow detector for the pump and signal pulses are shown in Fig. 3.11(b). We note that the slow detector could not resolve the individual picosecond scale pulses within each quasi-pulse. In fact, there are of the order of thousands of pulses within each quasi-pulse.

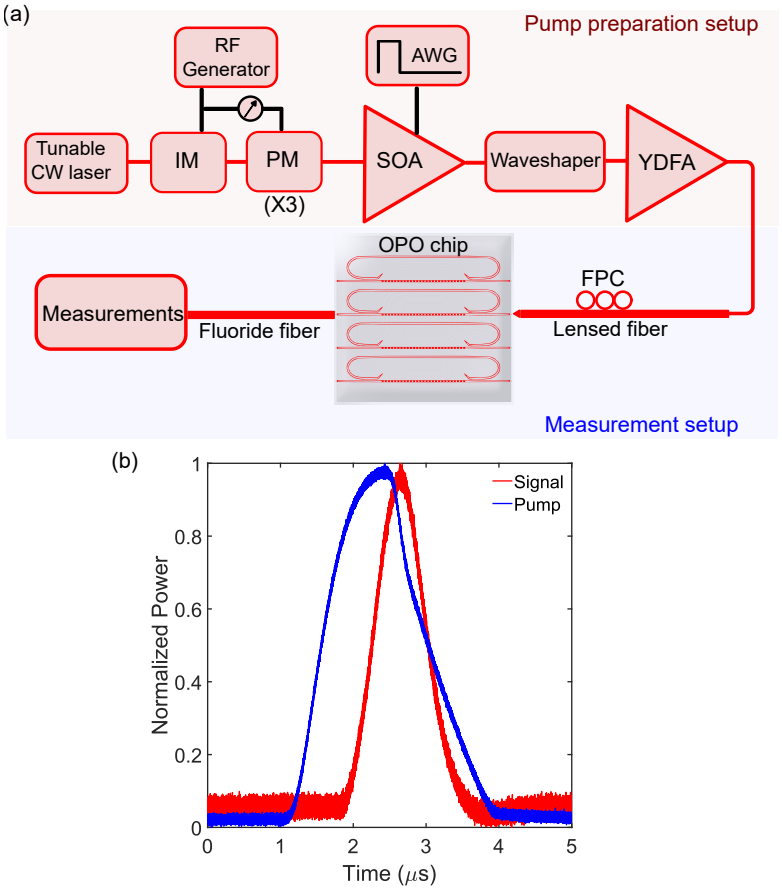

Figure 3.11: **Quasi sync-pump OPO setup.** a) Schematic of the setup for electro-optic comb generation that is used for the sync-pumping of the OPO in the quasi-mode of operation. Arbitrary Waveform Generator (AWG), Semiconductor Optical Amplifier (SOA), Intensity Modulator (IM), Phase Modulator (PM), Ytterbium Doped Fiber Amplifier (YDFA), Optical Spectrum Analyzer (OSA). b) Measured time domain trace of the quasi pulses for the pump (blue) and the signal (red) quasi pulses using a slow detector.

3.6.5 Estimating the cavity free spectral range

Estimating the free spectral range of the cavity (FSR) is central to determining the repetition rate of the synchronously pumped OPO. This is absolutely necessary since the sync pump (EO comb) cannot be tuned continuously to search for the right FSR. Each setting of the EO comb requires a specific combination of the electronic phase delay line parameters and the waveshaper dispersion parameter, adjusting which is an arduous task. The design of our OPO precludes the use of a tunable CW source around 1 μm to scan through multiple cavity resonances. The situation is exacerbated in the absence of a high-power tunable CW source of around 2 μm

at our disposal. Under these circumstances, we estimate the cavity FSR using a measurement setup as shown in Fig. 3.12.

In this approach, we have to operate the OPO in CW mode. We apply a variable modulation on top of the CW using an intensity modulator (IM). The frequency of modulation is varied using an arbitrary waveform generator. The output of the OPO will be maximized in the vicinity of the correct cavity FSR. This setup unlike the EO comb can be continuously tuned.

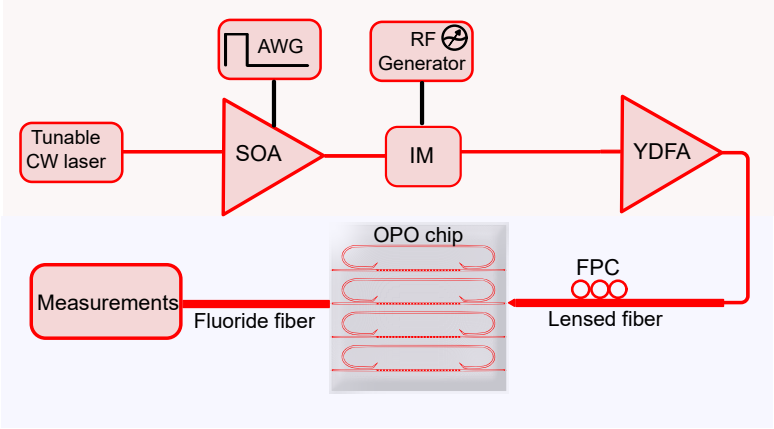

Figure 3.12: **Schematic of the setup for estimating cavity FSR**. Arbitrary Waveform Generator (AWG), Semiconductor Optical Amplifier (SOA), Intensity Modulator (IM), Ytterbium Doped Fiber Amplifier (YDFA).

3.6.6 Spectral broadening/ Pulse compression in the degenerate OPO

The measured pump pulse width (assuming a Gaussian pulse as extracted from the intensity auto-correlation trace) is $\sim$ 1 ps. The estimated transform-limited pulse width for the OPO operating at degeneracy is 380 fs. The experimental spectrum of both the pump and signal are translated in frequency and overlaid on top of each other as shown in Fig. 3.13(a). The numerical simulation results obtained from a dual-envelope equation simulation are shown in Fig. 3.13(b-e), which closely agrees with the measured data. By proper dispersion engineering (group velocity dispersion and group velocity mismatch) [41], it is possible to generate OPO frequency comb with broad instantaneous bandwidth, leading to few optical cycle pulses.

3.6.7 Coherence verification using field cross-correlation technique

In order to evaluate the coherence of the spectrum, we perform a linear field cross-correlation (FCCR) of the output signal light, where each OPO pulse is interfered

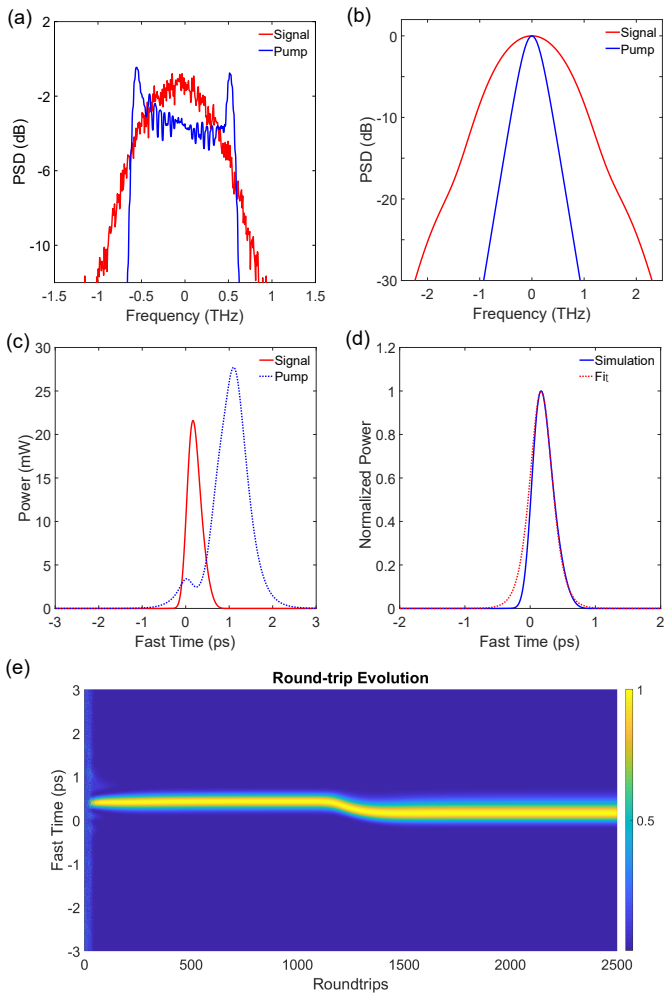

Figure 3.13: **Spectral broadening and associated pulse compression in the degenerate regime of OPO operation.** a) Experimentally obtained spectrum plotted in the frequency axis after spectral translation showing the effect of spectral broadening in the signal compared to the pump. b) Spectrum obtained from the numerical simulation showing the spectral broadening effect (assuming a sech-shaped pump pulse). c) Pump and signal pulses in the time domain as obtained from the numerical simulation. d) The numerically obtained signal pulse when fitted with a sech shaped pulse denotes a pulse compression by a factor of approximately 2. e) The normalized roundtrip evolution of the signal pulses that are initiated from the vacuum field till it reaches the steady state.

with another pulse delayed by 10 roundtrips. This can be thought of being a modified FTIR measurement, where instead of performing auto-correlation we are executing cross-correlation. The schematic of the setup used for this purpose is shown in Fig. 3.14(a). The delay line corresponds to a delay of 10 OPO pulses, and thus the coherence property evaluation is limited by the applied delay duration. The

scanning stage nonlinearity is corrected using a reference HeNe laser beam. This is important to match the optical spectrum obtained through the optical spectrum analyzer and which is calculated by performing the Fourier transform of the FCCR trace.

We also detect a sharp RF beat-frequency corresponding to the applied repetition rate of the sync-pumped OPO (Fig. 3.14(b)). The signal is obtained by measuring the OPO output pulses using a fast photo-detector. The pump is rejected using a wavelength de-multiplexer.

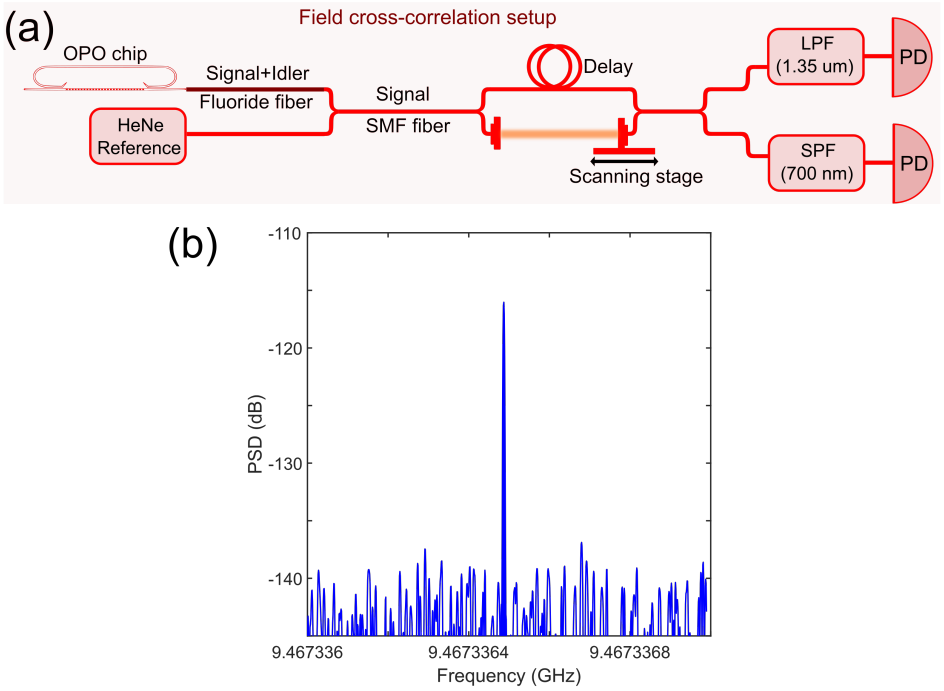

Figure 3.14: **[Coherence verification setup.** a) Schematic of the setup used to verify the coherence of the OPO output. b) Measured RF beat-note frequency corresponding to the applied repetition rate of the sync-pumped OPO.

3.6.8 Full system integration and a universal frequency comb source

We envision a complete integrated solution for frequency comb generation based on lithium niobate nanophotonics in conjunction with a laser chip. With several design enhancements, it is possible to lower the threshold for frequency comb generation substantially which can allow the pumping with commercially available DFB laser chips. Alternatively, an integrated external cavity along with a semiconductor gain chip can also be deployed for this purpose [28]. The other crucial building blocks are: a) near-IR picosecond pump pulse generation [18, 58], b) Mach Zehnder

interferometer mesh for routing the pump light to the desired OPO [51], c) an array of OPOs, and d) periodically poled lithium niobate waveguides supporting ultra-low power supercontinuum generation for f-2f based frequency comb stabilization [20, 38]. Our present work focuses on part c, while the rest has already been demonstrated in lithium-niobate nanophotonics.

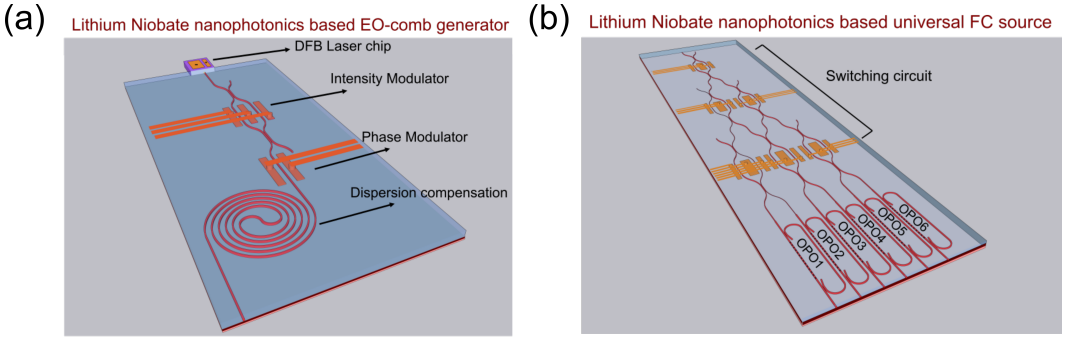

Figure 3.15: **Envisioned full integration of an universal frequency comb source.** a) Illustration of a lithium niobate nanophotonics-based near-IR picosecond pump source consisting of a cascade of intensity and phase modulators followed by a de-chirping spiral waveguide. b) Illustration of a lithium niobate OPO chip consisting of an array of OPOs dedicated to cover different spectral regions which can be programmatically pumped with the help of the MZI routing circuit preceding it.

3.6.9 Temperature tuning of the phase-matching curves

The fine-tuning of the quasi-phase-matching (QPM) in the present work has been performed by tuning the pump wavelength. The same can be achieved with the help of temperature tuning while keeping the pump wavelength fixed. Figure 3.15 shows the phase-matching curves as a function of temperature which is calculated by evaluating the effective index of the waveguides taking into consideration the temperature-dependent Sellmeier equation [10]. Temperature tuning can either be attained globally by placing the chip on top of a TEC heater element, or locally by implementing resistive heater elements close to the periodically poled regions. We note that the expected tuning curves (obtained from simulations) are more tunable than what is observed in experiments. We anticipate that it may be attributed to the presence of thermal resistance between the heater element and the nanophotonic chip, and/or the mismatch in the thermal expansion coefficients between the insulator layer and the thin-film lithium niobate layer. This is a subject of an ongoing investigation.

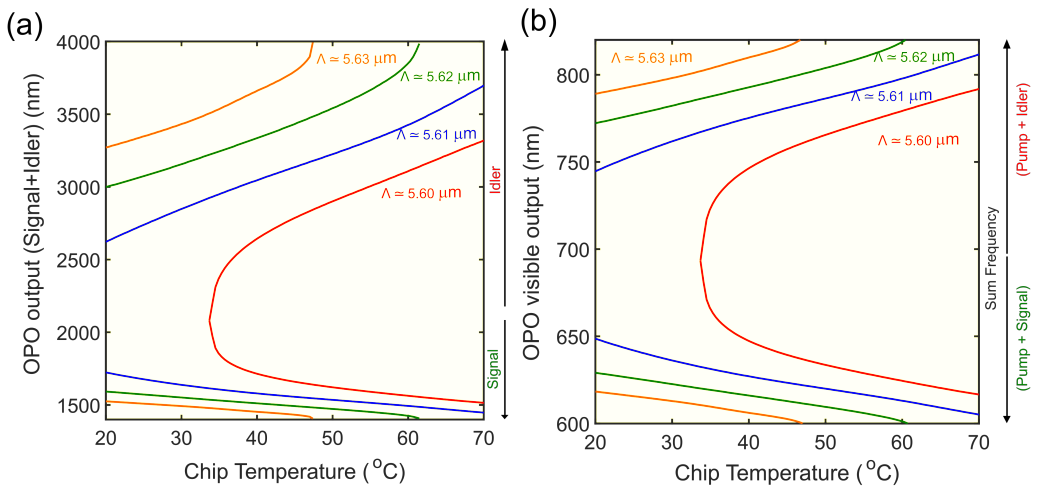

Figure 3.16: **Temperature tuning of the quasi-phase-matching.** Temperature tuning of the quasi-phase-matching obtained from simulation for the a) signal and the idler waves and b) their corresponding up-conversion with the pump leading to visible frequency combs. The pump wavelength is kept fixed at 1060 nm.

References

[1] Florian Adler, Kevin C Cossel, Michael J. Thorpe, Ingmar Hartl, Martin E Fermann, and Jun Ye. Phase-stabilized, 1.5 w frequency comb at 2.8–4.8 μm. *Optics Letters*, 34(9):1330–1332, 2009.

[2] Mark A. Arbore and Martin M. Fejer. Singly resonant optical parametric oscillation in periodically poled lithium niobate waveguides. *Optics Letters*, 22(3):151–153, 1997.

[3] Alexander W. Bruch, Xianwen Liu, Zheng Gong, Joshua B. Surya, Ming Li, Chang-Ling Zou, and Hong X. Tang. Pockels soliton microcomb. *Nature Photonics*, 15(1):21–27, 2021.

[4] Ian Coddington, Nathan Newbury, and William Swann. Dual-comb spectroscopy. *Optica*, 3(4):414–426, 2016.

[5] Matteo Conforti, Fabio Baronio, and Costantino De Angelis. Nonlinear envelope equation for broadband optical pulses in quadratic media. *Physical Review A*, 81(5):053841, 2010.

[6] Camiel Op de Beeck, Felix M. Mayor, Stijn Cuyvers, Stijn Poelman, Jason F Herrmann, Okan Atalar, Timothy P. McKenna, Bahawal Haq, Wentao Jiang, Jeremy D. Witmer, et al. Iii/v-on-lithium niobate amplifiers and lasers. *Optica*, 8(10):1288–1289, 2021.

[7] Scott A. Diddams, Kerry Vahala, and Thomas Udem. Optical frequency combs: Coherently uniting the electromagnetic spectrum. *Science*, 369(6501): eaay3676, 2020.

[8] Majid Ebrahim-Zadeh and Irina T. Sorokina. *Mid-infrared coherent sources and applications*. Springer Science & Business Media, 2007.

[9] Robert C. Eckardt, C. D. Nabors, William J. Kozlovsky, and Robert L. Byer. Optical parametric oscillator frequency tuning and control. *Journal of the Optical Society of America B*, 8(3):646–667, 1991.

[10] Ofer Gayer, Z. Sacks, E. Galun, and Ady Arie. Temperature and wavelength dependent refractive index equations for mgo-doped congruent and stoichiometric linbo3. *Applied Physics B*, 91(2):343–348, 2008.

[11] Austin G. Griffith, Ryan K. W. Lau, Jaime Cardenas, Yoshitomo Okawachi, Aseema Mohanty, Romy Fain, Yoon Ho Daniel Lee, Mengjie Yu, Christopher T. Phare, Carl B. Poitras, et al. Silicon-chip mid-infrared frequency comb generation. *Nature Communications*, 6(1):1–5, 2015.

[12] Hairun Guo, Clemens Herkommer, Adrien Billat, Davide Grassani, Chuankun Zhang, Martin H. P. Pfeiffer, Wenle Weng, Camille-Sophie Bres, and Tobias J. Kippenberg. Mid-infrared frequency comb via coherent dispersive wave generation in silicon nitride nanophotonic waveguides. *Nature Photonics*, 12(6):330–335, 2018.

[13] Qiushi Guo, Ryoto Sekine, Luis Ledezma, Rajveer Nehra, Devin J. Dean, Arkadev Roy, Robert M. Gray, Saman Jahani, and Alireza Marandi. Femtojoule femtosecond all-optical switching in lithium niobate nanophotonics. *Nature Photonics*, 16(9):625–631, 2022.

[14] Xiang Guo, Chang-Ling Zou, Hojoong Jung, Zheng Gong, Alexander Bruch, Liang Jiang, and Hong X. Tang. Efficient generation of a near-visible frequency comb via cherenkov-like radiation from a Kerr microcomb. *Physical Review Applied*, 10:014012, Jul 2018. doi: 10.1103/PhysRevApplied.10.014012. URL https://link.aps.org/doi/10.1103/PhysRevApplied.10.014012.

[15] Ryan Hamerly, Alireza Marandi, Marc Jankowski, Martin M. Fejer, Yoshihisa Yamamoto, and Hideo Mabuchi. Reduced models and design principles for half-harmonic generation in synchronously pumped optical parametric oscillators. *Physical Review A*, 94(6):063809, 2016.

[16] Yang He, Qi-Fan Yang, Jingwei Ling, Rui Luo, Hanxiao Liang, Mingxiao Li, Boqiang Shen, Heming Wang, Kerry Vahala, and Qiang Lin. Self-starting bi-chromatic linbo 3 soliton microcomb. *Optica*, 6(9):1138–1144, 2019.

[17] Changran Hu, An Pan, Tingan Li, Xuanhao Wang, Yuheng Liu, Shiqi Tao, Cheng Zeng, and Jinsong Xia. High-efficient coupler for thin-film lithium niobate waveguide devices. *Optics Express*, 29(4):5397–5406, 2021.

[18] Yaowen Hu, Mengjie Yu, Brandon Buscaino, Neil Sinclair, Di Zhu, Rebecca Cheng, Amirhassan Shams-Ansari, Linbo Shao, Mian Zhang, Joseph M. Kahn, et al. High-efficiency and broadband on-chip electro-optic frequency comb generators. *Nature Photonics*, 16(10):679–685, 2022.

[19] Andreas Hugi, Gustavo Villares, Stéphane Blaser, H. C. Liu, and Jérôme Faist. Mid-infrared frequency comb based on a quantum cascade laser. *Nature*, 492 (7428):229–233, 2012.

[20] Marc Jankowski, Carsten Langrock, Boris Desiatov, Alireza Marandi, Cheng Wang, Mian Zhang, Christopher R. Phillips, Marko Lončar, and Martin M. Fejer. Ultrabroadband nonlinear optics in nanophotonic periodically poled lithium niobate waveguides. *Optica*, 7(1):40–46, 2020.

[21] Xingchen Ji, Xinwen Yao, Alexander Klenner, Yu Gan, Alexander L. Gaeta, Christine P. Hendon, and Michal Lipson. Chip-based frequency comb sources for optical coherence tomography. *Optics Express*, 27(14):19896–19905, 2019.

[22] Tobias J. Kippenberg, Alexander L. Gaeta, Michal Lipson, and Michael L. Gorodetsky. Dissipative Kerr solitons in optical microresonators. *Science*, 361(6402):eaan8083, 2018.

[23] Abijith S. Kowligy, David R. Carlson, Daniel D. Hickstein, Henry Timmers, Alexander J. Lind, Peter G. Schunemann, Scott B. Papp, and Scott A. Diddams. Mid-infrared frequency combs at 10 ghz. *Optics Letters*, 45(13):3677–3680, 2020.

[24] Luis Ledezma, Arkadev Roy, Luis Costa, Ryoto Sekine, Robert Gray, Qiushi Guo, Ryan M Briggs, and Alireza Marandi. Widely-tunable optical parametric oscillator in lithium niobate nanophotonics. *arXiv preprint arXiv:2203.11482*, 2022.

[25] Luis Ledezma, Ryoto Sekine, Qiushi Guo, Rajveer Nehra, Saman Jahani, and Alireza Marandi. Intense optical parametric amplification in dispersion-engineered nanophotonic lithium niobate waveguides. *Optica*, 9(3):303–308, 2022.

[26] Hansuek Lee, Tong Chen, Jiang Li, Oskar Painter, and Kerry J. Vahala. Ultra-low-loss optical delay line on a silicon chip. *Nature Communications*, 3(1): 1–7, 2012.

[27] Jiang Li, Chengying Bao, Qing-Xin Ji, Heming Wang, Lue Wu, Stephanie Leifer, Charles Beichman, and Kerry Vahala. Efficiency of pulse pumped soliton microcombs. *Optica*, 9(2):231–239, 2022.

[28] Mingxiao Li, Lin Chang, Lue Wu, Jeremy Staffa, Jingwei Ling, Usman A. Javid, Shixin Xue, Yang He, Raymond Lopez-Rios, Morin, et al. Integrated pockels laser. *Nature Communications*, 13(1):1–10, 2022.

[29] Juanjuan Lu, Ayed Al Sayem, Zheng Gong, Joshua B. Surya, Chang-Ling Zou, and Hong X. Tang. Ultralow-threshold thin-film lithium niobate optical parametric oscillator. *Optica*, 8(4):539–544, 2021.

[30] Xiyuan Lu, Gregory Moille, Ashutosh Rao, Daron A. Westly, and Kartik Srinivasan. On-chip optical parametric oscillation into the visible: Generating red, orange, yellow, and green from a near-infrared pump. *Optica*, 7(10): 1417–1425, 2020.

[31] Luke Maidment, Peter G. Schunemann, and Derryck T. Reid. Molecular fingerprint-region spectroscopy from 5 to 12 μm using an orientation-patterned gallium phosphide optical parametric oscillator. *Optics Letters*, 41(18):4261–4264, 2016.

[32] Pablo Marin-Palomo, Juned N. Kemal, Maxim Karpov, Arne Kordts, Joerg Pfeifle, Martin H. P. Pfeiffer, Philipp Trocha, Stefan Wolf, Victor Brasch, Miles H. Anderson, et al. Microresonator-based solitons for massively parallel coherent optical communications. *Nature*, 546(7657):274–279, 2017.

[33] Andrew J. Metcalf, Connor D. Fredrick, Ryan C. Terrien, Scott B. Papp, and Scott A. Diddams. 30 ghz electro-optic frequency comb spanning 300 thz in the near infrared and visible. *Optics Letters*, 44(11):2673–2676, 2019.

[34] Jatadhari Mishra, Timothy P. McKenna, Edwin Ng, Hubert S. Stokowski, Marc Jankowski, Carsten Langrock, David Heydari, Hideo Mabuchi, Martin M. Fejer, and Amir H. Safavi-Naeini. Mid-infrared nonlinear optics in thin-film lithium niobate on sapphire. *Optica*, 8(6):921–924, 2021.

[35] Sean Molesky, Zin Lin, Alexander Y. Piggott, Weiliang Jin, Jelena Vucković, and Alejandro W. Rodriguez. Inverse design in nanophotonics. *Nature Photonics*, 12(11):659–670, 2018.

[36] Ewelina Obrzud, Steve Lecomte, and Tobias Herr. Temporal solitons in microresonators driven by optical pulses. *Nature Photonics*, 11(9):600–607, 2017.

[37] Ewelina Obrzud, Monica Rainer, Avet Harutyunyan, Miles H. Anderson, Junqiu Liu, Michael Geiselmann, Bruno Chazelas, Stefan Kundermann, Steve Lecomte, Massimo Cecconi, et al. A microphotonic astrocomb. *Nature Photonics*, 13(1):31–35, 2019.

[38] Yoshitomo Okawachi, Mengjie Yu, Boris Desiatov, Bok Young Kim, Tobias Hansson, Marko Lončar, and Alexander L. Gaeta. Chip-based self-referencing using integrated lithium niobate waveguides. *Optica*, 7(6):702–707, 2020.

[39] Alexandre Parriaux, Kamal Hammani, and Guy Millot. Electro-optic frequency combs. *Advances in Optics and Photonics*, 12(1):223–287, 2020.

[40] Arkadev Roy, Saman Jahani, Carsten Langrock, Martin Fejer, and Alireza Marandi. Spectral phase transitions in optical parametric oscillators. *Nature Communications*, 12(1):1–9, 2021.

[41] Arkadev Roy, Rajveer Nehra, Saman Jahani, Luis Ledezma, Carsten Langrock, Martin Fejer, and Alireza Marandi. Temporal walk-off induced dissipative quadratic solitons. *Nature Photonics*, 16(2):162–168, 2022.

[42] Anatoliy A. Savchenkov, Vladimir S. Ilchenko, Fabio Di Teodoro, Paul M. Belden, William T. Lotshaw, Andrey B. Matsko, and Lute Maleki. Generation of Kerr combs centered at 4.5 μm in crystalline microresonators pumped with quantum-cascade lasers. *Optics Letters*, 40(15):3468–3471, 2015.

[43] Albert Schliesser, Nathalie Picqué, and Theodor W. Hänsch. Mid-infrared frequency combs. *Nature Photonics*, 6(7):440–449, 2012.

[44] Brian Stern, Xingchen Ji, Yoshitomo Okawachi, Alexander L. Gaeta, and Michal Lipson. Battery-operated integrated frequency comb generator. *Nature*, 562(7727):401–405, 2018.

[45] Liron Stern, Jordan R. Stone, Songbai Kang, Daniel C. Cole, Myoung-Gyun Suh, Connor Fredrick, Zachary Newman, Kerry Vahala, John Kitching, Scott A. Diddams, et al. Direct Kerr frequency comb atomic spectroscopy and stabilization. *Science Advances*, 6(9):eaax6230, 2020.

[46] Myoung-Gyun Suh and Kerry J. Vahala. Soliton microcomb range measurement. *Science*, 359(6378):884–887, 2018.

[47] Myoung-Gyun Suh, Xu Yi, Yu-Hung Lai, Stephanie Leifer, Ivan S. Grudinin, Gautam Vasisht, Emily C. Martin, Michael P. Fitzgerald, Greg Doppmann, Ji Wang, et al. Searching for exoplanets using a microresonator astrocomb. *Nature Photonics*, 13(1):25–30, 2019.

[48] Yuxing Tang, Logan G. Wright, Kriti Charan, Tianyu Wang, Chris Xu, and Frank W. Wise. Generation of intense 100 fs solitons tunable from 2 to 4.3 μm in fluoride fiber. *Optica*, 3(9):948–951, 2016.

[49] Philipp Trocha, Maxim Karpov, Denis Ganin, Martin H. P. Pfeiffer, Arne Kordts, Stefan Wolf, Jonas Krockenberger, Pablo Marin-Palomo, Claudius Weimann, Sebastian Randel, et al. Ultrafast optical ranging using microresonator soliton frequency combs. *Science*, 359(6378):887–891, 2018.

[50] Paul A. Verrinder, Lei Wang, Joseph Fridlander, Fengqiao Sang, Victoria Rosborough, Michael Nickerson, Guangning Yang, Mark Stephen, Larry Coldren, and Jonathan Klamkin. Gallium arsenide photonic integrated circuit

platform for tunable laser applications. *IEEE Journal of Selected Topics in Quantum Electronics*, 28(1):1–9, 2021.

[51] Cheng Wang, Mian Zhang, Xi Chen, Maxime Bertrand, Amirhassan Shams-Ansari, Sethumadhavan Chandrasekhar, Peter Winzer, and Marko Lončar. Integrated lithium niobate electro-optic modulators operating at cmos-compatible voltages. *Nature*, 562(7725):101–104, 2018.

[52] Christine Y. Wang, Lyuba Kuznetsova, Vasileios-Marios Gkortsas, Laurent Diehl, Franz X. Kaertner, Mikhail A. Belkin, Alexey Belyanin, Xiaofeng Li, Donhee Ham, Harald Schneider, et al. Mode-locked pulses from mid-infrared quantum cascade lasers. *Optics Express*, 17(15):12929–12943, 2009.

[53] Xingyuan Xu, Mengxi Tan, Bill Corcoran, Jiayang Wu, Andreas Boes, Thach G. Nguyen, Sai T. Chu, Brent E. Little, Damien G. Hicks, Roberto Morandotti, et al. 11 tops photonic convolutional accelerator for optical neural networks. *Nature*, 589(7840):44–51, 2021.

[54] Ni Yao, Junxia Zhou, Renhong Gao, Jintian Lin, Min Wang, Ya Cheng, Wei Fang, and Limin Tong. Efficient light coupling between an ultra-low loss lithium niobate waveguide and an adiabatically tapered single mode optical fiber. *Optics Express*, 28(8):12416–12423, 2020.

[55] Yu Yao, Anthony J. Hoffman, and Claire F. Gmachl. Mid-infrared quantum cascade lasers. *Nature Photonics*, 6(7):432–439, 2012.

[56] Pan Ying, Heyun Tan, Junwei Zhang, Mingbo He, Mengyue Xu, Xiaoyue Liu, Renyou Ge, Yuntao Zhu, Chuan Liu, and Xinlun Cai. Low-loss edge-coupling thin-film lithium niobate modulator with an efficient phase shifter. *Optics Letters*, 46(6):1478–1481, 2021.

[57] Mengjie Yu, Yoshitomo Okawachi, Austin G. Griffith, Michal Lipson, and Alexander L Gaeta. Mode-locked mid-infrared frequency combs in a silicon microresonator. *Optica*, 3(8):854–860, 2016.

[58] Mengjie Yu, Christian Reimer, David Barton, Prashanta Kharel, Rebecca Cheng, Lingyan He, Linbo Shao, Di Zhu, Yaowen Hu, Grant, et al. Femtosecond pulse generation via an integrated electro-optic time lens. *arXiv preprint arXiv:2112.09204*, 2021.

[59] Mian Zhang, Brandon Buscaino, Cheng Wang, Amirhassan Shams-Ansari, Christian Reimer, Rongrong Zhu, Joseph M Kahn, and Marko Lončar. Broadband electro-optic frequency comb generation in a lithium niobate microring resonator. *Nature*, 568(7752):373–377, 2019.

Chapter 4

SPECTRAL PHASE TRANSITIONS IN OPTICAL PARAMETRIC OSCILLATORS

Roy, Arkadev, Saman Jahani, Carsten Langrock, Martin Fejer, and Alireza Marandi. Spectral phase transitions in optical parametric oscillators. ***Nature Communications***, 12(1):835, 2021. doi: https://doi.org/10.1038/s41467-021-21048-z.
A.R. contributed to the conception of the project, executed the experiments, performed numerical simulations, and participated in the writing of the manuscript.

4.1 Abstract

Driven nonlinear resonators provide a fertile ground for phenomena related to phase transitions far from equilibrium, which can open opportunities unattainable in their linear counterparts. Here, we show that optical parametric oscillators (OPOs) can undergo second-order phase transitions in the spectral domain between degenerate and non-degenerate regimes. This abrupt change in the spectral response follows a square-root dependence around the critical point, exhibiting high sensitivity to parameter variation akin to systems around an exceptional point. We experimentally demonstrate such a phase transition in a quadratic OPO. We show that the divergent susceptibility of the critical point is accompanied by spontaneous symmetry breaking and distinct phase noise properties in the two regimes, indicating the importance of a beyond nonlinear bifurcation interpretation. We also predict the occurrence of first-order spectral phase transitions in coupled OPOs. Our results on non-equilibrium spectral behaviors can be utilized for enhanced sensing, advanced computing, and quantum information processing.

4.2 Introduction

Photonic resonators appearing in myriad forms ranging from macro-scale to nano-scale have been the mainstay of light-based fundamental studies and applications [51]. The ability to engineer the resonant spectral features of these cavities unveils tremendous possibilities in sensing and light-matter interactions. The interplay of gain/loss and coupling in coupled linear photonic resonators can lead to the occurrence of a multitude of intriguing phenomena ranging from Fano resonance, electromagnetically induced transparency, [33] and exceptional point associated

with parity-time symmetry breaking [39, 43].

Strong nonlinearities in photonic resonators can lead to a variety of rich phenomena. Nonlinear driven dissipative systems existing in non-equilibrium steady states exhibit self-organization [44], pattern formation [3, 35, 42, 49, 52], and emergent phase and dynamical phase transitions [7]. Other salient examples include behaviors in laser systems [21, 28, 37] at threshold [10] and around mode-locking transitions [17, 20, 32], soliton-steps in Kerr micro-resonators [24], and in polaritonic quantum fluids [4]. Similar phenomena are also explored outside photonics for instance in the form of Rayleigh-Benard convection and Faraday waves [2, 14]. Specific to the parametric oscillation regime, a variety of nonlinear dynamical behaviors has been predicted and demonstrated such as bi-stability, self-pulsation, limit-cycles [11], pattern formation [3, 35, 42, 49, 52] and phase transitions [8, 12], albeit not explicitly in the spectral domain.

Phase transition marks a universal qualitative regime change in system properties as the control parameter is varied around a critical/transition point [47]. The behavior of the system around the critical point is characterized by the order parameter (OP). Second-order phase transitions display continuity in the OP while exhibiting a discontinuity in the derivative of the OP. On the other hand, a first-order transition is known to possess a discontinuous OP around the transition point.

Realizing phase transitions based on the optical parametric processes can provide unique opportunities for sensing. For instance, in phase-transition-based detectors and transition-edge sensors [19], the reset time (return time to the critical bias point) can be significantly reduced using an ultrafast nonlinear process compared to thermodynamic transitions. Moreover, similar to the exceptional points in optical systems [39, 43], an enhanced sensitivity [25, 29] can be realized using a driven dissipative-based phase transition. However, in contrast to exceptional points in PT-symmetric systems, this enhancement is not accompanied by eigenvectors non-orthogonality and can potentially provide high sensitivity combined with high precision [31, 53]. The noiseless nature of parametric amplification [5] can be another unique resource for enhancing the signal-to-noise ratio; a property that is not readily available in current implementations of exceptional points. Divergent susceptibility of the critical point supported by the parametric gain in a driven-dissipative setting can open unexplored avenues in the context of non-Hermitian sensing.

We exploit the rich dynamics of nonlinear driven-dissipative systems in OPOs to formulate and engineer their spectral behaviors as phase transitions. We demonstrate second-order spectral phase transition in quadratic OPOs and identify the critical point demarcating the degenerate and non-degenerate oscillation regimes and the associated spontaneous symmetry breaking. We mapped the OPO dynamics to the universal Swift-Hohenberg equation [9, 34] and extend it to Kerr OPOs. We predict the occurrence of complex collective behavior like first-order phase transitions in coupled OPOs. Our results on non-equilibrium spectral behaviors can be utilized for enhanced sensing that leverages the diverging susceptibility of the critical point, and advanced computing paradigms exploiting the criticality of the spectral phase transition.

4.3 Results

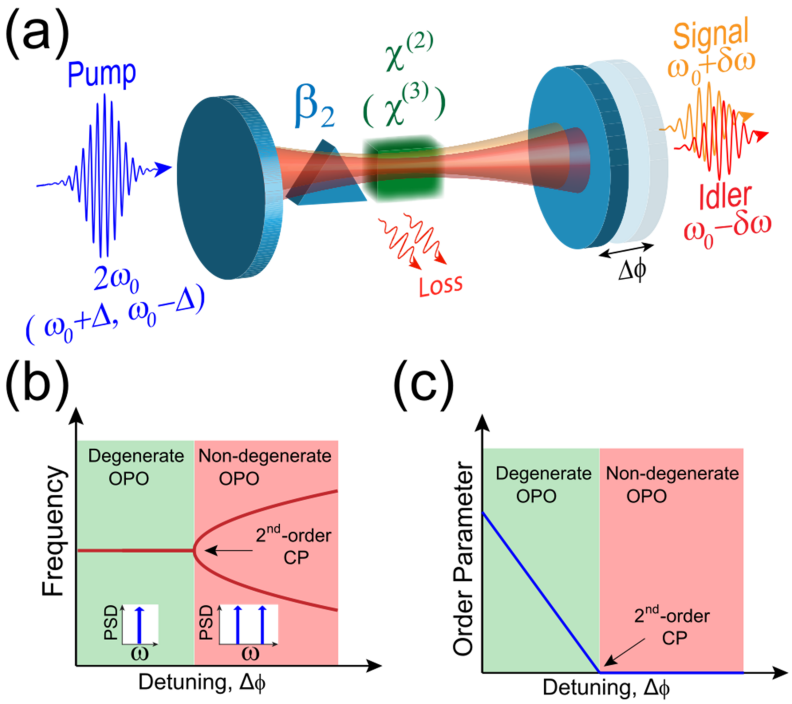

Figure 4.1: **Spectral phase transition in nonlinear photonic resonators**. a) OPO with the resonant signal and idler in the cavity with variable detuning ($\Delta\phi$) and second-order group-velocity dispersion (β_2). The nonlinearity can be provided by a quadratic ($\chi^{(2)}$) or a Kerr ($\chi^{(3)}$) medium. b) A second-order phase transition occurs at the critical detuning that marks the transition between the degenerate and the non-degenerate spectrum. c) This transition is characterized by a continuous order parameter, but a discontinuous derivative of the order parameter at the critical point (CP).

We consider a doubly-resonant OPO [22, 50] as a driven-dissipative system in a non-equilibrium steady state. The OPO driving is accomplished by the synchronous pulsed pump centered around the frequency $2\omega_0$, while the resonant signal and the idler constitute the longitudinal modes of the resonator centered around the half-harmonic frequency (ω_0).The interaction among the modes is engendered by the quadratic non-linearity (Fig. 4.1(a)). The inherent coupled nature of the signal and idler in a doubly-resonant OPO gives rise to rich nonlinear dynamics including the appearance of bi-phase states around degeneracy [36]. The mutual interplay between the cavity detuning and the temporal group velocity dispersion provides another degree of freedom, which governs the dynamics of signal/idler in synchronously pumped doubly resonant OPOs. This leads to discontinuities typical of a second-order phase transition around the critical cavity detuning (Fig. 4.1(b) and 4.1(c)). This spectral phase transition demarcates the sharp boundary between the degenerate and non-degenerate parametric oscillation.

In the CW-driven high-finesse limit, the OPO is governed by the mean-field evolution equation:

$$\frac{\partial a}{\partial \xi} = (-\alpha + i\Delta\phi)a + ga^* - i\frac{\beta_2}{2}\frac{\partial^2 a}{\partial t^2} - \left[\frac{\epsilon^2}{2u^2}\int_0^{Lu}(Lu-\tau)a(t-\tau)^2 d\tau\right]a^* \quad (4.1)$$

where a describes the signal envelope under the slowly varying envelope approximation limit. Here ξ, t refers to the slow time and the fast time, respectively [6]. α, $\Delta\phi$, β_2, and g denote the loss, detuning, group-velocity dispersion (GVD), and the phase-sensitive parametric gain, respectively. g in the CW-limit is expressed as $\epsilon b L$, where b is the pump amplitude. L refers to the cavity round trip length where the nonlinear interaction is encountered, ϵ includes the strength of the nonlinear interaction and u is the walk-off parameter. The last term to the right of the equation is responsible for the gain saturation. Each of these terms is normalized by suitable normalization factors (see Supplementary section 4.5.2).

We assume a perturbation in the field (signal/idler) around the half-harmonic frequency (ω_0) to be of the form: $a = a_+ e^{i\delta\omega t} + a_- e^{-i\delta\omega t}$. We perform linear stability analysis (neglecting gain saturation) to determine the most unstable longitudinal mode, which is given as:

$$\frac{d}{d\xi}\begin{bmatrix} a_+ \\ a_-^* \end{bmatrix} = \begin{bmatrix} -\alpha + i\Gamma & g \\ g^* & -\alpha - i\Gamma \end{bmatrix}\begin{bmatrix} a_+ \\ a_-^* \end{bmatrix} \quad (4.2a)$$

$$\lambda_{\pm} = -\alpha \pm \sqrt{|g|^2 - \Gamma^2} \tag{4.2b}$$

where $\Gamma = \Delta\phi + \frac{\beta_2}{2}(\delta\omega)^2$. Analyzing the eigenvalue (growth rate) (Eq. (4.2b)) of the linear stability matrix we arrive at two scenarios. First, when $\mathrm{sgn}(\Delta\phi)$ =$\mathrm{sgn}(\beta_2)$, we find that the most unstable frequency of oscillation is $\delta\omega = 0$, and the corresponding threshold (i.e., when $\lambda_+ = 0$) is $|g|_{\mathrm{th}} = \sqrt{\alpha^2 + (\Delta\phi)^2}$, leaving the OPO in the degenerate phase. However, when $\mathrm{sgn}(\Delta\phi) = -\mathrm{sgn}(\beta_2)$, the most unstable frequency of oscillation is given by $\delta\omega = |\frac{2\Delta\phi}{\beta_2}|^{\frac{1}{2}}$, and the associated threshold is $|g|_{\mathrm{th}} = \alpha$, leaving the OPO in the non-degenerate phase. This can be understood as cavity detuning ($\Delta\phi$) counterbalancing the GVD-induced detuning in the non-degenerate regime. This can happen for positive cavity detuning in the anomalous regime, where GVD-induced detuning is negative and they cancel exactly at $\omega_0 \pm \delta\omega$, thereby experiencing more gain in the non-degenerate phase resulting in OPO selecting non-degeneracy over degenerate oscillation. This proves the existence of the spectral phase transition which is demonstrated in Fig. 4.2. The spectral phase transition takes place around the detuning, $\Delta\phi = 0$. The behavior in the normal GVD regime (Fig. 4.2(d)) is reversed as compared to the anomalous GVD scenario (Fig. 4.2(b)). Results obtained experimentally (Fig. 4.2(c), Fig. 4.2(e)) agree well with the simulation.

The spectral transition can be interpreted as an order-disorder transition whereby the OPO transits from an ordered bi-phase state in the degenerate regime, to a disordered phase state in the non-degenerate regime with the signal assuming random phases and the idler following it. Thus the critical point marks the onset of the spontaneous U(1) symmetry breaking. In our context, we define OP as, $OP = \frac{d\lambda_{\mathrm{max}}}{d\Delta\phi}$, which represents the derivative of the gain with respect to the detuning. The phase-dependent parametric gain is sensitive to detuning-induced phase accumulation more acutely in the degenerate regime as opposed to the non-degenerate regime where it varies slowly with detuning. The order-disorder transition has important implications for the phase noise and coherence properties of the OPO. While the phase noise of OPO operating at degeneracy is dominated by the driving pump, in the non-degenerate regime phase diffusion leads to Schawlow-Townes limit for each of the signal and the idler [40], albeit with anti-correlation in their phases and potential phase-sum quadrature squeezing [15]. The phase transition description reveals interesting correlation properties in the dis-ordered regime, i.e., the non-

degenerate regime. The phase difference diffusion follows a power-law dependence as a function of detuning (i.e., distance from the critical point) which mimics the behavior of correlation functions in continuous phase transitions.

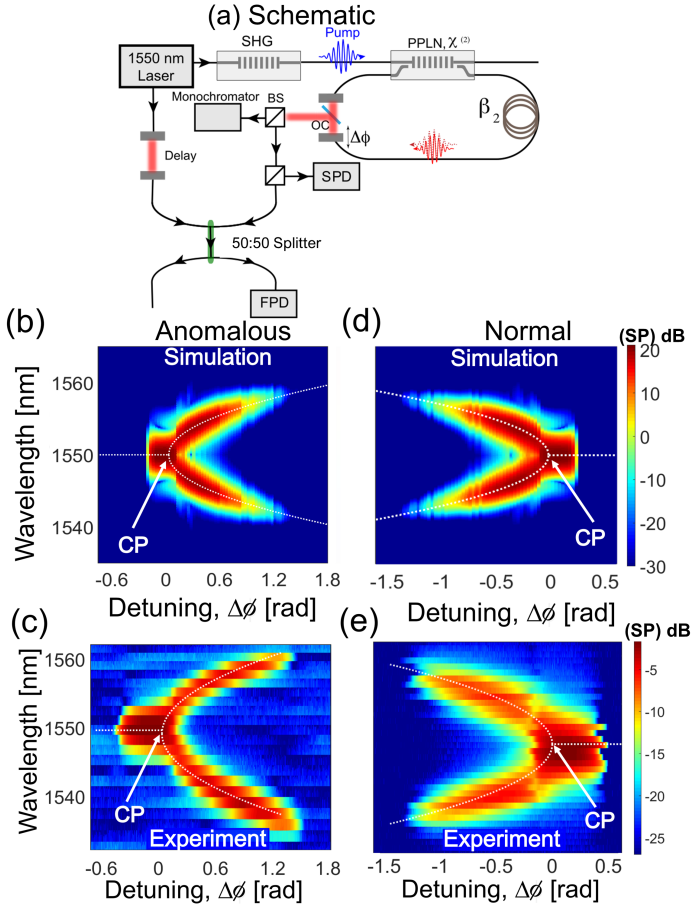

Figure 4.2: **Second-order spectral phase transition in an OPO**. a) Schematic of the experimental setup, which implements the spectral phase transition in a guided-wave OPO based on PPLN. Beam Splitter (BS), Output Coupler (OC), Slow Photo-detector (SPD), Fast Photo-detector (FPD), and Second Harmonic Generation (SHG). Spectrum (SP) as a function of detuning obtained through numerical simulation b) in anomalous dispersion regime (dotted line plots the theoretically expected spectral splitting, which in the non-degenerate regime is given by: $\delta\omega = \sqrt{\frac{-2\Delta\phi}{\beta_2}}$, d) in the normal dispersion regime. Experimental results capturing the second-order critical point c) in anomalous dispersion regime, e) in normal dispersion regime. It closely follows the square-root behavior (dotted line) in the non-degenerate regime. Colorbar represents power spectral density in dB.

We further characterize the quadratic OPO around the phase transition point (Fig. 4.3). The critical point coincides with the maximum output power of the OPO as observed numerically and experimentally (Fig. 4.3(a) and 4.3(b)). This behavior

can be explained by the gain calculations (inset of Fig. 4.3(c)). The threshold is a function of detuning and dispersion (see Supplementary section 4.5.3). The order parameter displays characteristics (Fig. 4.3(c)) typical of second-order phase transitions or soft transitions [48]. Additionally, in the pulsed regime as the OPO undergoes the phase transition the signal and idler combs split and interfere with each other with a beat frequency equal to the difference of their respective carrier-envelope offset frequencies. This leads to the spontaneous emergence of beat notes as shown in the measurement results of Fig. 4.3(d). This is a manifestation of a critical slowing-down phenomenon, where the time period of the beat-note tends to infinity as we approach the critical point from the non-degenerate regime. Note that, the detuning range of the parametric oscillation, as well as the ratio of degenerate and non-degenerate regimes above the threshold, is determined by the gain, which is a function of the pump power and cavity dispersion.

When two OPOs are coupled, the transition from degenerate to non-degenerate operation can occur as a first-order phase transition. Figure 4.4(a) depicts a schematic representation of the coupled OPO configuration. In the presence of the coupling, the competition between the two second-order phase transitions (as shown by the gain curve in Fig. 4.4(d)) results in the emergence of a first-order spectral phase transition (Fig. 4.4(e)). This first-order transition point causes a sudden discontinuity/hard transition in the spectrum (Fig. 4.4(b), Fig. 4.4(c)) as the coupled OPO transits from the non-degenerate to the degenerate spectral regime (Fig. 4.4(e)). The coupling in the linear regime induces a mode splitting which is expected to introduce a second-order phase transition around the split resonances as evident from the plot of OP in Fig. 4.4(d). This can be understood by the argument that a positive cavity detuning applied to individual cavities can appear both as a positive or a negative detuning in the coupled basis depending on the relative magnitude of the cavity detuning and the coupling strength. Further details regarding the modeling of coupled OPOs are presented in the supplementary section 5.5.2.

The demonstrated spectral phase transitions can be described by the universal Swift-Hohenberg equation which is also known to govern nonlinear pattern formation dynamics [9, 34] see Supplementary section 4.5.5. The same equation we derived in this context can describe degenerate four-wave mixing dynamics contingent on certain conditions. Thus, spectral phase transitions are also expected to occur in Kerr OPOs (Fig. 4.5(a)). For the Kerr OPO, we consider a conservative system governed

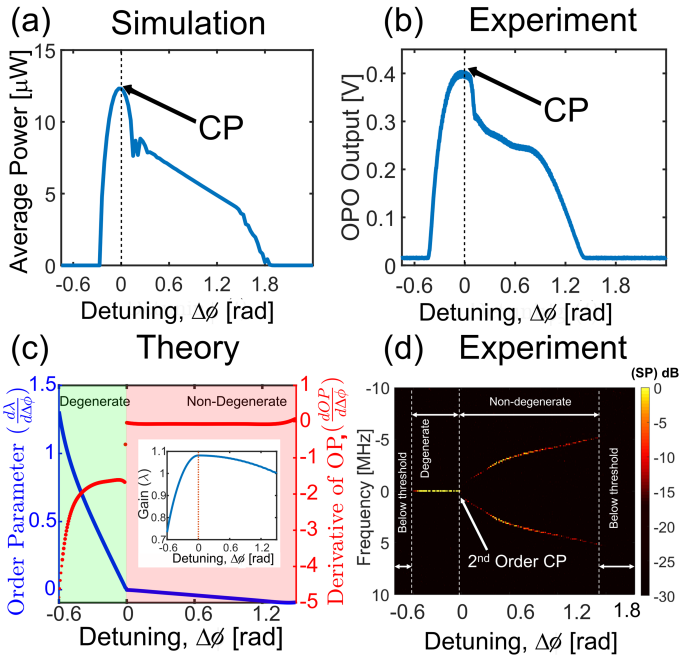

Figure 4.3: **Characterization of the second-order critical point.** OPO average output power as a function of cavity detuning obtained numerically (a) and experimentally (b) using a slow detector. This demonstrates the maximum conversion efficiency at the critical point. c) continuous order parameter but discontinuous derivative typical of a second order phase transition. The inset shows the gain curve as a function of cavity detuning, which has its maximum at the critical point. d) Spontaneous emergence of beat-note around the critical point. Measured RF spectrum (SP) captured using a fast detector in a multi-heterodyne measurement showing the co-existence of the signal and idler combs in the non-degenerate regime and their offset tuning.

by the nonlinear Schroedinger equation. $\frac{\partial A}{\partial z} = -i\frac{\beta_2}{2}\frac{\partial^2 A}{\partial \tau^2} + i\gamma|A|^2 A$. γ represents the effective third-order nonlinear co-efficient and β_2 stands for the second order GVD co-efficient. Degenerate parametric oscillation can be realized in a Kerr medium using dual pumps (Fig. 4.5(b) and 4.5(c)) [26, 41]. We represent the dual pumps as having amplitudes A_1 and A_2 and assume that they have equal power ($P = |A_1|^2 = |A_2|^2$) and possesses a detuning of Δ from the center of degeneracy. Owing to the symmetry, we assume the parametrically generated signal (A_s) and idler (A_i) to be detuned by $\delta\omega$ from the center of degeneracy. We express the field as given by the following expansion: $A(z,\tau) = A_1 e^{i\Delta\tau} + A_2 e^{-i\Delta\tau} + A_s(z)e^{i\delta\omega\tau} + A_i(z)e^{-i\delta\omega\tau}$. Parametric gain at the onset of the phase conjugation parametric process can be determined via a linear stability analysis. The growth rate due to the phase conjugation parametric process can be expressed as $e^{\lambda z}$ where λ is given by

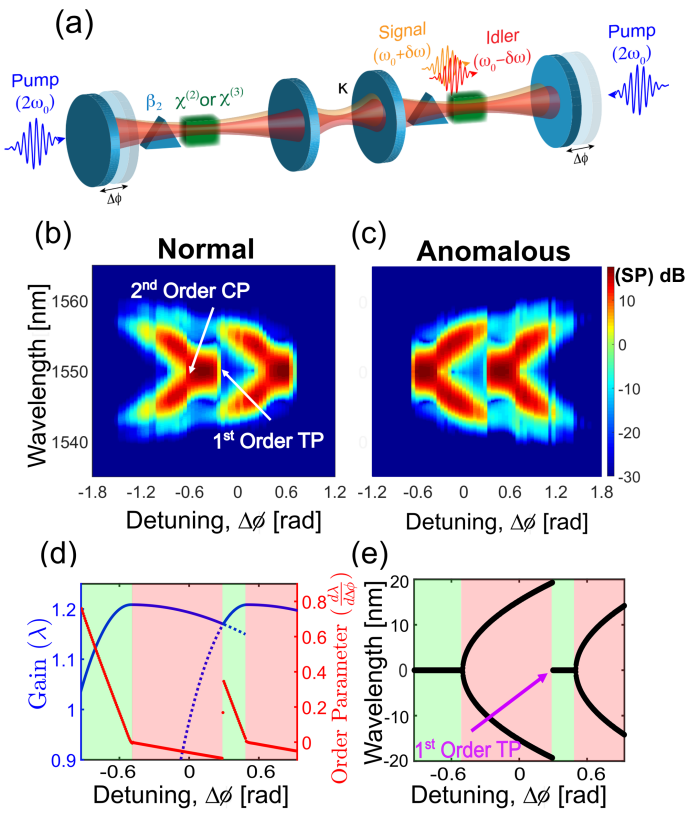

Figure 4.4: **First-order spectral phase transition in coupled OPOs.** a) Schematic configuration of a coupled OPO (coupling factor (κ)). b,c) Simulated spectrum (SP) as a function of cavity detuning b) in the normal dispersion regime, c) in the anomalous dispersion regime. d) Order parameter as a function of detuning showing the discontinuity at the location of the first-order transition point. The gain curve is also plotted alongside. The OPO selects the gain maximum and therefore does not follow the dashed portion of the gain curve. This gain competition between two second-order critical points gives rise to the first-order transition point. e) The spectrum considering the wavelength experiencing the maximum gain around which the signal/idler is centered. At the first-order transition, there is a discontinuous jump from the non-degenerate spectrum to the degenerate spectrum.

[41]:

$$\lambda = \sqrt{\left\{6\gamma P - \beta_2(\Delta^2 - (\delta\omega)^2)\right\}\left\{2\gamma P + \beta_2(\Delta^2 - (\delta\omega)^2)\right\}}. \tag{4.3}$$

The spectral phase transition is shown in Fig. 4.5(d). The fact that the associated critical point is second-order is established by analyzing the OP as depicted in Fig. 4.5(e).

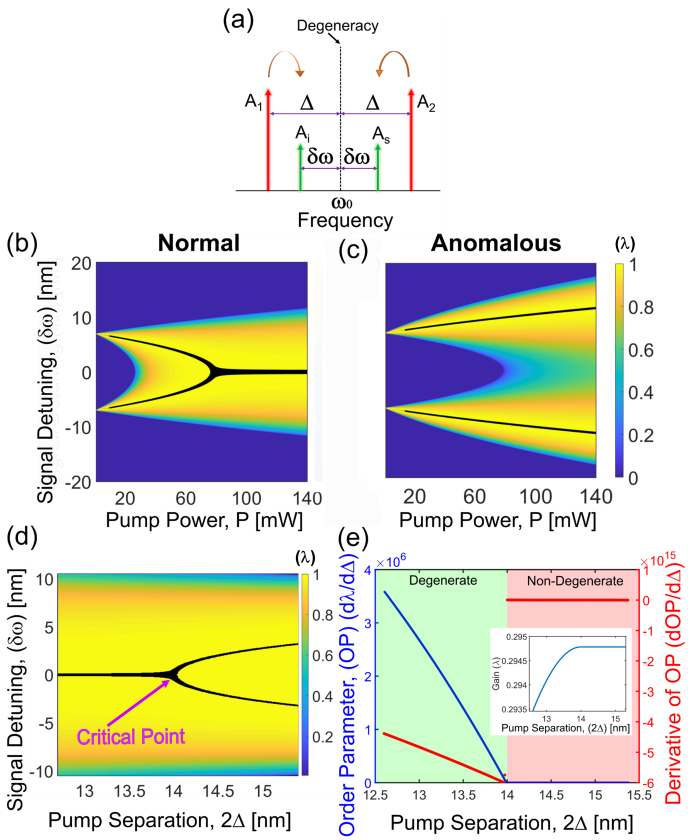

Figure 4.5: **Spectral phase transition in dual-pump four-wave mixing.** a) Illustration of the two pump fields getting converted to the signal and idler. b) The phase conjugation parametric instability gain (λ) (Eq. 4.3) curve in the normal dispersion regime as the pump power is varied. The maximum of the gain where the signal/idler is supposed to oscillate is marked by the black lines. Degenerate and non-degenerate oscillations are both expected in this case. c) The phase conjugation parametric process gain curve in the anomalous dispersion regime. Only non-degenerate oscillation is expected in this case. d) spectral phase transition (normal dispersion regime) as the pump separation (Δ) is varied. A degenerate to non-degenerate transition happens across the critical point. e) The critical point is characterized to be a second-order which displays continuous behavior in order-parameter but exhibits discontinuity in its derivative. Parameters used in the simulation are taken from [41].

4.4 Discussion

The abrupt frequency splitting around the critical point in these spectral phase transitions can be utilized for enhanced sensing. A sensor can be based on the second-order spectral phase transition biased at the critical point, that will exhibit a scaling of $\delta\omega \sim \varepsilon^{\frac{1}{2}}$, where ε is the small perturbation (e.g., in detuning) under consideration, similar to a second-order exceptional point [25]. However, if we

leverage the first-order spectral phase transition for a critical detector, we can utilize the discontinuity in the spectrum for highly enhanced sensitivity [19, 54]. The proportionality constant in the scaling law is a function of the cavity group-velocity dispersion. The smaller the dispersion, the higher the sensitivity (see Supplementary section 4.5.4). Spectral phase transitions in OPOs can also open opportunities for computing and quantum information processing. Phase transition occurring at the oscillation threshold of OPOs has been utilized as a promising computing resource in optical Ising machines [23, 36]. Phase transition occurring in the spectral domain can provide additional computing capabilities. For example, in the OPO-based Ising machines, which have been strictly operating at degeneracy so far [23, 36], the spectral phase transition can act as an additional search mechanism leveraging the symmetry breaking and additional phase noise in the non-degenerate regime. Moreover, our results on spectral phase transition can extend the foundation for phase-transition-based computing platforms [27].

Tuning the spectrum of parametric oscillation between degeneracy and non-degeneracy is a well-known concept, and the same is achieved by manipulating the phase matching curve via temperature, voltage control, etc. [13]. Distinctively, the presented spectral phase transition occurs as a multi-mode co-operative phenomenon [21] triggered by cavity phase detuning, where dispersion plays a crucial role, while the phase-matching enabled by the periodically poled waveguide remains unaltered.

The presented spectral phase transition is in sharp contrast to intensity-dependent bifurcation ubiquitous in nonlinear optical systems. The spectral bifurcation does not arise due to the gain saturation-induced nonlinearity. This is also corroborated by the existence of the quantum image of this above-threshold phenomenon below the threshold (where gain saturation is absent) which is consistent with the theoretical predictions in the spatial domain [18].

4.5 Supplementary

4.5.1 Experimental details

The OPO pump is derived from the mode-locked laser through second harmonic generation (SHG) in a quasi-phase-matched periodically poled lithium niobate (PPLN) crystal. The pump is centered around 775 nm. The main cavity is composed of a PPLN waveguide (reverse proton exchange, 40 mm long, periodically poled to phase-match 775-1550 nm interaction) [30] with

fiber-coupled output ports, fiber phase shifter, free-space section (to adjust the pump repetition rate to be multiple of the free spectral range of the cavity.), additional fiber segment to engineer the cavity dispersion, and a beam splitter which provides the output coupling.

To obtain the optical spectrum in scanning mode we used a tunable filter (1 nm bandwidth). The round-trip loss of the cavity amounts to approximately 9 dB. All fibers and devices existing in the optical path are single modes, polarization maintaining and connectors are angle polished. A tunable band-pass filter (Agiltron FOTF) is used as a monochromator. A combination of a Fast Detector (Menlo Systems FPD-510) and RF-Spectrum Analyser is used to measure the radio-frequency spectrum after beating the OPO output with that of the fully stabilized frequency comb (Menlo Systems FC1500-250-WG). In our configuration, we have 4 pulses circulating per round-trip.

The threshold in our setup is observed to be 680 μW of average power. The measurement is taken at a pump average power of 820 μW. This implies $p \approx 1.1$. The pump is centered around 775 nm (approximately 12 ps long pulses, 250 MHz repetition rate). The pigtail of the PPLN waveguide measures ~2 m in length and is made up of single mode, polarization maintaining (PM) fiber. Additionally, we have another PM fiber of length 15 cm. The combination of the pigtail, non-poled portion of the waveguide, fiber section of the phase shifter, and the additional fiber contribute to ϕ_2.

We measure the radio-frequency spectrum/beat-note by beating the OPO output with that of the broadband fully stabilized frequency comb (Menlo Comb). On account of the pulsed nature, we had to adjust the delay line in order to temporally overlap the OPO output and the fully stabilized frequency comb output.

4.5.2 Derivation of high Finesse limit OPO mean-field evolution equation

In the high finesse limit, we consider the doubly resonant OPO to be governed by parametric nonlinear interaction, group velocity dispersion (cavity averaged) induced chirp, round-trip loss, and detuning of the cavity. The quadratic nonlinear interaction considered is given by Eq. 4.4. Eq. 4.4b can be integrated by the method of characteristics to yield Eq. 4.5a. This when substituted in Eq. 4.4a gives Eq. 4.5b. The resultant nonlinear interaction is summarized in Eq. 4.6a, while the effect of GVD is included in Eq. 4.6b. Combining all the relevant cavity effects we get the evolution of the signal field on a round-trip basis as given in Eq. 4.7a. Under

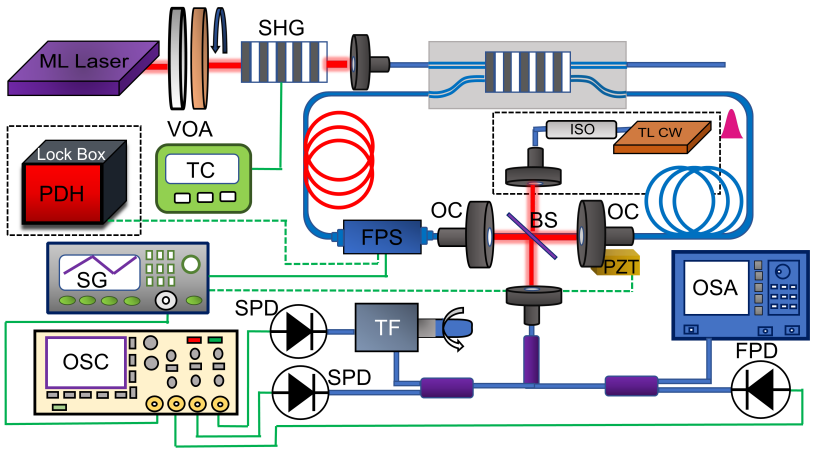

Figure 4.6: **Detailed experimental schematic** showing all optical pathways, electrical connections, and locking arrangement. Components included inside the dashed boundary are deployed for locking arrangement. OSC: Oscilloscope, SG: Signal Generator, TF: Tunable Band-pass filter, OSA: Optical Spectrum Analyser, ISO: Isolator, OC: Output Coupler, FPS: Fiber phase shifter(General Photonics-FPS-001), ML Laser: Mode-Locked Laser (Menlo Systems FC1500-250-WG, 250 MHz repetition rate, 1550 nm), SHG: Second Harmonic Generation (Covesion MSHG1550-1.0-40), SPD: Slow Photo Detector, FPD: Fast Photo Detector, TC: Temperature Controller(Covesion OC2 Temperature Controller), BS: Beam Splitter, VOA: Variable Optical Attenuator, PZT: Piezo Transducer, PDH: Pound Drever Hall Lock Box, TL CW: Tunable Continous Wave Laser.

the assumptions of the high finesse cavity, we convert the difference equation to a partial differential equation (Eq. 4.7b). We define several normalization factors (Eq. 4.8) and express the signal evolution in the mean-field approximation by Eq. 4.9.

$$\frac{\partial a}{\partial z} = \epsilon a^* b \tag{4.4a}$$

$$\frac{\partial b}{\partial z} = -u\frac{\partial b}{\partial t} - \frac{\epsilon}{2}a^2 \tag{4.4b}$$

$$b(z,t) = b_0(t-uz) - \frac{\epsilon}{2u}\int_{t-uz}^{t} a(z-\frac{t-t'}{u},t')^2 dt' \tag{4.5a}$$

$$\frac{\partial a(z,t)}{\partial z} = \epsilon b_0(t-uz)a(z,t)^* - \frac{\epsilon^2}{2u}a(z,t)^*\int_{t-uz}^{t} a(z-\frac{t-t'}{u},t')^2 dt' \tag{4.5b}$$

$$a_{out}(t) = a_{in}(t) + \left[\frac{\epsilon}{u}\int_0^{Lu} b_0(t-\tau)d\tau\right] a_{in}^*(t) - \left[\frac{\epsilon^2}{2u^2}\int_0^{Lu}(Lu-\tau)a_{in}(t-\tau)^2 d\tau\right] a_{in}^*(t) \quad (4.6a)$$

$$\frac{da}{dt} = \left[-i\frac{\beta_2}{2!}\frac{\partial^2}{\partial t^2} + \frac{\beta_3}{3!}\frac{\partial^3}{\partial t^3}\right] a(t) \quad (4.6b)$$

$$a_{n+1}(t) - a_n(t) = (-\alpha + i\Delta\phi)a_n(t) + \left[-i\frac{\beta_2}{2!}\frac{\partial^2}{\partial t^2} + \frac{\beta_3}{3!}\frac{\partial^3}{\partial t^3}\right] a_n(t) + \left[\frac{\epsilon}{u}\int_0^{Lu} b_0(t-\tau)d\tau - \frac{\epsilon^2}{2u^2}\int_0^{Lu}(Lu-\tau)a_n(t-\tau)^2 d\tau\right] a_n^*(t) \quad (4.7a)$$

$$T_R\frac{\partial a(\xi,t)}{\partial \xi} = (-\alpha + i\Delta\phi)a(\xi,t) + \left[-i\frac{\beta_2}{2!}\frac{\partial^2}{\partial t^2} + \frac{\beta_3}{3!}\frac{\partial^3}{\partial t^3}\right] a(\xi,t) + \left[\frac{\epsilon}{u}\int_0^{Lu} b_0(t-\tau)d\tau - \frac{\epsilon^2}{2u^2}\int_0^{Lu}(Lu-\tau)a(t-\tau)^2 d\tau\right] a^*(\xi,t) \quad (4.7b)$$

$$\xi' = \frac{\xi}{T_R}, g = \frac{\epsilon}{u}\int_0^{Lu} b_0(t-\tau)d\tau \quad (4.8)$$

$$\frac{\partial a}{\partial \xi} = (-\alpha + i\Delta\phi)a + ga^* - \left[\frac{\epsilon^2}{2u^2}\int_0^{Lu}(Lu-\tau)a(t-\tau)^2 d\tau\right] a^* - i\frac{\beta_2}{2}\frac{\partial^2 a}{\partial t^2} \quad (4.9)$$

4.5.3 CW gain limit of OPO (without mean-field approximation)

While Eq. 4.9 predicts the occurrence of the spectral phase transition in the high-Q limit, it also occurs in the low Q limit (where the mean-field approximation is not valid and lumped interaction is to be considered) as well. In fact, our experimental realization deals with low Finesse cavity. In such scenarios where the mean-field equation is no more valid, we present a model that captures the spectral phase transition assuming that the pump is CW. Note that, the analysis for the pulsed pumping case is not trivial, and one has to resort to full numerical simulation.

Reference [22] suggest that the CW gain approximation can predict the frequency of oscillation with a good agreement. However, one has to include the gain clipping component as well to obtain the signal/idler pulse shapes, and power spectrum in the case of synchronously pumped OPO. Thus for studying spectral phase transition, the CW gain limit is a reliable approach. In any case, one can always perform a full spatiotemporal simulation to judge if the approximation holds good or not.

We assume signal (a_s) to be centered at frequency $\omega_0+\delta\omega$, and idler (a_i) at $\omega_0-\delta\omega$, when the pump frequency is $2\omega_0$. We define: $a_+ = \frac{(a_s+a_i^*)}{2}$, and $a_- = \frac{(a_s-a_i^*)}{2}$. In the near-threshold limit, we neglect the effect of gain saturation. We obtain:

$$\begin{bmatrix} \dot{a_+} \\ \dot{a_-} \end{bmatrix} = \begin{bmatrix} -\frac{\alpha^{(a)}}{2} + \epsilon b & i\frac{\beta_2^{(a)}(\delta\omega)^2}{2} \\ i\frac{\beta_2^{(a)}(\delta\omega)^2}{2} & -\frac{\alpha^{(a)}}{2} - \epsilon b \end{bmatrix} \begin{bmatrix} a_+ \\ a_- \end{bmatrix}. \tag{4.10}$$

Eq. 4.10 describes the interaction within the PPLN waveguide. After exiting the gain medium, the signal/idler fields encounter cavity dispersion, out-coupling loss, and round-trip feedback. This leads to: $a_s \rightarrow G_0^{-\frac{1}{2}} e^{i(\phi+\psi)} a_s$, $a_i \rightarrow G_0^{-\frac{1}{2}} e^{i(\phi-\psi)} a_i$, where $\phi = \Delta\phi + \frac{1}{2}\phi_2(\delta\omega)^2$ (symmetric phase shift) and $\psi = \frac{l\lambda^{(a)}}{2c}\delta\omega$ (asymmetric phase shift).

$$\begin{bmatrix} a_+ \\ a_- \end{bmatrix}_{n+1} \rightarrow G_0^{-\frac{1}{2}} e^{-\frac{\alpha^{(a)}L}{2}} e^{i\psi} \begin{bmatrix} \cos(\phi) & i\sin(\phi) \\ i\sin(\phi) & \cos(\phi) \end{bmatrix} \exp\left(\begin{bmatrix} \epsilon b & i\frac{\beta_2^{(a)}(\delta\omega)^2}{2} \\ i\frac{\beta_2^{(a)}(\delta\omega)^2}{2} & -\epsilon b \end{bmatrix} L \right) \begin{bmatrix} a_+ \\ a_- \end{bmatrix}_n \tag{4.11}$$

The round-trip evolution of $a_\pm$ is dictated by Eq. 4.11. This equation has two eigenvalues: $\lambda_\pm$. The larger of them (λ_+) denotes the round-trip gain. The frequency of oscillation ($\delta\omega$) will be determined by λ_{max}.

One can posit that this essentially happens when the phase shift ($\Delta\phi$) is compensated by the total GVD (waveguide + cavity) contribution ($\beta_2 = \phi_2 + \beta_2^{(a)} L$) and is given by:

$$\Delta\phi + \frac{\beta_2}{2}(\delta\omega)^2 = n\pi. \tag{4.12}$$

The zeroth order resonance condition gives $\Delta\phi + \frac{\beta_2}{2}(\delta\omega)^2 = 0$. This means in the non-degenerate regime: $\delta\omega = \sqrt{-\frac{2\Delta\phi}{\beta_2}}$. When the perturbation is caused by the

critical point ($\Delta\phi = 0$), we can write $\Delta\phi = \epsilon$, where ϵ is the small perturbation. This gives the square-root dependence of frequency splitting (similar to second-order exceptional point) for sensors based on second-order spectral phase transition, biased at the critical point.

4.5.4 Effect of group velocity dispersion

The spectral splitting in the non-degenerate regime that accompanies the spectral phase transition can be engineered. Here, we study how spectral splitting is dependent on cavity dispersion.

From Eq. 4.12 it is evident that the spectral splitting in the non-degenerate regime is a function of the second order (β_2) group velocity dispersion (GVD) for a fixed detuning. The sensitivity of sensors based on this spectral phase transition will be higher in cavities with lower β_2. At the same time, we also find, that GVD influences the gain and thereby the order parameter in the non-degenerate phase. The change in slope of the order parameter for different values of GVD also highlights the variation of the sensitivity.

To investigate the effect of GVD on the spectral splitting, we assume that the cavity is homogeneous with finite β_2. Higher-order dispersions are neglected. Fig. 4.7(a) suggests that the spectral splitting diverges as it approaches zero GVD. However, in practice, higher-order dispersions will contribute to the limit of near zero β_2. Also, the dispersion of nonlinearity needs to be accounted for distantly separated signal/idler peaks. In the near-zero GVD limit the lumped assumption of $\beta_2^{(a)}$ and ϕ_2 contributing to net GVD β_2 breaks down, and Eq. 4.12 cease to be valid. One has to resort to numerical simulation to study this scenario. For Fig. 4.7(b) and Fig. 4.7(c) we are operating away from near zero GVD, and the lumped approximation is valid. We thus change the net GVD by varying ϕ_2.

4.5.5 Swift- Hohenberg Equation/ Order Parameter Description

Diverse nonlinear systems in laser physics although being described by distinct equations, sometimes exhibit identical nonlinear dynamics. All these systems can be reduced to a normal form under certain assumptions, which is also known as the order parameter description or the Swift-Hohenberg equation (SHE) [46]. SHE provides a generalized framework to study pattern formation/ localized structures.

$$\frac{\partial A}{\partial t} = \underbrace{\mu A - qA^3}_{\substack{\text{super-critical} \\ \text{pitchfork bifurcation}}} \underbrace{- r(\nabla^2 + \Omega_0^2)^2 A}_{\text{SPT}} \tag{4.13}$$

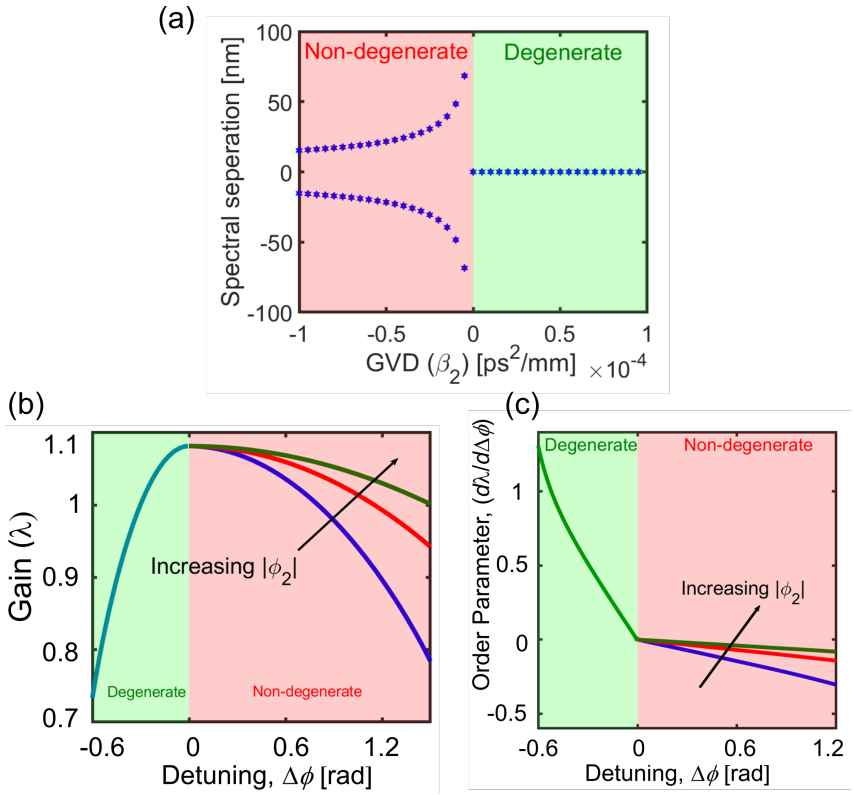

Figure 4.7: **Effect of GVD on spectral phase transition**. a) Spectral splitting as a function of cavity GVD. The detuning is kept fixed at $\Delta\phi = 0.3$. The dependence of gain (b) and order parameter (c) as the GVD is varied. These results are obtained from numerical simulation.

We provide the derivation for the real SHE here. Here we assume a crude approximation of the gain saturation term and represent it by $q|a|^2a$. Therefore, the mean-field equation (Eq. 4.9) reduces to the simpler form (Eq. 4.13).

$$\frac{\partial a}{\partial \xi} = (-\alpha + i\Delta\phi)a + ga^* - q|a|^2a - i\frac{\beta_2}{2}\frac{\partial^2 a}{\partial t^2} \tag{4.14}$$

We introduce a small parameter ϵ. We express the signal field as $a = \sum_n \epsilon^n a_n$. The gain parameter is expanded about the threshold value at zero detuning as: $g = \alpha + p\epsilon^2$. We assume $(\Delta\phi - \frac{\beta_2}{2}\frac{\partial^2}{\partial t^2}) = \epsilon\Phi$. We introduce the slow time scale: $T = \epsilon^2\xi$. Substituting these in Eq. 4.14, segregating terms with different orders of ϵ, satisfying the solvability conditions in successive orders we obtain the order parameter equation/ real SHE as follows:

$O(\epsilon)$: $-a_1 + a_1^* = 0$. This implies to the first order the signal field is a real quantity.

$O(\epsilon^2)$: $-\alpha a_2 + \alpha a_2^* + i\Phi a_1$=0

$O(\epsilon^3)$: $\frac{\partial a_1}{\partial T} = -\alpha a_3 + i\Phi a_2 + \alpha a_3^* + p a_1^* - q|a_1|^2 a_1$. Taking a conjugate of this and adding it to itself, we get: $\frac{\partial a_1}{\partial T} = p a_1 - q a_1^3 - \frac{(\Phi)^2}{2\alpha} a_1$.

We define $A = \epsilon a_1$. We get the resultant real SHE as:

$$\frac{\partial A}{\partial \xi} = (g - \alpha)A - qA^3 - \frac{1}{2\alpha}\left(\Delta\phi - \frac{\beta_2}{2}\frac{\partial^2}{\partial t^2}\right)^2 A. \tag{4.15}$$

4.5.6 Degenerate optical parametric oscillator in Kerr nonlinear medium

Phase-sensitive phase conjugation process occurring in a Kerr nonlinear medium in the presence of two pumps can emulate the quadratic OPO behavior. We obtain the parametric gain associated with the phase conjugation process in such a scenario.

We can realize degenerate parametric oscillation in Kerr medium if dual pumps are employed [38]. Let us assume we inject two CW pumps of equal power in a non-resonant Kerr nonlinear medium. Our analysis can be extended to resonant cases easily. We represent pump 1 as $A_1 = \sqrt{P}e^{i(\phi_1(z) - \omega_1 t)}$, where $\omega_1 = \omega_0 - \Delta$, such that Δ is the detuning from the center of degeneracy (ω_0). Pump 2 is given by: $A_2 = \sqrt{P}e^{i(\phi_2(z) - \omega_2 t)}$, where $\omega_2 = \omega_0 + \Delta$.

If a small signal perturbation is considered, then it can undergo the following nonlinear interactions, namely modulation instability (MI), four-wave mixing Bragg Scattering, and phase conjugation. These processes are depicted in Fig. 4.8. For parametric oscillation that mimics a second-order nonlinear down conversion process, we are interested in the phase conjugation interaction. MI does not appear in the normal GVD regime, which is the dispersion of interest to observe spectral phase transition. However, in the anomalous dispersion regime, the generated MI sidebands are also transferred by the Kerr interaction to higher-order FWM (four-wave mixing) sidebands. This leads to the collective behavior of the instability [1, 16].

We consider a signal of the form: $A_s = B_s(z)e^{i(\phi_2(z) - \omega_s t)}$, where $\omega_s = \omega_0 + \delta\omega$, such that $\delta\omega$ is the detuning from the center of degeneracy (ω_0). Another idler counterpart is assumed to be: $A_i = B_i(z)e^{i(\phi_1(z) - \omega_i t)}$, where $\omega_i = \omega_0 - \delta\omega$. Clearly, $\delta\omega = 0$

implies degenerate parametric oscillation. The signal and idler are considered to be small signals such that it is amenable to linearization/ linear stability analysis.

The evolution of the optical fields in the non-resonant Kerr nonlinear medium is governed by the Schrodinger equation which is given by:

$$\frac{\partial A}{\partial z} = i\beta(i\frac{\partial}{\partial t})A + i\gamma|A|^2A \tag{4.16}$$

where, $\beta(\omega)$ is the Taylor expansion of the dispersion function, incorporating all orders of GVDs, and γ is the nonlinearity coefficient. The total complex optical field at the input is given by: $A = A_1 + A_2 + A_i + A_s$. The leading order expansion in the undepleted pump approximation yields: $\phi_1(z) = \beta(\omega_1)z + \gamma(3P)z$, and $\phi_2(z) = \beta(\omega_2)z + \gamma(3P)z$.

The evolution of the signal and idler will be governed by:

$$\frac{d}{dz}\begin{bmatrix} B_i \\ B_s^* \end{bmatrix} = \begin{bmatrix} i[\beta(\omega_i) - \beta(\omega_1) + \gamma P] & i2\gamma P \\ -i2\gamma P & -i[\beta(\omega_s) - \beta(\omega_2) + \gamma P] \end{bmatrix}\begin{bmatrix} B_i \\ B_s^* \end{bmatrix}. \tag{4.17}$$

Considering only second order GVD, we have $\beta(\omega_i) - \beta(\omega_1) = \beta(\omega_s) - \beta(\omega_2) = \frac{\beta_2}{2}\left((\delta\omega)^2 - \Delta^2\right)$. The larger eigenvalue of the linear stability matrix determines the gain and is given by:

$$\lambda = \sqrt{\left\{6\gamma P - \beta_2(\Delta^2 - (\delta\omega)^2)\right\}\left\{2\gamma P + \beta_2(\Delta^2 - (\delta\omega)^2)\right\}}. \tag{4.18}$$

It should be noted that the complete dynamics of the dual-pump mediated interactions in a Kerr medium cannot be described by the incoherently coupled nonlinear Schrodinger equations which neglect the multiple FWM interactions [45].

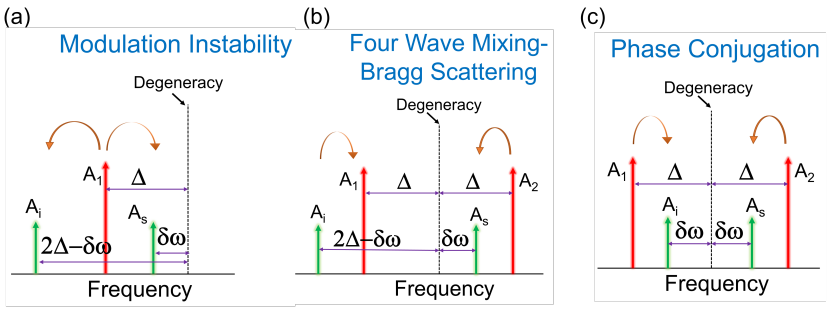

Figure 4.8: **Dual pumped Kerr nonlinear medium.** Nonlinear interactions can be classified as: a) Modulation Instability b) Four-wave Mixing Bragg Scattering c) Phase Conjugation.

References

[1] Andrea Armaroli and Stefano Trillo. Collective modulation instability of multiple four-wave mixing. *Optics Letters*, 36(11):1999–2001, 2011.

[2] Eberhard Bodenschatz, Werner Pesch, and Guenter Ahlers. Recent developments in Rayleigh-Bénard convection. *Annual Review of Fluid Mechanics*, 32(1):709–778, 2000.

[3] Umberto Bortolozzo, Paolo Villoresi, and Pier Luigi Ramazza. Experimental evidence for detuning induced pattern selection in nonlinear optics. *Physical Review Letters*, 87(27):274102, 2001.

[4] Iacopo Carusotto and Cristiano Ciuti. Quantum fluids of light. *Reviews of Modern Physics*, 85(1):299, 2013.

[5] Carlton M. Caves. Quantum limits on noise in linear amplifiers. *Physical Review D*, 26(8):1817, 1982.

[6] Stéphane Coen, Hamish G Randle, Thibaut Sylvestre, and Miro Erkintalo. Modeling of octave-spanning Kerr frequency combs using a generalized mean-field lugiato–lefever model. *Optics Letters*, 38(1):37–39, 2013.

[7] Mark C. Cross and Pierre C. Hohenberg. Pattern formation outside of equilibrium. *Reviews of modern physics*, 65(3):851, 1993.

[8] Galbadrakh Dagvadorj, J. M. Fellows, S Matyjaśkiewicz, Francesca M. Marchetti, Iacopo Carusotto, and Marzena H. Szymańska. Nonequilibrium phase transition in a two-dimensional driven open quantum system. *Physical Review X*, 5(4):041028, 2015.

[9] G. J. De Valcarcel, Kcstutis Staliunas, Eugenio Roldán, and VJ Sánchez-Morcillo. Transverse patterns in degenerate optical parametric oscillation and degenerate four-wave mixing. *Physical Review A*, 54(2):1609, 1996.

[10] Vittorio DeGiorgio and Marlan O. Scully. Analogy between the laser threshold region and a second-order phase transition. *Physical Review A*, 2(4):1170, 1970.

[11] Peter D. Drummond, K. J. McNeil, and D. F. Walls. Non-equilibrium transitions in sub/second harmonic generation. *Optica Acta: International Journal of Optics*, 27(3):321–335, 1980.

[12] K. Dunnett and Marzena H. Szymańska. Keldysh field theory for nonequilibrium condensation in a parametrically pumped polariton system. *Physical Review B*, 93(19):195306, 2016.

[13] Robert C. Eckardt, C. D. Nabors, William J Kozlovsky, and Robert L. Byer. Optical parametric oscillator frequency tuning and control. *Journal of the Optical Society of America B*, 8(3):646–667, 1991.

[14] Peter Engels, Collin Atherton, and Mark Hoefer. Observation of Faraday waves in a Bose-Einstein condensate. *Physical Review Letters*, 98(9):095301, 2007.

[15] Claude Fabre, Elisabeth Giacobino, Antoine Heidmann, and Serge Reynaud. Noise characteristics of a non-degenerate optical parametric oscillator-application to quantum noise reduction. *Journal de Physique*, 50(10):1209–1225, 1989.

[16] Julien Fatome, Christophe Finot, Andrea Armaroli, and Stefano Trillo. Observation of modulationally unstable multi-wave mixing. *Optics Letters*, 38(2):181–183, 2013.

[17] Baruch Fischer and Alexander Bekker. Many-body photonics. *Optics and Photonics News*, 24(9):40–47, 2013.

[18] Alessandra Gatti and Luigi Lugiato. Quantum images and critical fluctuations in the optical parametric oscillator below threshold. *Physical Review A*, 52(2): 1675, 1995.

[19] Gregory N. Gol'Tsman, O. Okunev, Galina Chulkova, A. Lipatov, Andrew Semenov, Konstantin Smirnov, B. Voronov, A. Dzardanov, C. Williams, and Roman Sobolewski. Picosecond superconducting single-photon optical detector. *Applied Physics Letters*, 79(6):705–707, 2001.

[20] Ariel Gordon and Baruch Fischer. Phase transition theory of many-mode ordering and pulse formation in lasers. *Physical Review Letters*, 89(10): 103901, 2002.

[21] Hermann Haken. Cooperative phenomena in systems far from thermal equilibrium and in nonphysical systems. *Reviews of Modern Physics*, 47 (1):67, 1975.

[22] Ryan Hamerly, Alireza Marandi, Marc Jankowski, Martin M. Fejer, Yoshihisa Yamamoto, and Hideo Mabuchi. Reduced models and design principles for half-harmonic generation in synchronously pumped optical parametric oscillators. *Physical Review A*, 94(6):063809, 2016.

[23] Ryan Hamerly, Takahiro Inagaki, Peter L. McMahon, Davide Venturelli, Alireza Marandi, Tatsuhiro Onodera, Edwin Ng, Carsten Langrock, Kensuke Inaba, Toshimori Honjo, et al. Experimental investigation of performance differences between coherent Ising machines and a quantum annealer. *Science advances*, 5(5):eaau0823, 2019.

[24] Tobias Herr, Victor Brasch, John D. Jost, Christine Y. Wang, Nikita M. Kondratiev, Michael L. Gorodetsky, and Tobias J. Kippenberg. Temporal solitons in optical microresonators. *Nature Photonics*, 8(2):145, 2014.

[25] Hossein Hodaei, Absar U. Hassan, Steffen Wittek, Hipolito Garcia-Gracia, Ramy El-Ganainy, Demetrios N. Christodoulides, and Mercedeh Khajavikhan. Enhanced sensitivity at higher-order exceptional points. *Nature*, 548(7666): 187, 2017.

[26] Takahiro Inagaki, Kensuke Inaba, Ryan Hamerly, Kyo Inoue, Yoshihisa Yamamoto, and Hiroki Takesue. Large-scale Ising spin network based on degenerate optical parametric oscillators. *Nature Photonics*, 10(6):415, 2016.

[27] Kirill P. Kalinin, Alberto Amo, Jacqueline Bloch, and Natalia G. Berloff. Polaritonic XY-Ising machine. *arXiv preprint arXiv:2003.09414*, 2020.

[28] A. V. Kuznetsov. Optical bistability driven by a first order phase transition. *Optics Communications*, 81(1-2):106–111, 1991.

[29] Yu-Hung Lai, Yu-Kun Lu, Myoung-Gyun Suh, and Kerry Vahala. Enhanced sensitivity operation of an optical gyroscope near an exceptional point. *arXiv preprint arXiv:1901.08217*, 2019.

[30] Carsten Langrock and Martin M. Fejer. Fiber-feedback continuous-wave and synchronously-pumped singly-resonant ring optical parametric oscillators using reverse-proton-exchanged periodically-poled lithium niobate waveguides. *Optics Letters*, 32(15):2263–2265, 2007.

[31] Hoi-Kwan Lau and Aashish A. Clerk. Fundamental limits and non-reciprocal approaches in non-hermitian quantum sensing. *Nature Communications*, 9(1): 4320, 2018.

[32] Marco Leonetti, Claudio Conti, and Cefe Lopez. The mode-locking transition of random lasers. *Nature Photonics*, 5(10):615, 2011.

[33] Mikhail F. Limonov, Mikhail V. Rybin, Alexander N. Poddubny, and Yuri S. Kivshar. Fano resonances in photonics. *Nature Photonics*, 11(9):543, 2017.

[34] Stefano Longhi and Angelo Geraci. Swift-Hohenberg equation for optical parametric oscillators. *Physical Review A*, 54(5):4581, 1996.

[35] Luigi A. Lugiato and René Lefever. Spatial dissipative structures in passive optical systems. *Physical Review Letters*, 58(21):2209, 1987.

[36] Alireza Marandi, Zhe Wang, Kenta Takata, Robert L. Byer, and Yoshihisa Yamamoto. Network of time-multiplexed optical parametric oscillators as a coherent Ising machine. *Nature Photonics*, 8(12):937, 2014.

[37] G. Marowsky and W. Heudorfer. Second and first order phase transition analogy in the operation of an organic dye laser. *Optics Communications*, 26 (3):381–383, 1978.

[38] Colin J. McKinstrie, Stojan Radic, and Andrew R. Chraplyvy. Parametric amplifiers driven by two pump waves. *IEEE Journal of Selected Topics in Quantum Electronics*, 8(3):538–547, 2002.

[39] Mohammad-Ali Miri and Andrea Alu. Exceptional points in optics and photonics. *Science*, 363(6422), 2019.

[40] C. D. Nabors, S. T. Yang, Tim Day, and Robert L. Byer. Coherence properties of a doubly resonant monolithic optical parametric oscillator. *Journal of the Optical Society of America B*, 7(5):815–820, 1990.

[41] Yoshitomo Okawachi, Mengjie Yu, Kevin Luke, Daniel O. Carvalho, Sven Ramelow, Alessandro Farsi, Michal Lipson, and Alexander L. Gaeta. Dual-pumped degenerate Kerr oscillator in a silicon nitride microresonator. *Optics Letters*, 40(22):5267–5270, 2015.

[42] Gian-Luca Oppo, Alison M. Yao, and Domenico Cuozzo. Self-organization, pattern formation, cavity solitons, and rogue waves in singly resonant optical parametric oscillators. *Physical Review A*, 88(4):043813, 2013.

[43] Şahin K. Özdemir, Stefan Rotter, Franco Nori, and Lan Yang. Parity–time symmetry and exceptional points in photonics. *Nature Materials*, 18(8):783–798, 2019.

[44] Chad Ropp, Nicolas Bachelard, David Barth, Yuan Wang, and Xiang Zhang. Dissipative self-organization in optical space. *Nature Photonics*, 12(12):739, 2018.

[45] Joshua E. Rothenberg. Modulational instability of copropagating frequencies for normal dispersion. *Physical Review Letters*, 64(7):813, 1990.

[46] Kestutis Staliunas and Victor J. Sanchez-Morcillo. *Transverse patterns in nonlinear optical resonators*, volume 183. Springer Science & Business Media, 2003.

[47] Harry Eugene Stanley. *Phase transitions and critical phenomena*. Clarendon Press, Oxford, 1971.

[48] Steven H. Strogatz. *Nonlinear dynamics and chaos: with applications to physics, biology, chemistry, and engineering*. CRC Press, 2018.

[49] Victor B. Taranenko, Kestutis Staliunas, and C. O. Weiss. Pattern formation and localized structures in degenerate optical parametric mixing. *Physical Review Letters*, 81(11):2236, 1998.

[50] Stefano Trillo and Marc Haelterman. Parametric solitons in passive structures with feedback. In *Spatial Solitons*, pages 359–393. Springer, 2001.

[51] Kerry J. Vahala. Optical microcavities. *Nature*, 424(6950):839, 2003.

[52] M. Vaupel, A. Maitre, and Claude Fabre. Observation of pattern formation in optical parametric oscillators. *Physical Review Letters*, 83(25):5278, 1999.

[53] Heming Wang, Yu-Hung Lai, Zhiquan Yuan, Myoung-Gyun Suh, and Kerry Vahala. Petermann-factor limited sensing near an exceptional point. *arXiv preprint arXiv:1911.05191*, 2019.

[54] Li-Ping Yang and Zubin Jacob. Quantum critical detector: Amplifying weak signals using discontinuous quantum phase transitions. *Optics Express*, 27(8): 10482–10494, 2019.

Chapter 5

FIRST-ORDER SPECTRAL PHASE TRANSITION IN COUPLED OPTICAL PARAMETRIC OSCILLATORS

Roy, Arkadev, Rajveer Nehra, Carsten Langrock, Martin Fejer, and Alireza Marandi. Non-equilibrium spectral phase transitions in coupled nonlinear optical resonators. ***Nature Physics***, pages 1–8, 2023. doi: https://doi.org/10.1038/s41567-022-01874-8.
A.R. contributed to the conception of the project, executed the experiments, performed numerical simulations alongside associated analytical results, and participated in the writing of the manuscript.

5.1 Abstract

Coupled systems with multiple interacting degrees of freedom provide a fertile ground for emergent dynamics, which is otherwise inaccessible in their solitary counterparts. Here we show that coupled nonlinear optical resonators can undergo self-organization in their spectrum leading to a first-order phase transition. We experimentally demonstrate such a spectral phase transition in time-multiplexed coupled optical parametric oscillators. We switch the nature of mutual coupling from dispersive to dissipative and access distinct spectral regimes of the parametric oscillator dimer. We observe abrupt spectral discontinuity at the first-order transition point. Furthermore, we show how non-equilibrium phase transitions can lead to enhanced sensing, where the applied perturbation is not resolvable by the underlying linear system. Our approach could be exploited for sensing applications that use nonlinear driven-dissipative systems, leading to performance enhancements without sacrificing sensitivity.

5.2 Introduction

Coupled systems are omnipresent ranging from neuronal connections in biological brains, artificial neural networks, social networks, power grids, circadian rhythms, and reaction-diffusion chemical systems [53]. The nonlinear dynamics and the ensuing collective behaviors of coupled systems are remarkably richer than isolated individual ones [13, 34, 36, 41, 46, 58, 60, 61]. These networks are endowed with complex physics that can have profound consequences in sensing [15] and computing [31, 32].

Emergent phenomena in complex systems are ubiquitous and some paradigmatic examples of these non-equilibrium phenomena include synchronization [9, 20], and pattern formation [1, 16, 37, 40, 42, 45, 49]. Gain competition/ energy exchange among the components of a many-body system in the microscopic scale can lead to emergent macroscopic behaviors [56] including the appearance of Turing patterns [47], coherent oscillation [3], and mode-locking [12, 55]. Understanding and engineering phase transitions in driven-dissipative systems constitute a new frontier of many-body physics and non-equilibrium dynamics [38, 44]. Non-equilibrium driven-dissipative systems open new possibilities and opportunities that are not present in their equilibrium counterparts. For instance, time crystal is a non-equilibrium phase of matter that is believed to be realizable in out-of-equilibrium settings [8, 54]. Photonics provides a congenial platform to engineer the drive and the dissipation for the exploration of non-equilibrium emergent phases and dynamical phase transitions [2, 7, 24, 42, 46].

Phase transition is associated with the qualitative change in the system behavior as a control parameter is varied across a critical/transition point. An order parameter is often used to characterize systems exhibiting critical behaviors. Discontinuity in the order parameter (its derivative) is a universal signature of first-order (second-order) phase transitions [44]. Such abrupt discontinuities have been leveraged in transition-edge sensors to perform ultra-sensitive measurements down to single-photon levels [11]. Engineering such discontinuities in driven-dissipative systems are highly desirable to develop high-sensitivity transition-edge sensors that are governed by non-equilibrium dynamics and thereby are not impaired by the slow dynamics that limit their counterparts based on thermodynamic equilibrium phase transitions [59]. A promising approach to quantum sensing involves the exploitation of quantum fluctuations in the vicinity of a critical point to improve measurement precision. Theoretical studies indicate that sensors based on driven-dissipative phase transitions in parametric nonlinear resonators can be a useful resource in this regard [5].

Nonlinearity can potentially endow superior sensing capabilities that can attain orders of magnitude performance enhancement over those that rely on linear dynamics alone [4, 22, 51]. For instance, nonlinearity-induced non-reciprocity can amplify the Sagnac effect in the vicinity of a symmetry-breaking instability [22]. Similarly, it has been proposed that operating close to the region of bistability can lead to a strong enhancement to refractive-index sensitivity [50]. However,

experimental demonstrations of the aforementioned nonlinear advantage remain scarce.

We exploit the rich dynamics of coupled optical parametric oscillators (OPOs) to realize non-equilibrium phase transitions. We demonstrate first-order spectral phase transition and observe abrupt discontinuity at the transition point corresponding to the system's sudden self-organization between degenerate and non-degenerate oscillation regimes. We show that the system of coupled OPOs exhibits qualitatively different behavior with the alteration of their mutual coupling from dispersive to dissipative. We also present nonlinearly enhanced sensing in the driven-dissipative system under consideration where the applied perturbation remains unresolved by the underlying linear system. Our results on non-equilibrium behavior in a system of coupled nonlinear resonators can have far-reaching consequences in the domains of sensing and computing.

5.3 Results

The building block of our coupled system is a doubly resonant OPO which is parametrically driven by a pulsed pump centered around $2\omega_0$ (see Fig. 5.1(a)) [17]. The cavity hosts multiple longitudinal frequency modes around the half-harmonic frequency (ω_0), where the signal/ idler resides. The distribution of these frequency modes is determined by the cavity group velocity dispersion (GVD, β_2), while the interaction between them is facilitated by the quadratic nonlinearity ($\chi^{(2)}$). The energy exchange between the pump and the signal ($\omega_0 + \delta\omega$) and the idler ($\omega_0 - \delta\omega$) modes is governed by the energy and momentum conservation relations. The OPO exists in a trivial state (zero mean field) below the threshold, which loses stability leading to parametric oscillation as the gain is increased above the oscillation threshold. The oscillation proceeds via the modulational instability, and the OPO assumes a temporal frequency (fast-time scale dynamics) ($\Omega = \delta\omega$, centered around the half-harmonic), corresponding to the maximum growth-rate of perturbations. $\delta\omega = 0$ corresponds to the degenerate oscillation, while $\delta\omega \neq 0$ corresponds to the non-degenerate oscillation regime. The temporal mode with zero effective detuning experiences the maximum parametric gain. This can happen even in the presence of non-zero cavity detuning, where the GVD-induced detuning counterbalances the linear cavity detuning $\Delta\phi$. This mutual interplay of cavity detuning and GVD leads to a second-order spectral phase transition as shown in Fig. 5.1(b) [42]. The critical detuning ($\Delta\phi = 0$) marks a soft transition between the degenerate and the non-degenerate parametric oscillation regimes.

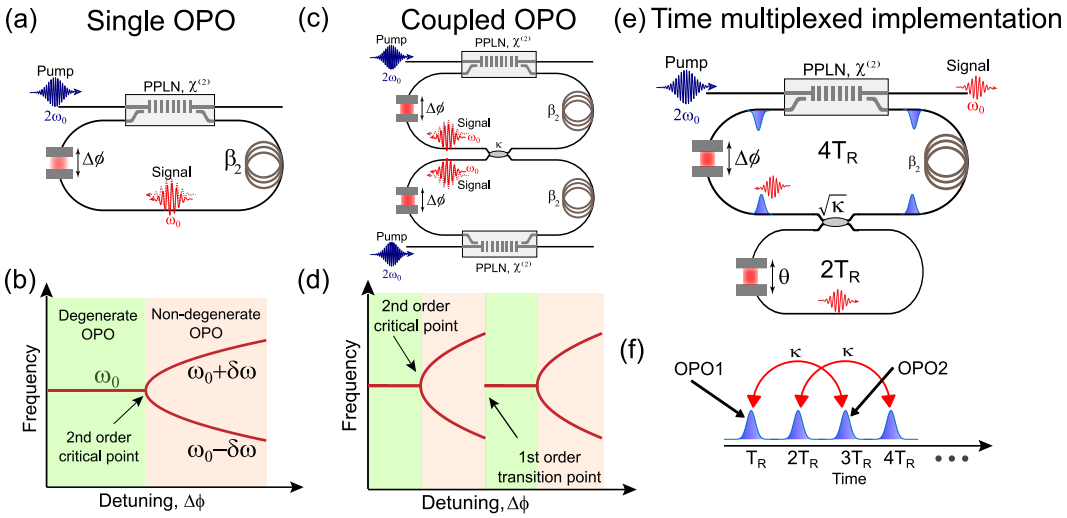

Figure 5.1: **Non-equilibrium phase transitions in single and coupled OPOs.** a) Schematic of a single OPO showing the non-resonant pump (2ω) and the resonant signal/idler (ω) interacting via phase-matched quadratic ($\chi^{(2)}$) nonlinearity alongside the detuning ($\Delta\phi$) element and the intra-cavity dispersion β_2. b) Existence of a second-order spectral phase transition in a single OPO where at the critical detuning the OPO transits between the degenerate and the non-degenerate oscillation regimes. c) Schematic of a coupled OPO system with the mutual coupling κ. d) Existence of a first-order spectral phase transition in coupled OPOs featuring an abrupt spectral discontinuity at the first-order transition point. e) Time-multiplexed implementation of the coupled OPOs consisting of a main OPO cavity (with a roundtrip time of $4T_R$) that is twice as long as the linear coupling cavity. The cavity detuning is controlled using a detuning element ($\Delta\phi$) in the main cavity, while the detuning element in the coupling cavity affects the coupling phase θ. f) Illustration of the pulses circulating in the time-multiplexed implementation where the pulse-to-pulse separation is given by the repetition period of the driving pump laser, and the coupling exists between alternate pulses, thereby constituting a coupled OPO system.

However, this rich spectral behavior observed in a single OPO does not extend linearly with the increase in system size, i.e., to a network of coupled OPOs (see Fig. 5.1(c)). It is well known that in the realm of parity-time symmetric non-Hermitian systems, increasing the system size, increases the order of the exceptional point [19]. Strikingly, we show that it is possible to realize a hard transition (first-order transition) in a system of coupled OPOs, where a single OPO is only capable of featuring a soft transition (second-order transition). Our system of coupled OPOs represents a complex system enabling a rich interplay of nonlinearity, linear coupling (κ), multimode dynamics, dispersion, drive, and dissipation. This can lead to an abrupt spectral discontinuity between the degenerate and non-degenerate

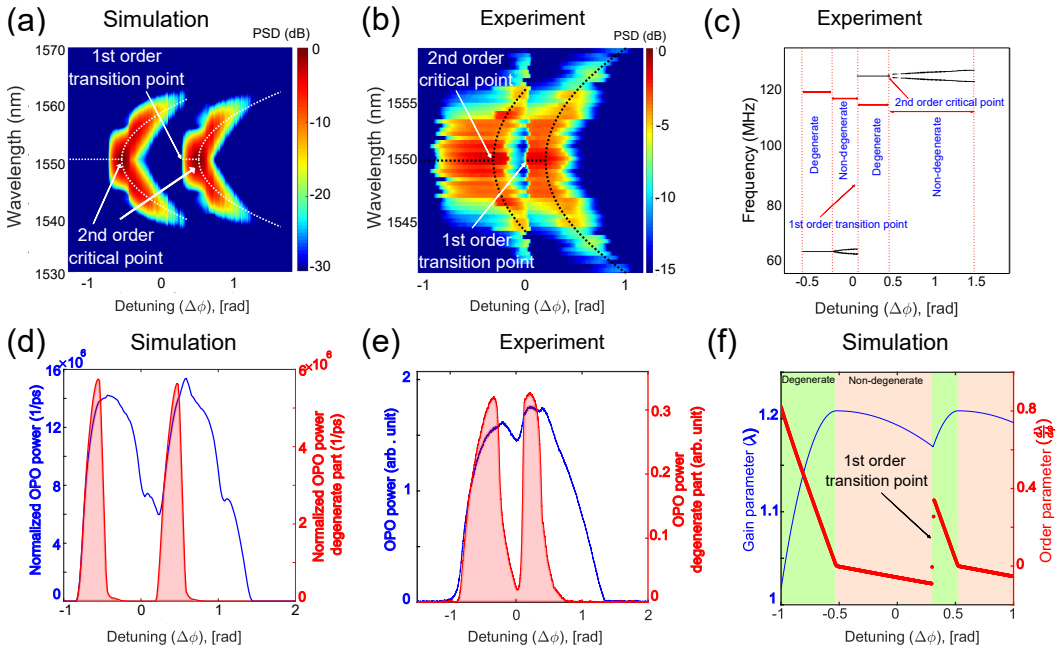

Figure 5.2: **First-order spectral phase transition in coupled OPOs**. a) Numerical simulation of the optical spectrum of coupled OPOs as a function of cavity detuning featuring the second-order phase transitions at the mode-splitting locations as well as the first-order phase transition. b) Experimentally obtained optical spectrum as a function of cavity detuning highlighting the abrupt spectral discontinuity at the first-order transition point. The idler part of the spectrum is constructed by mirror reflection about the half-harmonic line. c) Radio-frequency beat-note spectrum indicating the distinct degenerate and non-degenerate oscillation regimes demarcated by the second-order critical points and the first-order transition point. d) Numerical simulation of the OPO power as a function of the detuning. The power contained in the degenerate part of the spectrum (1 nm of bandwidth around the half-harmonic frequency ω) is also plotted alongside showing two distinct degenerate oscillation regimes flanked by non-degenerate oscillation regimes. e) Coupled OPOs power as a function of detuning obtained experimentally. The power contained in the degenerate regime has been extracted using a bandpass filter centered around the half-harmonic frequency. f) Order parameter (derivative of the gain function) shows a discontinuity at the transition point suggesting the existence of a first-order phase transition.

oscillation regimes (see Fig. 5.1(d)). We note that the phase transition considered here is of non-equilibrium nature which is distinct from the typical thermodynamic transitions.

We implement coupled OPOs using time multiplexing [27, 31, 32] (see Fig. 5.1(e)). This represents a synthetic dimension implementation where the

discrete-time dimension provided by the equidistant pulses of a mode-locked laser has been utilized to realize a coupled OPO system without increasing the spatial complexity of realizing OPOs in two different cavities. In this two-cavity configuration, the main-cavity is twice as long as the coupling cavity. Specifically, in our experiments, we chose the main cavity round-trip time to be four times the repetition period of the mode-locked laser (T_R). This ensures that the coupling cavity executes coupling between alternate pulses. Thus pulses occurring at time instants given by $(4n+1)T_R$ and $(4n+3)T_R$ or $(4n)T_R$ and $(4n+2)T_R$ (where n is an integer) constitutes two sets of coupled OPOs (see Fig. 5.1(f)). Moreover, our time-multiplexed implementation allows us to mimic different types of coupling (dispersive, dissipative, or hybrid) [6] because the phase of the coupling path can be altered by modifying the detuning of the coupling cavity. The detuning elements in the main cavity and the coupling cavity control the cavity detuning parameter ($\Delta\phi$) and the coupling phase θ independently.

The first-order phase transition in coupled OPOs emerges from the interplay of the supermodes of the coupled cavities and parametric gain. The dispersive coupling κ leads to mode-hybridization. These supermodes can be either symmetric when the resonant fields are in phase, or anti-symmetric when they are out-of-phase. The frequency separation between them depends on the coupling strength κ. At a given excitation frequency, there exists a range of cavity detunings where one of the supermodes is close to resonance, while the other one is off-resonant. In those circumstances, we can consider the dominant supermode only, and the dynamics of the coupled system resemble a single OPO, albeit now in the supermode basis. This results in second-order phase transitions around the mode-splitting points as shown in Fig. 5.2(a). However, in the range of cavity detunings where the contribution from the supermodes is comparable, there occurs a competition between the two second-order spectral phase transitions (one centered around the symmetric supermode and the other centered around the asymmetric supermode). This gain competition enforces spectral self-organization of the coupled OPOs leading to a sharp transition between non-degenerate and degenerate oscillation regimes as shown in Fig. 5.2(a). This proceeds via a first-order phase transition when the gain of the non-degenerate branch of the symmetric super-mode ceases to be greater than the gain experienced by the degenerate branch of the asymmetric supermode (see Supplementary section 5.5.2, 5.5.3). The experimental results (Fig. 5.2(b)) of the optical spectrum corroborate the theory and the numerical simulations (the coupling factor realized experimentally is lower than the value assumed in the simulation).

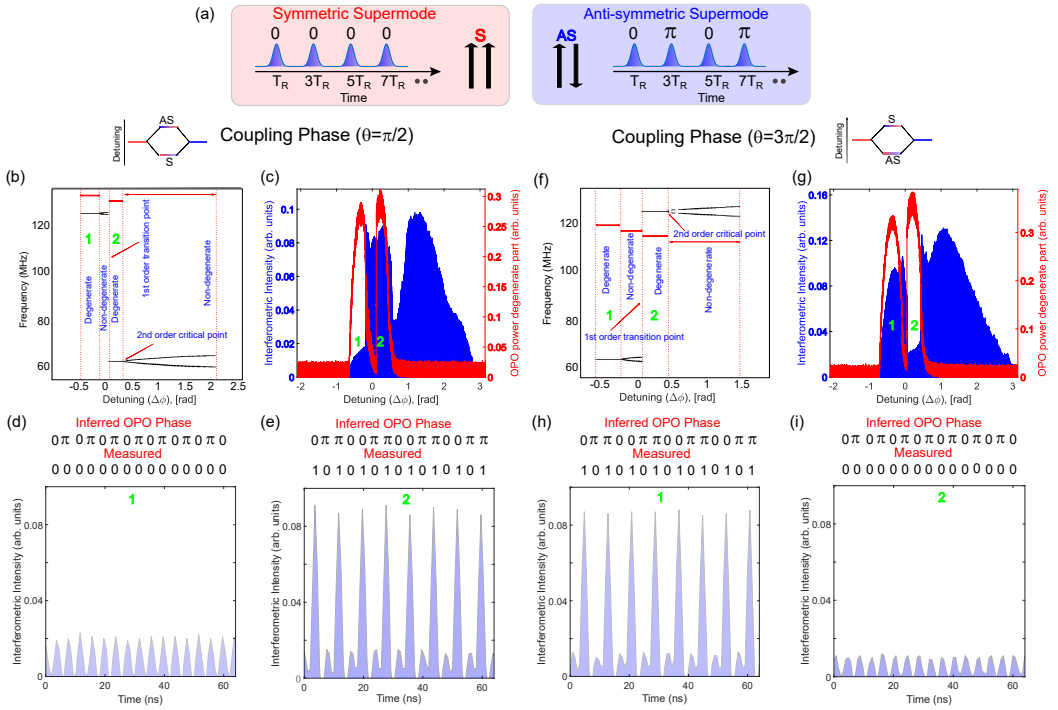

Figure 5.3: **Supermodes of the coupled OPOs.** a) Illustration of the supermodes and their associated manifestation in the time-multiplexed implementation. b) Radio-frequency beat-note spectrum as a function of detuning in the presence of dispersive coupling with coupling phase $\theta = \pi/2$. c) Corresponding pulse pattern at the output of a single-pulse delayed Mach-Zehnder interferometer. The OPO power in the degenerate band is also plotted alongside. d) Interferometric pulse pattern in the degenerate regime (marked as 1) shows that the OPO pulses are in-phase representing the symmetric super-mode. e) Pulse pattern in the degenerate regime (marked as 2) shows that the OPO pulses are out of phase representing the anti-symmetric super-mode. Similarly, the case with the dispersive coupling and coupling phase $\theta = 3\pi/2$ is considered, where the radio-frequency spectrum and the interferometer pulse pattern are displayed in f) and g), respectively. h) The degenerate regime (marked as 1) shows the OPO pulses constituting the coupled OPO are out-of-phase implying the anti-symmetric super-mode, while i) shows the degenerate regime (marked as 2) with OPO pulses in-phase indicating the symmetric super-mode.

The non-equilibrium phase transitions in coupled OPOs are further characterized by the radio-frequency (RF) measurements (see Fig. 5.2(c)). A sync-pumped doubly-resonant OPO in the non-degenerate regime generates a signal and an idler frequency comb with two carrier-envelope offset frequencies which can be measured through beating with a local oscillator. The abrupt spectral discontinuity of this beat-note measurement unequivocally confirms the occurrence of the

first-order phase transition. For non-degenerate (near-degenerate) doubly resonant OPO, the f_{CEO} can be deterministically estimated based on the OPO cavity detuning [26]. The doubly resonance condition is satisfied simultaneously for the signal and the idler to achieve the maximum parametric gain. This fixes the carrier phase velocity, leaving the f_{CEO} to be determined by the effective group velocity of the signal and idler envelopes. The effective group velocity comprises of the linear component that arises due to the material dispersion, as well as the contribution due to the nonlinear acceleration of the pulses arising due to the cavity nonlinear dynamics. The constraint to satisfy $f_{CEO,p} = f_{CEO,s} + f_{CEO,i}$ along with the fixed frequency splitting relationship (maximum gain principle described above) hinges the respective f_{CEO} of the signal and idler pulses uniquely to the cavity detuning. The output power of the coupled OPOs as a function of detuning is representative of the parametric gain and leads to maximum conversion efficiencies at the second-order critical points where the supermodes are resonant. This can be seen from the simulation and experimental results in Fig. 5.2(d,e). The power contained in the spectrum centered around degeneracy is indicative of the degenerate regime of operation. The OPO output after passing through a band-pass filter centered around the half-harmonic frequency is also shown in Fig. 5.2(d,e) which indicates the presence of two distinct degenerate regimes of operation separated by the non-degenerate oscillation regime. The order parameter (defined as the derivative of the gain parameter with respect to the detuning) exhibits behavior typical of a first-order phase transition with the characteristic discontinuity at the first-order transition point (see Fig. 5.2(f)). The gain parameter (λ) reveals the underlying gain competition between the two supermodes.

The eigenvector composition of the supermodes can be unveiled from the pulse-pattern measurements in the time domain as illustrated in Fig. 5.3(a). When the coupling phase (θ) equals $\pi/2$, the anti-symmetric eigenmode has a higher frequency (corresponding to larger detuning) than its symmetric counterpart. The symmetric and the anti-symmetric supermodes have distinct carrier envelope offset frequencies as evident from the RF spectrum (see Fig. 5.3(b)). The pulse pattern is measured using a one-pulse delayed Mach-Zehnder interferometer (see Fig. 5.3(c)) to infer the phases of the OPO pulses constituting the coupled OPOs. The coupled OPOs in the symmetric supermode dominated degenerate regime (1) features OPO pulses that are in phase (see Fig. 5.3(d)). In the anti-symmetric supermode degenerate regime (2), the OPO pulses comprising the coupled OPOs are out of phase (see Fig. 5.3(e)). When the coupling phase is $3\pi/2$, the frequency spectrum of the supermodes is

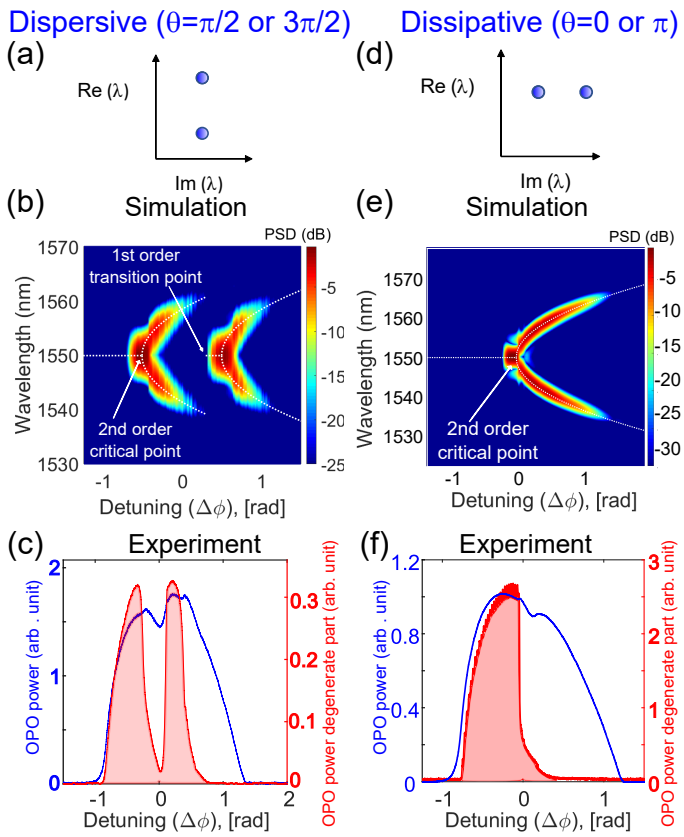

Figure 5.4: **Dispersive vs dissipative coupling.** a) Dispersive coupling between coupled resonators results in the splitting of the real part of the eigenvalue (spectrum), where both the super-modes experience identical dissipation. b) The existence of mode-hybridization in the real part of the spectrum enables the observation of two second-order spectral phase transitions centered around the mode-splitting and the associated first-order transition point. c) OPO power as a function of detuning along with the power contained in the degenerate regime corroborates the existence of the underlying mode-splitting. d) In the presence of dissipative coupling the super-modes experience different dissipation while their real part remains identical. e) The absence of mode-hybridization in the real part of the spectrum precludes the observation of the first-order phase transition and only leads to features representative of the spectral behavior of a single OPO. f) OPO power as a function of detuning showing the existence of a single degenerate regime confirming the absence of mode-splitting with dissipative coupling.

reversed, with the symmetric supermode now associated with larger detuning. This is revealed in the corresponding measurements shown in Fig. 5.3(f,g,h,i). This agrees with the results obtained from numerical simulation.

The spectral behavior of the coupled OPOs drastically differs with the alteration of the nature of mutual coupling (κ). Modification of the coupling phase (θ) enables

us to mimic dispersive ($\pi/2$ or $3\pi/2$), dissipative (0 or π), or hybrid (intermediate phases) (see supplementary section 5.5.4). Dispersive coupling results in splitting in the real part of the eigenvalues (i.e., mode-splitting) where the supermodes experience identical rates of dissipation (the imaginary part of the eigenvalue is the same) (see Fig. 5.4(a)). This leads to spectral and temporal features resembling the aforementioned discussions (see Fig. 5.4(b,c)). In stark contrast, dissipative coupling leads to splitting in the imaginary part of the eigenvalue where the supermodes experience disparate dissipation [6]. This property of the dissipative coupling is at the heart of the operation of optical coherent Ising machines [31], and recent demonstrations of topological dissipation [27]. Consequently, the absence of mode-splitting is also reflected in the spectral (Fig. 5.4(e)) and the power (Fig. 5.4(f)) characteristics of dissipatively coupled OPOs. Dissipative coupling precludes the occurrence of a first-order spectral phase transition and shows the mere presence of a second-order phase transition.

The presence of non-equilibrium phase transitions with characteristic discontinuities opens up new opportunities in the domain of sensing. High quality-factor optical resonators have been utilized for highly sensitive refractive index perturbation measurements [23]. However, the requirement of a high quality factor for enhanced sensitivity results in an unavoidable trade-off with the bandwidth and hence limits the sensing speed. The non-equilibrium phase transition in coupled OPOs can circumvent this trade-off. Figure 5.5(a) shows the transmission of coupled optical resonators with different round-trip losses. The mode-splitting is observed in the regime of high-Q (lower round-trip loss), while low-Q (high-bandwidth) resonators cannot resolve the mode-splitting structure. Remarkably, this mode-splitting can be revealed even in the low-Q regime in the nonlinear case where the coupled resonators are parametrically driven as coupled OPOs (see Fig. 5.5(b)). The sensing parameter can be the phase detuning in the coupling cavity of the time-multiplexed architecture leading to perturbation ($\delta\theta$) in the coupling phase (θ). In the presence of this coupling phase perturbation, coupled high-Q linear resonators will respond with asymmetric mode-splitting, where the degree of the asymmetry depends on the strength of the perturbation (see Fig. 5.5(c)). The asymmetry also reflects the sign of the phase perturbation which is an added advantage over high-Q linear cavity based simple sensing arrangements where the sensors can suffer from directional ambiguity [18]. This asymmetric mode-splitting behavior cannot be resolved by low-Q coupled linear resonators. However, low-Q coupled OPOs can extract these features which are

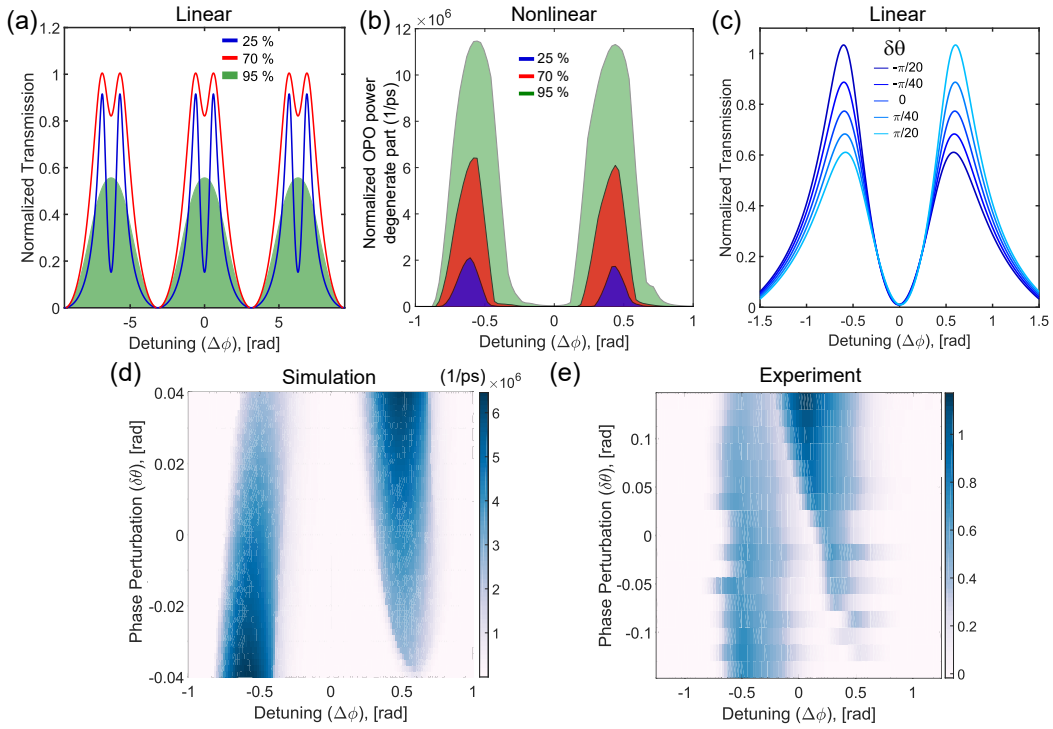

Figure 5.5: **Enhanced sensing using non-equilibrium phase transitions.** a) Transmission through coupled linear resonators with varying round-trip loss. With lower loss values (high-Q) the mode-splitting is conspicuous, which disappears in the low-Q regime. b) Power contained in the degenerate regime of the coupled OPO as a function of detuning for various values of round-trip loss. In contrast to the linear case, this nonlinear regime could resolve the mode-splitting even in the low-Q regime. c) Transmission in coupled linear resonators (high-Q regime) in the presence of applied perturbation expressed as the perturbation in the coupling phase ($\delta\theta$). The perturbation renders the coupling to be a hybrid of dispersive and dissipative leading to asymmetric mode-splitting. The power contained in the degenerate regime of the coupled OPO with varying perturbation in the low-Q regime obtained through d) numerical simulation, e) experiments. Despite operating in the low-Q regime the nonlinear dynamics could resolve the underlying asymmetric mode-splitting in response to small coupling-phase perturbation.

shown in Fig. 5.5(d,e) by displaying the power contained in the degenerate part (using a band-pass filter). Results obtained from our low-Q (high gain and bandwidth) experimental setup agree well with the simulation.

We quantify the sensitivity of the system using a normalized sensitivity metric and benchmark its performance in comparison with linear high-Q resonator-based sensors. Our sensing protocol is described in Fig. 5.6(a), which constitutes a photo-detector that registers the band-pass filtered (centered around degeneracy) output signal. The system should be biased near the spectral phase transition critical points to exploit the maximum sensitivity, which can be ensured by active locking means [39]. The change of detected power y in the response of a detuning ($\Delta\phi$) perturbation ϵ can be drastically enhanced in the vicinity of the spectral phase transition point owing to the transition from degeneracy to the non-degenerate regime which lies outside the spectral acceptance bandwidth of the bandpass filter. Our simplified sensing scheme is compatible with high-bandwidth measurements and does not involve the complex process of laser frequency scanning/sweeping. The normalized sensitivity is defined as: $S = \frac{1}{y_{\max}} \frac{dy}{d\Delta\phi}$. The sensitivity at the first-order transition point (Fig. 5.6(c)) is much higher as compared to its second-order counterpart (Fig. 5.6(b)) [59]. The enhanced sensitivity near the first-order transition point comes at a cost of drastically reduced dynamic range as compared to that based on the second-order critical point. Our simulation agrees with the data obtained experimentally (Fig. 5.6(d)). We provide further details on the experimental approaches to access such sensitivities in the supplementary section (supplementary section 5.5.6). The observed sensitivity enhancement is equivalent to a critically-coupled linear high-Q cavity based sensor with a Finesse of approximately 250 (Quality factor of 1 million at 1550 nm with a cavity of 50 GHz free-spectral range). This represents a dramatic enhancement of more than three orders of magnitude in terms of sensitivity compared to the cold-cavity system which had a Finesse of $\sim$ 0.5. The sensitivity for a linear high-Q based sensor is shown in Fig. 5.6(e) as a reference. With a combination of proper dispersion engineering and system design it is possible to exhibit sensitivity that is equivalent to a linear high-Q based system with a Finesse exceeding 10^4. This is extremely important in circumventing the difficulties associated with achieving high quality factor cavities in integrated platforms when interfacing with sensing technologies. Our work highlights the possibility of achieving sensitivity levels that are at par with state-of-art sensing systems using easily accessible low-Q based systems. The other alternative in terms of the sensing scheme is to resort to radio-frequency domain measurements

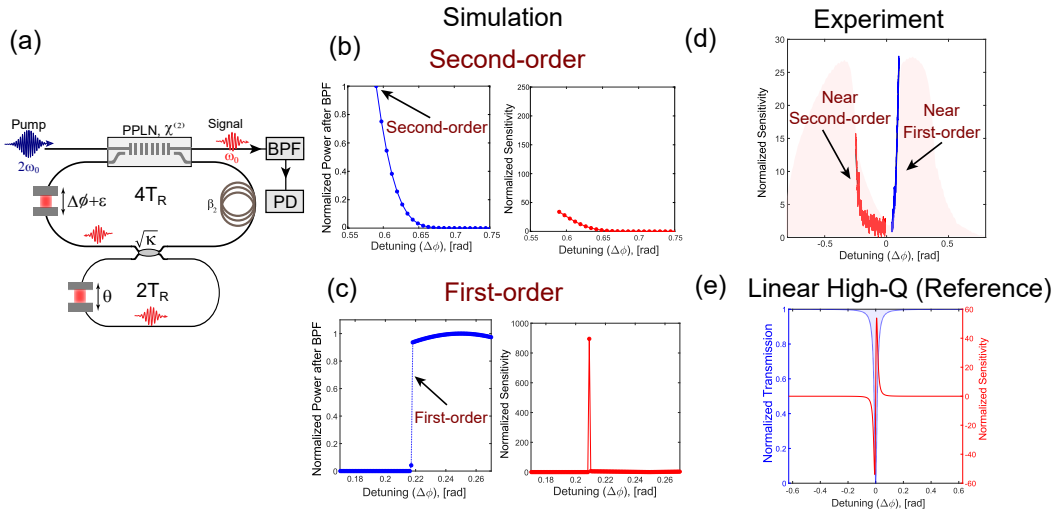

Figure 5.6: **Sensitivity near the spectral phase transition points.** a) Schematic depicting the sensing protocol involving the detection of the coupled OPOs output on a photodetector (PD) after passing through a bandpass filter (BPF) centered around degeneracy. b) Detected power (y) as a function of detuning ($\Delta\phi$) perturbation from the second-order critical point. The normalized sensitivity (S) is shown alongside as obtained from numerical simulation. c) Same as in (b), but for perturbations around the first-order transition point, showing enhanced sensitivity compared to its second-order counterpart. d) Normalized sensitivity obtained experimentally for operation near both the second-order critical point and the first-order transition point. This does not include the sharp discontinuity at the first-order transition point. e) Sensitivity that can be obtained from a critically-coupled linear high-Q cavity based sensor is shown for reference. The bandpass filter bandwidth is assumed to be 1 nm.

(Fig. 5.2(c)) where the SNR can be improved by performing coherent averaging at the cost of reduced sensing bandwidth. These results indicate the potential of non-equilibrium spectral phase transitions for enhanced sensing (see supplementary section 5.5.5).

5.4 Discussion

The results presented here can be directly relevant to other systems including Faraday waves in hydrodynamics and parametrically forced mechanical or chemical systems. With the recent progress in the nanophotonic lithium niobate platform [14, 21, 30], exploration of extended lattices can become feasible, paving the way towards the study of emergent nonlinear phenomena in soliton networks and higher dimensional lattices [48]. The demonstrated phase transition can be modeled using the universal coupled Swift-Hohenberg equation and can be implemented in Kerr nonlinear resonators as well [29, 35]. The semi-classical

regime considered in this work can be probed below the oscillation threshold [57], where a quantum image of the above threshold spectral phase transition exists, which may lead to the co-existence of a quantum phase transition [10]. Our study mainly focuses on the adiabatic regime where the control parameter is varied gradually. The introduction of non-adiabaticity can lead to the Floquet dynamics with enriched phase diagrams [28]. Intriguing dynamics is also expected in the case of nonlinearly coupled resonators [33]. Analysis of noise mechanisms that could possibly constrain the achievable precision will be the subject of future work. Our work lays the foundation for the exploration of emergent dynamics and critical phenomena beyond the single-particle description and insinuates potential advances in sensing and computing.

5.5 Supplementary

5.5.1 Experimental schematic

The detailed schematic of the experimental setup is shown in Fig. 5.7. Here, red solid lines (with glows) refer to the free space optical path, blue//red solid lines represent polarization maintaining (PM) fiber guided optical path (PM/ PM-DCF), and black solid lines represent electrical connections. The wavelength of the light is represented as 775 (775 nm) or 1550 (1550 nm) at various places in the schematic. The pump at 775 nm is prepared by Second Harmonic Generation (SHG) of 1550 nm light coming from a mode-locked Menlo optical frequency comb via a Periodically Poled Lithium Niobate (PPLN) bulk crystal. The pump power is controlled by a combination of a Half-wave plate and a polarizer which acts as a Variable Optical Attenuator (VOA). The pump wavelength is controlled by temperature tuning (TC) of the PPLN SHG crystal.

The OPO consists of a 40 mm long PPLN reverse-proton exchange waveguide with fiber pigtails [25]. The rest of the main cavity is composed of a combination of polarization-maintaining single-mode fibers and polarization-maintaining dispersion compensating fibers (DCF) to keep the cavity dispersion close to zero GVD. A free-space portion terminated by fiber collimators (OC) is incorporated in order to ensure the cavity round-trip time is approximately equal to four times ($4T_R$) the inverse of the mode-locked laser pulse repetition rate (4 ns/ 250 MHz). A Piezo Transducer (PZT) is used to scan the cavity length, and to change the cavity detuning. The OPO is sampled using a Pellicle Beam Splitter (BS) having 45% reflectivity.

The coupling cavity is made up of six unprotected gold mirrors. Unprotected gold mirrors were used to minimize the dispersion. This is completely a free-space resonator with plane mirrors. The cavity is marginally stable, and thus multiple round-trip buildup is unlikely. A single round-trip interference was enough for our purpose. The total length of the cavity was adjusted to ensure that it amounts to twice ($2T_R$) the inverse of the mode-locked laser pulse repetition rate. The coupling between the main cavity and the coupling cavity was implemented using another pellicle beam splitter with 45% reflectivity. The Piezo transducer attached to the coupling cavity allowed alteration of the phase of the coupling, thereby switching between the dispersive and dissipative coupling. Perturbation to this PZT was also used for obtaining the sensing results. The coupling cavity can be locked using an auxiliary laser launched from the opposite direction while placing an isolator in the main cavity such that the auxiliary signal does not see the main cavity.

The OPO output is filtered by a long-pass filter ensuring that there is no residual 775 nm light. Beat-note measurement (green dashed rectangle) has been performed by mixing the OPO output with the 1550 nm local oscillator (LO). Here the LO is delayed by a suitable amount to ensure temporal overlap between the LO pulses and OPO pulses at the PM fiber coupler. An Electrical Spectrum Analyzer (ESA) measures the beat-note from the signal received using a fast photo-detector (FPD).

The pulse pattern measurement (red dashed rectangle) was performed using a self-delayed Mach-Zehnder Interferometer (MZI). The delay was equal to the repetition rate of the mode-locked laser. The MZI was locked using the auxiliary LO signal that was injected from the opposite direction. PDH locking was used for the locking purpose.

The detuning-dependent optical spectrum and OPO output measurements were performed using a pair of slow photo-detectors (blue dashed rectangle). One photo-detector received the unfiltered OPO output, while the filtered OPO output was sent to the other. The filter employed was a tunable bandpass filter with 1 nm bandwidth.

5.5.2 First order spectral phase transition in coupled OPO

Additional to the dynamics of individual OPOs, the OPO fields experience the effect of the coupling every roundtrip.

$$a_1^{'} = \sqrt{1 - |\kappa|^2}a_1 + |\kappa|e^{i\theta}a_2 \tag{5.1a}$$

$$a_2^{'} = \sqrt{1 - |\kappa|^2}a_2 + |\kappa|e^{i\theta}a_1 \tag{5.1b}$$

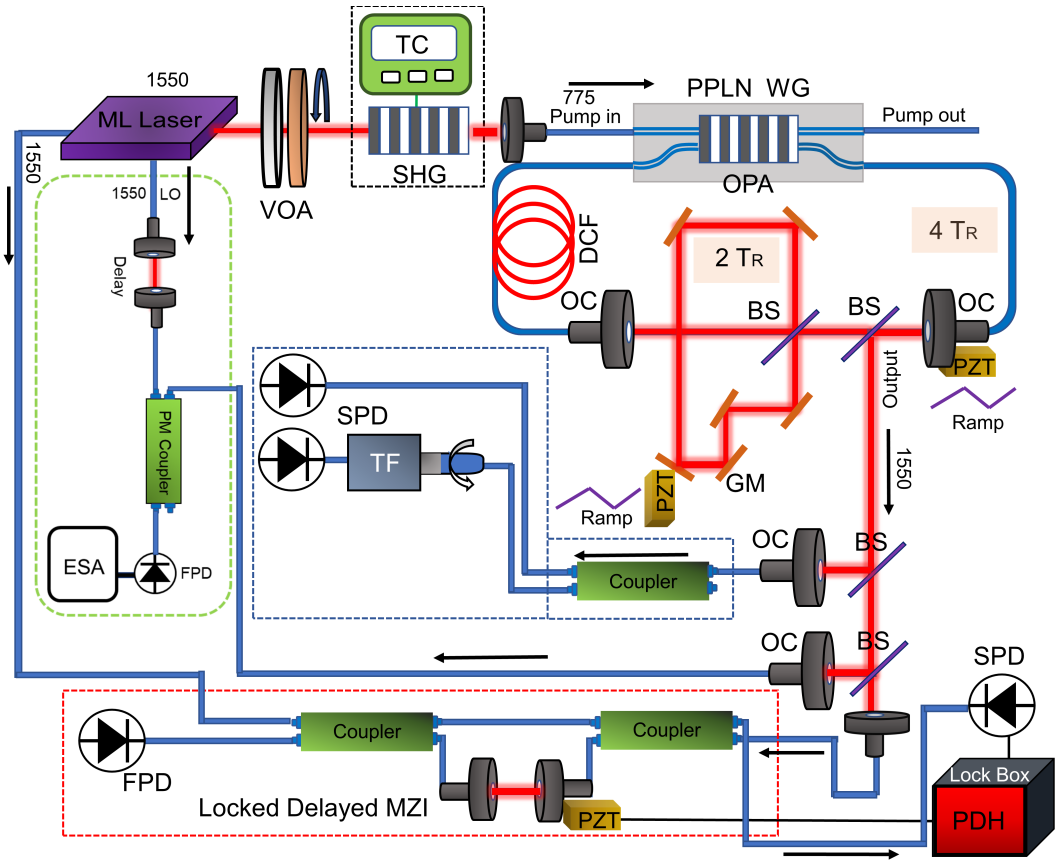

Figure 5.7: **Detailed schematic of the experimental setup.** Abbreviations used are: OPA- Optical Parametric Amplification, SHG- Second Harmonic Generation, VOA- Variable Optical Attenuator, LO- Local Oscillator, OC- Optical Collimator, BS- Beam Splitter, TF- Tunable Band-pass Filter, ESA- Electrical Spectrum Analyser, PZT- Piezo Transducer, PDH-Pound Drever Hall, DCF- Dispersion Compensating Fiber, SPD- Slow Photo-detector, FPD- Fast Photo-detector, GM- Gold Mirror, MZI- Mach Zehnder Interferometer, PM- Polarization Maintaining.

where the subscripts (1,2) refer to the OPO1 and the OPO2 comprising the coupled OPO. The coupling strength is denoted by $|\kappa|$, and θ is the coupling phase.

CW gain limit (Without mean-field approximation)

We consider low Finesse lumped cavity scenario. Our experiment is reflective of this case. We assume signal (a_s) to be centered at frequency $\omega_0 + \delta\omega$, and idler (a_i) at $\omega_0 - \delta\omega$, when the pump frequency is $2\omega_0$. We define: $a_+ = \frac{(a_s + a_i^*)}{2}$, and $a_- = \frac{(a_s - a_i^*)}{2}$. In the near-threshold limit, we neglect the effect of gain saturation. We obtain:

$$\begin{bmatrix} \dot{a_+} \\ \dot{a_-} \end{bmatrix} = \begin{bmatrix} -\frac{\alpha^{(a)}}{2} + \epsilon b & i\frac{\beta_2^{(a)}(\delta\omega)^2}{2} \\ i\frac{\beta_2^{(a)}(\delta\omega)^2}{2} & -\frac{\alpha^{(a)}}{2} - \epsilon b \end{bmatrix} \begin{bmatrix} a_+ \\ a_- \end{bmatrix}. \tag{5.2}$$

Eq. 5.2 describes the interaction within the PPLN waveguide. After exiting the gain medium, the signal/idler fields encounter cavity dispersion, out-coupling loss, and round-trip feedback. This leads to: $a_s \rightarrow G_0^{-\frac{1}{2}} e^{i(\phi+\psi)} a_s$, $a_i \rightarrow G_0^{-\frac{1}{2}} e^{i(\phi-\psi)} a_i$, where $\phi = \Delta\phi + \frac{1}{2}\phi_2(\delta\omega)^2$ (symmetric phase shift) and $\psi = \frac{l\lambda^{(a)}}{2c}\delta\omega$ (asymmetric phase shift) .

$$\begin{bmatrix} a_+ \\ a_- \end{bmatrix}_{n+1} \rightarrow G_0^{-\frac{1}{2}} e^{-\frac{\alpha^{(a)}L}{2}} e^{i\psi} \begin{bmatrix} \cos(\phi) & i\sin(\phi) \\ i\sin(\phi) & \cos(\phi) \end{bmatrix} \exp\left(\begin{bmatrix} \epsilon b & i\frac{\beta_2^{(a)}(\delta\omega)^2}{2} \\ i\frac{\beta_2^{(a)}(\delta\omega)^2}{2} & -\epsilon b \end{bmatrix} L \right) \begin{bmatrix} a_+ \\ a_- \end{bmatrix}_n \tag{5.3}$$

The round-trip evolution of $a_\pm$ is dictated by Eq. 5.3. Now we consider two identical OPOs (A and B) coupled with each other via conservative coupling.

We assume signal (A_s, B_s) to be centered at frequency $\omega_0 + \delta\omega$, and idler (A_i, B_i) at $\omega_0 - \delta\omega$, when the pump frequency is $2\omega_0$. We define: $A_+ = \frac{(A_s + A_i^*)}{2}$, $A_- = \frac{(A_s - A_i^*)}{2}$, $A_+ = \frac{(A_s + A_i^*)}{2}$, and $A_- = \frac{(A_s - A_i^*)}{2}$. Apart from the usual effects of parametric gain, out-coupling loss, cavity feedback, and cavity dispersion that is encountered in a single OPO configuration, there exists the effect of conservative coupling (κ) which is given by Eq. 5.4. The round-trip evolution of $A_\pm, B_\pm$ is dictated by Eq. 5.5. We are interested in the eigenvalues of this evolution equation to find the oscillation threshold and the frequency of oscillation.

$$\begin{bmatrix} A_s \\ A_i \\ B_s \\ B_i \end{bmatrix} \rightarrow \begin{bmatrix} \sqrt{1-\kappa^2} & 0 & i\kappa & 0 \\ 0 & \sqrt{1-\kappa^2} & 0 & i\kappa \\ i\kappa & 0 & \sqrt{1-\kappa^2} & 0 \\ 0 & i\kappa & 0 & \sqrt{1-\kappa^2} \end{bmatrix} \begin{bmatrix} A_s \\ A_i \\ B_s \\ B_i \end{bmatrix} \tag{5.4}$$

$$\begin{bmatrix} A_+ \\ A_- \\ B_+ \\ B_- \end{bmatrix}_{n+1} \rightarrow G_0^{-\frac{1}{2}} e^{-\frac{\alpha^{(a)}L}{2}} e^{i\psi} \begin{bmatrix} \sqrt{1-\kappa^2} & 0 & 0 & i\kappa \\ 0 & \sqrt{1-\kappa^2} & i\kappa & 0 \\ 0 & i\kappa & \sqrt{1-\kappa^2} & 0 \\ i\kappa & 0 & 0 & \sqrt{1-\kappa^2} \end{bmatrix}$$
$$\begin{bmatrix} \cos(\phi) & i\sin(\phi) & 0 & 0 \\ i\sin(\phi) & \cos(\phi) & 0 & 0 \\ 0 & 0 & \cos(\phi) & i\sin(\phi) \\ 0 & 0 & i\sin(\phi) & \cos(\phi) \end{bmatrix}$$
$$\exp\left(\begin{bmatrix} \epsilon b & i\frac{\beta_2^{(a)}(\delta\omega)^2}{2} & 0 & 0 \\ i\frac{\beta_2^{(a)}(\delta\omega)^2}{2} & -\epsilon b & 0 & 0 \\ 0 & 0 & \epsilon b & i\frac{\beta_2^{(a)}(\delta\omega)^2}{2} \\ 0 & 0 & i\frac{\beta_2^{(a)}(\delta\omega)^2}{2} & -\epsilon b \end{bmatrix} L \right) \begin{bmatrix} A_+ \\ A_- \\ B_+ \\ B_- \end{bmatrix}_n \tag{5.5}$$

Mean-field approximation

Here we present the mean-field version of the modeling of coupled OPO. However, it must be noted that the CW-driven, high finesse limit leading to the mean-field approximation is unable to predict the occurrence of the first-order phase transition. This is because, in the mean-field limit, it is assumed that the detuning is very small, and only a truncated approximation of the detuning is included in the modeling. However, it is able to predict the existence of two second-order phase transitions each centered around the split-mode resonance. First-order transition happens as a result of the interplay between these two second-order phase transitions.

Here, a and b denote the signal amplitude of the OPOs comprising the coupled OPO. They are assumed to have identical detuning ($\Delta\phi$), GVD (β_2). ξ and t represent the slow time and fast time, respectively. The parametric gain term is given by p. The coupling term is designated as κ. Lu represents the product of the length of parametric interaction (L), and the walk-off parameter (u). Equal detuning and parametric gain can be easily implemented in the time-multiplexed architecture. The system of coupled equations describing the coupled OPO is given by [42]:

$$\frac{\partial a}{\partial \xi} = (-\alpha + i\Delta\phi)a + pa^* - \left[\frac{\epsilon^2}{2u^2}\int_0^{Lu}(Lu-\tau)a(t-\tau)^2 d\tau\right]a^* - i\frac{\beta_2}{2}\frac{\partial^2 a}{\partial t^2} + i\kappa b \tag{5.6a}$$

$$\frac{\partial b}{\partial \xi} = (-\alpha + i\Delta\phi)b + pb^* - \left[\frac{\epsilon^2}{2u^2}\int_0^{Lu}(Lu-\tau)b(t-\tau)^2 d\tau\right]b^* - i\frac{\beta_2}{2}\frac{\partial^2 b}{\partial t^2} + i\kappa a. \tag{5.6b}$$

We assume a perturbation of the form as given in Eq. 5.7a. We perform the linear stability analysis (Eq. 5.7b), where the gain saturation term has been neglected. We define $\Gamma = \Delta\phi + \frac{\beta_2}{2}(\delta\omega)^2$. We obtain the most unstable eigenvalue that determines the oscillation frequency and the corresponding threshold in Eq. 5.7e.

$$a = a_+ e^{i\delta\omega t} + a_- e^{-i\delta\omega t}, \quad b = b_+ e^{i\delta\omega t} + b_- e^{-i\delta\omega t} \tag{5.7a}$$

$$\frac{d}{d\xi}\begin{bmatrix} a_+ \\ a_-^* \\ b_+ \\ b_-^* \end{bmatrix} = \begin{pmatrix} M_1 & M_2 \\ M_2 & M_1 \end{pmatrix}\begin{bmatrix} a_+ \\ a_-^* \\ b_+ \\ b_-^* \end{bmatrix} \tag{5.7b}$$

$$M_1 = \begin{bmatrix} -\alpha + i(\Delta\phi + \frac{\beta_2}{2}(\delta\omega)^2) & p \\ p^* & -\alpha - i(\Delta\phi + \frac{\beta_2}{2}(\delta\omega)^2) \end{bmatrix} \tag{5.7c}$$

$$M_2 = \begin{bmatrix} i\kappa & 0 \\ 0 & -i\kappa \end{bmatrix} \tag{5.7d}$$

$$(\lambda_{max} + \alpha)^2 = |p|^2 - \Gamma^2 - \kappa^2 \pm 2\kappa\Gamma. \tag{5.7e}$$

Clearly, we can obtain the presence of two second-order spectral phase transition points: one located at $\Delta\phi = \kappa$ and the other at $\Delta\phi = -\kappa$.

For $\Delta\phi = \kappa$, the dominant eigenvector is given by $[-1, -1, 1, 1]^T$. This is the anti-symmetric eigenvector. While, when $\Delta\phi = -\kappa$, the dominant eigenvector is given by $[1, 1, 1, 1]^T$. This is the symmetric eigenvector.

The situation is reversed, when the coupling phase in the dispersive coupling is $3\frac{\pi}{2}$. Then the system of coupled equations will be given by:

$$\frac{\partial a}{\partial \xi} = (-\alpha + i\Delta\phi)a + pa^* - \left[\frac{\epsilon^2}{2u^2}\int_0^{Lu}(Lu-\tau)a(t-\tau)^2 d\tau\right]a^* - i\frac{\beta_2}{2}\frac{\partial^2 a}{\partial t^2} - i\kappa b \tag{5.8a}$$

$$\frac{\partial b}{\partial \xi} = (-\alpha + i\Delta\phi)b + pb^* - \left[\frac{\epsilon^2}{2u^2}\int_0^{Lu}(Lu-\tau)b(t-\tau)^2 d\tau\right]b^* - i\frac{\beta_2}{2}\frac{\partial^2 b}{\partial t^2} - i\kappa a. \tag{5.8b}$$

In this case, for $\Delta\phi = \kappa$, the dominant eigenvector is given by $[1, 1, 1, 1]^T$. This is the symmetric eigenvector. While, when $\Delta\phi = -\kappa$, the dominant eigenvector is given by $[-1, -1, 1, 1]^T$. This is the anti-symmetric eigenvector.

5.5.3 Effect of group velocity dispersion and coupling

Now we investigate the effect of group velocity dispersion (GVD) and coupling strength on the first-order spectral phase transition. With increasing dispersion, the gain in the non-degenerate regime is a slow function of detuning. This is shown in Fig. 5.8(a). Thus the non-degenerate regime of one branch crosses over the degenerate regime of the other branch earlier for low values of GVD. The first-order phase transition is more pronounced for low values of GVD. Therefore, we kept the GVD of the main cavity very low, by a proper combination of polarization maintaining anomalous fiber, and normal dispersion compensating fiber. The dispersion in the coupling cavity was kept at a minimum, by using an uncoated gold mirror. It should be noted that in the presence of large cavity GVD, the first-order dispersion may be difficult to observe. The spectral splitting is also a function of dispersion [42]. For lower values of GVD, the spectral splitting is wider as shown in Fig. 5.8(b). The coupling between the OPOs (κ) determines the location of the critical point corresponding to the second-order spectral phase transition. With the increasing value of the coupling the separation between the critical points increases as shown in Fig. 5.8(c). The variation of the order parameter with dispersion and cavity detuning is shown in Fig. 5.8(d).

The spectral phase transition is reversed with respect to detuning in the normal and anomalous dispersion regimes as shown in Fig. 5.9.

5.5.4 Dispersive vs dissipative coupling

Coupling between optical cavities can be either purely dispersive, purely dissipative, or a hybrid admixture of both. In the presence of dispersive coupling, resonance frequency hybridization takes place, resulting in mode-splitting/ avoided mode-

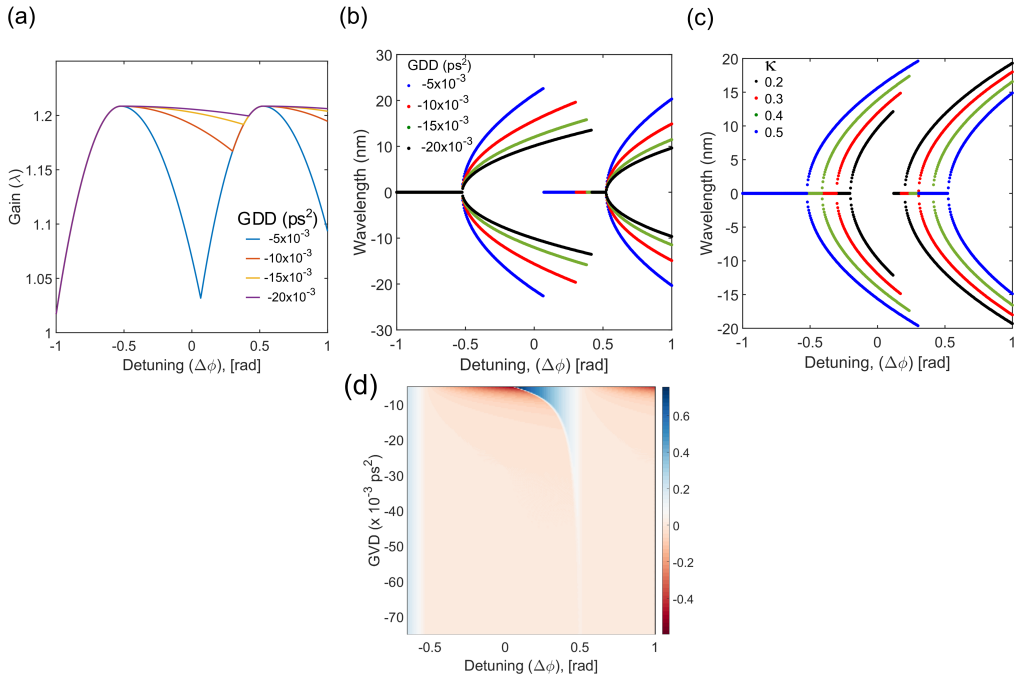

Figure 5.8: **Effect of cavity GVD and coupling factor on the first order spectral phase transition.** a) The gain variation with detuning between the degenerate and non-degenerate regime is more pronounced at low GVD values. The first-order phase transition will be more conspicuous for low GVD values. b) spectral splitting as a function of GVD. The splitting in the non-degenerate regime is more for lower values of GVD. c) Effect of varying coupling factor on the spectral phase transition.

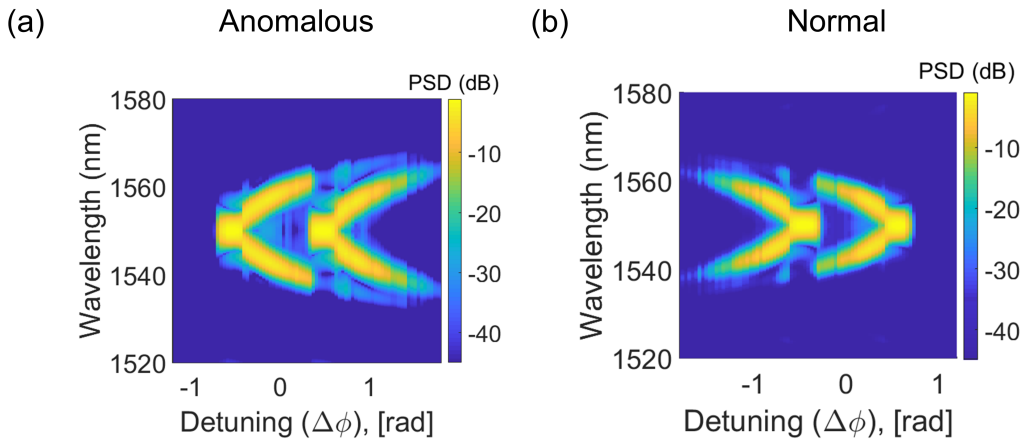

Figure 5.9: **Optical spectrum as a function of detuning in a) anomalous dispersion regime and b) normal dispersion regime.**

crossing. While in the presence of dissipative coupling, the resonance frequencies remain unaltered, while the energy in terms of loss and gain is modified. One

supermode will be lossier than the other. This is the basis of the coherent Ising machine, where the optically realized Ising spins interact via dissipative coupling.

The dispersive coupling will allow the observation of first-order spectral phase transition. This is shown in Fig. 5.10(a). In the presence of dissipative coupling, first-order spectral phase transition will not occur, and only second-order spectral phase transition can be observed. This is shown in Fig. 5.10(b). It is to be noted that in the time-multiplexed implementation, the first-order spectral phase transition is only observed in the alternate peaks.

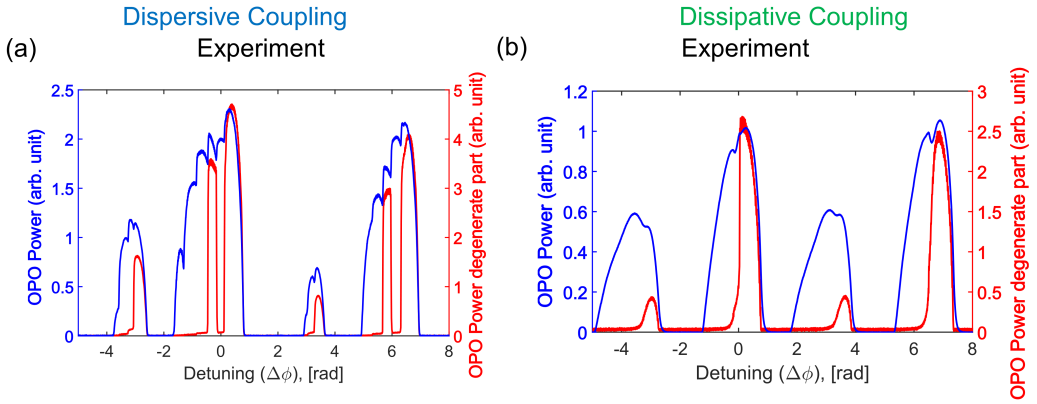

Figure 5.10: **Coupled OPO response in the time-multiplexed implementation in the presence of a) dispersive coupling, and b) dissipative coupling.**

The coupling can be modified from dispersive to dissipative coupling, by changing the phase of the coupling cavity.

The coupled OPO threshold is also a function of the coupling phase. The threshold is minimum when the coupling is dissipative (both ferromagnetic and anti-ferromagnetic). The threshold is the maximum for purely dispersive coupling. This is shown in terms of the OPO output modulation as the coupling phase is varied using PZTB as shown in Fig. 5.11.

This can be seen using a simplified CW mean field model of coupled OPO in the linearized form:

$$\frac{da}{dt} = -\alpha a + g a^* + \mathrm{i}\kappa \mathrm{e}^{\mathrm{i}\theta} b \tag{5.9a}$$

$$\frac{db}{dt} = -\alpha b + g b^* + \mathrm{i}\kappa \mathrm{e}^{\mathrm{i}\theta} a \tag{5.9b}$$

where α, g, κ, and θ are the loss, parametric gain, coupling strength, and coupling phase, respectively.

$$\frac{d}{dt}\begin{bmatrix} a \\ a^* \\ b \\ b^* \end{bmatrix} = \begin{bmatrix} -\alpha & g & i\kappa e^{i\theta} & 0 \\ g & -\alpha & 0 & -i\kappa e^{i\theta} \\ i\kappa e^{i\theta} & 0 & -\alpha & g \\ 0 & -i\kappa e^{i\theta} & g & -\alpha \end{bmatrix}\begin{bmatrix} a \\ a^* \\ b \\ b^* \end{bmatrix} \tag{5.10}$$

The threshold is determined by the maximum eigenvalue. λ_{max} is given by: $\lambda_{max} + \alpha = \sqrt{g^2 - e^{2i\theta}\kappa^2}$. Clearly, for the dissipative coupling $\theta = \frac{\pi}{2}$ (anti-ferromagnetic) and $\theta = \frac{3\pi}{2}$ (ferromagnetic) the threshold is lowest. The threshold is highest for purely dispersive coupling $\theta = 0$ and $\theta = \pi$.

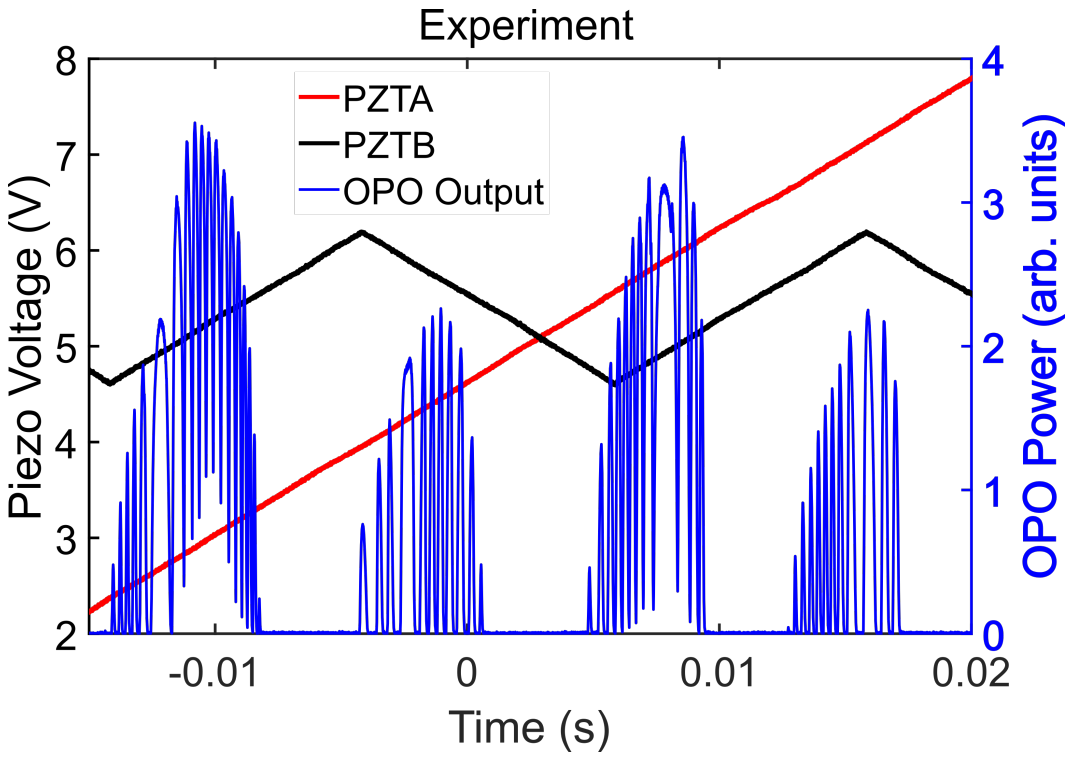

Figure 5.11: **Variation of the coupled OPO threshold as a function of coupling phase.**

5.5.5 Advantage of parametrically driven spectral phase transition based sensing

Advantages: Our sensing system is also advantageous over linear enhancement techniques due to the following reasons:

- Our sensing system does not require a high-Q cavity (cold-cavity) to begin with. Despite being low-Q it can exhibit sensitivity comparable to its high-Q counterparts. This is very important in light of system integration. High-Q cavities can be made with due fabrication diligence. However, these cavities remain high-Q when kept in isolation, and may be extremely challenging to retain their high-quality nature when integrated with sensing platforms like micro-fluidic systems/ micro-scale vacuum cells that may be utilized to deliver the analyte/sample to the sensor. On the other hand, our system can still operate with low Q, albeit with higher thresholds/power requirements. This will not be an issue in integrated optical parametric oscillators, where the thresholds are relatively low (can be less than 1 mW) [24].

- The system response is tunable. Aggregation of loss due to interaction with the sample can be compensated by increasing the pump power (adjustment due to the changing threshold). This is in stark contrast with high-Q cavity based systems where the sensitivity drops significantly with an accumulation of loss (degradation of Q factor).

- The system is expected to enhance the signal-to-noise ratio of sensing and not just the sensitivity. While in high-Q-based systems the SNR can be enhanced by increasing the pump power, novel sensing mechanisms based on exceptional points [19] can suffer from SNR performance owing to enhanced fluctuations near the vicinity of exceptional point [52]. Our system behaves differently thanks to the phase-sensitive gain mechanism which exhibits quadrature-dependent fluctuations behavior. Although the fluctuations diverge in the phase quadrature, the fluctuation in the amplitude quadrature can be restricted [43].

- We have also shown that the spectral phase transition can not only be used to measure the magnitude of perturbation but can also be leveraged to identify the sign of the phase perturbation (please refer to Fig. 5.5 and the discussion thereof).

Boosting the sensitivity with proper dispersion engineering and its use as transition-edge sensor:

The sensitivity that we have observed experimentally can be boosted by several means:

- The bandwidth of the bandpass filter (centered around the degeneracy point) can be made narrower. In the experiment, we used a bandwidth of 1 nm. Using a bandpass filter with lower bandwidth (0.1 nm) will further boost the sensitivity, owing to higher spectral selectivity between the degenerate and non-degenerate regimes. This is shown in Fig. 5.12(a,b).

- The sensitivity of the system based on second-order spectral transition is a function of the intra-cavity dispersion. The sensitivity is expected to improve with minimizing second-order dispersion co-efficient β_2 [42]. Thus, the smaller the intra-cavity dispersion, the higher the sensitivity. The flexibility to design the dispersion in integrated platforms will enable to realization of very low dispersion systems, thereby boosting the sensitivity [25]. The scaling with varying intra-cavity dispersion is shown in Fig. 5.12(c). In the experiment, we attempted to minimize the dispersion by using a combination of standard and dispersion-compensating fibers. However, it is still much higher than what can be achieved on an integrated platform.

We also mention that instead of using a bandpass filter centered exactly around the degenerate point of operation, one could also use a bandpass filter centered around the non-degenerate end of the spectrum. This configuration applies to detecting the sensitivity around the first-order transition point, and will not work for measurements around the second-order critical point. Around the first-order transition point, the non-degenerate bandpass filter can discriminate the abrupt transition from far non-degeneracy to exact degeneracy as shown in Fig. 5.13.

5.5.6 Observation of spectral discontinuity using a combination of slow-detector and band-pass filter

Our experimental design was motivated by the fact that larger spectral splitting would lead to a more conspicuous spectral discontinuity at the first-order transition point. Here, larger spectral splitting refers to more non-degenerate oscillation. As shown in Fig. 5.14(a), this translates to a higher coupling coefficient (κ). In our experiment, the coupling coefficient is close to κ =0.5. This helped us in observing the clear discontinuity in the radio-frequency spectrum for the carrier-envelope frequency beat-notes. The discontinuity is also apparent in the optical spectrum measurements. This dependence on coupling co-efficient is however conflicting when one considers the measurement protocol using a slow photo-detector preceded by a band-pass filter. In this case, we need a large jump in the registered

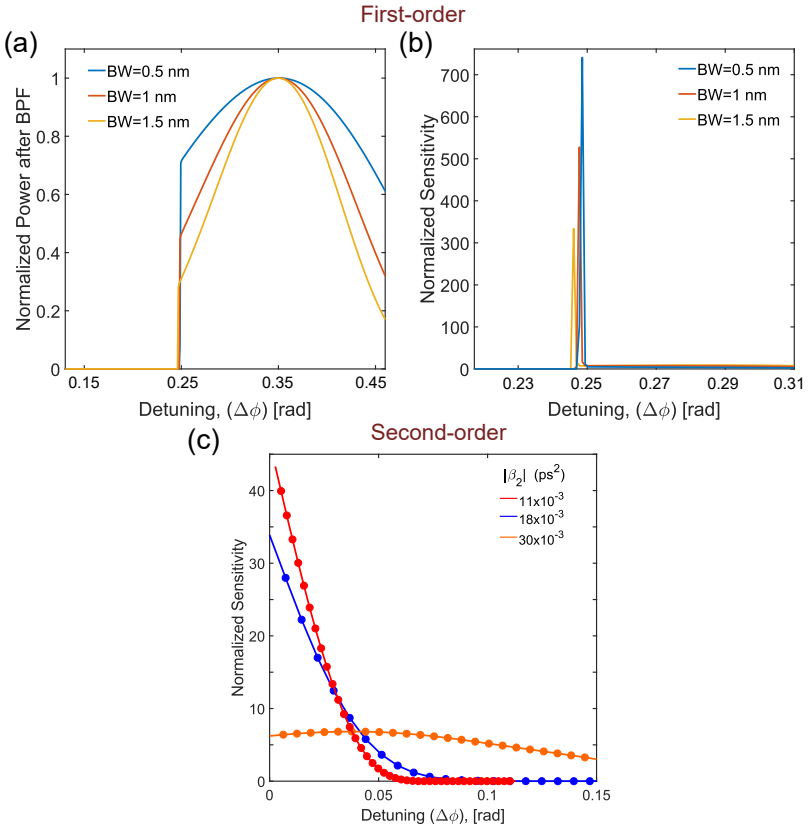

Figure 5.12: **Effect of varying filter bandwidth.** Numerical simulation showing a) the normalized filtered output power with varying filter bandwidth, b) and the corresponding sensitivity. Narrower bandwidth of the bandpass filter results in a more abrupt jump (when normalized to the maximum power) leading to higher sensitivity enhancement at the first-order transition point. A similar trend follows in the case of second-order critical points as well. c) Sensitivity for operation around the second-order critical point is plotted for various dispersion parameters. The normalized sensitivity enhances with smaller intra-cavity integrated dispersion.

power, when the coupled OPO transitions from non-degeneracy to degeneracy at the first-order transition point. This means that the coupled OPO should oscillate at higher power (corresponding to higher degenerate gain) when it transitions to degeneracy so that the abrupt change in power between extreme non-degenerate and degenerate operation is apparent. This translates to lower values of coupling co-efficient as shown in Fig. 5.14(b). As can be seen from the results obtained through numerical calculations (Fig. 5.14(b)), the one with the least value of coupling co-efficient starts oscillating with higher gain in the degenerate mode near the first-order transition point.

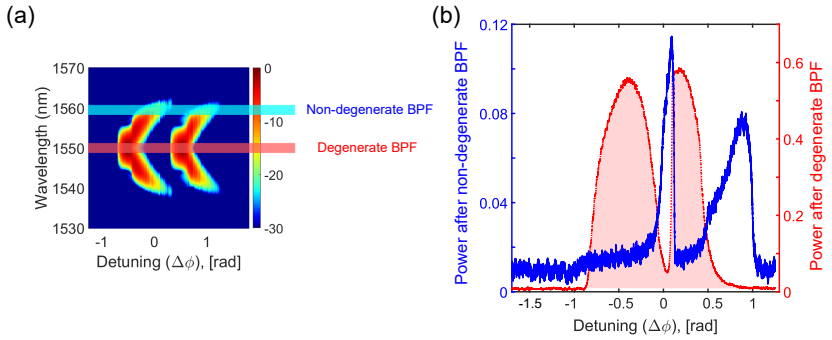

Figure 5.13: **Non-degenerate filtering based sensing protocol.** a) Using a bandpass filter located towards the extreme end of the non-degenerate spectrum instead of using one that is centered around the degeneracy point for the sensing configuration. b) Measured data showing a similar sensitivity enhancement can be captured using the configuration based on a bandpass filter (BPF) around the non-degenerate end of the spectrum.

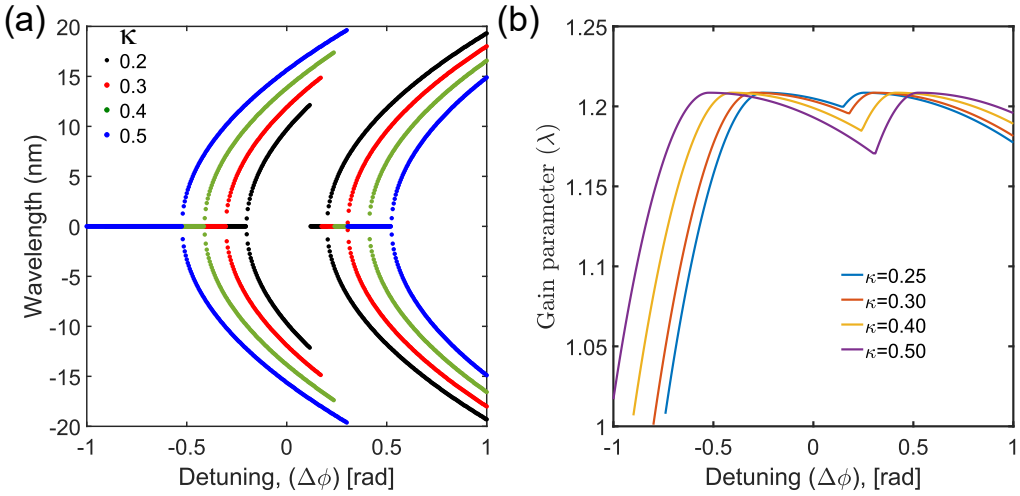

Figure 5.14: **Effect of the coupling co-efficient on the spectral splitting.** a) Effect of the coupling co-efficient on the spectral splitting (κ). b) Behavior of the gain parameter with varying coupling coefficient.

This behavior is confirmed by performing numerical simulations for the dynamics of coupled OPOs for various values of the coupling coefficient at a fixed pump power. Figure 5.15(a) shows that indeed lower values of the coupling coefficient lead to a more abrupt jump in the normalized OPO output power. Unfortunately, for the case of higher coupling co-efficient ($\kappa = 0.5$, which is close to the experimental scenario), the jump corresponding to the discontinuity is not conspicuous when the coupled OPO is operated near the threshold. This has precluded us from observing

the sharp discontinuity corresponding to the first-order transition point using this protocol. The associated normalized sensitivity is shown in Fig. 5.15(b), where higher sensitivity is expected for lower values of coupling co-efficient.

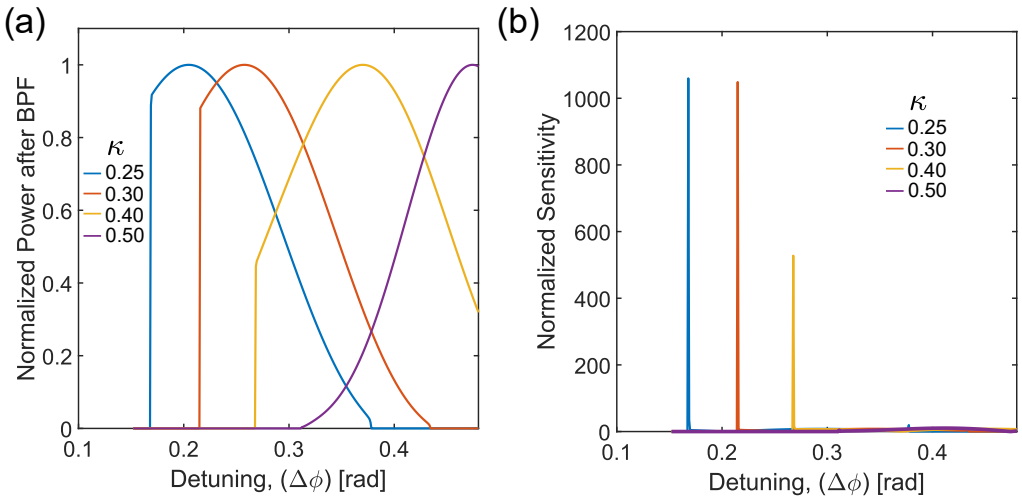

Figure 5.15: **Effect of coupling co-efficient** (κ) on the observation of sharp discontinuity in the power recorded through a band-pass filter at the first-order transition point. a) shows the normalized power, b) shows the corresponding normalized sensitivity for various values of κ. The pump power is fixed at 1.50 P_0, where P_0 is a single OPO threshold.

We note that this discontinuity in the power recorded through a band-pass filter is also a function of the pump power, i.e., number of times above threshold operation. Higher pump powers result in more abrupt discontinuity (Fig. 5.16(a)) and lead to higher sensitivity (Fig. 5.16(b)). For the case of higher coupling, co-efficient one can still operate at higher pump powers and observe some discontinuity too. However, in the experiment, we were limited by other effects (photo-refractive damage) that prevented us to operate at those higher pump power levels. We note here that, the threshold for coupled OPOs increases with an increase in the value of coupling co-efficient.

Imperfections in the experimental setup (imperfect locking and associated phase instability of the coupling cavity) have also contributed to lower values of the SNR, which made the observation of the abrupt discontinuity using this protocol difficult. The realization of coupled OPOs in an integrated photonics platform will most likely help alleviate this issue. Moreover, we should follow the design guideline of deploying a lower value of coupling co-efficient in this approach. However direct spectral domain measurements would benefit from a higher value of coupling co-

efficient. Thus one has to tweak the coupled OPO design based on the specific requirement.

The discontinuity corresponding to the first-order transition point exists irrespective of how fine of a grid in detuning we consider in the simulations. The derivative is technically ill-defined at that point and the sensitivity quantification at the first-order transition point is a representation for the ease of comparison.

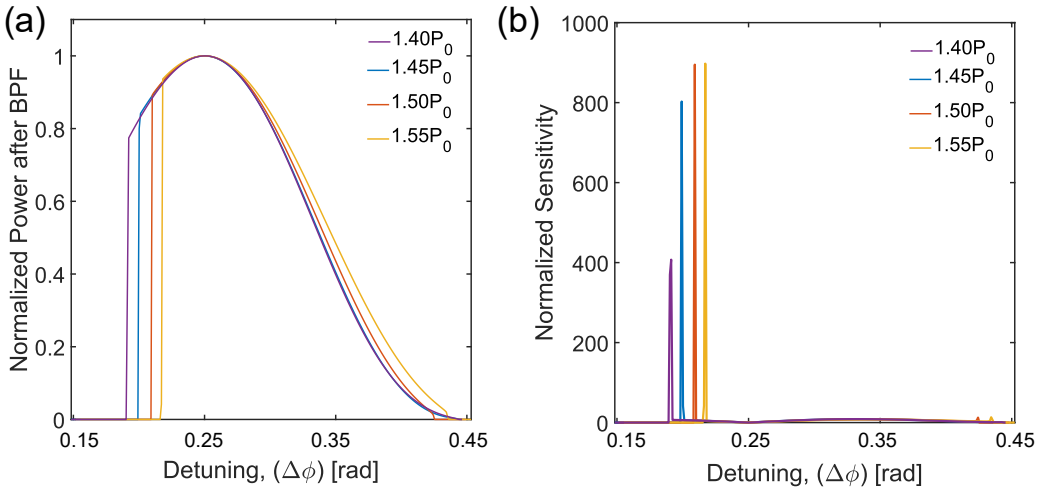

Figure 5.16: **Effect of pump power (number of times above threshold operation) on the observation of sharp discontinuity in the power recorded through a band-pass filter at the first-order transition point.** Here, P_0 represents the threshold pump power for a single OPO. a) shows the normalized power, b) shows the corresponding normalized sensitivity for various values of pump power. The coupling coefficient is chosen to be κ =0.30.

References

[1] Mark C. Cross and Pierre C. Hohenberg. Pattern formation outside of equilibrium. *Reviews of Modern Physics*, 65(3):851, 1993.

[2] Kaled Dechoum, Laura Rosales-Zárate, and Peter D. Drummond. Critical fluctuations in an optical parametric oscillator: When light behaves like magnetism. *Journal of the Optical Society of America B*, 33(5):871–883, 2016.

[3] Vittorio DeGiorgio and Marlan O. Scully. Analogy between the laser threshold region and a second-order phase transition. *Physical Review A*, 2(4):1170, 1970.

[4] Leonardo Del Bino, Jonathan M. Silver, Sarah L. Stebbings, and Pascal Del'Haye. Symmetry breaking of counter-propagating light in a nonlinear resonator. *Scientific Reports*, 7(1):1–6, 2017.

[5] Roberto Di Candia, Fabrizio Minganti, Kirill Petrovnin, Gheorghe S. Paraoanu, and Simone Felicetti. Critical parametric quantum sensing. *arXiv preprint arXiv:2107.04503*, 2021.

[6] Jiajie Ding, Igor Belykh, Alireza Marandi, and Mohammad-Ali Miri. Dispersive versus dissipative coupling for frequency synchronization in lasers. *Physical Review Applied*, 12(5):054039, 2019.

[7] Peter D. Drummond, K. J. McNeil, and D. F. Walls. Non-equilibrium transitions in sub/second harmonic generation. *Optica Acta: International Journal of Optics*, 27(3):321–335, 1980.

[8] Dominic V. Else, Bela Bauer, and Chetan Nayak. Floquet time crystals. *Physical Review Letters*, 117(9):090402, 2016.

[9] Michel Fruchart, Ryo Hanai, Peter B. Littlewood, and Vincenzo Vitelli. Non-reciprocal phase transitions. *Nature*, 592(7854):363–369, 2021.

[10] Alessandra Gatti and Luigi Lugiato. Quantum images and critical fluctuations in the optical parametric oscillator below threshold. *Physical Review A*, 52(2): 1675, 1995.

[11] Gregory N. Gol'Tsman, O. Okunev, Galina Chulkova, A. Lipatov, Andrew Semenov, Konstantin Smirnov, B. Voronov, A. Dzardanov, C. Williams, and Roman Sobolewski. Picosecond superconducting single-photon optical detector. *Applied Physics Letters*, 79(6):705–707, 2001.

[12] Ariel Gordon and Baruch Fischer. Phase transition theory of many-mode ordering and pulse formation in lasers. *Physical Review Letters*, 89(10): 103901, 2002.

[13] Victor Grigoriev and Fabio Biancalana. Resonant self-pulsations in coupled nonlinear microcavities. *Physical Review A*, 83(4):043816, 2011.

[14] Qiushi Guo, Ryoto Sekine, Luis Ledezma, Rajveer Nehra, Devin J. Dean, Arkadev Roy, Robert M. Gray, Saman Jahani, and Alireza Marandi. Femtojoule femtosecond all-optical switching in lithium niobate nanophotonics. *Nature Photonics*, 16(9):625–631, 2022.

[15] Xueshi Guo, Casper R Breum, Johannes Borregaard, Shuro Izumi, Mikkel V. Larsen, Tobias Gehring, Matthias Christandl, Jonas S. Neergaard-Nielsen, and Ulrik L. Andersen. Distributed quantum sensing in a continuous-variable entangled network. *Nature Physics*, 16(3):281–284, 2020.

[16] Hermann Haken. Cooperative phenomena in systems far from thermal equilibrium and in nonphysical systems. *Reviews of Modern Physics*, 47 (1):67, 1975.

[17] Ryan Hamerly, Alireza Marandi, Marc Jankowski, Martin M. Fejer, Yoshihisa Yamamoto, and Hideo Mabuchi. Reduced models and design principles for half-harmonic generation in synchronously pumped optical parametric oscillators. *Physical Review A*, 94(6):063809, 2016.

[18] RG Heideman and PV Lambeck. Remote opto-chemical sensing with extreme sensitivity: design, fabrication and performance of a pigtailed integrated optical phase-modulated Mach-Zehnder interferometer system. *Sensors and Actuators B: Chemical*, 61(1-3):100–127, 1999.

[19] Hossein Hodaei, Absar U. Hassan, Steffen Wittek, Hipolito Garcia-Gracia, Ramy El-Ganainy, Demetrios N. Christodoulides, and Mercedeh Khajavikhan. Enhanced sensitivity at higher-order exceptional points. *Nature*, 548(7666): 187–191, 2017.

[20] Jae K. Jang, Alexander Klenner, Xingchen Ji, Yoshitomo Okawachi, Michal Lipson, and Alexander L. Gaeta. Synchronization of coupled optical microresonators. *Nature Photonics*, 12(11):688–693, 2018.

[21] Marc Jankowski, Carsten Langrock, Boris Desiatov, Alireza Marandi, Cheng Wang, Mian Zhang, Christopher R Phillips, Marko Lončar, and Martin M. Fejer. Ultrabroadband nonlinear optics in nanophotonic periodically poled lithium niobate waveguides. *Optica*, 7(1):40–46, 2020.

[22] Alexander E. Kaplan and Pierre Meystre. Enhancement of the Sagnac effect due to nonlinearly induced nonreciprocity. *Optics Letters*, 6(12):590–592, 1981.

[23] E Krioukov, DJW Klunder, A Driessen, Jan Greve, and Cornelis Otto. Sensor based on an integrated optical microcavity. *Optics Letters*, 27(7):512–514, 2002.

[24] A. V. Kuznetsov. Optical bistability driven by a first order phase transition. *Optics communications*, 81(1-2):106–111, 1991.

[25] Carsten Langrock and Martin M. Fejer. Fiber-feedback continuous-wave and synchronously-pumped singly-resonant ring optical parametric oscillators using reverse-proton-exchanged periodically-poled lithium niobate waveguides. *Optics Letters*, 32(15):2263–2265, 2007.

[26] Kevin F. Lee, Jie Jiang, Christian Mohr, J. Bethge, Martin E. Fermann, Nick Leindecker, Konstantin L. Vodopyanov, Peter G. Schunemann, and Ingmar Hartl. Carrier envelope offset frequency of a doubly resonant, nondegenerate, mid-infrared GaAs optical parametric oscillator. *Optics Letters*, 38(8):1191–1193, 2013.

[27] Christian Leefmans, Avik Dutt, James Williams, Luqi Yuan, Midya Parto, Franco Nori, Shanhui Fan, and Alireza Marandi. Topological dissipation in a time-multiplexed photonic resonator network. *Nature Physics*, 18(4):442–449, 2022.

[28] Stefano Longhi. Nonadiabatic pattern formation in optical parametric oscillators. *Physical Review Letters*, 84(25):5756, 2000.

[29] Stefano Longhi and Angelo Geraci. Swift-Hohenberg equation for optical parametric oscillators. *Physical Review A*, 54(5):4581, 1996.

[30] Juanjuan Lu, Ayed Al Sayem, Zheng Gong, Joshua B. Surya, Chang-Ling Zou, and Hong X. Tang. Ultralow-threshold thin-film lithium niobate optical parametric oscillator. *Optica*, 8(4):539–544, 2021.

[31] Alireza Marandi, Zhe Wang, Kenta Takata, Robert L. Byer, and Yoshihisa Yamamoto. Network of time-multiplexed optical parametric oscillators as a coherent Ising machine. *Nature Photonics*, 8(12):937–942, 2014.

[32] Peter L. McMahon, Alireza Marandi, Yoshitaka Haribara, Ryan Hamerly, Carsten Langrock, Shuhei Tamate, Takahiro Inagaki, Hiroki Takesue, Shoko Utsunomiya, Kazuyuki Aihara, et al. A fully programmable 100-spin coherent Ising machine with all-to-all connections. *Science*, 354(6312):614–617, 2016.

[33] Matteo Menotti, Blair Morrison, Kang Tan, Zachary Vernon, John E. Sipe, and Marco Liscidini. Nonlinear coupling of linearly uncoupled resonators. *Physical Review Letters*, 122(1):013904, 2019.

[34] Steven A. Miller, Yoshitomo Okawachi, Sven Ramelow, Kevin Luke, Avik Dutt, Alessandro Farsi, Alexander L. Gaeta, and Michal Lipson. Tunable frequency combs based on dual microring resonators. *Optics Express*, 23(16):21527–21540, 2015.

[35] Yoshitomo Okawachi, Mengjie Yu, Kevin Luke, Daniel O. Carvalho, Sven Ramelow, Alessandro Farsi, Michal Lipson, and Alexander L. Gaeta. Dual-pumped degenerate Kerr oscillator in a silicon nitride microresonator. *Optics letters*, 40(22):5267–5270, 2015.

[36] Yoshitomo Okawachi, Mengjie Yu, Jae K. Jang, Xingchen Ji, Yun Zhao, Bok Young Kim, Michal Lipson, and Alexander L. Gaeta. Demonstration of chip-based coupled degenerate optical parametric oscillators for realizing a nanophotonic spin-glass. *Nature Communications*, 11(1):1–7, 2020.

[37] Gian-Luca Oppo, Alison M. Yao, and Domenico Cuozzo. Self-organization, pattern formation, cavity solitons, and rogue waves in singly resonant optical parametric oscillators. *Physical Review A*, 88(4):043813, 2013.

[38] Ilya Prigogine and René Lefever. Symmetry breaking instabilities in dissipative systems. II. *The Journal of Chemical Physics*, 48(4):1695–1700, 1968.

[39] Jinhan Ren, Hossein Hodaei, Gal Harari, Absar U. Hassan, Weng Chow, Mohammad Soltani, Demetrios Christodoulides, and Mercedeh Khajavikhan. Ultrasensitive micro-scale parity-time-symmetric ring laser gyroscope. *Optics Letters*, 42(8):1556–1559, 2017.

[40] Chad Ropp, Nicolas Bachelard, David Barth, Yuan Wang, and Xiang Zhang. Dissipative self-organization in optical space. *Nature Photonics*, 12(12):739, 2018.

[41] Arkadev Roy, Saman Jahani, Qiushi Guo, Avik Dutt, Shanhui Fan, Mohammad-Ali Miri, and Alireza Marandi. Nondissipative non-Hermitian dynamics and exceptional points in coupled optical parametric oscillators. *Optica*, 8(3):415–421, 2021.

[42] Arkadev Roy, Saman Jahani, Carsten Langrock, Martin Fejer, and Alireza Marandi. Spectral phase transitions in optical parametric oscillators. *Nature Communications*, 12(1):1–9, 2021.

[43] Kestutis Staliunas. Spatial and temporal spectra of noise driven stripe patterns. *Physical Review E*, 64:066129, Nov 2001. doi: 10.1103/PhysRevE.64.066129. URL https://link.aps.org/doi/10.1103/PhysRevE.64.066129.

[44] H. Eugene Stanley. *Phase transitions and critical phenomena*. Clarendon Press, Oxford, 1971.

[45] Victor B. Taranenko, Kestutis Staliunas, and C. O. Weiss. Pattern formation and localized structures in degenerate optical parametric mixing. *Physical Review Letters*, 81(11):2236, 1998.

[46] Alexey Tikan, Johann Riemensberger, Kenichi Komagata, Simon Hönl, Mikhail Churaev, Connor Skehan, Hairun Guo, Rui Ning Wang, Junqiu Liu,

Paul Seidler, et al. Emergent nonlinear phenomena in a driven dissipative photonic dimer. *Nature Physics*, 17(5):604–610, 2021.

[47] Alan Mathison Turing. The chemical basis of morphogenesis. *Bulletin of Mathematical Biology*, 52(1):153–197, 1990.

[48] Aleksandr K. Tusnin, Alexey M. Tikan, Kenichi Komagata, and Tobias J. Kippenberg. Coherent dissipative structures in chains of coupled $\chi^{(3)}$ resonators. *arXiv e-prints*, pages arXiv–2104, 2021.

[49] M. Vaupel, A. Maitre, and Claude Fabre. Observation of pattern formation in optical parametric oscillators. *Physical Review Letters*, 83(25):5278, 1999.

[50] Chao Wang et al. Nonlinearly enhanced refractive index sensing in coupled optical microresonators. *Optics Letters*, 39(1):26–29, 2014.

[51] Chao Wang et al. A nonlinear microresonator refractive index sensor. *Journal of Lightwave Technology*, 33(20):4360–4366, 2015.

[52] Heming Wang, Yu-Hung Lai, Zhiquan Yuan, Myoung-Gyun Suh, and Kerry Vahala. Petermann-factor sensitivity limit near an exceptional point in a Brillouin ring laser gyroscope. *Nature Communications*, 11(1):1–6, 2020.

[53] Duncan J. Watts and Steven H. Strogatz. Collective dynamics of 'small-world'networks. *Nature*, 393(6684):440–442, 1998.

[54] Frank Wilczek. Quantum time crystals. *Physical Review Letters*, 109(16): 160401, 2012.

[55] Logan G. Wright, Demetrios N. Christodoulides, and Frank W. Wise. Spatiotemporal mode-locking in multimode fiber lasers. *Science*, 358(6359): 94–97, 2017.

[56] Fan O. Wu, Absar U. Hassan, and Demetrios N. Christodoulides. Thermodynamic theory of highly multimoded nonlinear optical systems. *Nature Photonics*, 13(11):776–782, 2019.

[57] Ling-An Wu, Harry Jeff Kimble, John L. Hall, and Huifa Wu. Generation of squeezed states by parametric down conversion. *Physical Review Letters*, 57 (20):2520, 1986.

[58] Xiaoxiao Xue, Xiaoping Zheng, and Bingkun Zhou. Super-efficient temporal solitons in mutually coupled optical cavities. *Nature Photonics*, 13(9):616–622, 2019.

[59] Li-Ping Yang and Zubin Jacob. Quantum critical detector: Amplifying weak signals using discontinuous quantum phase transitions. *Optics Express*, 27(8): 10482–10494, 2019.

[60] Mian Zhang, Cheng Wang, Yaowen Hu, Amirhassan Shams-Ansari, Tianhao Ren, Shanhui Fan, and Marko Lončar. Electronically programmable photonic molecule. *Nature Photonics*, 13(1):36–40, 2019.

[61] Yanbing Zhang, Matteo Menotti, Kang Tan, Varun D. Vaidya, Dylan H. Mahler, Luke G. Helt, L. Zatti, Marco Liscidini, Blair Morrison, and Zachary Vernon. Squeezed light from a nanophotonic molecule. *Nature Communications*, 12 (1):1–6, 2021.

Chapter 6

ISING-KURAMOTO MACHINE: COMPUTATION AT THE SPECTRAL PHASE TRANSITION

6.1 Abstract

Several combinatorial optimization problems are of utmost importance with regard to their connections to a plethora of applications ranging from portfolio optimization, scheduling, and routing to solving physics-based problems. Some of them are computationally hard belonging to the NP complexity class, and efficient algorithms to find the solution to these problems are absent to date. Several heuristics-based approaches promise to provide near-optimal solutions and many of which are inspired by dynamics in physical systems like simulated annealing, quantum annealing, adiabatic Hamiltonian engineering, stimulated bifurcation, etc. Thus physics-based analog machines are more suitable for the implementation of these algorithms compared to their digital von-Neumann-based counterparts. A coherent Ising machine composed of a network of coupled optical parametric oscillators has been investigated in this regard to simulate the Ising Hamiltonian which corresponds to the steady-state phase configuration of the constituent parametric oscillators. Several enhancements have been proposed to improve the solution accuracy of these coherent Ising machines ranging from amplitude homogenization to the application of error correction feedback, etc. In this work, we propose a new protocol for these coherent Ising machines involving a dimensional relaxation that relaxes the dynamics of the Ising Hamiltonian to the XY problem. We show that we can leverage the spectral phase transition that occurs in optical parametric oscillators to adiabatically switch from the XY dynamics dictated by the Kuramoto synchronization of nonlinear oscillators to the Ising dynamics that corresponds to the combinatorial optimization problem of interest. We leverage the additional phase degree of freedom for OPOs operating in the non-degenerate regime displaying the XY dynamics to explore the energy landscape. Our simulations indicate enhanced solution accuracy for Mobius ladder based graphs as well as broader solution distribution for several benchmark problems. We map the dynamics to a physical platform comprising synchronously pumped optical parametric oscillators apart from developing a simplified model for investigating the stability of the fixed points. Our results highlight a new protocol

for coherent Ising machines paves the way for achieving improved optimal solutions by leveraging the new degrees of freedom provided by the proposed Ising-Kuramoto model.

6.2 Introduction

Several combinatorial optimization problems belonging to the NP-hard complexity class lack an efficient classical algorithm. The time complexity grows exponentially with the problem size which soon becomes intractable for real-life problems of interest. Some of these problems when formulated in the quantum domain also remain hard to solve for a potential fault-tolerant quantum computer and are described by the corresponding QMA-hard complexity class. There exist deterministic classical algorithms that can guarantee a solution that is no worse than the optimal solution by a factor. However, the cost between the optimal solution and the obtained approximate result can be enormous from a practical standpoint. Consequently, there is huge interest in developing heuristics-based algorithms and/or physics-inspired algorithms to obtain a near-optimal solution [2, 22].

Many of these hard optimization problems can be recast into spin Hamiltonians where the optimal solutions correspond to the ground state configuration of the Hamiltonian [14]. The Ising Hamiltonian that describes the dynamics of binary spins can be directly mapped to a wide range of combinatorial optimization problems [24]. Thus physics-based analog hardware is a natural candidate for realizing these solvers. Possible hardware implementation range from superconducting circuits, trapped ions, cold atoms, a system of nonlinear oscillators in CMOS/ spin-torque based devices [3, 23], coupled optical parametric oscillators [5, 6, 12, 13, 20], polaritonic oscillators [10], photonic devices [15, 16], etc. Here, we will be focusing on the optics-based platform using networks of coupled parametric oscillators also known as coherent Ising machines.

Degenerate optical parametric oscillators (OPO) can occupy one of the two binary phase states above the threshold. Thus these two phase configurations that are offset by π, can be mapped to the binary spin states in the Ising Hamiltonian and can form the nodes of the so-called coherent Ising machines (CIM). The coupling between the OPOs (dissipative coupling) is engineered according to the graph adjacency matrix. Several successful demonstrations of large-scale CIMs have shown the promise that exploits the potential of all-to-all connectivity and high-clock speed.

However, these systems do not always converge to the optimum solution in the steady state and oftentimes get stuck in local minima that exist in the complex energy landscape [19]. This may be explained by several reasons including the issue of amplitude heterogeneity. Several improvements have been suggested with regard to the operation of CIMs to alleviate this problem. This includes among other chaotic amplitude control [11], application of error correction feedback [8], etc. It is of active research interest to investigate protocols that lead to improving the solution accuracy of these CIMs.

One viable route in this regard is to increase the degrees of freedom of the CIM which can allow one to explore the energy landscape more effectively. The XY Hamiltonian represents the rank 2 relaxations of the Ising problem [4] where the phase degree of freedom is unconstrained. This introduces the phase of the nonlinear oscillators as an additional degree of freedom that can be exploited. However, the combinatorial optimization problem is related to the Ising Hamiltonian and thus dimensional annealing leading to binarization (can also be thought of as rounding procedure) of the spin is warranted at the end of the computation. Motivated by this concept, we propose the Ising-Kuramoto protocol for CIM.

In this work, we propose to utilize the spectral phase transition phenomena occurring in a network of coupled optical parametric oscillators to realize the Ising-Kuramoto machine. We show that the system of coupled OPOs in their non-degenerate oscillation regime undergoes the Kuramoto synchronization and minimizes the XY Hamiltonian. BY traversing the spectral phase transition [17, 18] we undergo dimensional annealing [1] from the XY phase to the Ising phase whereby the OPOs transition into degenerate oscillation regime and approximates the Ising Hamiltonian. We perform numerical simulations of our proposed protocol on Mobius ladder based graphs and observe enhancements in solution accuracy. We investigate a simplified model to analyze the dynamics including the stability of fixed points and report the computational results on benchmark problems that exhibit a broader distribution of the optimal solutions compared to the Ising-only counterpart. We also explore the possibility of multiple annealing schedules involving the transition between the XY and the Ising phases and investigate the resultant improvements.

6.3 Results

The CIM is programmed to solve the Ising Hamiltonian where one needs to find N binary spins $s_i \in -1, 1$, that minimize:

$$H_{\text{Ising}} = -\frac{1}{2}\sum_{i,j=1}^{N} J_{i,j} s_i s_j - \sum_{i=1}^{N} h_i s_i \tag{6.1}$$

where $J_{i,j}$ is the real coupling matrix and h_i represents external fields. This maps to the MAXCUT problem belonging to the NP-hard complexity class with minimum overhead. CIMs realized with degenerate OPOs can faithfully replicate this dynamics thanks to the binary phase solutions in the steady state. Here we will be mostly concerned with unweighted, undirected (bi-directional) graphs. The antiferromagnetic interaction represented by the real $J_{i,j}$ matrix can be easily realized using dissipative coupling in a network of degenerate OPOs. Although complex $J_{i,j}$ matrix can also be realized via a combination of dispersive and dissipative coupling.

The conventional operation principle of CIMs composed of degenerate OPOs is described in Fig. 6.1(a). It involves gradually ramping up the pump power of the OPOs from below to above the threshold [24]. The rate at which the pump power is increased has to be judiciously chosen to prevent getting stuck at local minima [25]. The OPOs start below the threshold in a squeezed state with an undetermined phase. As the system approaches the oscillation threshold, they undergo a spontaneous symmetry breaking to occupy one of the binary phase states. The degenerate OPOs get classified into clusters of two spins (with unequal amplitude in general) corresponding to one of the minimum energy configurations. On account of the amplitude heterogeneity, this configuration may not correspond to the optimum solution of the combinatorial optimization problem.

We propose a new protocol for operating these CIMs, in the Ising-Kuramoto regime as illustrated in Fig. 6.1(b). Here instead of leveraging the spontaneous symmetry breaking at the threshold transition, we utilize the spontaneous symmetry breaking at the spectral phase transition. This spectral transition corresponds to a symmetry breaking from $U(1)$ symmetry to Z_2 symmetry [17]. This corresponds to a rank 2 relaxation of the Ising problem. Further details regarding the spectral phase transition and their connection to OPO dynamics are discussed in the next subsection.

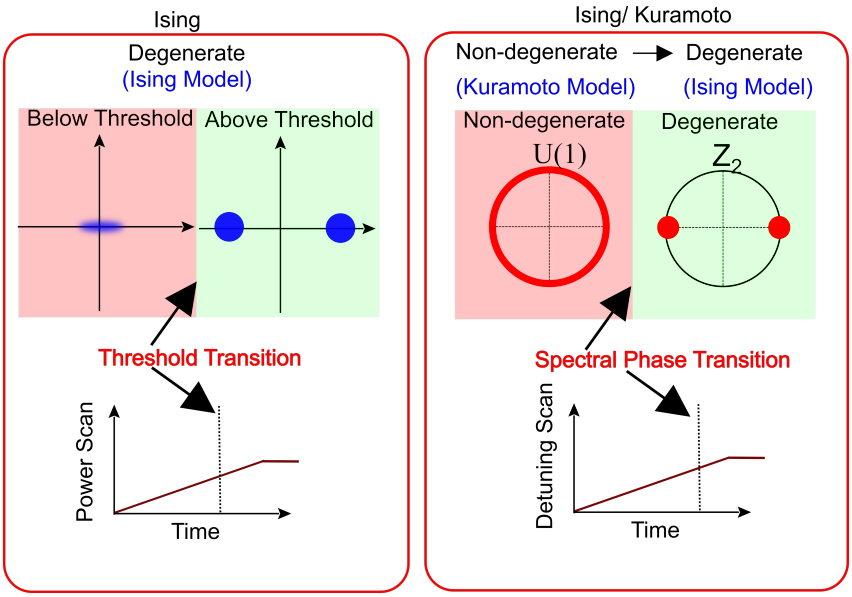

Figure 6.1: **Comparison of protocol between the conventional CIM operation and our proposed approach.** a) Conventional operation of a CIM involves gradually ramping the pump power from below to above the threshold. Individual OPOs operating in the degenerate regime start from being in the squeezed state to occupying one of the two possible coherent states (bi-phase states) as it crosses the spontaneous symmetry breaking at the threshold, b) our proposed operation of Ising-Karamoto machine where the governing dynamics are gradually tuned from being XY to being Ising. This maps directly to the non-degenerate and degenerate regime of operation of OPOs, respectively.

The U_1 symmetry in the XY regime provides the phase degree of freedom. While in the regime, two stable fixed solutions exist as shown by the potential picture in Fig. 6.2(a), the fixed points in the XY regime can occupy any phase and can lie on the circle centered around the origin. This is illustrated by the potential diagram in Fig. 6.2(b). Now, we assume the dynamics of two OPOs operating above the threshold, and the coupling is switched on. In the Ising case, if the spins of the OPOs happen to be wrongly oriented, they have to crossover the potential barrier (or in other words traverse a trajectory crossing the zero amplitude) and flip over to the desired phase. This is shown as the color plot in the bottom panel of Fig. 6.2(a) where the variation of color from blue to red represents propagation in time. In contrast to the XY regime of operation, the OPOs can adopt a detoured trajectory whereby instead of crossing the potential barrier it utilizes the phase degree of freedom to reorient itself to the correct phase configuration which is shown in the bottom panel of Fig. 6.2(b).

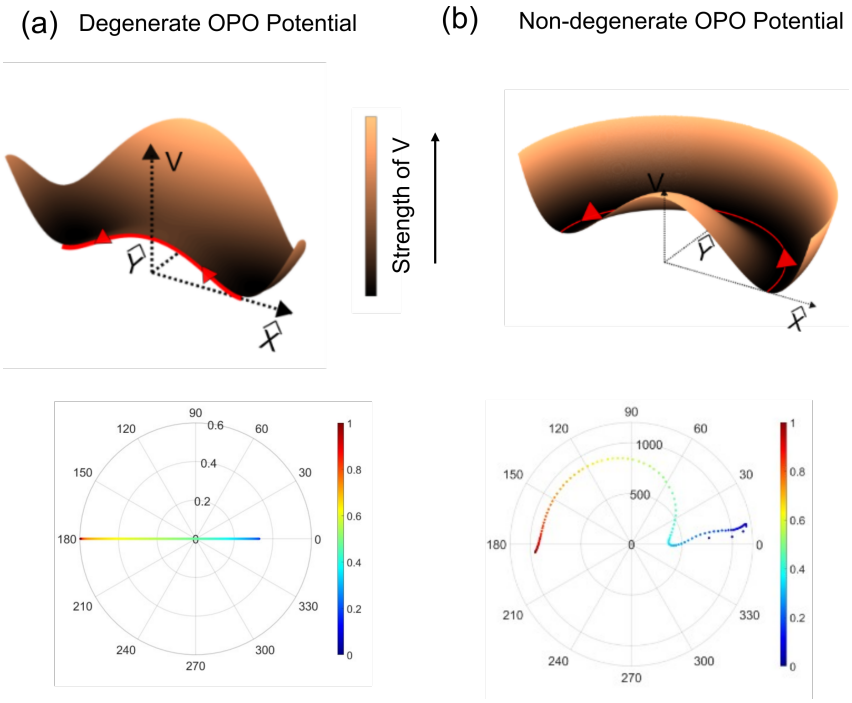

Figure 6.2: **Phase degree of freedom for non-degenerate OPO operation.** a) Potential landscape for degenerate OPOs characterized by two stable fixed points segregated by a potential barrier centered around zero amplitude. In this case, spin-flip has to occur by passing through zero amplitude. b) Potential landscape for non-degenerate OPOs characterized by the phase degree of freedom allowing the spin-flip without traversing the trajectory that passes through zero amplitude.

Spectral phase transition in synchronously pumped OPOs

Synchronously pumped OPOs are used in time-multiplexed configuration to realize large-scale CIMs [6, 13]. Sync-pumped OPOs exhibit intriguing spectral dynamics thanks to the multimode behavior characterized by temporal super-modes [17]. They can undergo a continuous spectral phase transition when the cavity detuning is varied. The OPO switches between the non-degenerate and degenerate oscillation regimes across the transition point. In the non-degenerate regime, the OPO signal enjoys the U_1 symmetry which is spontaneously broken to Z_2 symmetry in the degenerate oscillation regime owing to phase and frequency locking. The dynamics of a network of non-degenerate OPOs are dictated by the XY Hamiltonian involving phase synchronization a.k.a Kuramoto synchronization [21]. Thus in our proposed protocol the cavity detuning is adiabatically varied similar to its pump power counterpart in the conventional mode of operation of CIMs.

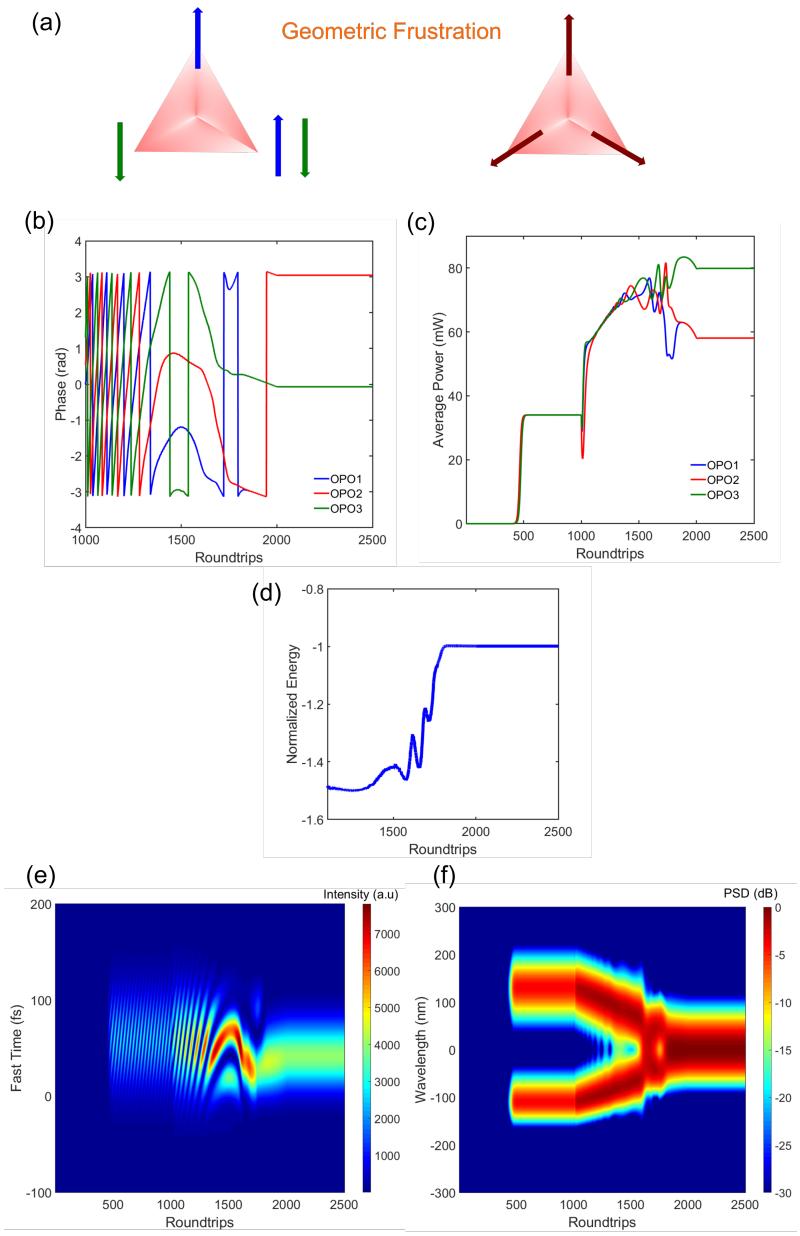

Figure 6.3: **Spectral phase transition and a simple case of geometric frustration.** a) A 3-spin configuration displaying geometric frustration when the spins are constrained to be binary. The ground state degeneracy is broken when the spin constraint is relaxed. b) Evolution of the phase of individual OPOs as the detuning is varied through the spectral phase transition. It features both the XY (before the spectral phase transition) and the Ising phase (after the spectral phase transition). c) corresponding evolution of the average OPO power. d) The evolution of the energy of the spin configuration featuring lower energy in the XY ground state compared to the Ising case. The color plots represent the temporal (e) and spectral (f) evolution of the OPOs across the spectral phase transition.

The rich dynamics exhibited by sync-pumped OPOs in the presence of detuning variation is illustrated by a simple example of 3 connected spins that displays geometric frustration. If the spins are constrained to be binary then the ground-state becomes degenerate in the 3-spin triangular arrangement as shown in Fig. 6.3(a). However, if the spins have the U_1 phase degree of freedom then they can occupy the minimum energy configuration represented by the spins being 120 degrees apart from each other. This energy cost incurred by the spin constraint can be captured by sync-pumped OPOs undergoing the spectral phase transition. We assume 3 sync-pumped OPOs with the coupling matrix reflecting the all-to-all coupling. The OPOs are initiated in the non-degenerate oscillation regime and the detuning is gradually varied in 1000 roundtrips (roundtrip number 1000 to 2000) until the spectral phase transition happens and the OPOs are forced to oscillate in the degenerate regime. Figures 6.3(b) and (c) shows the evolution of the phases and the average power of the individual OPOs as the detuning is varied. We can identify that during the XY dynamics (i.e., the non-degenerate oscillation regime) the phases of the OPOs are 120 degrees apart from each other, and they display geometric frustration as soon as they enter the Ising regime (i.e., the degenerate oscillation regime). The corresponding variation of the energy of the spin configuration is shown in Fig. 6.3(d) which also highlights that the XY energy minimum was lower than the Ising one. The color plots for the temporal and spectral evolution of the OPOs through the spectral phase transition are shown in Fig. 6.3(e) and (f), respectively. The spectral phase transition is apparent in Fig. 6.3(f).

Simplified Model of the XY-Ising dynamics

The complete temporal dynamics of sync-pumped OPOs involving dispersion and nonlinearity (coupling dynamics between the signal/idler and the pump) are dictated by systems of coupled partial differential equations. This is not only analytically intractable but also the computational resource requirements also become huge for a decent problem size consisting of the order of 100 OPOs only. In view of this, we develop a simplified model that is capable of capturing the essential dynamics which is given by:

$$\dot{a}_i = -\alpha a_i + g(\eta a_i + (1-\eta)a_i^*) - |a_i|^2 a_i + \sum_j J_{i,j} a_j \tag{6.2a}$$

$$V(x,y) = \frac{1}{2}\sum_i \left((\alpha - g)x_i^2 + [\alpha - g(2\eta - 1)]\, y_i^2 + \frac{1}{2}(x_i^2 + y_i^2)^2 \right) - \frac{1}{2}\sum_{i,j} J_{i,j}(x_i x_j + y_i y_j). \quad (6.2b)$$

Here, the non-degenerate oscillation regime is substituted with phase-insensitive gain dynamics while the degenerate oscillation regime is replaced by the phase-sensitive gain. The term η interpolates between the phase-sensitive and phase-insensitive gain where $\eta = 1$ corresponds to complete phase-insensitive gain. g is the overall gain factor, which has to be large enough to operate above the threshold which in turn is dependent on the loss factor α. The signal envelope of individual OPOs is denoted by a_i, and the graph connectivity is encoded using $J_{i,j}$. The gain saturation term resulting from pump depletion is also included. The potential function $V(x, y)$ is given in eq. 6.2b is used to investigate the linear stability of the Ising fixed points under XY dynamics.

Numerical Findings

We put to test our protocol by investigating the success probability in Mobius ladder type graphs. The Mobius graph connectivity is displayed in Fig. 6.4(a). Although, the Mobius ladder graph is an easy instance [9], it serves as a good testbed since it allows us to compare the performance with previously reported experimental results. We have also verified our protocol with benchmark problems as well as rewired Mobius ladder instances. We explore various annealing routines. The simplest of them is a single annealing schedule between the non-degenerate and degenerate regimes (alternatively the phase-insensitive to phase-sensitive dynamics). Other annealing protocols involve multiple iterations. These protocols are schematically shown in Fig. 6.4(b) and (c), respectively.

We note that the computation in our protocol happens above the oscillation threshold. This is distinct from the convention CIM operation whereby the threshold symmetry breaking is integral to the solution capability of CIMs. We show the results on the Mobius ladder graph for various protocols using the simplified model in Fig. 6.4(d). Figure 6.4(e) shows the corresponding results by taking the full dynamics (governed by coupled partial differential equations) under consideration. We can see the multiple iterations of annealing do help in the success rate albeit at the cost of increased time consumption. Multiple iterations of annealing may be vaguely thought of as shaking the potential landscape multiple times.

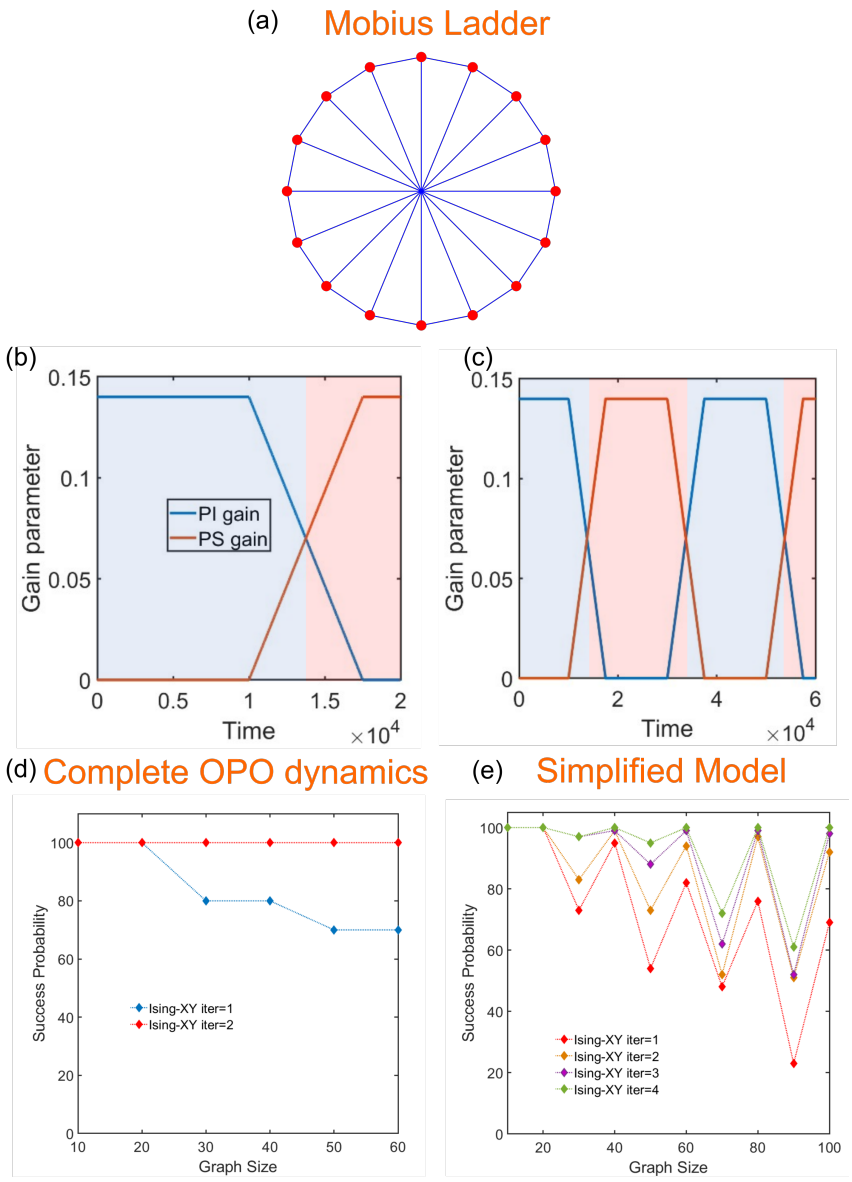

Figure 6.4: **Numerical results on the Mobius ladder graph in various annealing routines.** a) Mobius ladder graph configuration with 16 nodes. Schematic representation of different annealing schedules featuring a single annealing in b) and multiple annealing iterations in c). d) Numerical results for Mobius ladder graph problems using the simplified model and various annealing routines. Probabilities are calculated based on 100 runs of each graph. e) Numerical results for Mobius ladder graph problems using the complete model and various annealing routines. Probabilities are calculated based on 10 runs of each graph.

6.4 Discussion

Our proposed protocol will most likely require an all-optical version of CIM [12]. Measurement-feedback-based optoelectronic architectures [13] may not be able to

faithfully replicate the dynamics around the spectral phase transition. It will be very interesting to investigate the dynamics of the first-order spectral phase transition that occurs in a network of dispersively coupled OPOs [18]. Note that, it has been reported that dispersively coupled OPOs can exhibit dynamics reminiscent of spiking neurons[7]. Based on the simplified model, one may think of an alternative implementation based on phase-insensitive gain provided by gain amplifiers and gradually decreasing the phase-insensitive gain magnitude while increasing the phase-sensitive gain associated with degenerate OPOs. This may allow one to completely get rid of the non-degenerate OPO dynamics. However, one has to take into account that non-degenerate OPO provides ultra-fast phase-insensitive dynamics while a phase-insensitive gain provided by gain amplifiers may not be ultra-fast leading to an undesired coupling between neighboring pulses owing to gain-saturation nonlinearity.

References

[1] Marcello Calvanese Strinati and Claudio Conti. Multidimensional hyperspin machine. *Nature Communications*, 13(1):1–10, 2022.

[2] Gyorgy Csaba and Wolfgang Porod. Coupled oscillators for computing: A review and perspective. *Applied Physics Reviews*, 7(1):011302, 2020.

[3] Sourav Dutta, Abhishek Khanna, Adou S. Assoa, Hanjong Paik, Darrell G. Schlom, Zoltan Toroczkai, Arijit Raychowdhury, and Suman Datta. An Ising Hamiltonian solver based on coupled stochastic phase-transition nano-oscillators. *Nature Electronics*, 4(7):502–512, 2021.

[4] Mikhail Erementchouk, Aditya Shukla, and Pinaki Mazumder. Computational capabilities of nonlinear oscillator networks. *arXiv preprint arXiv:2105.07591*, 2021.

[5] Ryan Hamerly, Takahiro Inagaki, Peter L. McMahon, Davide Venturelli, Alireza Marandi, Tatsuhiro Onodera, Edwin Ng, Carsten Langrock, Kensuke Inaba, Toshimori Honjo, et al. Experimental investigation of performance differences between coherent Ising machines and a quantum annealer. *Science Advances*, 5(5):eaau0823, 2019.

[6] Takahiro Inagaki, Yoshitaka Haribara, Koji Igarashi, Tomohiro Sonobe, Shuhei Tamate, Toshimori Honjo, Alireza Marandi, Peter L. McMahon, Takeshi Umeki, Koji Enbutsu, et al. A coherent Ising machine for 2000-node optimization problems. *Science*, 354(6312):603–606, 2016.

[7] Takahiro Inagaki, Kensuke Inaba, Timothée Leleu, Toshimori Honjo, Takuya Ikuta, Koji Enbutsu, Takeshi Umeki, Ryoichi Kasahara, Kazuyuki Aihara, and Hiroki Takesue. Collective and synchronous dynamics of photonic spiking neurons. *Nature Communications*, 12(1):2325, 2021.

[8] Satoshi Kako, Timothée Leleu, Yoshitaka Inui, Farad Khoyratee, Sam Reifenstein, and Yoshihisa Yamamoto. Coherent ising machines with error correction feedback. *Advanced Quantum Technologies*, 3(11):2000045, 2020.

[9] Kirill P. Kalinin and Natalia G. Berloff. Computational complexity continuum within ising formulation of np problems. *Communications Physics*, 5(1):1–10, 2022.

[10] Kirill P. Kalinin, Alberto Amo, Jacqueline Bloch, and Natalia G. Berloff. Polaritonic XY-Ising machine. *Nanophotonics*, 9(13):4127–4138, 2020.

[11] Timothée Leleu, Yoshihisa Yamamoto, Peter L. McMahon, and Kazuyuki Aihara. Destabilization of local minima in analog spin systems by correction of amplitude heterogeneity. *Physical Review Letters*, 122(4):040607, 2019.

[12] Alireza Marandi, Zhe Wang, Kenta Takata, Robert L. Byer, and Yoshihisa Yamamoto. Network of time-multiplexed optical parametric oscillators as a coherent Ising machine. *Nature Photonics*, 8(12):937–942, 2014.

[13] Peter L. McMahon, Alireza Marandi, Yoshitaka Haribara, Ryan Hamerly, Carsten Langrock, Shuhei Tamate, Takahiro Inagaki, Hiroki Takesue, Shoko Utsunomiya, Kazuyuki Aihara, et al. A fully programmable 100-spin coherent Ising machine with all-to-all connections. *Science*, 354(6312):614–617, 2016.

[14] Naeimeh Mohseni, Peter L. McMahon, and Tim Byrnes. Ising machines as hardware solvers of combinatorial optimization problems. *Nature Reviews Physics*, 4(6):363–379, 2022.

[15] Midya Parto, William Hayenga, Alireza Marandi, Demetrios N. Christodoulides, and Mercedeh Khajavikhan. Realizing spin Hamiltonians in nanoscale active photonic lattices. *Nature Materials*, 19(7):725–731, 2020.

[16] Davide Pierangeli, Giulia Marcucci, and Claudio Conti. Adiabatic evolution on a spatial-photonic Ising machine. *Optica*, 7(11):1535–1543, 2020.

[17] Arkadev Roy, Saman Jahani, Carsten Langrock, Martin Fejer, and Alireza Marandi. Spectral phase transitions in optical parametric oscillators. *Nature Communications*, 12(1):1–9, 2021.

[18] Arkadev Roy, Rajveer Nehra, Carsten Langrock, Martin Fejer, and Alireza Marandi. Non-equilibrium spectral phase transitions in coupled nonlinear optical resonators. *Nature Physics*, pages 1–8, 2023.

[19] Marcello Calvanese Strinati, Leon Bello, Emanuele G Dalla Torre, and Avi Pe'er. Can nonlinear parametric oscillators solve random Ising models? *Physical Review Letters*, 126(14):143901, 2021.

[20] Kenta Takata, Alireza Marandi, Ryan Hamerly, Yoshitaka Haribara, Daiki Maruo, Shuhei Tamate, Hiromasa Sakaguchi, Shoko Utsunomiya, and Yoshihisa Yamamoto. A 16-bit coherent Ising machine for one-dimensional ring and cubic graph problems. *Scientific Reports*, 6(1):1–7, 2016.

[21] Yutaka Takeda, Shuhei Tamate, Yoshihisa Yamamoto, Hiroki Takesue, Takahiro Inagaki, and Shoko Utsunomiya. Boltzmann sampling for an XY model using a non-degenerate optical parametric oscillator network. *Quantum Science and Technology*, 3(1):014004, 2017.

[22] Sri Krishna Vadlamani, Tianyao Patrick Xiao, and Eli Yablonovitch. Physics successfully implements Lagrange multiplier optimization. *Proceedings of the National Academy of Sciences*, 117(43):26639–26650, 2020.

[23] Tianshi Wang and Jaijeet Roychowdhury. Oscillator-based Ising machine. *arXiv preprint arXiv:1709.08102*, 2017.

[24] Zhe Wang, Alireza Marandi, Kai Wen, Robert L. Byer, and Yoshihisa Yamamoto. Coherent Ising machine based on degenerate optical parametric oscillators. *Physical Review A*, 88(6):063853, 2013.

[25] Atsushi Yamamura, Hideo Mabuchi, and Surya Ganguli. The random energy landscape of soft-spin networks and its application to combinatorial optimizations. In *APS March Meeting Abstracts*, volume 2022, pages K09–002, 2022.

Chapter 7

NOISE ANALYSIS IN ABOVE-THRESHOLD OPTICAL PARAMETRIC OSCILLATORS

7.1 Abstract

Understanding the noise characteristics in coherent frequency sources is of paramount importance for applications ranging from precision measurements to high-capacity telecommunication. Optical parametric oscillators are a ubiquitous source of coherent radiation providing access to spectral regions that lie outside the gain window of laser sources. Here, we provide a comprehensive description of noise behavior in optical parametric oscillators including the effect of the pump phase noise which constitutes the dominant contribution in most scenarios. We introduce the concept of linewidth enhancement factor in optical parametric oscillators, arising from the intensity-phase coupling analogous to the case of lasers. We extend our analysis to include the case of synchronously pumped oscillators and investigate the fundamental limitations to timing jitter noise. Our formalism provides important insights into the use of optical parametric oscillators as frequency dividers with far-reaching consequences in precision spectroscopy and atomic clock applications.

7.2 Introduction

Low-noise lasers are an important constituent in a multitude of scientific and technological applications, ranging from precision atomic clocks [22, 32], and coherent ranging [26], to high-capacity coherent telecommunication [33]. Lasers without adequate phase-noise suppression often contribute to infidelities in quantum computing protocols that rely on light-matter interactions [7]. There are significant ongoing efforts in realizing integrated low-phase noise lasers that promise to unlock a lot of opportunities involving coherent optical systems [21, 44]. While the phase noise of lasers dictates the performance of coherent communication systems, the relative intensity noise (RIN) determines the performance metrics of direct detection-based protocols.

The fundamental limit of laser phase noise arises due to the presence of unavoidable vacuum fluctuations and is dictated by the celebrated Schawlow-Townes limit [41].

More often than not lasers operate above the aforementioned fundamental limit, and careful consideration of these noise contributions are pivotal for the mitigation of the same. For instance, the linewidth enhancement factor [16, 45] resulting from the intensity-phase crosstalk in the context of semiconductor lasers represents an additional source of noise beyond the fundamental limit. Several techniques have been developed over the years to reduce the laser phase noise in the pursuit of reaching close to the fundamental limit. This includes among others the use of external cavities possessing a high-quality factor [44] and detuned cavity operation [46]. Engineering the semiconductor gain medium itself in the form of quantum-dot-based design also aids in achieving a low linewidth enhancement coefficient [42]. The importance of investigating the noise characteristics is also elucidated in the fact that one can extract the relevant device parameters from noise measurements [11]. Phase noise of lasers also impacts the spectral purity of the optically generated radio-frequency signals and investigating the noise transfer characteristics is key to the design of optimal microwave-photonic systems [29].

Lasers however span a limited spectral window depending on the bandwidth of the constituent gain medium. For accessing coherent radiation outside the typical spectral window where lasers operate, one has to rely on nonlinear optical sources. Optical parametric oscillators (OPOs) based on second-order nonlinear optical medium have been the mainstay for accessing tunable coherent radiation in these unconventional spectral bands extending into the mid-infrared [9, 23, 38]. Understanding the noise characteristics of OPOs is therefore of paramount interest which will not only allow us to probe the fundamental limits of intensity and phase noise but also to engineer the device design in order to minimize the same. Most of the prior theoretical works that considered the noise behavior of OPOs have focused only on the quantum noise source arising from vacuum fluctuations [6, 10, 13, 48]. This however neglects the contribution of pump phase noise which represents the dominant contribution of parametrically driven sources in practice [5, 12, 19, 30, 47]. Apart from the continuous mode of operation, lasers operating in pulsed mode, i.e., the mode-locked lasers have their own associated nose characteristics that also include the timing jitter/ repetition rate fluctuations [15, 34]. Noise analysis of these pulsed sources is crucial for optimizing the performance of frequency combs [2, 25, 28]. The pulsed counterpart in OPOs appears in the context of synchronous pumping [14, 39]. There is a lack of analytical studies that investigates the noise behavior in synchronously pumped OPOs. We develop a comprehensive noise formalism for OPOs operating above

the oscillation threshold. We consider different regimes of OPO operation ranging from degeneracy to non-degeneracy which includes both the doubly-resonant and singly-resonant cases. We introduce the analogous linewidth enhancement factor in OPOs arising from the phase-mismatched operation. We develop the noise analysis for synchronously-pumped OPOs and highlight the role of the group-velocity mismatch parameter that is unique to OPOs and does not arise in the context of mode-locked lasers. Our results provide crucial insights and design guidelines for engineering OPOs in the landscape of trade-offs comprising conversion efficiency, linewidth, and oscillation threshold thereby informing the development of next-generation integrated parametric oscillator-based devices.

7.3 Results

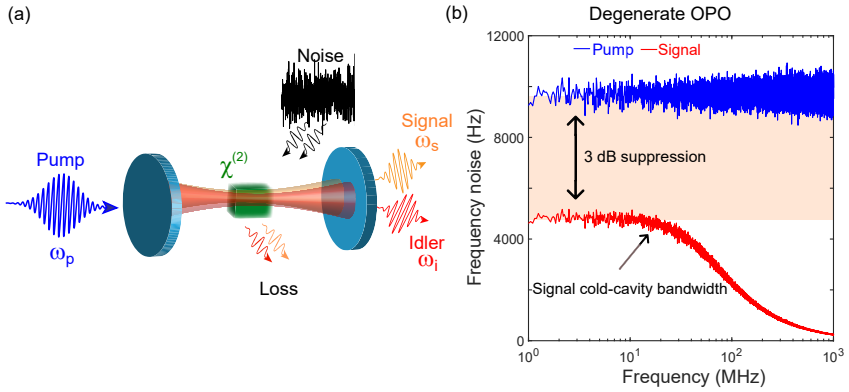

Figure 7.1: **Phase noise of optical parametric oscillators operating above-threshold.** a) Schematic of an optical parametric oscillator consisting of a $\chi^{(2)}$ nonlinear medium that facilitates the parametric interaction between the pump, signal, and the idler waves. Noise enters the system from both the drive and the dissipation. b) Phase noise spectrum of a degenerate OPO showing the 3 dB reduction in the phase noise compared to the pump. The low-pass filtering effect arising due to the cold-cavity linewidth is also apparent.

The schematic of the OPO device is shown in Fig. 7.1(a). The OPO consists of a second-order nonlinear medium placed inside a cavity that is parametrically driven by a pump (at frequency ω_p). The nonlinear medium can be engineered to phase-match parametric interactions either at degeneracy (signal photons with frequency $\omega_s = \omega_p/2$) or at non-degeneracy (signal photons with frequency ω_s and idler photons with frequency ω_i, such that $\omega_s + \omega_i = \omega_p$). The noise introduced in the system is contributed both by quantum vacuum fluctuations (associated with various dissipation mechanisms) and by the noise contained in the driving laser. In some cases, the driving pump can also be derived from another OPO as well [27].

We note that here we neglect noise contributions resulting from thermomechanical, photorefractive effects, etc.. that operate on a slow-time scale, and the effects of which can be eliminated via active feedback [17].

We begin by analyzing the case of OPOs operating in the continuous mode.

$$\frac{da}{dt} = -\alpha a + \mathrm{i}\Delta a + \kappa b a^{*} \tag{7.1}$$

where a and b denote the complex envelope of the signal and pump fields, respectively, such that $|a|^2$ represents the signal photon number and t is normalized with respect to the cavity roundtrip time (T_R). The other parameters are the intra-cavity loss (α), and the detuning (Δ) for the resonant signal, while κ is the effective nonlinear coupling coefficient. κ can be expressed in terms of the second-harmonic efficiency (η expressed in units of $\mathrm{W}^{-1}\mathrm{mm}^{-2}$) as $\kappa = \sqrt{\frac{2hf\eta}{T_R}}L$, where L is the length of the parametric interaction region (in mm), h is the Planck's constant, and f is the frequency of the signal photon. We consider the pump to be non-resonant and its dynamics can be adiabatically eliminated to obtain the approximate expression for the pump field as: $b = F\mathrm{e}^{\mathrm{i}\psi} - \frac{\kappa}{2}a^2$. Here, F is the strength of the driving pump and ψ is its instantaneous phase. Substituting this in Eq. 7.1, and expanding the complex signal field envelope as $a = \sqrt{n}\mathrm{e}^{\mathrm{i}\theta}$, where n represents the intracavity signal photon number, and θ is the phase corresponding to the signal field, we obtain:

$$\frac{dn}{dt} = -2\alpha n + 2\kappa F n\cos(\psi - 2\theta) - \kappa^2 n^2 + 2\sqrt{D_1 n}\xi_1(t) \tag{7.2a}$$

$$\frac{d\theta}{dt} = \Delta + \kappa F\sin(\psi - 2\theta) + \sqrt{\frac{D_1}{n}}\xi_2(t) \tag{7.2b}$$

$$\frac{d\psi}{dt} = \sqrt{D_p}\xi_3(t) \tag{7.2c}$$

where $\xi_i(t)$ $i \in \{1, 2, 3\}$ are zero mean, unity variance random gaussian noise, and the correlation between these fluctuations satisfies $< \xi_i(t)\xi_j(t^{'}) >= \delta_{i,j}\delta(t - t^{'})$. The diffusion coefficient corresponding to the dissipation experienced by the resonant signal is given by $D_1 = 2\alpha$ [4], and the diffusion coefficient (D_p) related to the pump phase noise is related as $D_p = \Delta\omega_p$, where $\Delta\omega_p$ is the linewidth of the driving pump laser. We have assumed the pump phase as a reference. We have ignored the pump intensity noise, whose effect on the OPO linewidth is of higher order and can also be incorporated into our formalism. The OPO signal at

degeneracy experiences sub-harmonic entrainment as revealed by Eq. 7.2b, which bears resemblance with the Adler equation of injection locking, albeit in this case the signal is locked to its harmonic. This leads to a 3 dB suppression of OPO phase noise (or 6 dB in terms of power spectral density) compared to the pump as shown in Fig. 7.1(b). The roll-off at higher frequencies is attributed to the low-pass filtering effect of the cold cavity.

The pump non-resonant design is less constrained than the triply-resonant scenario (all three waves signal, idler, and the pump are resonant) [1] and is more amenable towards wider tunability and higher stability [23, 24, 38]. The doubly-resonant case for a non-degenerate OPO involves both the resonant signal and the idler and the equations governing the dynamics are described in the supplementary section 7.5.1. Distinct from the degenerate case, the signal and the idler waves diffuse randomly with characteristic diffusion coefficients and correlation properties, assuming the pump is noiseless (see supplementary section 7.5.4). The signal and the idler phases remain anti-correlated and the sum of their phases can be a squeezed observable. In the presence of a noisy pump, the pump noise gets transferred to the signal and the idler waves and is distributed according to their respective losses (see supplementary section 7.5.4). This can be expressed as: $\frac{\nu_s}{\nu_i} = \frac{\alpha_s^2}{\alpha_i^2}$, where ν_s and ν_i are the signal and idler linewidth, respectively, and α_s and α_i are their corresponding losses. This is depicted in Fig. 7.2(a). Figure 7.2(b) shows an evolution of the instantaneous frequencies for the signal and idler waves. The singly-resonant case, whereby only the signal is resonant, can be considered the extreme version of the doubly-resonant scenario. Here, $\alpha_i >> \alpha_s$, leading to the pump noise getting transferred entirely to the non-resonant idler, leaving behind the resonant signal which is unaffected by the pump noise [5]. The resonant signal follows phase-insensitive gain dynamics akin to lasers and is subject to fundamental noise-limited performance dictated by Schawlow-Townes linewidth [41] (see supplementary section 7.5.2). The continuum which represents a gradual transition from the doubly-resonant to the singly-resonant mode of operation is shown in Fig. 7.2(c). Thus singly-resonant OPO-based design provides an attractive solution to realize widely tunable sources of ultra-coherent radiation starting from a noisy near-infrared source. As shown in Fig. 7.2(d), when the idler is much lossier than the signal (emulating a close to singly-resonant scenario) the pump noise can be almost entirely transferred to the non-resonant idler leaving behind the resonant signal that experiences low phase noise. This may open

exciting possibilities for applications demanding tunable narrow-width coherent light sources in the mid-infrared. A caveat to be noted in this context is that the threshold for singly-resonant OPOs is considerably higher than their doubly-resonant counterparts.

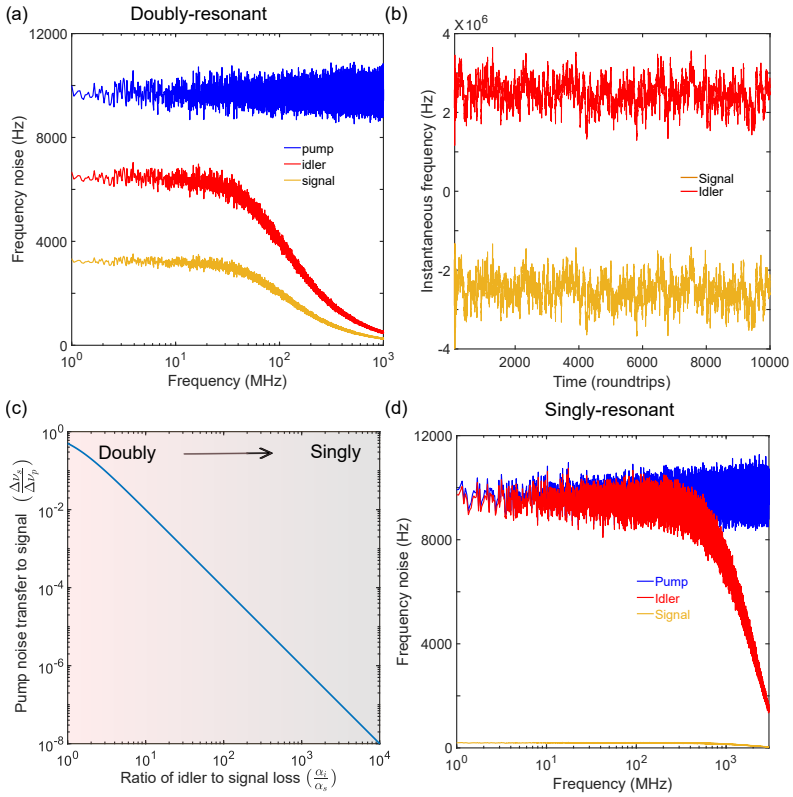

Figure 7.2: **Phase noise characteristics of a non-degenerate OPO** a) Phase noise spectrum in the doubly-resonant scenario where the pump noise is distributed between the signal and the idler waves according to their corresponding loss coefficients. Parameters used are: $\alpha_i = 2\alpha_s$ and cold-cavity linewidth for the signal and pump are 10 MHz and 10 KHz, respectively, b) The evolution of the instantaneous frequency of the signal and the idler showing their anti-correlation. c) The non-degenerate OPO transitions from doubly-resonant to singly-resonant as the loss corresponding to the idler component increases. Less proportion of the pump noise is transferred to the signal as the OPO becomes more singly-resonant like, d) Phase noise spectrum in an extreme doubly-resonant scenario (resembling a singly-resonant case) where the pump noise is mostly transferred to the idler, leaving behind a low-phase noise resonant signal component. Parameters used are: $\alpha_i = 50\alpha_s$ and cold-cavity linewidth for the signal and pump are 10 MHz and 10 KHz, respectively.

We explore the origin of an analogous linewidth-enhancement factor in the context

of OPOs. We consider a degenerate OPO with a slight phase-mismatch (η). The phase dynamics of the doubly-resonant degenerate OPO, in this case, is modified as (see supplementary section 7.5.3):

$$\frac{d\theta}{dt} = \kappa F \mathrm{sinc}\left(\frac{\eta}{2}\right)\sin(\psi - 2\theta) + \Delta + \underbrace{\kappa^2 \frac{1-\mathrm{sinc}(\eta)}{\eta} n}_{\text{Amplitude-phase coupling}} + \sqrt{\frac{D}{n}}\xi_2. \quad (7.3)$$

We can identify the appearance of an effective Kerr-like term in the dynamics [31]. This induces a coupling between the intensity and the phase of the OPO signal which contributes to the excess phase noise. This excess phase noise that arises in phase-mismatched OPOs is highlighted in Fig. 7.3(a).

Similar to lasers, the phase fluctuations in the OPO signal are suppressed by the corresponding intra-cavity photon number as can be seen from the dynamics in Eq. 7.2b. Thus the OPO signal linewidth can be significantly smaller than the OPO cold-cavity linewidth corresponding to the signal frequency. Apart from the instances either involving very low intra-cavity photon numbers or ultra-low linewidth of the pump laser, the OPO phase noise will be primarily dominated by the classical phase noise in the pump over the quantum fluctuations. Their relative contribution in the case of a non-degenerate OPO is highlighted in Fig. 7.3(b). The variation of the OPO conversion efficiency and the phase noise behavior as a function of the number of times above the threshold is depicted in Fig. 7.3(c). We can identify that while the OPO external efficiency is maximized at 4 times above the threshold, the linewidth diverges at the threshold.

We now proceed to analyze the noise behavior of synchronously pumped OPOs which is schematically represented in Fig. 7.4(a). Here, in contrast to the CW case, the OPO is driven by a periodic pump pulse sequence, where the pump repetition rate closely matches the cavity free spectral range [14, 39]. The dynamics of a sync-pumped OPO resemble that of an active mode-locked laser where the periodic pump provides an external reference for the temporal location of the OPO signal pulses along the fast time scale. This can be analytically described by an equivalent gain-clipping function that defines a temporal gain window within which the OPO pulses can oscillate [14, 39] (see Fig. 7.4(b)). We analyze the timing-jitter performance of sync-pumped OPOs that is limited by quantum fluctuations (see supplementary section 7.5.7). While deriving the results we

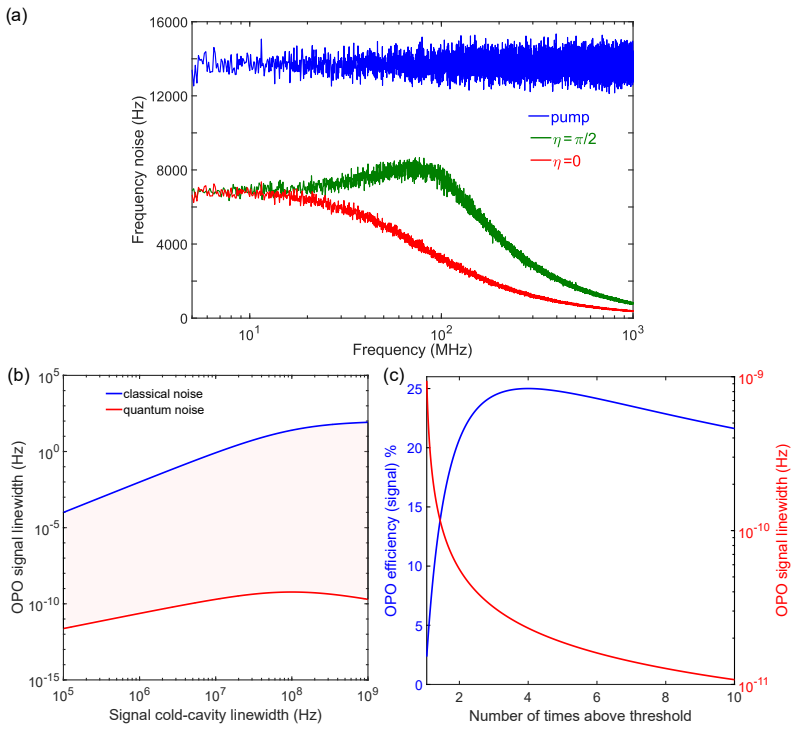

Figure 7.3: **Linewidth enhancement in OPOs and scaling properties of OPO phase noise.** a) Enhanced phase noise in a phase-mismatched ($\eta = \frac{\pi}{2}$) degenerate OPO as compared to a phase-matched one ($\eta = 0$), b) Scaling of quantum-limited (only considering fluctuations from dissipation) OPO linewidth and classically (considering a noisy pump) imposed OPO linewidth as a function of cold-cavity linewidth corresponding to the signal. The OPO is assumed to be maintained at 4 times above the threshold throughout. It highlights the dominance of classical noise contribution even assuming a pump with 100 Hz linewidth, c) Scaling of the OPO output efficiency and the quantum-limited OPO linewidth as a function of the number of times above threshold operation. While the OPO external efficiency is maximized at 4 times above the threshold, the linewidth diverges at the threshold and monotonically decreases.

assumed a noiseless pump both in terms of the phase noise and the repetition rate noise. The timing jitter is related to the dynamics of the centroid of the OPO pulse (see supplementary equation 7.13b). We can identify the presence of a restoring force arising from the gain-clipping mechanism akin to active mode-locking [18, 35]. Thus we can draw a parallel between the terms $\frac{3\tau^2}{4T_p}\ln(G_0)\tanh\left(\frac{T}{\tau}\right)$ and $\frac{\pi^2}{4}M\omega_M^2\tau^2T$ that arise in the context of sync-pumped OPOs and active mode-locked lasers, respectively. Here, τ, T refers to the pulse width and the centroid, respectively, T_p denotes the pump pulse width, M, ω_M describes the modulation index and the modulation frequency in the context of a mode-locked

laser, and G_0 is related to the OPO roundtrip loss. The existence of this restoring force arising due to the gain-clipping prevents the OPO pulse from drifting away from the gain-clipping region which is manifested by the absence of divergent behavior of the timing-jitter power spectral density (Fig. 7.4(c)) at low frequencies in stark contrast with passively mode-locked laser. The group-velocity-mismatch (GVM) parameter is unique to OPOs since it involves parametric interaction between waves with disparate frequencies [39]. GVM can be engineered to facilitate the exotic case of incoherently pumped OPO operation, whereby all the pump noise is dumped in the idler and a coherent signal ensues [36]. We investigate the effect of varying this GVM parameter on the timing jitter spectral density as shown in Fig. 7.4(c). Although an increase in the walk-off parameter can potentially allow the generation of ultra-short pulses starting with longer (picosecond scale) pump pulses [39], it also broadens the gain-clipping window [14] which results in the enhanced timing-jitter spectral density at low frequencies. Similarly, we also study the effect of increasing the pump power on the timing jitter (Fig. 7.4(d)), and the observed behavior can be explained by the dependence of the width of the gain-clipping window on the number of times above the threshold parameter.

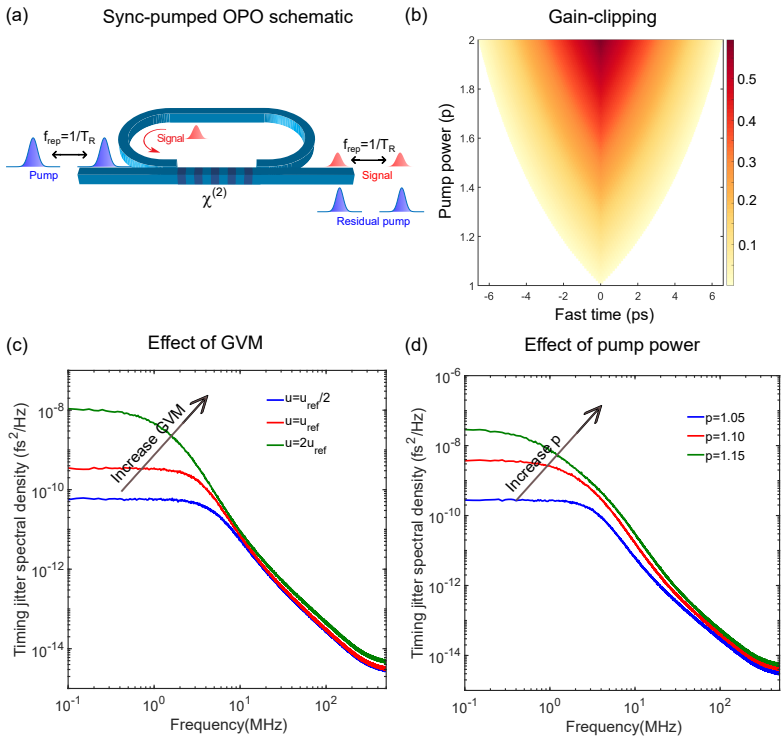

Figure 7.4: **Noise behavior of a synchronously-pumped OPO** a) Schematic of a doubly resonant sync-pumped OPO showing that the system is driven by a periodic train of pulses, b) Gain-clipping, i.e., the temporal gain window function for a sync-pumped OPO. The temporal width of the gain window increases with pump power, c) The timing jitter power spectral density for a sync-pumped OPO shows the flattening of the noise spectral density curve at low frequencies. This behavior akin to active mode-locked lasers arising from the restoring force prevents the divergence of fluctuations related to the pulse centroid at long times. Also highlighted is the variation of the jitter spectral density curves as a function of changing GVM parameter (u). The trend is attributed to the widening of the gain-clipping window with increasing GVM parameter, d) Dependence of the jitter spectral density curves as a function of changing pump power (parameter p represents the number of times above threshold).

7.4 Discussion

Nonlinear dynamical systems with parametric nonlinearity and featuring phase-sensitive gain can be deployed for highly sensitive sensing [8, 37]. These systems have to be engineered to maximize the signal-to-noise ratio to reap the benefits of enhanced sensitivity. Our OPO noise analysis can be extended to these systems consisting of a network of OPOs [40]. It will also be interesting to explore the case of a more complex and enriched noise phenomenon involving non-markovianity and structured noise [3]. Our formalism can be easily modified to encompass the case of

$\chi^{(3)}$-based OPO [43]. Understanding the noise characteristics in wavelength-scale OPOs [20] and their unique behaviors is also an exciting direction to pursue [49]. The noise characteristics investigated above for the intra-cavity field can be extended to the output field depending on the specific coupling configuration (add-through or add-drop types) [4].

7.5 Supplementary

7.5.1 Doubly-resonant non-degenerate OPO

$$\frac{dn_s}{dt} = -2\alpha_s n_s + 2\kappa_1 F\sqrt{n_s n_i}\cos(\psi - \theta_s - \theta_i) - \kappa_1\kappa_3 n_s n_i + 2\sqrt{n_s D_s}\xi_1 \tag{7.4a}$$

$$\frac{dn_i}{dt} = -2\alpha_i n_i + 2\kappa_2 F\sqrt{n_s n_i}\cos(\psi - \theta_s - \theta_i) - \kappa_2\kappa_3 n_s n_i + 2\sqrt{n_i D_i}\xi_2 \tag{7.4b}$$

$$\frac{d\theta_s}{dt} = \Delta_s + \kappa_1 F\sqrt{\frac{n_i}{n_s}}\sin(\psi - \theta_s - \theta_i) + \sqrt{\frac{D_s}{n_s}}\xi_3 \tag{7.4c}$$

$$\frac{d\theta_i}{dt} = \Delta_i + \kappa_2 F\sqrt{\frac{n_s}{n_i}}\sin(\psi - \theta_s - \theta_i) + \sqrt{\frac{D_i}{n_i}}\xi_4 \tag{7.4d}$$

where n_s and n_i represent photon numbers corresponding to the signal and idler fields, respectively. θ_s and θ_i denote the phase of the signal and the idler fields, respectively. The respective loss coefficients are α_s and α_i, and the detunings from the cold-cavity resonances are given by Δ_s and Δ_i, which in general is different because of the presence of group velocity dispersion of the resonant medium. The frequencies of the signal, idler, and pump photons are represented as f_1, f_2, and f_3, respectively. The effective nonlinear coefficients are $\kappa_1 = \sqrt{\frac{hf_3f_2\eta}{f_1T_R}}L$, $\kappa_2 = \sqrt{\frac{hf_3f_1\eta}{f_2T_R}}L$, and $\kappa_3 = \sqrt{\frac{hf_1f_2\eta}{f_3T_R}}L$, where η is the sum-frequency generation efficiency of the signal and idler photons into pump photons.

where $\xi_i(t)$ $i \in \{1, 2, 3, 4\}$ are zero mean, unity variance random gaussian noise, and the correlation between these fluctuations satisfies $< \xi_i(t)\xi_j(t') >= \delta_{i,j}\delta(t-t')$. The diffusion coefficient corresponding to the dissipation experienced by the resonant signal and the resonant idler is given by $D_s = 2\alpha_s$ and $D_i = 2\alpha_i$, respectively.

7.5.2 Singly-resonant non-degenerate OPO

The doubly-resonant case reduces to the singly-resonant one when the idler is non-resonant. Assuming, $\alpha_i >> \alpha_s$, the dynamics of the idler can be adiabatically

eliminated. The above governing equations can then be approximated for the signal field as:

$$\frac{dn_s}{dt} = -2\alpha_s n_s + \frac{2\kappa_1\kappa_2|F|^2 n_s}{\alpha_i + \kappa_2\kappa_3 n_s} - \frac{2\kappa_1\kappa_3\kappa^2|F|^2 n_s^2}{(\alpha_i + \kappa_2\kappa_3 n_s)^2} + 2\sqrt{n_s D_s}\xi_1 \tag{7.5a}$$

$$\frac{d\theta_s}{dt} = \Delta_s + \sqrt{\frac{D_s}{n_s}}\xi_2. \tag{7.5b}$$

For more accurate modeling of the dynamics of singly-resonant OPOs, one can refer to the formalism in reference [43].

7.5.3 Phase-mismatch and effective $\chi^{(3)}$

Phase mismatch can arise due to residual momentum mismatch between the participating waves in the nonlinear process along with the contribution of the periodic poling. We represent the phase-mismatch parameter as $\eta = \Delta k L$, where Δk is the momentum mismatch and L is the length of the parametric interaction region.

The evolution equation for the signal field in the presence of phase-mismatch (considering the degenerate case where the pump is non-resonant) is given by Eq. 7.6a [31]:

$$\frac{da}{dt} = -\alpha a + \mathrm{i}\Delta a + \kappa F \mathrm{e}^{\mathrm{i}\psi}\mathrm{sinc}\left(\frac{\eta}{2}\right)a^* - \underbrace{\frac{\kappa^2}{4}\mathrm{sinc}^2\left(\frac{\eta}{2}\right)|a|^2 a}_{\text{effective TPA coefficient}} + \underbrace{\mathrm{i}\kappa^2\frac{1-\mathrm{sinc}\,(\eta)}{\eta}|a|^2 a}_{\text{effective Kerr coefficient}} \tag{7.6a}$$

$$\frac{dn}{dt} = -2n\alpha + 2n\kappa F\cos(\psi - 2\theta)\mathrm{sinc}\left(\frac{\eta}{2}\right) - \frac{\kappa^2}{2}\mathrm{sinc}^2\left(\frac{\eta}{2}\right)n^2 + 2\sqrt{nD}\xi_1 \tag{7.6b}$$

$$\frac{d\theta}{dt} = \kappa F\mathrm{sinc}\left(\frac{\eta}{2}\right)\sin(\psi - 2\theta) + \Delta + \underbrace{\kappa^2\frac{1-\mathrm{sinc}(\eta)}{\eta}n}_{\text{Amplitude-phase coupling}} + \sqrt{\frac{D}{n}}\xi_2. \tag{7.6c}$$

The phase-mismatch gives rise to the effective Kerr co-efficient ($\kappa^2\frac{1-\mathrm{sinc}(\eta)}{\eta}$) and a modified two-photon absorption (TPA) loss term ($\frac{\kappa^2}{4}\mathrm{sinc}^2\left(\frac{\eta}{2}\right)$). The effective Kerr-coefficient leads to coupling between the intensity and the phase variables as shown in Eq. 7.6b and 7.6c. This is responsible for the additional linewidth broadening in the presence of phase-mismatch.

7.5.4 Validation of the numerical simulation

The noise in OPO is a result of the contribution from the pump noise as well as the quantum fluctuations accompanying the linear losses. To understand different regimes where either of these noise sources dominates we decouple these noise sources and study the OPO noise behavior for doubly-resonant non-degenerate OPO:

In the limit of zero pump phase noise

Here we assume a noiseless pump and only consider noise from dissipation-induced fluctuations. This will define the fundamental limit of OPOs driven by classical pump sources. The signal and the idler phases will diffuse randomly with characteristic diffusion coefficients, where the corresponding spectral linewidths are expressed in Eq. 7.7a and Eq. 7.7b, respectively [6, 12, 48]. This agrees with the results of our numerical simulation as shown in Fig. 7.5(a).

$$\Delta\nu_s = \frac{\alpha_i^2}{(\alpha_s+\alpha_i)^2}\frac{\alpha_s}{n_s} \tag{7.7a}$$

$$\Delta\nu_i = \frac{\alpha_s^2}{(\alpha_s+\alpha_i)^2}\frac{\alpha_i}{n_i} \tag{7.7b}$$

While the signal and the idler phases diffuse randomly, they are not independent and their cross-correlation is given by Eq. 7.8 [48]. This agrees with the results of our numerical simulation as shown in Fig. 7.5(b).

$$D_{s,i} = 2\frac{(\alpha_s\alpha_i)^{\frac{3}{2}}}{(\alpha_s+\alpha_i)^2}\frac{1}{\sqrt{n_s n_i}} \tag{7.8}$$

Above the threshold, the intensity of the signal and idler waves (doubly-resonant OPO), satisfies $\alpha_s n_s = \alpha_i n_i$. Therefore we have $\Delta\nu_s \simeq \Delta\nu_i$.

In the limit of neglecting dissipation-induced fluctuations, i.e., only pump noise

Next, we hypothetically assume the absence of dissipation-induced fluctuation, i.e., $D_s = D_i = 0$ in Eq. 7.4. In this limit, only the pump phase noise related to the pump linewidth ($\Delta\nu_p$) contributes to the OPO phase noise. The spectral linewidth of the

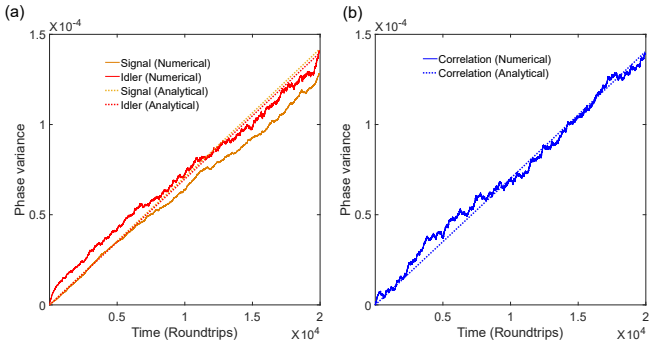

Figure 7.5: **Quantum-limited phase diffusion of non-degenerate OPO assuming no pump-noise.** a) Variance of the phase noise for the signal and the idler waves in a non-degenerate OPO. Parameters used are: cold-cavity linewidth for the signal and idler are 1 and 2.5 MHz respectively. b) Correlation between the phases of the signal and the idler waves.

signal and the idler waves in this limit is given by Eq. 7.9a and 7.9b, respectively [12].

$$\Delta\nu_s = \Delta\nu_p \frac{\alpha_s^2}{(\alpha_s + \alpha_i)^2} \tag{7.9a}$$

$$\Delta\nu_i = \Delta\nu_p \frac{\alpha_i^2}{(\alpha_s + \alpha_i)^2} \tag{7.9b}$$

Here, we have $\frac{\Delta\nu_s}{\Delta\nu_i} = \frac{\alpha_s^2}{\alpha_i^2}$. Thus, more phase noise is transferred from the pump to the wave experiencing larger intra-cavity loss. The extreme limit is the singly-resonant case where the idler is almost non-resonant and therefore the bulk of the pump phase noise is dumped in the non-resonant idler leaving the signal unaffected [5]. This agrees with the results of our numerical simulation as shown in Fig. 7.6(a). The limit for the degenerate OPO can be obtained by assuming $\alpha_s = \alpha_i = \alpha$. The agreement between the numerical simulation and the analytical results for a degenerate OPO is shown in Fig. 7.6(b).

7.5.5 Transition in the noise characteristics between degenerate and non-degenerate (doubly-resonant) OPOs in the limit of zero pump phase noise

If we assume the absence of classical noise sources (pump noise, etc.), and only consider the noise that is entering the system to be of quantum origin (dissipation-induced fluctuations) that will determine the fundamental limit when driving the OPO with a classical pump. In this limit of operation for a

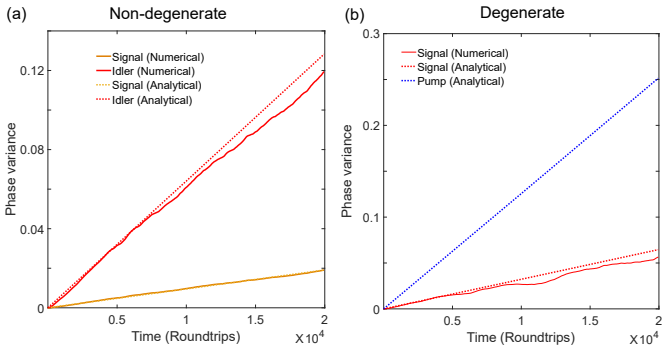

Figure 7.6: **Phase diffusion of OPOs in the presence of noisy pump and assuming no noise contributions from dissipation.** a) Variance of the phase noise for the signal and the idler waves in a non-degenerate OPO. Parameters used are: cold-cavity linewidth for the signal and idler are 1 and 2.5 MHz, respectively. b) Variance of the phase noise for the degenerate OPO, highlighting a factor of 4 reductions in the slope (diffusion coefficient) of the random walk. Parameters used are: pump linewidth 10 KHz.

non-degenerate OPO, the signal and idler will diffuse randomly with a defined correlation that is governed by equations 7.7 and 7.8. However, in the case of degenerate OPO, owing to the subharmonic locking the signal will not diffuse randomly and in turn, will be locked to the pump. Since we assumed the pump to be noiseless, the degenerate signal will also follow likewise. This hypothetical scenario is depicted in Fig. 7.7(b). This is contrasted with the behavior of the non-degenerate OPO that still exhibits random walk even in the presence of a noiseless pump which is shown in Fig. 7.7(a).

The expressions that are used to generate the plots in Fig. 7.3 are presented below. The quantum-limited OPO signal linewidth (assuming no classical pump noise) is given by:

$$\Delta\nu_s = \frac{\alpha_s\alpha_i}{(\alpha_s+\alpha_i)^2}\frac{\kappa^2}{2(\sqrt{N}-1)} \tag{7.10}$$

where N is the number of times above the threshold (in terms of power) operation. We have assumed that the non-degenerate OPO is near-degenerate so that we can assume $\kappa_1 \simeq \kappa_2 \simeq \kappa$, and $\omega_s \simeq \omega_i \simeq \frac{\omega_p}{2}$. Relaxing these simplifications will make the expressions more complicated, but the qualitative trend will remain similar.

The expression for the OPO signal efficiency (outside the cavity) is given by:

$$\eta_{eff} = \frac{\sqrt{N} - 1}{N}. \tag{7.11}$$

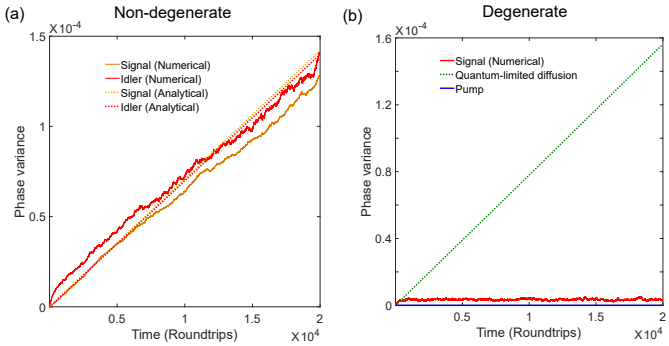

Figure 7.7: **Phase diffusion of OPOs in the presence of noiseless pump.** a) Variance of the phase noise for the signal and the idler waves in a non-degenerate OPO. b) Variance of the phase noise for the signal in the degenerate case.

7.5.6 Relative Intensity Noise

The relative intensity noise of the OPO which captures the power fluctuations is shown in Fig. 7.8. Note that we have ignored the intensity noise in the pump.

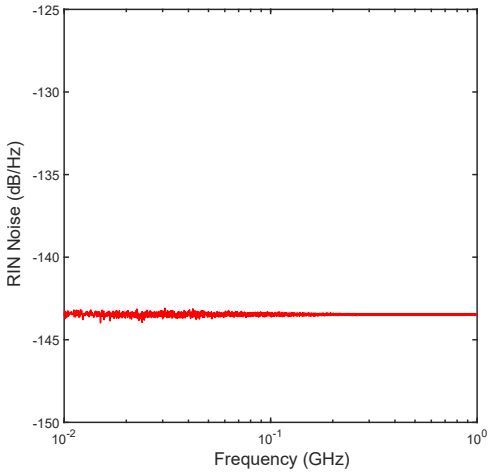

Figure 7.8: **RIN noise spectrum for a degenerate OPO.**

7.5.7 Synchronously pumped OPO dynamics including Noise terms

We add the effect of noise by modifying the derivation in section 2.5.2 as:

$$a^{n+1}(0,t) = \mathcal{F}^{-1}\left[G_0^{-\frac{1}{2}} \exp^{-i\phi} \mathcal{F}\left[a_\omega^n(L,t)\right]\right] + F(t) \tag{7.12}$$

where F(t) is the noise term and is given by $\left\langle F(t)F(t^{'})\right\rangle = \frac{(1-\frac{1}{G_0})^{\frac{1}{2}}T_R}{dt}\delta(t-t^{'})$. Here, T_R is the cavity roundtrip time, and dt is the temporal resolution of the fast-time window. We describe the diffusion coefficient as $D = \frac{(1-\frac{1}{G_0})^{\frac{1}{2}}T_R}{dt}$ for brevity. Projecting the noise term into the space of the pulse parameters we get:

$$\frac{dA}{dn} = \left[\frac{p-1}{2}\ln(G_0) - \frac{\ln(G_0)}{2T_p}\ln\left[2\cosh\left(\frac{T}{\tau}\right)\right]\tau - \frac{1}{3}\frac{\phi_2^{'}\tan(\pi l)}{2\tau^2}\right]A - \frac{7}{15}\frac{\left(\phi_2^{'}\sec(\pi l)\right)^2}{8\tau^4}A - \beta A^3 + F_A \quad (7.13a)$$

$$\frac{dT}{dn} = \frac{\lambda_a l}{2c} - \tau\beta A^2 - \frac{3\tau^2}{4T_p}\ln(G_0)\tanh\left(\frac{T}{\tau}\right) + F_T \quad (7.13b)$$

$$\frac{d\tau}{dn} = \frac{18}{3+\pi^2}\frac{\ln(G_0)}{2T_p}\left[\frac{T}{\tau}\tanh\left(\frac{T}{\tau}\right) - \ln\left[2\cosh\left(\frac{T}{\tau}\right)\right]\right]\tau^2 + \frac{12}{3+\pi^2}\frac{\phi_2^{'}\tan(\pi l)}{2\tau} + \frac{168}{5(3+\pi^2)}\frac{\left(\phi_2^{'}\sec(\pi l)\right)^2}{8\tau^3} + F_\tau \quad (7.13c)$$

where the correlation properties of the projected noise terms are expressed as:

$$< F_A(t)F_A(t^{'}) >= D\delta(t-t^{'}) \quad (7.14a)$$

$$< F_T(t)F_T(t^{'}) >= \frac{\tau^2}{3A^2}D\delta(t-t^{'}) \quad (7.14b)$$

$$< F_\tau(t)F_\tau(t^{'}) >= \frac{2\tau^2}{A^2}\frac{18}{3+\pi^2}D\delta(t-t^{'}) \quad (7.14c)$$

$$< F_i(t)F_j(t^{'}) >= 0 \text{ for } i \neq j. \quad (7.14d)$$

These noise dynamics are derived by only taking into consideration the quantum-limited performance, i.e., the contribution from the dissipation-induced fluctuations. We have assumed the pump is noiseless. In practice, there will be repetition rate noise of the sync-pump arising due to the phase noise in the microwave oscillator to which it is entrained. Additionally, it will also possess phase noise/ carrier-envelope offset noise. We have also neglected the presence of cavity length fluctuations which in principle can be compensated using an active servo-locking mechanism.

We present the results obtained numerically for the timing jitter power spectral density in Fig. 7.9(a). The numerical simulation is performed using the split-step Fourier algorithm. Although the results obtained numerically do not match exactly with the semi-analytical model-based results (Fig. 7.9(b)), they agree qualitatively. The most striking feature to note is the flattening of the noise power spectral density curve at low frequencies. This is markedly different from results obtained via numerical simulation for passively mode-locked lasers cases which exhibit divergence at low frequencies. More investigation is needed to establish a close agreement between the two models.

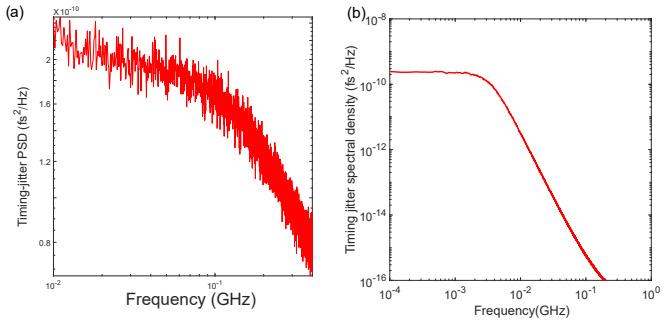

Figure 7.9: **Timing jitter power spectral density for a sync-pumped OPO** obtained a) numerically, b) semi-analytically.

References

[1] Nicolas Amiune, KT Zawilski, PG Schunemann, Karsten Buse, and Ingo Breunig. Pump tuning of a mid-infrared whispering gallery optical parametric oscillator. *Optics Express*, 30(23):41084–41091, 2022.

[2] Chengying Bao, Myoung-Gyun Suh, Boqiang Shen, Kemal Şafak, Anan Dai, Heming Wang, Lue Wu, Zhiquan Yuan, Qi-Fan Yang, Andrey B. Matsko, et al. Quantum diffusion of microcavity solitons. *Nature Physics*, 17(4):462–466, 2021.

[3] Heinz-Peter Breuer, Elsi-Mari Laine, Jyrki Piilo, and Bassano Vacchini. Colloquium: Non-Markovian dynamics in open quantum systems. *Reviews of Modern Physics*, 88(2):021002, 2016.

[4] Yanne K. Chembo. Quantum dynamics of kerr optical frequency combs below and above threshold: Spontaneous four-wave mixing, entanglement, and squeezed states of light. *Physical Review A*, 93(3):033820, 2016.

[5] Yuning Chen, Myles C. Silfies, Grzegorz Kowzan, Jose Miguel Bautista, and Thomas K. Allison. Tunable visible frequency combs from a yb-fiber-laser-pumped optical parametric oscillator. *Applied Physics B*, 125(5):1–8, 2019.

[6] Anatoly S Chirkin. General formula for the natural width of optical parametric oscillator spectral lines. *Laser Physics Letters*, 17(11):115401, 2020.

[7] Matthew .L Day, Pei Jiang Low, Brendan M. White, Rajibul Islam, and Crystal Senko. Limits on atomic qubit control from laser noise. *arXiv preprint arXiv:2112.04946*, 2021.

[8] Roberto Di Candia, Fabrizio Minganti, Kirill V. Petrovnin, Gheorghe S. Paraoanu, and Simone Felicetti. Critical parametric quantum sensing. *arXiv preprint arXiv:2107.04503*, 2021.

[9] Majid Ebrahim-Zadeh and Irina T. Sorokina. *Mid-infrared coherent sources and applications*. Springer Science & Business Media, 2007.

[10] Claude Fabre, E Giacobino, Antoine Heidmann, and Serge Reynaud. Noise characteristics of a non-degenerate optical parametric oscillator-application to quantum noise reduction. *Journal de Physique*, 50(10):1209–1225, 1989.

[11] Irshaad Fatadin, David Ives, and Martin Wicks. Numerical simulation of intensity and phase noise from extracted parameters for cw DFB lasers. *IEEE Journal of Quantum Electronics*, 42(9):934–941, 2006.

[12] Robert Graham. Photon statistics of the optical parametric oscillator including the threshold region. *Zeitschrift für Physik A Hadrons and nuclei*, 211(5): 469–482, 1968.

[13] Robert Graham and Hermann Haken. The quantum-fluctuations of the optical parametric oscillator. i. *Zeitschrift für Physik A Hadrons and nuclei*, 210(3): 276–302, 1968.

[14] Ryan Hamerly, Alireza Marandi, Marc Jankowski, Martin M. Fejer, Yoshihisa Yamamoto, and Hideo Mabuchi. Reduced models and design principles for half-harmonic generation in synchronously pumped optical parametric oscillators. *Physical Review A*, 94(6):063809, 2016.

[15] Herman A Haus and Antonio Mecozzi. Noise of mode-locked lasers. *IEEE Journal of Quantum Electronics*, 29(3):983–996, 1993.

[16] Charles Henry. Phase noise in semiconductor lasers. *Journal of Lightwave Technology*, 4(3):298–311, 1986.

[17] Christopher Hilweg, Danial Shadmany, Philip Walther, Nergis Mavalvala, and Vivishek Sudhir. Limits and prospects for long-baseline optical fiber interferometry. *Optica*, 9(11):1238–1252, 2022.

[18] Dag Roar Hjelme and Alan Rolf Mickelson. Theory of timing jitter in actively mode-locked lasers. *IEEE journal of Quantum Electronics*, 28(6):1594–1606, 1992.

[19] Takeshi Ikegami, Sergey Slyusarev, Shin-ichi Ohshima, and Eiichi Sakuma. Accuracy of an optical parametric oscillator as an optical frequency divider. *Optics Communications*, 127(1-3):69–72, 1996.

[20] Saman Jahani, Arkadev Roy, and Alireza Marandi. Wavelength-scale optical parametric oscillators. *Optica*, 8(2):262–268, 2021.

[21] Warren Jin, Qi-Fan Yang, Lin Chang, Boqiang Shen, Heming Wang, Mark A. Leal, Lue Wu, Maodong Gao, Avi Feshali, Mario Paniccia, et al. Hertz-linewidth semiconductor lasers using cmos-ready ultra-high-Q microresonators. *Nature Photonics*, 15(5):346–353, 2021.

[22] Thomas Kessler, Christian Hagemann, Christian Grebing, Thomas Legero, Uwe Sterr, Fritz Riehle, Michael J. Martin, Long Chen, and Jun Ye. A sub-40-mHz-linewidth laser based on a silicon single-crystal optical cavity. *Nature Photonics*, 6(10):687–692, 2012.

[23] Luis Ledezma, Arkadev Roy, Luis Costa, Ryoto Sekine, Robert Gray, Qiushi Guo, Ryan M. Briggs, and Alireza Marandi. Widely-tunable optical parametric oscillator in lithium niobate nanophotonics. *arXiv preprint arXiv:2203.11482*, 2022.

[24] D Lee and Ngai C. Wong. Stabilization and tuning of a doubly resonant optical parametric oscillator. *Journal of the Optical Society of America B*, 10 (9):1659–1667, 1993.

[25] Fuchuan Lei, Zhichao Ye, Óskar B Helgason, Attila Fülöp, Marcello Girardi, and Victor Torres-Company. Optical linewidth of soliton microcombs. *Nature Communications*, 13(1):1–9, 2022.

[26] Grigory Lihachev, Johann Riemensberger, Wenle Weng, Junqiu Liu, Hao Tian, Anat Siddharth, Viacheslav Snigirev, Vladimir Shadymov, Andrey Voloshin, Rui Ning Wang, et al. Low-noise frequency-agile photonic integrated lasers for coherent ranging. *Nature Communications*, 13(1):1–10, 2022.

[27] Alireza Marandi, Kirk A. Ingold, Marc Jankowski, and Robert L. Byer. Cascaded half-harmonic generation of femtosecond frequency combs in the mid-infrared. *Optica*, 3(3):324–327, 2016.

[28] Andrey B. Matsko and Lute Maleki. On timing jitter of mode locked kerr frequency combs. *Optics Express*, 21(23):28862–28876, 2013.

[29] Andrey B. Matsko and Lute Maleki. Noise conversion in kerr comb rf photonic oscillators. *Journal of the Optical Society of America B*, 32(2):232–240, 2015.

[30] C. D. Nabors, S. T. Yang, Tim Day, and Robert L. Byer. Coherence properties of a doubly resonant monolithic optical parametric oscillator. *Journal of the Optical Society of America B*, 7(5):815–820, 1990.

[31] Mingming Nie and Shu-Wei Huang. Quadratic solitons in singly resonant degenerate optical parametric oscillators. *Physical Review Applied*, 13(4): 044046, 2020.

[32] Eric Oelker, Ross B. Hutson, Colin J. Kennedy, Lindsay Sonderhouse, Tobias Bothwell, Akihisa Goban, Dhruv Kedar, Christian Sanner, John M. Robinson, et al. Demonstration of 4.8× 10- 17 stability at 1 s for two independent optical clocks. *Nature Photonics*, 13(10):714–719, 2019.

[33] Takanori Okoshi. Recent advances in coherent optical fiber communication systems. *Journal of Lightwave Technology*, 5(1):44–52, 1987.

[34] Rudiger Paschotta. Noise of mode-locked lasers (part i): Numerical model. *Applied Physics B*, 79(2):153–162, 2004.

[35] Rüdiger Paschotta. Timing jitter and phase noise of mode-locked fiber lasers. *Optics Express*, 18(5):5041–5054, 2010.

[36] Antonio Picozzi, Carlos Montes, and Marc Haelterman. Coherence properties of the parametric three-wave interaction driven from an incoherent pump. *Physical Review E*, 66(5):056605, 2002.

[37] Arkadev Roy, Saman Jahani, Qiushi Guo, Avik Dutt, Shanhui Fan, Mohammad-Ali Miri, and Alireza Marandi. Nondissipative non-Hermitian dynamics and exceptional points in coupled optical parametric oscillators. *Optica*, 8(3):415–421, 2021.

[38] Arkadev Roy, Luis Ledezma, Luis Costa, Robert Gray, Ryoto Sekine, Qiushi Guo, Mingchen Liu, Ryan M. Briggs, and Alireza Marandi. Visible-to-mid-ir tunable frequency comb in nanophotonics. *arXiv preprint arXiv:2212.08723*, 2022.

[39] Arkadev Roy, Rajveer Nehra, Saman Jahani, Luis Ledezma, Carsten Langrock, Martin Fejer, and Alireza Marandi. Temporal walk-off induced dissipative quadratic solitons. *Nature Photonics*, 16(2):162–168, 2022.

[40] Arkadev Roy, Midya Parto, Rajveer Nehra, Christian Leefmans, and Alireza Marandi. Topological optical parametric oscillation. *Nanophotonics*, 11(8): 1611–1618, 2022.

[41] Arthur L. Schawlow and Charles H. Townes. Infrared and optical masers. *Physical Review*, 112(6):1940, 1958.

[42] Chen Shang, Yating Wan, Jennifer Selvidge, Eamonn Hughes, Robert Herrick, Kunal Mukherjee, Jianan Duan, Frederic Grillot, Weng W. Chow, and John E. Bowers. Perspectives on advances in quantum dot lasers and integration with si photonic integrated circuits. *ACS Photonics*, 8(9):2555–2566, 2021.

[43] Yutaka Takeda, Shuhei Tamate, Yoshihisa Yamamoto, Hiroki Takesue, Takahiro Inagaki, and Shoko Utsunomiya. Boltzmann sampling for an xy model using a non-degenerate optical parametric oscillator network. *Quantum Science and Technology*, 3(1):014004, 2017.

[44] Minh A. Tran, Duanni Huang, and John E. Bowers. Tutorial on narrow linewidth tunable semiconductor lasers using si/iii-v heterogeneous integration. *APL Photonics*, 4(11):111101, 2019.

[45] Kerry Vahala and Amnon Yariv. Semiclassical theory of noise in semiconductor lasers-Part ii. *IEEE Journal of Quantum Electronics*, 19(6): 1102–1109, 1983.

[46] Kerry Vahala and Amnon Yariv. Detuned loading in coupled cavity semiconductor lasers—effect on quantum noise and dynamics. *Applied Physics Letters*, 45(5):501–503, 1984.

[47] Chenchen Wan, Peng Li, Axel Ruehl, and Ingmar Hartl. Coherent frequency division with a degenerate synchronously pumped optical parametric oscillator. *Optics Letters*, 43(5):1059–1062, 2018.

[48] Dennis Ray White and William H. Louisell. Noise calculations for optical parametric oscillators. *Physical Review A*, 1(5):1347, 1970.

[49] Yi Yu, Aref Rasoulzadeh Zali, and Jesper Mørk. Theory of linewidth narrowing in Fano lasers. *Physical Review Research*, 4(4):043194, 2022.

Chapter 8

NON-DISSIPATIVE NON-HERMITIAN DYNAMICS AND EXCEPTIONAL POINTS IN COUPLED OPTICAL PARAMETRIC OSCILLATORS

Roy, Arkadev, Saman Jahani, Qiushi Guo, Avik Dutt, Shanhui Fan, Mohammad-Ali Miri, and Alireza Marandi. Nondissipative non-Hermitian dynamics and exceptional points in coupled optical parametric oscillators. ***Optica***, 8(3):415–421, 2021. doi: https://doi.org/10.1364/OPTICA.415569.
A.R. contributed to the conception of the project, developed the modeling, performed numerical simulations, and participated in the writing of the manuscript.

8.1 Abstract

Engineered non-Hermitian systems featuring exceptional points can lead to a host of extraordinary phenomena in diverse fields ranging from photonics, acoustics, optomechanics, and electronics, to atomic physics. In optics, non-Hermitian dynamics are typically realized using dissipation and phase-insensitive gain which are accompanied by unavoidable fluctuations. Here we introduce and present non-Hermitian dynamics of coupled optical parametric oscillators (OPOs) arising from phase-sensitive amplification and de-amplification, and show their distinct advantages over conventional non-Hermitian systems relying on laser gain and loss. OPO-based non-Hermitian systems can benefit from the instantaneous nature of the parametric gain, noiseless phase-sensitive amplification, and rich quantum and classical nonlinear dynamics. We show that two coupled OPOs can exhibit spectral anti-PT symmetry and an exceptional point between their degenerate and non-degenerate operation regimes. To demonstrate the distinct potentials of the coupled OPO system compared to conventional non-Hermitian systems, we present higher-order exceptional points with two OPOs, tunable Floquet exceptional points in a reconfigurable dynamic non-Hermitian system, and generation of squeezed vacuum around exceptional points, all of which are not easy to realize in other non-Hermitian platforms. Our results show that coupled OPOs are an outstanding non-Hermitian setting with unprecedented opportunities in realizing nonlinear dynamical systems for enhanced sensing and quantum information processing.

8.2 Introduction

Non-Hermitian systems with engineered gain and dissipation have attracted a lot of attention thanks to their remarkable properties and functionalities which are absent in their counterparts based on closed Hermitian setups [34, 37]. A plethora of phenomena have spawned out by judiciously manipulating these non-Hermitian physical systems namely, spontaneous parity-time symmetry breaking [34], unidirectional invisibility [26], coherent perfect absorption and lasing [27, 45], single-mode lasing [14], generation of structured light with a controllable topological charge of the orbital angular momentum mode [32], to name a few.

Non-Hermitian systems are often characterized by the presence of an exceptional point (EP), where the eigenvalues and eigenvectors simultaneously coalesce (non-Hermitian degeneracies), and have been explored in the context of parity-time symmetric systems with balanced gain/loss and even in purely dissipative arrangements. The presence of an EP leads to several counter-intuitive phenomena including loss-induced lasing [12, 38], breakdown of adiabaticity [10, 17], lasing without inversion [11]. However, most non-Hermitian optical systems realize gain/dissipation by deploying laser gain which limits its viability in certain spectral regions [39].

Here we utilize parametric amplification and de-amplification in coupled OPOs to implement EP in parametric non-Hermitian systems [2, 13, 44], thereby presenting a system that can exhibit unique phenomena not observed in their laser-gain based counterparts. Parametric non-Hermitian systems can extend beyond the spectral coverage of laser gain [33], and the instantaneous nature of parametric gain also enables the realization of tunable/reconfigurable non-Hermitian systems that are otherwise difficult to achieve in conventional optics based non-Hermitian setups. We leverage this tunable aspect of parametric gain to realize interesting functionalities. Fundamentally, the presented OPO-based non-Hermitian system is in sharp contrast with conventional optical systems and can enable unique opportunities for sensing, non-Hermitian nonlinear dynamics, and quantum information processing.

EPs in non-Hermitian systems have been extensively studied for potentially enhanced sensing capabilities [7, 18, 22]. In spite of the underlying high sensitivity near an EP, these class of sensors relying on the resonant frequency splitting are not capable of improving the SNR (Signal-to-Noise Ratio) owing to the non-orthogonality of eigenvectors near an EP [6, 23, 24]. This leads to Peterman factor limited sensing [43] where the noise is enhanced proportional to the signal

enhancement, thereby limiting the efficacy of this class of sensors for quantum-limited sensing [9]. Fluctuations accompanying the gain/dissipation in conventional non-Hermitian systems limit the achievable precision. In fact, it has been shown that any linear reciprocal sensor is bounded in terms of SNR performance, and conventional EP-based sensing cannot surpass this limit [24]. Recently, a sensing protocol that does not measure the eigenfrequency splitting but rather measures the superposition of output quadratures using heterodyne detection has shown the possibility of alleviating the problem of noise enhancement and realizing EP-enhanced sensing when operated near the lasing threshold [49]. The noiseless nature of phase-sensitive degenerate parametric amplification motivates studying non-Hermitian dynamics of coupled OPOs for sensing. In this regard, we explore the possibility of reduced uncertainty of fluctuations manifested in the form of squeezed noise in the vicinity of parametric EP to leverage the high sensitivity of EP in the pursuit of obtaining high SNR. It must be noted that phase-sensitive parametric gain-based systems are not bounded by the limit outlined in Ref. [24].

Non-Hermitian dynamics of coupled OPOs can be extended to the nonlinear regime which can lead to several intriguing possibilities. It has been previously shown that the interplay of nonlinearity and gain/loss in conventional non-Hermitian systems can result in unidirectional transport [40], one parameter family of solitons [1] (in contrast to an isolated attractor based dissipative solitons) in parity-time symmetric systems, robust wireless power transfer [3]. Previous studies implementing parametric amplification to realize non-Hermitian systems have focused on the linear dynamics only [2, 13, 44]. We exploit rich nonlinear dynamics in our parametric non-Hermitian system (operating in the parametric oscillator regime) arising from the interplay of phase-sensitive gain and the gain saturation owing to the signal to pump back-conversion.

The presented coupled OPO system is also an appealing platform to investigate quantum non-Hermitian physics. Previous studies of the quantum behavior in non-Hermitian systems have identified the criticality of information flow between the system and environment around the EP in a parity-time symmetric system [20], a shift of the position of Hong-Ou-Mandel dip [21], and delaying of entanglement sudden death near an EP [4]. Opto-mechanical systems provide a versatile testbed to study non-Hermitian dynamics in the quantum regime [19]. We demonstrate non-classical behavior including quadrature squeezing and tunable squeezing of parametric EP. These behaviors may also be extended to the non-Gaussian regime[36].

8.3 Results

We consider a system of evanescently coupled degenerate OPOs as illustrated in Fig. 8.1(a). The coupled-mode equations governing our system are given by:

$$\frac{da}{dt} = -\gamma_1 a + i\Delta_1 a + g a^* - g_{s_1}|a|^2 a + i\kappa b \tag{8.1a}$$

$$\frac{db}{dt} = -\gamma_2 b + i\Delta_2 b + f e^{i\phi} b^* - g_{s_2}|b|^2 b + i\kappa a. \tag{8.1b}$$

The OPOs considered are phase matched to oscillate around the half-harmonic frequency [15]. The continuous-wave (CW) pump is non-resonant and its dynamics is adiabatically eliminated. The signal field envelopes in the two resonators are designated by a and b, respectively. The signal in the first resonator experiences a round-trip loss (intrinsic+out-coupling) of γ_1, a detuning of Δ_1, and a parametric gain of g provided by the non-resonant pump. The gain can be assumed constant for the frequency range of interest around the half-harmonic frequency. The parametric gain is phase-sensitive, and the phase of the pump driving the first resonator is taken as a reference. The gain saturation term is denoted by g_{s_1} which originates from the signal to pump back-conversion due to second-harmonic generation which is the reverse of the down-conversion process. The strength of the dispersive coupling is represented by κ. Similar terms appearing in Eq.(8.1b) describe associated quantities in the second resonator. The pump driving the parametric interaction in the second resonator is phase shifted by ϕ as compared to the first pump. The parametric gain is proportional to the pump strength and is given by f. Both the pumps are at $2\omega_0$, where ω_0 is the half harmonic frequency. The time scale is normalized to the round-trip time.

We assume that the resonators are identical in terms of the loss (γ) and gain-saturation (g_s) terms for simplicity. This can be achieved by accessing the two degrees of freedom of a single resonator namely the clockwise and counter-clockwise propagation modes. In the absence of these assumptions, the results discussed in this work will still hold true, albeit with some quantitative differences.

There are two regimes of parametric oscillation, namely the non-degenerate regime and the degenerate regime [41]. In the degenerate regime, the system oscillates at ω_0, while in the non-degenerate regime owing to energy conservation constraint the system oscillates with symmetric sidebands centered around ω_0. First, we consider that both the half-harmonic signals are on resonance, i.e. $\Delta_1 = \Delta_2 = 0$.

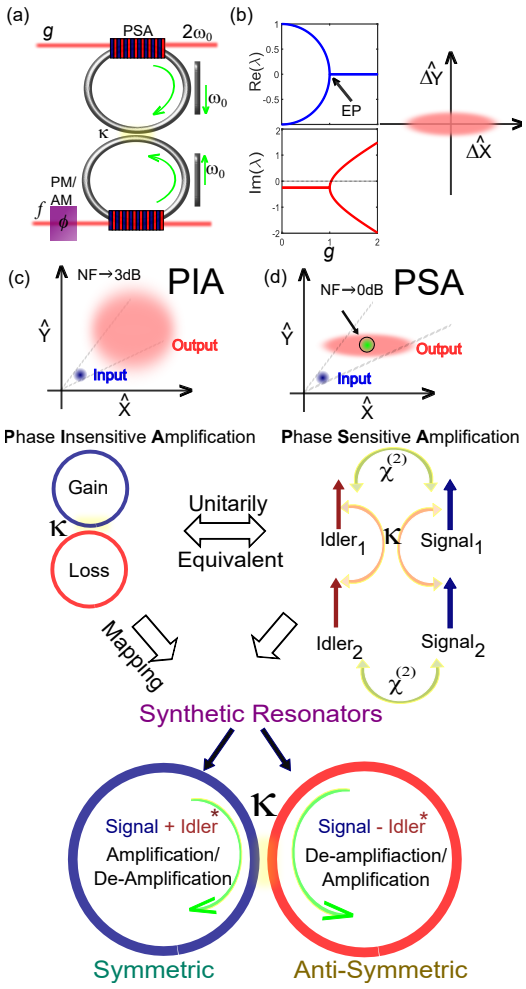

Figure 8.1: **Schematic depicting the concept of parametric EP**. a) Coupled OPO with evanascent coupling κ, driven by non-resonant pumps at $2\omega_0$. The strength of the drive in the first OPO is g and the strength of the drive in the second OPO is f. The pumps can be phase (PM)/amplitude (AM) modulated, and the resonant signals at half-harmonic (ω_0) are extracted from the respective out-couplers. b) The appearance of an EP as the parametric gain parameter g is varied at a fixed coupling rate κ. In the vicinity of this EP apart from enhanced responsivity due to the branch point singularity nature of EP, there exists squeezed noise which can reduce the uncertainty of the output field below the standard noise limit in a suitable quadrature. c) Conventional non-Hermitian systems employ phase-insensitive amplification (PIA) mechanism and thus the noise figure of the system under consideration cannot go below 3dB. d) We leverage the phase sensitive amplification (PSA) in the realization of parametric EP which can ideally approach noiseless amplification. We map the usual gain-loss coupling in the conventional non-Hermitian systems to phase-sensitive quadrature parametric amplification and de-amplification and represent the equivalent process in synthetic resonators.

In the non-degenerate regime (under the scope of linearized analysis, i.e., ignoring gain saturation) we can consider the following ansatz for the signal envelopes in the two resonators as:

$$a = Ae^{(\lambda_I - i\lambda_R)t} + Be^{(\lambda_I + i\lambda_R)t} \tag{8.2a}$$

$$b = Ce^{(\lambda_I - i\lambda_R)t} + De^{(\lambda_I + i\lambda_R)t} \tag{8.2b}$$

where A and B represent the complex envelopes for the symmetric primary sidebands for resonator 1, and C and D represent the same for resonator 2. Here, the real part of eigenvalues (λ_R) corresponds to the spectral splitting, while the imaginary part (λ_I) is related to the growth/decay rate. A, C can also be read as the signals and B, D as the idlers. The eigenvalues can be obtained from the following equation:

$$(\lambda_R + i\lambda_I)\begin{bmatrix} A \\ B^* \\ C \\ D^* \end{bmatrix} = \begin{bmatrix} -i\gamma & ig & -\kappa & 0 \\ ig & -i\gamma & 0 & \kappa \\ -\kappa & 0 & -i\gamma & ife^{i\phi} \\ 0 & \kappa & ife^{-i\phi} & -i\gamma \end{bmatrix}\begin{bmatrix} A \\ B^* \\ C \\ D^* \end{bmatrix}. \tag{8.2c}$$

The underlying Hamiltonian of the coupled OPO system exhibits spectral anti-PT symmetry [2]. The Hamiltonian governs the dynamics as: $i\frac{d\tilde{V}}{dt} = H\tilde{V}$, where $\tilde{V} = \left[\tilde{A}, \tilde{B}^*, \tilde{C}, \tilde{D}^*\right]^T$, $\tilde{A} = Ae^{(\lambda_I - i\lambda_R)t}$, $\tilde{B} = Be^{(\lambda_I + i\lambda_R)t}$, $\tilde{C} = Ce^{(\lambda_I - i\lambda_R)t}$, and $\tilde{D} = De^{(\lambda_I + i\lambda_R)t}$. The discrete symmetry of the system can be expressed as: $P_1P_2TH = -HP_1P_2T$, where T is the time reversal operator, and the parity operators action in the spectral domain are defined by: $P_1 = \{A \leftrightarrow B^*\}$ and $P_2 = \{C \leftrightarrow D^*\}$. The system dynamics is also unitarily equivalent to a PT-symmetric system, where the unitary transformation $\mathbb{U} = \frac{1}{\sqrt{2}}\begin{bmatrix} 1 & -1 & 0 & 0 \\ 0 & 0 & 1 & -1 \\ 1 & 1 & 0 & 0 \\ 0 & 0 & 1 & 1 \end{bmatrix}$, such that $H_{\mathrm{PT}} = \mathbb{U}H\mathbb{U}^\dagger$. This mapping is shown schematically in Fig. 8.1(c) and 8.1(d). The signals of the two OPOs are coupled by the evanescent linear coupling κ, and so do the idlers. While the signal and the idler within the same OPO are coupled nonlinearly by the nonlinear phase-sensitive coupling engendered by $\chi^{(2)}$. Under the said unitary transformation ($\mathbb{U}$), this process can be mapped to a PT-symmetric system of coupled synthetic resonators with the positive superposition of the signal and the idler conjugated fields experiencing amplification, while the negative superposition of the signal and idler fields get de-amplified. It should be noted that due to the onset of nonlinearity arising due to

back conversion (g_s) additional sidebands will appear in the complete nonlinear solution.

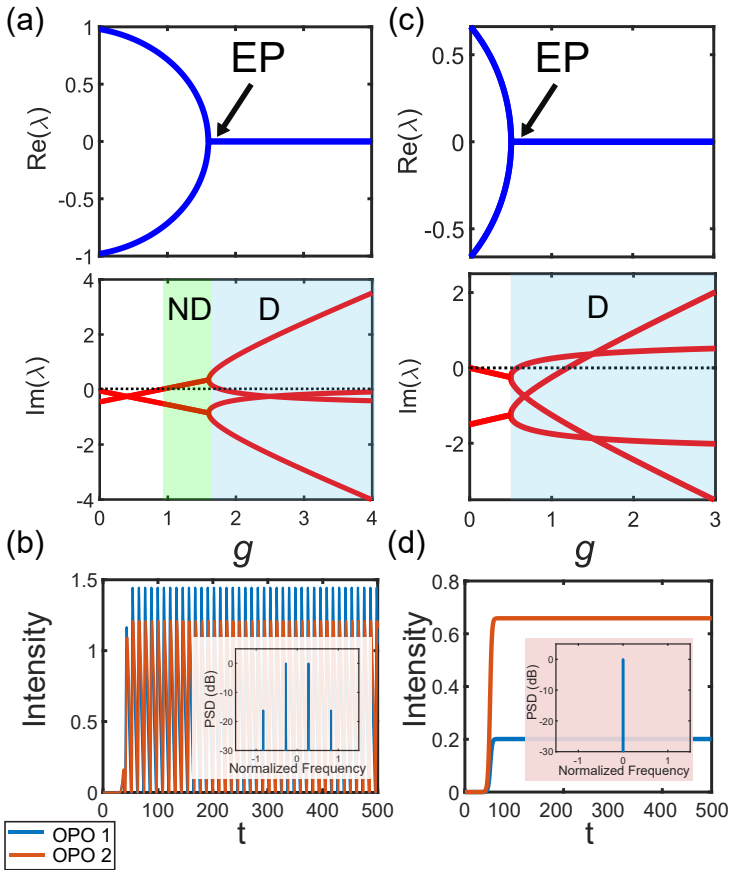

Figure 8.2: **Parametric Oscillation in Coupled OPO in the presence of EP**. a,b) Coupled OPO system initiates parametric oscillation in the non-degenerate (ND) phase at the threshold. The parameters used are: $f = 0.4$, $\kappa = 1$, $g_s = 0.3$, and $\gamma = 0.25$. At higher values of g above the threshold, the system operates in the degenerate (D) phase. In a) the real and imaginary part of the eigenvalues (λ) are shown that emanates from the linearized analysis. The threshold is indicated by the dashed black line. The time domain profile of the intra-cavity intensity (for $g = 1.5$) in both the resonators is shown in b). The corresponding spectral domain information appearing in the inset confirms the non-degenerate oscillation phase. c,d) Coupled OPO system initiates parametric oscillation in the degenerate phase at the threshold. The parameters used are: $f = 1.5$, $\kappa = 1$, and $\gamma = 0.75$. There is no occurrence of non-degenerate oscillation. In c) the real and imaginary part of the eigenvalues are shown that emanates from the linearized analysis. The time domain profile of the intra-cavity intensity (for $g = 1$) in both the resonators is shown in d). The corresponding spectral domain information appearing in the inset confirms the degenerate oscillation phase.

In the degenerate regime, the signals in both resonators are half harmonics. Here we can express the signal evolution in terms of their quadrature components. We define $X_1 = (a + a^*), Y_1 = \frac{a-a^*}{i}$ and $X_2 = (b + b^*), Y_2 = \frac{b-b^*}{i}$. These quadrature components evolve as $e^{\lambda_I t}$. The eigenvalues can be obtained from the following evolution equation:

$$i\lambda_I \begin{bmatrix} X_1 \\ Y_1 \\ X_2 \\ Y_2 \end{bmatrix} = \begin{bmatrix} -i\gamma + ig & 0 & 0 & -i\kappa \\ 0 & -i\gamma - ig & i\kappa & 0 \\ 0 & -i\kappa & -i\gamma + if\cos(\phi) & if\sin\phi \\ i\kappa & 0 & if\sin\phi & -i\gamma - if\cos\phi \end{bmatrix} \begin{bmatrix} X_1 \\ Y_1 \\ X_2 \\ Y_2 \end{bmatrix}. \quad (8.3)$$

The transition from the non-degenerate oscillation regime to the degenerate oscillation regime is marked by the presence of an exceptional point. This point in the parameter space is characterized by the simultaneous collapse of eigenvectors and the coalescence of the eigenvalues. The disparity between the geometric and the algebraic multiplicity at the exceptional point is determined by the order of the exceptional point.

The threshold for parametric oscillation in the coupled OPO is determined by the linear eigenvalues, i.e., $\lambda_I = 0$, with oscillation occurring for $\lambda_I > 0$ (see Supplementary section 8.5.1). This extra caution is because of the possibility of the occurrence of oscillation self-termination analogous to laser self-termination [12, 38]. Just above the threshold, the system of coupled OPOs can oscillate either in non-degenerate (Fig. 8.2(a) and 8.2(b)) or in degenerate mode (Fig. 8.2(c) and 8.2(d)). However, far above the threshold the effect of nonlinearity becomes significant and the system is no longer governed by the linearized dynamics (Eq. 8.2,8.3). In this regime, nonlinearity can induce a phase transition from non-degeneracy to degeneracy as shown in Fig. 8.3(b) and 8.3(c), similar to laser systems [16, 28]. This transition resembles a soft/ super-critical bifurcation.

The phase-sensitive nature of parametric gain provides an additional tuning knob in the form of a phase difference between the two driving pumps (ϕ) that do not exist in the conventional phase-insensitive gain/loss-based non-Hermitian systems. Figure 8.3(a) illustrates the solution space as the phase difference is varied, identifying the degenerate and the non-degenerate oscillation regimes.

The order of exceptional points determines the rate of eigenvalues splitting in the presence of a perturbation away from EP [34]. If the perturbation appears in the

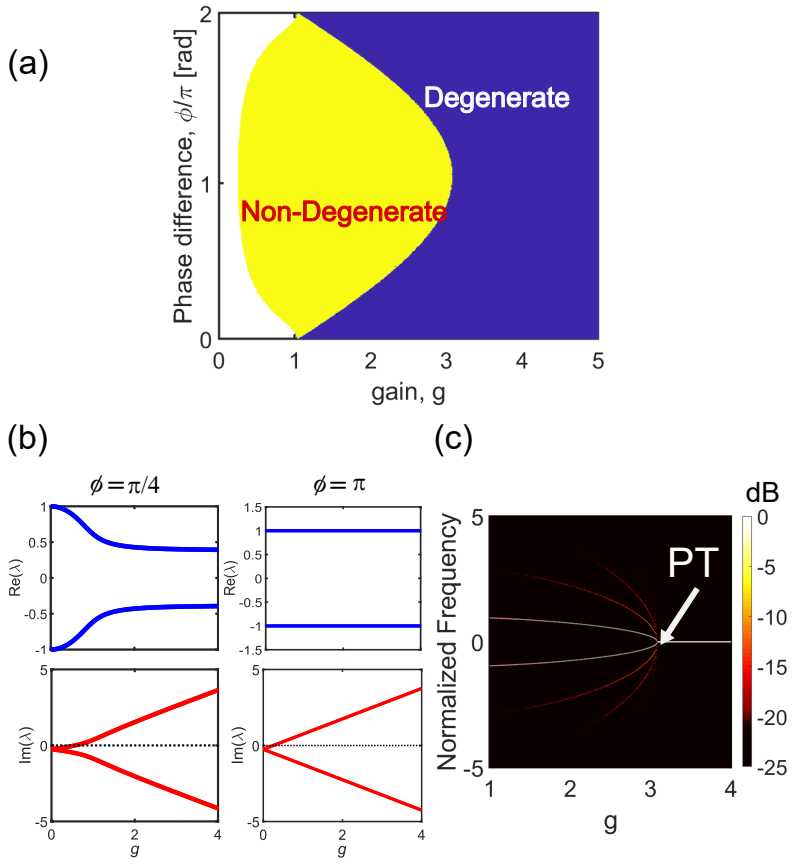

Figure 8.3: **Occurrence of nonlinearity induced phase transition**. a) Phase diagram of coupled OPO driven with a pump of similar strength g with a relative phase difference ϕ. The phase diagram clearly shows the presence of two phases of oscillation above the threshold, namely the non-degenerate and degenerate. The white region indicates that the coupled OPO system is below the threshold. The phase diagram is obtained by solving the coupled nonlinear equations for the OPOs (Eq. 8.1) including the gain saturation. b) Linearized analysis predicts the possibility of non-degenerate oscillation only, however, a phase transition into a degenerate phase can be engendered when accounting for the back-conversion nonlinearity. Two representative cases for $\phi = \pi/4$ and $\phi = \pi$ are shown. c) Nonlinearity-induced phase transition from non-degenerate to degenerate (for $\phi = \pi$) highlighting the soft/super-critical nature of phase transition. The colorbar represents the spectral intensity in the dB scale.

form of detuning ($\delta\Delta$), then the splitting depends as: $\delta(Re(\lambda)) = (\delta\Delta)^{\frac{1}{n}}$, where n is the order of EP. This leads to enhanced sensitivity in the proximity of an EP, which is given by $\frac{d(\delta(Re(\lambda)))}{d(\delta\Delta)} \sim (\delta\Delta)^{\frac{1-n}{n}}$. This sensitivity function diverges at EP, which is the basis for enhanced sensitivity of EP-based sensors [7, 18, 22]. This scaling law arising due to the branch point singularity nature of non-Hermitian degeneracies

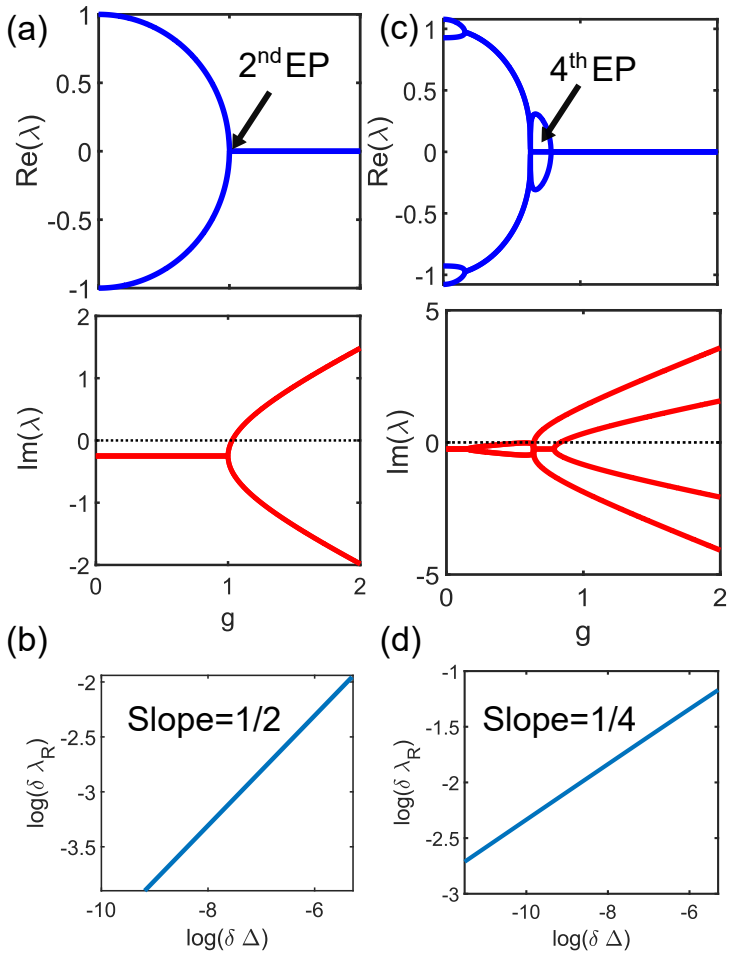

Figure 8.4: **Different orders of EP realized in coupled OPO**. a) Second order EP. Parameters used are $f = g$, $\kappa = 1$, and $\gamma = 0.25$. b) Dependence of the spectral splitting $(\delta Re(\lambda))$in the vicinity of EP, when a perturbation in the form of detuning $(\Delta_1 = \delta\Delta)$is applied. It varies as $\delta Re(\lambda) = (\delta\Delta)^{\frac{1}{2}}$. c) Fourth order EP. Parameters used are $f = 2g$, $\kappa = 1$, $\Delta_1 = 0.1501$ and $\gamma = 0.25$. d) Dependence of the spectral splitting $(\delta Re(\lambda))$ in the vicinity of EP, which varies as $\delta Re(\lambda) = (\delta\Delta)^{\frac{1}{4}}$.

does not arise in the case of Hermitian degeneracies characterized by diabolical points. We present the occurrence of both a second-order EP and a higher-order EP (4th-order) in the coupled OPO system. Second-order EP is accompanied by the collapse of eigenvalues and eigenvectors in pairs and is shown in Fig. 8.4(a) and 8.4(b) by considering $f = g, \Delta_1 = \Delta_2 = 0$. We identify a family of higher-order exceptional points (see Supplementary section 8.5.3), by biasing the coupled OPOs at suitable detuning. In Fig. 8.4(c) and 8.4(d) we considered $f = mg, \Delta_2 = 0$, where m is the parameter describing the family of exceptional points which determines the critical g and Δ_1 for the occurrence of the 4th order EP. In this case, four eigenvectors

and eigenvalues coalesce resulting in higher order dependence of sensitivity. This enhanced sensitivity of the 4th-order EP is reflected in the slope of the log-log plot in Fig. 8.4(d) as compared to the case in Fig. 8.4(b) corresponding to a second-order EP.

The instantaneous nature of parametric gain and the ability to modulate the gain by applying phase/ amplitude modulation to the pump opens unprecedented avenues in exploring time-modulated dynamic non-Hermitian systems in the coupled OPO arrangement. Time periodic Floquet non-Hermitian systems have been utilized to tailor the EP and realize re-configurable non-Hermitian systems with an enriched phase space depending on the amplitude and frequency of the modulation [8, 25, 29]. Previous demonstrations relied on periodically modulating the coupling to realize Floquet-driven systems. Parametric non-Hermitian systems enable us to modulate the gain instead of the coupling, by modulating the pump and realizing tunable Floquet EP. In Fig. 8.5(a) and 8.5(b), we explore Floquet control of EP when the pump is amplitude modulated as: $g = g_0 + F\sin(\omega t)$. The eigenvalues of the Floquet periodic system can be extracted by analyzing the associated Monodromy matrix. As shown in Fig. 8.5(b) with increasing values of the pump amplitude modulation parameter F, the EP is progressively shifted to higher values of g_0.

Similarly, we can dynamically encircle the EP by periodically modulating the parametric gain. Dynamical encirclement involves adiabatically tracing a close path in the parameter space enclosing an EP, which has been utilized to realize robust and asymmetric switching [10], non-reciprocal energy transfer [47] and omni-polarizer [17]. However these promising results have only been demonstrated in lossy systems [10, 48], due to the stringent requirement of non-Hermitian system tunability. Here we propose that the tunable nature of the parametric gain provides a very promising platform to realize these chiral dynamics that is contingent on the topological structure of the EP. We perform adiabatic encirclement in the parametric space (Fig. 8.5(c) and 8.5(d)) of detuning and gain by undergoing the following adiabatic evolution: $f = g = g_0 + r\cos(\omega t)$ and $\Delta_1 = r\sin(\omega t)$, where r is the radius of encirclement, and $g_0 = \kappa$ is the EP. Due to the breakdown of adiabaticity in the non-Hermitian system, we obtain an asymmetric/ chiral behavior, where the final state at the end of the encirclement, depends on the direction of the loop and is independent of the starting point. The distinct outcome by parametrically traversing a loop enclosing the EP counter-clockwise (Fig. 8.5(c)) and clockwise (Fig. 8.5(d)) is shown.

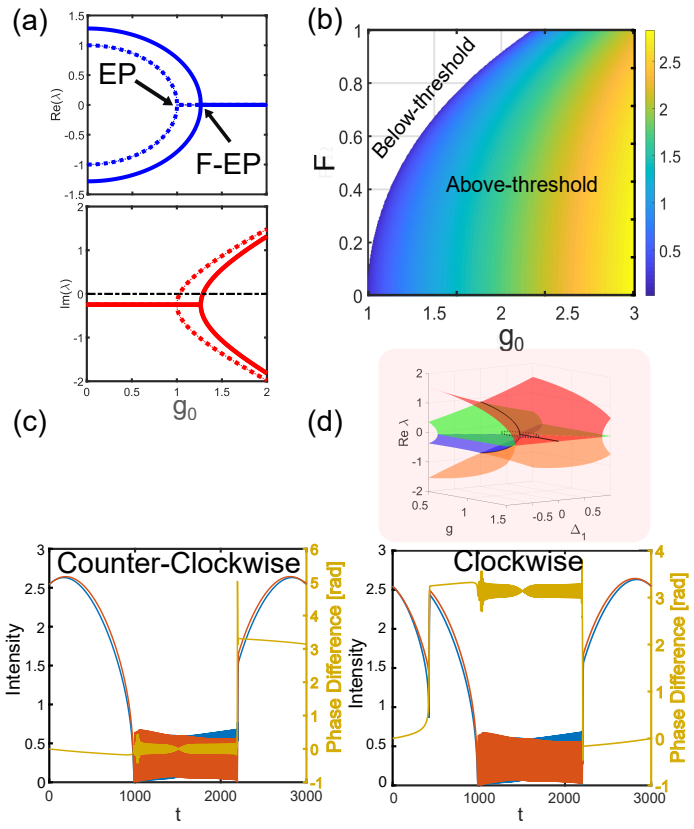

Figure 8.5: **Periodically modulated coupled OPO**. a) Floquet control of EP. Real and Imaginary parts (solid lines) of the Floquet exponent of the associated monodromy matrix. Floquet EP (F-EP) can be tuned from the static EP (dotted lines represent the eigenvalues for the static system without periodic modulation). Parameters for the pump amplitude modulation used are $F = 5, \omega = 10$. b) Tuning the F-EP by varying F, the amplitude modulation depth. The threshold in the coupled OPO system can be varied by changing F (white region corresponds to below threshold). The color-bar represents gain $(\mathrm{Im}(\lambda) + \gamma)$. c) Adiabatically encircling the EP, and the emergence of chirality. Counter-clockwise encirclement and the system ends up in a different final state. d) Clockwise encirclement where an abrupt jump occurs during the evolution, and the system returns to the initial state at the end of the encirclement. Highlighted is shown the Riemann eigen-surfaces. The dotted loop represents the encirclement trajectory on the $\Delta_1 - g$ parameter space. The black solid line indicates the eigen-frequency splitting for $\Delta_1 = 0$. Parameters used are: $r = 0.2, \omega = \frac{2\pi}{3000}$.

OPOs have been the workhorse for generating quantum states of light for decades [46], and coupled OPOs have also been predicted to exhibit nonclassical properties [35]. When we approach the EP from below the threshold the vacuum fluctuations in the quadratures of the intra-cavity field can be squeezed below the standard noise limit. We assume the vacuum fluctuations entering the cavity from different open

channels, to be delta-correlated white Gaussian noise and obtain the power spectral density of the output quadrature fields via a linearized analysis of the Langevin equations [5]. The formalism including the relevant noise operators is derived in (see Supplementary Section 9.5.5). Figures 8.6(a) and 8.6(b) show that there exists a bandwidth where the intra-cavity field is squeezed as we approach the EP. The reduced noise in one quadrature is accompanied by increased uncertainty (anti-squeezing) in the conjugate quadrature. Although the maximum squeezing attainable in the vicinity of EP is 3dB (see Supplementary 8.5.6), it can potentially allow combining the high sensitivity of EP and the reduced uncertainty in parametric EP, to realize unparalleled sensing capabilities in an optimum sensing arrangement. The amount of squeezing depends on the OPO escape efficiency, which is the ratio between the out-coupling loss and the total round-trip loss, with the higher squeezing attainable with larger escape efficiency. More so, one can tune the squeezing response by changing κ in coupled OPO as shown in Fig. 8.6(b), thereby operating at a frequency where the external/technical noise of the sensing system is minimum. In response to a perturbation in the form of detuning, only the optimum quadrature for squeezing is rotated, still preserving the noise reduction property (see Supplementary section 8.5.6). In this regard, our parametric EP can pave the way for ultra-sensitive detection with high SNR in shot noise-limited detection scenarios.

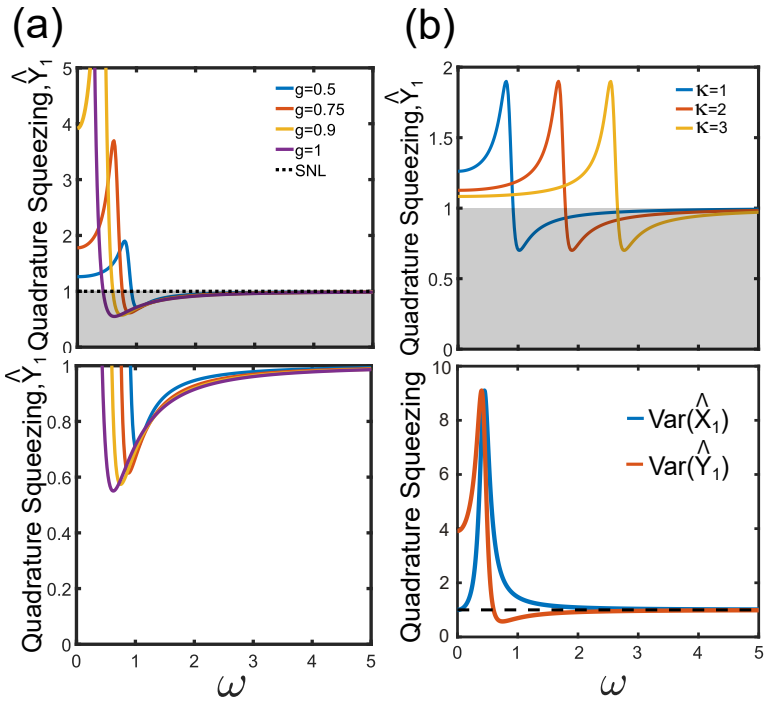

Figure 8.6: **Squeezing near the parametric EP in coupled OPO**. a) Quadrature squeezing spectrum as we approach the EP by varying g. There exists a bandwidth where the squeezing is below the standard noise limit indicated by the black-shaded region and bounded by the black dotted line. A zoomed-in version of the same is shown right below. b) The squeezing spectrum can be tuned by varying the coupling strength κ in the coupled OPO system. g is kept equal to 0.5κ. Below is shown the squeezing and anti-squeezing in the conjugate quadratures for $\kappa = 1, g = 0.9, \gamma = 0.1, \rho = 0.9$.

8.4 Discussion

Recent developments in the realization of large-scale time-multiplexed OPO networks [30] and integrated lithium niobate-based devices [42] can be ideal candidates for experimental realization of the presented concept. Entanglement can be used as a resource for increasing the sensor performance [9] based on parametric EP. An optimum sensing arrangement guided by Quantum Fischer information calculations needs to be designed in order to obtain high SNR sensing from parametric EP [24, 49]. Also, the enhancement provided by higher order parametric EP and the limits of sensors based on them including their dynamic range is worth exploring and will be subjects for future investigations. It will be interesting to extend it to the case of a lattice of parametric oscillators, where interesting non-equilibrium dynamics is expected [31].

8.5 Supplementary

8.5.1 Threshold

The threshold for parametric oscillation can be obtained from the linearized analysis.

The threshold for degenerate oscillation occurs when the following equality is satisfied:

$$-\gamma+\frac{1}{\sqrt{2}}\sqrt{f^2+g^2-2\kappa^2+\sqrt{f^4+g^4-4g^2\kappa^2-4f^2\kappa^2-2g^2f^2+8\kappa^2fg\cos(\phi)}}=0. \tag{8.4}$$

The threshold for non-degenerate oscillation occurs when the following equality is satisfied:

$$-\gamma+\max\left[\mathbf{Im}(E_+),\mathbf{Im}(E_-)\right]=0 \tag{8.5a}$$

where,

$$E_\pm=\pm\frac{1}{\sqrt{2}}\sqrt{2\kappa^2-f^2-g^2-\sqrt{f^4+g^4-4g^2\kappa^2-4f^2\kappa^2-2g^2f^2+8\kappa^2fgcos(\phi)}} \tag{8.5b}$$

provided, $\mathbf{Re}(E)\neq 0$.

Below the oscillation threshold, the linearized analysis determines the system dynamics and the properties can be accessed experimentally by probing it with a tunable laser.

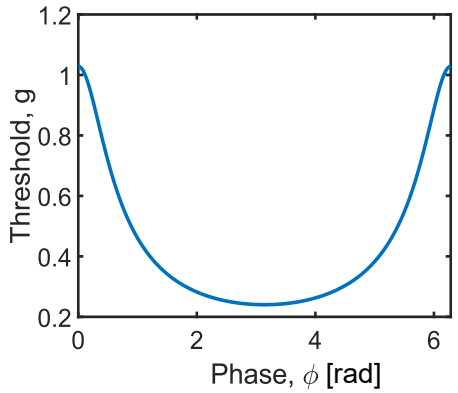

Figure 8.7: **Threshold as a function of the phase difference ϕ between the pumps**. The curve is obtained using Eq. 8.4 which matches that of the numerical simulation.

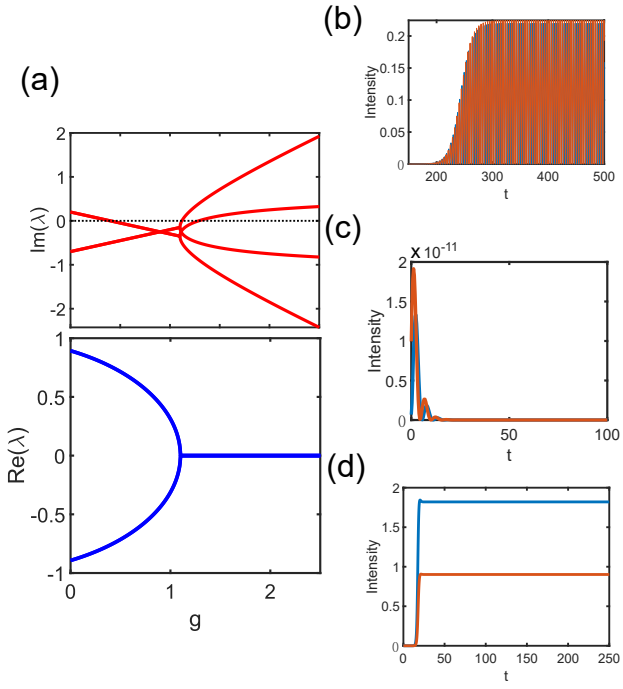

Figure 8.8: **Gain-induced oscillation suppression and revival of oscillation.** a) Eigenvalues from the linear analysis. Parameters used are: $f = 0.9, \gamma = 0.25, \kappa = 1$. b) Coupled OPO above the threshold and oscillating in the non-degenerate phase for $g = 0.3$ c) Oscillation is suppressed as the gain is increased to $g = 0.75$ indicating the occurrence of gain-induced oscillation suppression. d) Oscillation again re-emerges as the gain parameter is further increased ($g = 1.5$), signifying the revival of oscillation.

8.5.2 Nonlinearity induced Phase Transition

We analytically demonstrate the phenomenon of nonlinearity-induced phase transition in a simple case although a representative one, when $f = g$ and $\phi = \pi$. The linearized analysis suggests that the system of coupled OPOs under this set of conditions will oscillate in the non-degenerate regime. However, we find that beyond a critical g the system oscillates in degenerate mode.

Under this set of conditions when the system oscillates in the degenerate mode beyond a critical g, the signal envelopes can be assumed as: $a = x$ and $b = i\rho x$, where ρ determines the intensity contrast in the two resonators at steady state, and x is real. Substituting this ansatz in Eq. 8.1, we obtain at steady state:

$$G - g_s x^2 - \kappa\rho = 0 \tag{8.6a}$$

$$G\rho - g_s\rho^3 x^2 + \kappa = 0 \tag{8.6b}$$

where, G= g-γ. Solving these systems of equations yields:

$$x = \frac{1}{\sqrt{g_s}}\sqrt{\frac{3G}{4} + \frac{\sqrt{G^2 - 8\kappa^2}}{4} + \frac{\kappa}{2}\sqrt{2 + \frac{G^2}{2\kappa^2} - \kappa\frac{\frac{G^3}{\kappa^3} - \frac{8G}{\kappa}}{2\sqrt{G^2 - 8\kappa^2}}}} \tag{8.6c}$$

$$\rho = \frac{G}{4\kappa} - \frac{\sqrt{G^2 - 8\kappa^2}}{4\kappa} - \frac{1}{2}\sqrt{2 + \frac{G^2}{2\kappa^2} - \kappa\frac{\frac{G^3}{\kappa^3} - \frac{8G}{\kappa}}{2\sqrt{G^2 - 8\kappa^2}}}. \tag{8.6d}$$

The critical value of g beyond which the oscillation enters into a degenerate regime is given by: $g = \gamma + \sqrt{8\kappa^2}$. This analytical result matches the critical value of g obtained numerically.

8.5.3 Higher Order Exceptional Point

Here, we derive the conditions to obtain the family of higher-order (fourth-order) exceptional points.

$$(\lambda_R + i\lambda_I)\begin{bmatrix} A \\ B^* \\ C \\ D^* \end{bmatrix} = \begin{bmatrix} -i\gamma - \Delta & ig & -\kappa & 0 \\ ig & -i\gamma + \Delta & 0 & \kappa \\ -\kappa & 0 & -i\gamma & img \\ 0 & \kappa & img & -i\gamma \end{bmatrix}\begin{bmatrix} A \\ B^* \\ C \\ D^* \end{bmatrix} \tag{8.7a}$$

$$g = \sqrt{\frac{-\kappa^2}{m^3} + \frac{\kappa^2}{m^2} + \frac{\sqrt{\kappa^4 m^2(1 - 2m + 2m^2)}}{m^4}} \tag{8.7b}$$

$$\Delta = \pm\sqrt{-\kappa^2 - \frac{\kappa^2}{m^3} + \frac{\kappa^2}{m^2} - \frac{\kappa^2}{m} + \frac{\sqrt{\kappa^4 m^2(1 - 2m + 2m^2)}}{m^4} + \frac{\sqrt{\kappa^4 m^2(1 - 2m + 2m^2)}}{m^2}} \tag{8.7c}$$

with, $m \neq \{0, 1\}$.

8.5.4 Floquet Control of Exceptional Point

We show the time domain and frequency domain picture of the Floquet modulated parametric non-Hermitian system in Fig. 8.9. The Floquet phase diagram is shown in Fig. 8.10.

8.5.5 Fixed Points of Coupled OPO

We plot the steady-state fixed point solutions of the quadratures of coupled OPO in Fig. 8.11 and Fig. 8.12.

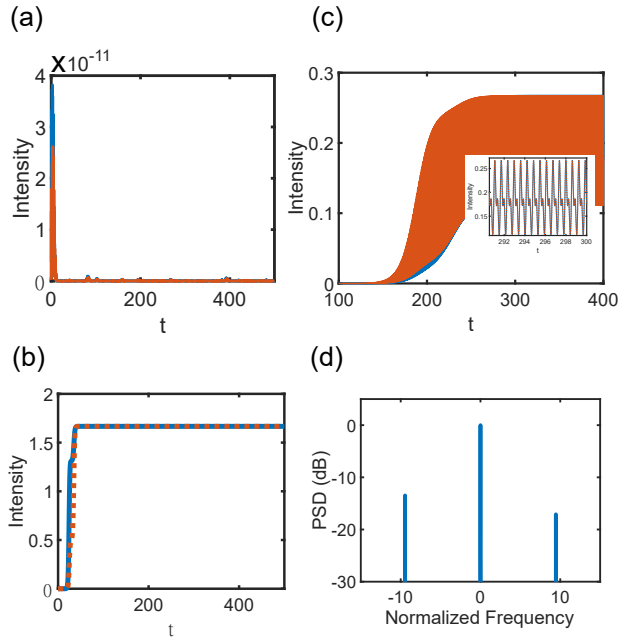

Figure 8.9: **Floquet control of EP.** Parameters used for the amplitude modulation are $F = 5, \omega = 10$. a) System of coupled OPO below the threshold for $g_0 = 1.25$. The time domain intra-cavity intensity waveforms are shown. b) However in the absence of periodic modulation, i.e., $F = 0$, the system oscillates above the threshold in the degenerate phase. This demonstrates that the Floquet control can tune the exceptional point and thereby the oscillation threshold. c) The modulated Floquet system goes above the threshold for $g_0 = 1.3$. The time domain intra-cavity intensity waveforms are shown. d) Spectral domain representation for the waveforms in c, depicting the presence of sidebands at the modulating frequency.

8.5.6 3 dB quadrature squeezing limit in the vicinity of EP in coupled OPO

The squeezing spectrum for the quadrature ($\hat{Y}$), is obtained from (Eq S.12) as $S(\omega) = C_{3,3}^{out}$. We are interested in the squeezing that is achievable at the EP. Assuming, $\kappa = 1$ and $g = \kappa$ (EP), we get:

$$S(\omega) = \frac{\gamma^4 - 4\gamma^3\rho - 4\gamma\rho\omega^2 + \omega^4 + 2\gamma^2(4\rho + \omega^2)}{(\gamma^2 + \omega^2)^2}. \tag{8.8}$$

Maximum, squeezing is obtained in the limit, $\rho = 1$. The function $S(\omega)$ reaches its minimum at $\omega = \sqrt{4\gamma - \gamma 2}$, if $0 \leq \gamma \leq 4$. The maximum attainable squeezing is 3dB below the shot noise level. If $\gamma > 4$, the minimum is obtained at $\omega = 0$.

Various aspects of the quadrature squeezing near the exceptional point are shown in Fig. 8.13.

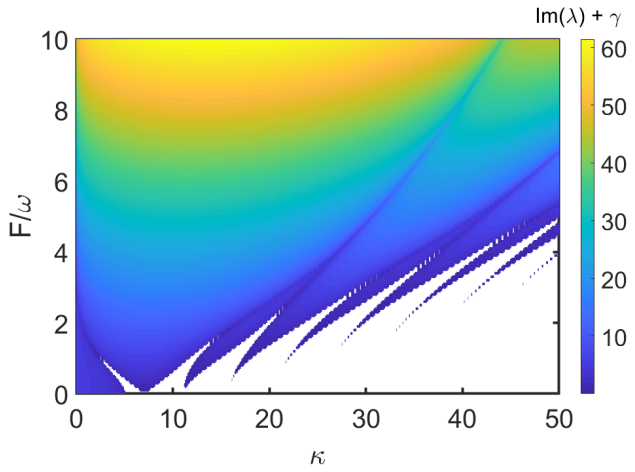

Figure 8.10: **Floquet phase diagram.** Multiple regions of below and above threshold regions (related to the anti-PT symmetry breaking) reflect the usual resonance-like behavior of periodically modulated systems. Plotted is the imaginary part of the eigenvalue shifted by the constant loss (γ). Here, the modulation amplitude F and the coupling factor κ are varied, with $\omega = 10$.

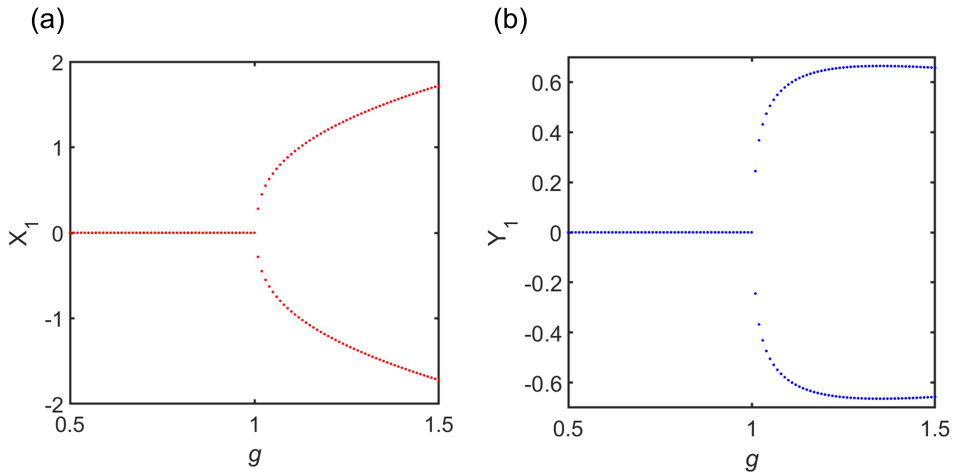

Figure 8.11: **Bifurcation diagram of coupled OPO.** Steady states appear as stable fixed points for the coupled OPO system when the gain parameter is varied. It displays features of a super-critical bifurcation at the threshold. Plotted are the quadratures of the complex field of one OPO in the coupled OPO system.

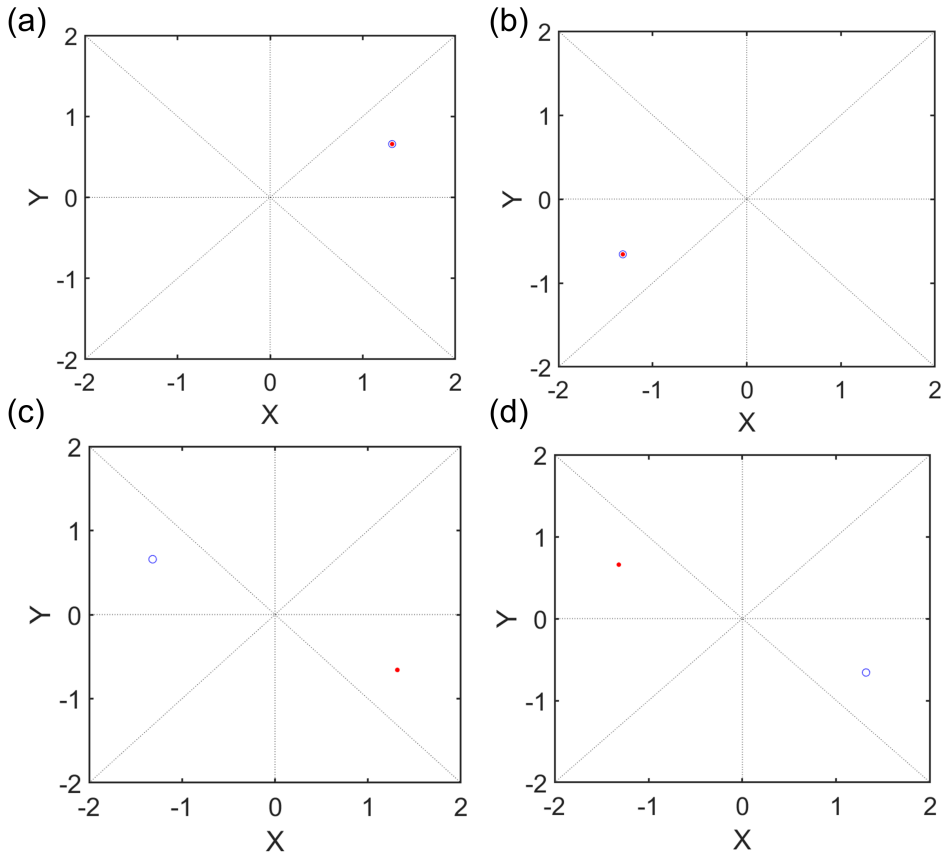

Figure 8.12: **Fixed points of coupled OPO.** Multiple steady states appear as stable fixed points for the coupled OPO system above the threshold. The parameters involved are: $f = g = 1.25, \gamma = 0.1, \kappa = 1$, and $g_s = 0.3$. These steady states have different in-phase and out-of-phase quadrature components. They can be accessed with suitable initial conditions lying in their domain of attraction. Red-filled circles represent the field in the first OPO, while open blue circles represent the same for the second OPO. Dotted lines depict X=0, Y=0, Y=X, and Y=-X.

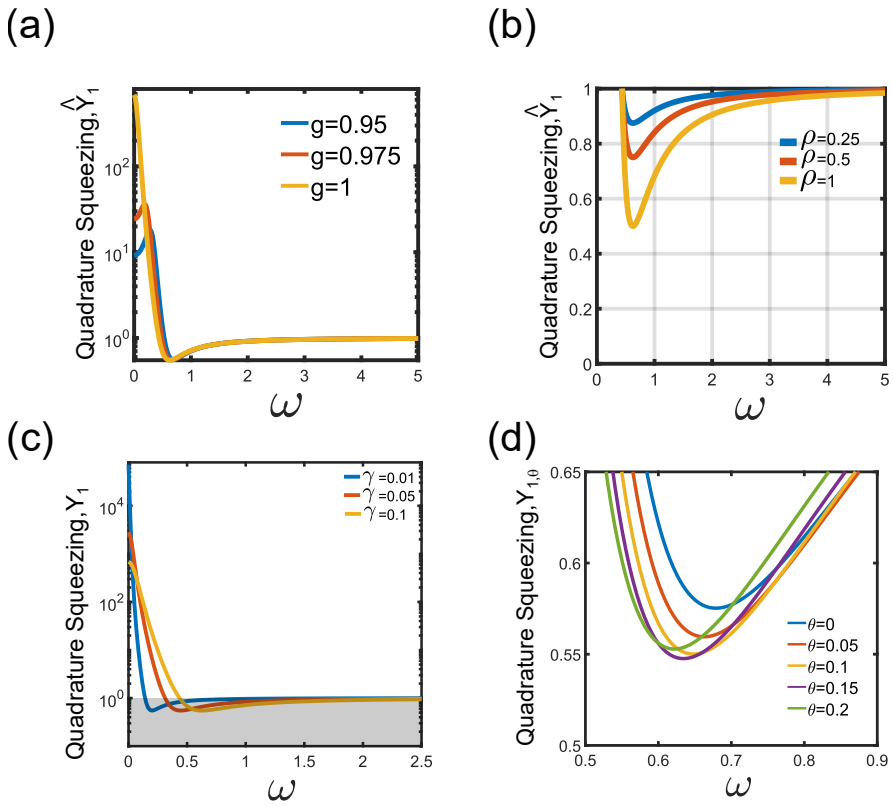

Figure 8.13: **Quadrature squeezing near EP.** a) The squeezing spectrum is plotted in log scale. The quadrature variance at DC diverges as we approach the exceptional point. Parameters used are: $f = g, \gamma = 0.1, \kappa = 1$, and $\rho = 0.9$. b) Squeezing spectrum as the parameter ρ is varied. Best squeezing performance is ideally obtained for $\rho = 1$. c) Divergence of the variance (PSD) at DC for different values of total round-trip loss γ. $\rho = 0.9$ is kept constant. d) Rotation of the optimum quadrature for squeezing. Parameters used are $f = g = 1, \gamma = 0.1, \rho = 0.9$, and $\Delta_1 = 0.1$. θ are measured in radians.

References

[1] Fatkhulla Kh Abdullaev, Yaroslav V. Kartashov, Vladimir V. Konotop, and Dmitry A Zezyulin. Solitons in PT-symmetric nonlinear lattices. *Physical Review A*, 83(4):041805, 2011.

[2] Diana A. Antonosyan, Alexander S. Solntsev, and Andrey A. Sukhorukov. Parity-time anti-symmetric parametric amplifier. *Optics Letters*, 40(20):4575–4578, 2015.

[3] Sid Assawaworrarit, Xiaofang Yu, and Shanhui Fan. Robust wireless power transfer using a nonlinear parity–time-symmetric circuit. *Nature*, 546(7658): 387, 2017.

[4] Subhadeep Chakraborty and Amarendra K. Sarma. Delayed sudden death of entanglement at exceptional points. *Physical Review A*, 100:063846, Dec 2019. doi: 10.1103/PhysRevA.100.063846. URL https://link.aps.org/doi/10.1103/PhysRevA.100.063846.

[5] Yanne K. Chembo. Quantum dynamics of Kerr optical frequency combs below and above threshold: Spontaneous four-wave mixing, entanglement, and squeezed states of light. *Physical Review A*, 93(3):033820, 2016.

[6] Chong Chen, Liang Jin, and Ren-Bao Liu. Sensitivity of parameter estimation near the exceptional point of a non-Hermitian system. *New Journal of Physics*, 21(8):083002, aug 2019. doi: 10.1088/1367-2630/ab32ab. URL https://doi.org/10.1088%2F1367-2630%2Fab32ab.

[7] Weijian Chen, Şahin Kaya Özdemir, Guangming Zhao, Jan Wiersig, and Lan Yang. Exceptional points enhance sensing in an optical microcavity. *Nature*, 548(7666):192, 2017.

[8] Mahboobeh Chitsazi, Huanan Li, F. M. Ellis, and Tsampikos Kottos. Experimental Realization of Floquet PT-Symmetric Systems. *Physical Review Letters*, 119(9):093901, 2017.

[9] Christian L. Degen, Friedemann Reinhard, and Paola Cappellaro. Quantum sensing. *Reviews of Modern Physics*, 89(3):035002, 2017.

[10] Jörg Doppler, Alexei A Mailybaev, Julian Böhm, Ulrich Kuhl, Adrian Girschik, Florian Libisch, Thomas J Milburn, Peter Rabl, Nimrod Moiseyev, and Stefan Rotter. Dynamically encircling an exceptional point for asymmetric mode switching. *Nature*, 537(7618):76, 2016.

[11] Ilya V. Doronin, Alexander A. Zyablovsky, Evgeny S. Andrianov, Alexander A. Pukhov, and A. P. Vinogradov. Lasing without inversion due to parametric instability of the laser near the exceptional point. *Physical Review A*, 100(2): 021801, 2019.

[12] Ramy El-Ganainy, Mercedeh Khajavikhan, and Li Ge. Exceptional points and lasing self-termination in photonic molecules. *Physical Review A*, 90(1): 013802, 2014.

[13] Ramy El-Ganainy, Jerry I. Dadap, and Richard M. Osgood. Optical parametric amplification via non-Hermitian phase matching. *Optics Letters*, 40(21):5086–5089, 2015.

[14] Liang Feng, Zi Jing Wong, Ren-Min Ma, Yuan Wang, and Xiang Zhang. Single-mode laser by parity-time symmetry breaking. *Science*, 346(6212): 972–975, 2014.

[15] Ryan Hamerly, Alireza Marandi, Marc Jankowski, Martin M. Fejer, Yoshihisa Yamamoto, and Hideo Mabuchi. Reduced models and design principles for half-harmonic generation in synchronously pumped optical parametric oscillators. *Physical Review A*, 94:063809, Dec 2016. doi: 10.1103/PhysRevA.94.063809. URL https://link.aps.org/doi/10.1103/PhysRevA.94.063809.

[16] Absar U. Hassan, Hossein Hodaei, Mohammad-Ali Miri, Mercedeh Khajavikhan, and Demetrios N. Christodoulides. Nonlinear reversal of the PT-symmetric phase transition in a system of coupled semiconductor microring resonators. *Physical Review A*, 92(6):063807, 2015.

[17] Absar U. Hassan, Bo Zhen, Marin Soljačić, Mercedeh Khajavikhan, and Demetrios N. Christodoulides. Dynamically encircling exceptional points: exact evolution and polarization state conversion. *Physical Review Letters*, 118(9):093002, 2017.

[18] Hossein Hodaei, Absar U. Hassan, Steffen Wittek, Hipolito Garcia-Gracia, Ramy El-Ganainy, Demetrios N. Christodoulides, and Mercedeh Khajavikhan. Enhanced sensitivity at higher-order exceptional points. *Nature*, 548(7666): 187, 2017.

[19] Ávila B. Jaramillo, C. Ventura-Velázquez, Yogesh N. Joglekar, B. M. Rodríguez-Lara, et al. PT-symmetry from Lindblad dynamics in a linearized optomechanical system. *Scientific Reports (Nature Publisher Group)*, 10(1), 2020.

[20] Kohei Kawabata, Yuto Ashida, and Masahito Ueda. Information retrieval and criticality in parity-time-symmetric systems. *Physical Review Letters*, 119 (19):190401, 2017.

[21] Friederike U. J. Klauck, Lucas Teuber, Marco Ornigotti, Matthias Heinrich, Stefan Scheel, and Alexander Szameit. Observation of PT-symmetric quantum interference. *arXiv preprint arXiv:1904.08135*, 2019.

[22] Yu-Hung Lai, Yu-Kun Lu, Myoung-Gyun Suh, Zhiquan Yuan, and Kerry Vahala. Observation of the exceptional-point-enhanced sagnac effect. *Nature*, 576(7785):65, 2019.

[23] Wolfgang Langbein. No exceptional precision of exceptional-point sensors. *Physical Review A*, 98(2):023805, 2018.

[24] Hoi-Kwan Lau and Aashish A. Clerk. Fundamental limits and non-reciprocal approaches in non-Hermitian quantum sensing. *Nature Communications*, 9 (1):4320, 2018.

[25] Jiaming Li, Andrew K. Harter, Ji Liu, Leonardo de Melo, Yogesh N. Joglekar, and Le Luo. Observation of parity-time symmetry breaking transitions in a dissipative Floquet system of ultracold atoms. *Nature Communications*, 10(1): 855, 2019.

[26] Zin Lin, Hamidreza Ramezani, Toni Eichelkraut, Tsampikos Kottos, Hui Cao, and Demetrios N Christodoulides. Unidirectional invisibility induced by P T-symmetric periodic structures. *Physical Review Letters*, 106(21):213901, 2011.

[27] Stefano Longhi. PT-symmetric laser absorber. *Physical Review A*, 82(3): 031801, 2010.

[28] Yaakov Lumer, Yonatan Plotnik, Mikael C. Rechtsman, and Mordechai Segev. Nonlinearly induced *pt* transition in photonic systems. *Physical Review Letters*, 111:263901, Dec 2013. doi: 10.1103/PhysRevLett.111.263901. URL https://link.aps.org/doi/10.1103/PhysRevLett.111.263901.

[29] Xiaobing Luo, Jiahao Huang, Honghua Zhong, Xizhou Qin, Qiongtao Xie, Yuri S. Kivshar, Chaohong Lee, et al. Pseudo-parity-time symmetry in optical systems. *Physical Review Letters*, 110(24):243902, 2013.

[30] Alireza Marandi, Zhe Wang, Kenta Takata, Robert L. Byer, and Yoshihisa Yamamoto. Network of time-multiplexed optical parametric oscillators as a coherent Ising machine. *Nature Photonics*, 8(12):937, 2014.

[31] Alexander McDonald, Tamar Pereg-Barnea, and Aashish A. Clerk. Phase-dependent chiral transport and effective non-Hermitian dynamics in a bosonic Kitaev-Majorana chain. *Physical Review X*, 8(4):041031, 2018.

[32] Pei Miao, Zhifeng Zhang, Jingbo Sun, Wiktor Walasik, Stefano Longhi, Natalia M. Litchinitser, and Liang Feng. Orbital angular momentum microlaser. *Science*, 353(6298):464–467, 2016.

[33] Mohammad-Ali Miri and Andrea Alù. Nonlinearity-induced PT-symmetry without material gain. *New Journal of Physics*, 18(6):065001, 2016.

[34] Mohammad-Ali Miri and Andrea Alù. Exceptional points in optics and photonics. *Science*, 363(6422):eaar7709, 2019.

[35] Murray K. Olsen and Peter D. Drummond. Entanglement and the Einstein-Podolsky-Rosen paradox with coupled intracavity optical down-converters. *Physical Review A*, 71(5):053803, 2005.

[36] Tatsuhiro Onodera, Edwin Ng, Niels Lörch, Atsushi Yamamura, Ryan Hamerly, Peter L McMahon, Alireza Marandi, and Hideo Mabuchi. Nonlinear quantum behavior of Ultrashort-Pulse Optical Parametric Oscillators. *arXiv preprint arXiv:1811.10583*, 2018.

[37] Şahin K. Özdemir, Stefan Rotter, Franco Nori, and Lan Yang. Parity–time symmetry and exceptional points in photonics. *Nature Materials*, 18(8):783–798, 2019.

[38] Bo Peng, Sahin K. Özdemir, Stefan Rotter, Huzeyfe Yilmaz, Matthias Liertzer, Faraz Monifi, Carl M. Bender, Franco Nori, and Lan Yang. Loss-induced suppression and revival of lasing. *Science*, 346(6207):328–332, 2014.

[39] Bo Peng, Şahin Kaya Özdemir, Fuchuan Lei, Faraz Monifi, Mariagiovanna Gianfreda, Gui Lu Long, Shanhui Fan, Franco Nori, Carl M. Bender, and Lan Yang. Parity–time-symmetric whispering-gallery microcavities. *Nature Physics*, 10(5):394, 2014.

[40] Hamidreza Ramezani, Tsampikos Kottos, Ramy El-Ganainy, and Demetrios N. Christodoulides. Unidirectional nonlinear PT-symmetric optical structures. *Physical Review A*, 82(4):043803, 2010.

[41] Arkadev Roy, Saman Jahani, Carsten Langrock, Martin Fejer, and Alireza Marandi. Spectral phase transitions in optical parametric oscillators. *arXiv preprint arXiv:2009.00930*, 2020.

[42] Cheng Wang, Mian Zhang, Xi Chen, Maxime Bertrand, Amirhassan Shams-Ansari, Sethumadhavan Chandrasekhar, Peter Winzer, and Marko Lončar. Integrated lithium niobate electro-optic modulators operating at CMOS-compatible voltages. *Nature*, 562(7725):101, 2018.

[43] Heming Wang, Yu-Hung Lai, Zhiquan Yuan, Myoung-Gyun Suh, and Kerry Vahala. Petermann-factor limited sensing near an exceptional point. *arXiv*, 2019.

[44] Yu-Xin Wang and Aashish A. Clerk. Non-Hermitian dynamics without dissipation in quantum systems. *Physical Review A*, 99(6):063834, 2019.

[45] Zi Jing Wong, Ye-Long Xu, Jeongmin Kim, Kevin O'Brien, Yuan Wang, Liang Feng, and Xiang Zhang. Lasing and anti-lasing in a single cavity. *Nature Photonics*, 10(12):796, 2016.

[46] Ling-An Wu, Harry J. Kimble, John L. Hall, and Huifa Wu. Generation of squeezed states by parametric down conversion. *Physical Review Letters*, 57 (20):2520, 1986.

[47] Haitan Xu, David Mason, Luyao Jiang, and Jack G. E. Harris. Topological energy transfer in an optomechanical system with exceptional points. *Nature*, 537(7618):80, 2016.

[48] Jae Woong Yoon, Youngsun Choi, Choloong Hahn, Gunpyo Kim, Seok Ho Song, Ki-Yeon Yang, Jeong Yub Lee, Yongsung Kim, Chang Seung Lee, Jai Kwang Shin, et al. Time-asymmetric loop around an exceptional point over the full optical communications band. *Nature*, 562(7725):86–90, 2018.

[49] Mengzhen Zhang, William Sweeney, Chia Wei Hsu, Lan Yang, A. Douglas Stone, and Liang Jiang. Quantum noise theory of exceptional point amplifying sensors. *Physical Review Letters*, 123(18):180501, 2019.

Chapter 9

TOPOLOGICAL OPTICAL PARAMETRIC OSCILLATION

Roy, Arkadev, Midya Parto, Rajveer Nehra, Christian Leefmans, and Alireza Marandi. Topological optical parametric oscillation. ***Nanophotonics***, 11(8):1611–1618, 2022. doi: https://doi.org/10.1515/nanoph-2021-0765.
A.R. contributed to the conception of the project, developed the analytical modeling, performed numerical simulations, and participated in the writing of the manuscript.

9.1 Abstract

Topological insulators possess protected boundary states which are robust against disorders and have immense implications in both fermionic and bosonic systems. Harnessing these topological effects in non-equilibrium scenarios is highly desirable and has led to the development of topological lasers. The topologically protected boundary states usually lie within the bulk bandgap, and selectively exciting them without inducing instability in the bulk modes of bosonic systems is challenging. Here, we consider topological parametrically driven nonlinear resonator arrays that possess complex eigenvalues only in the edge modes in spite of the uniform pumping. We show parametric oscillation occurs in the topological boundary modes of one and two dimensional systems as well as in the corner modes of a higher-order topological insulator system. Furthermore, we demonstrate squeezing dynamics below the oscillation threshold, where the quantum properties of the topological edge modes are robust against certain disorders. Our work sheds light on the dynamics of weakly nonlinear topological systems driven out-of-equilibrium and reveals their intriguing behavior in the quantum regime.

9.2 Introduction

Topological invariance and its consequences on material properties originally studied in condensed matter physics has expanded its ambit and has been investigated in diverse fields [18, 21, 22, 32, 36, 40]. Of prime interest is the presence of topologically protected edge modes which inherit their robustness from the non-trivial topology of the bulk. The introduction of topology in photonics promises a number of functionalities that leverage backscatter-free unidirectional light transport of such modes[17].

Topologically protected edge states usually lie within the bulk bandgap. Topological consequences in particle-conserving fermionic Hamiltonians are manifested when the Fermi energy level lies within this bandgap. Under these circumstances, the near-equilibrium dynamics are dictated by the degrees of freedom associated with the boundary/edge modes of the system. On the contrary, for bosonic systems, particles tend to condense in the lowest bulk band, resulting in the system dynamics being largely unaffected by the edge states. Thus ensuring selective participation of edge modes in bosonic topological insulators requires special attention, and most experimental investigations for these systems involved directly exciting bosons into these edge modes [18].

The topological insulator laser is a bosonic system driven out of equilibrium where lasing happens preferentially in the edge modes. These topologically protected lasers can outperform their topologically trivial counterpart in terms of slope efficiency, coherence, and robustness against disorders [2, 4, 19, 47]. To suppress the bulk modes in the topological lasing, the edge modes should be unstable while the bulk bands maintain stability. One potential approach in this regard is non-Hermitian PT-symmetric Hamiltonian engineering of 1D systems [37]. However, this cannot be extended in general to higher dimensions to realize chiral propagating edge states. Non-Hermitian coupling engineering has been proposed to realize robust and stable lasing [28, 29]. Another approach involves selective pumping of the edge sites to realize topological lasing [4, 19]. Nonetheless, it is highly desirable to achieve topological edge-gain effect under uniform pumping [3, 46].

Recently, much attention has been devoted to the rich interplay between optical nonlinearities and topology [23, 45]. The addition of nonlinearity leads to a variety of intriguing possibilities such as nonlinearity-driven topological phase transitions [33] and self-localization [26]. Incorporating parametrically driven quadratic nonlinearity into a topological system can result in topologically protected parametric amplification and chiral inelastic transport [5, 11, 38, 39]. Owing to the particle non-conserving nature of these parametric interactions, it can cause exponentially growing bosonic occupation, which in the suitable regime of operation can lead to edge-only dynamic instability [6, 15]. This parametric gain being inherently instantaneous is devoid of slow carrier dynamics that can cause deleterious effects in the case of topological lasers based on semiconductor gain medium [30]. Exploiting the squeezing dynamics in these quadratic nonlinear systems also opens new avenues for leveraging topological effects in the quantum

regime. The topological insulating phenomenon when applied to the quantum states can result in the topological protection of quantum statistics and quantum correlations [9, 41, 49].

We show topological optical parametric oscillation in a network of quadratic nonlinear resonators where the underlying linear Hamiltonian is topological. We drive the system in a parameter regime where it exhibits edge instability under uniform excitation. We demonstrate edge mode parametric oscillation in both 1D and 2D topological insulating systems as well as corner mode parametric oscillation in a higher-order topological insulator. We show the presence of squeezed quantum state below the oscillation threshold which is robust against perturbations arising from symmetry-preserving disorders.

9.3 Results

We aim to achieve the topological edge-gain effect using parametric interactions induced by quadratic nonlinearity. To illustrate the scenario, we begin with the 1D Su-Schrieffer-Heeger (SSH) model, which was originally proposed for the explanation of mobile neutral defects in polyacetylene [48]. The SSH model consists of a chain of coupled sites with intra-cell coupling ($\kappa_1 = J(1-\epsilon)$) and inter-cell coupling ($\kappa_2 = J(1+\epsilon)$), where ϵ denotes the asymmetry in the hopping strengths. Provided $\kappa_1 < \kappa_2$, the 1D lattice hosts topological edge modes. In the Hermitian case, the edge mode lies within the bulk bandgap as shown in Fig. 9.1(c), and the application of uniform laser gain leads to bulk instability. To ensure edge-only lasing, non-Hermitian PT-symmetric Hamiltonian can be engineered with alternate gain and loss as shown in Fig. 9.1(a) [37, 53]. Figure 9.1(d) shows that under the application of this non-uniform phase-insensitive laser gain, the edge mode selectively experiences instability while the bulk modes remain stable ($\mathrm{Im}(\lambda) = 0$). Alternatively, we can exploit the unitary correspondence between non-Hermitian dynamical systems and the Heisenberg equations of motion governing parametrically driven quadratically nonlinear systems to achieve the topological edge-gain effect [42, 50]. The system resembles a lattice of coupled nonlinear resonators that experience uniform parametric gain as shown in Fig. 9.1(b). The parametric amplification/ de-amplification can replicate the dynamics of the non-Hermitian PT-symmetric SSH model in a non-dissipative setting as shown in Fig. 9.1(b) and Fig. 9.2(a).

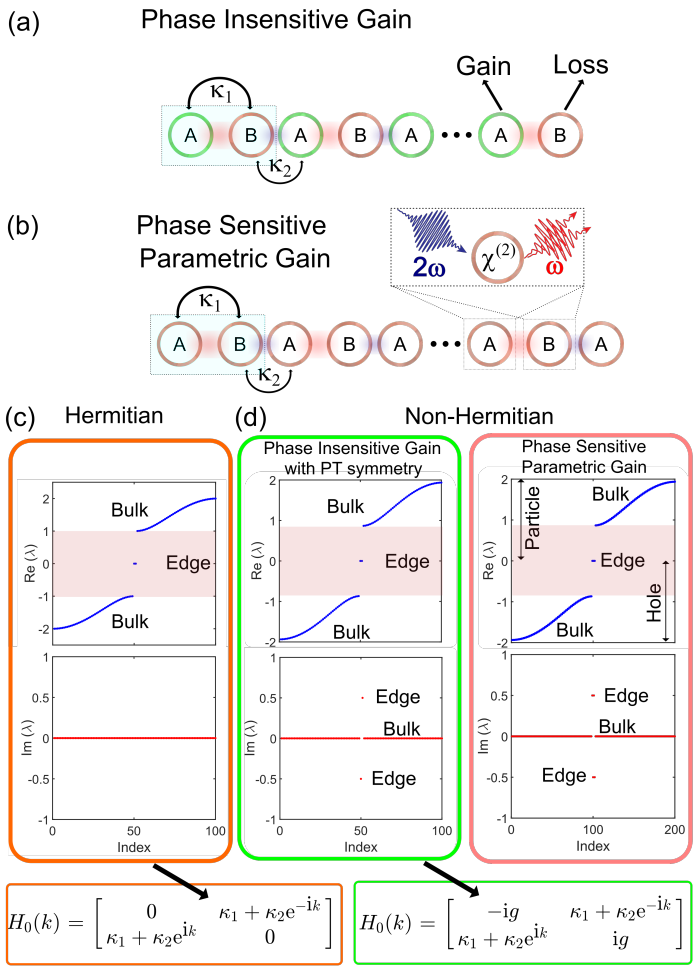

Figure 9.1: **Topological edge-gain induced by parametric interaction.** a) Conventional topological edge-gain realized with alternate phase-insensitive laser gain and loss arrangement in an SSH chain of resonators. b) Similar edge-gain can be implemented with uniform parametric gain in an SSH chain of nonlinear resonators, where the quadratic nonlinearity ($\chi^{(2)}$) couples the pump (2ω) and the signal (ω) waves. c) Eigenvalue diagram (real part (top) and imaginary part (bottom)) for a Hermitian SSH model showing the topologically protected edge mode lying within the bandgap. Edge-only instability is not possible in this case. d) Eigenvalue diagram for a non-Hermitian setting realized either utilizing phase-insensitive gain (left) as shown in (a) or using the phase-sensitive parametric gain as shown in (b). The eigenvalue diagram depicts the edge-gain effect where the topologically protected mode has non-zero while the bulk modes have zero imaginary parts, respectively. The momentum space (k) Hamiltonian (H_0) for the 1D Hermitian SSH and phase insensitive gain (g) with PT symmetry SSH are also shown. Here, Index refers to a sequential label for the eigenvalues corresponding to the number of interacting resonators/ OPOs (N).

We consider quadratic ($\chi^{(2)}$) nonlinear resonators with phase-matched parametric interaction between the pump at 2ω and signal at ω. The nonlinear part of the Hamiltonian is given by:

$$\hat{\mathcal{H}}_{NL} = \sum_n \frac{g}{2}(\hat{a}_n \hat{a}_n + H.c.) \tag{9.1}$$

where g is the strength of the parametric interaction that depends on the effective $\chi^{(2)}$ nonlinearity and the incident pump power. $\hat{a}, \hat{a}^\dagger$, represents the annihilation and the creation operators, respectively. The saturation effects of the parametric gain (assuming a non-resonant pump) are discussed in 9.5.4 of the Supplementary section. The linear part of the Hamiltonian according to the SSH model is given by:

$$\hat{\mathcal{H}}_L = J \sum_n (1 + \epsilon(-1)^n) \left(\hat{a}_n^\dagger \hat{a}_{n+1} + H.c. \right). \tag{9.2}$$

For a lattice of N sites, the full Hamiltonian can be expressed as $\hat{\mathcal{H}} = \frac{1}{2}\psi^\dagger H \psi$, where $\psi = (\hat{a}_1, \ldots \hat{a}_N, \hat{a}_1^\dagger, \ldots \hat{a}_N^\dagger)^T$, and $\hat{\mathcal{H}} = \hat{\mathcal{H}}_L + \hat{\mathcal{H}}_{NL}$. H is the 2N × 2N Bogoliubov-de Gennes (BdG) Hamiltonian. The dynamics of the system is determined by the eigenvalues of the BdG equation: $\sigma_z H \psi_{n\pm} = \pm E_n \psi_{n\pm}$, where σ_z is the Pauli matrix, $\psi_{n\pm}$ is a 2N dimensional eigenvector [6]. E_n are the eigenenergies. Because of the particle-hole symmetry of the BdG Hamiltonian, the eigenvalues $\pm E_n$ appear in pairs. For each pair of real eigenvalues, we can identify the eigenvector as being a particle with a positive norm $\psi_{n+}^\dagger \sigma_z \psi_{n+} > 0$, and the other being a hole with a negative norm $\psi_{n-}^\dagger \sigma_z \psi_{n-} < 0$ [15].

If $g < 2J\epsilon$, then we can ensure that the parametric gain will only induce instability in the edge modes, while the bulk will remain stable (see Supplementary Section 9.5.1). The eigenvalue distribution in such a scenario is shown in Fig. 9.1(d, right). When the parametric gain experienced by the edge modes exceeds the net loss, there will be a growth of photon number in the edge eigenmode. However, the onset of gain saturation prevents exponential growth and the parametric oscillation reaches a steady state (see Supplementary Section 9.5.4). The steady-state intensity distribution of the oscillating supermode is shown in Fig. 9.2(b). The intensity distribution bears the characteristics of the edge mode as evident from the alternate site occupation. However, if $g > 2J\epsilon$, the bulk modes will also become dynamically unstable (see Supplementary Section 9.5.1). Various non-Hermitian phase transitions characterizing the system (regions of instability) can also be revealed from the discontinuities in the derivatives of the imaginary part of the

complex Berry phase (see Supplementary section 9.5.7). The steady-state intensity distribution in this scenario is shown in Fig. 9.2(c).

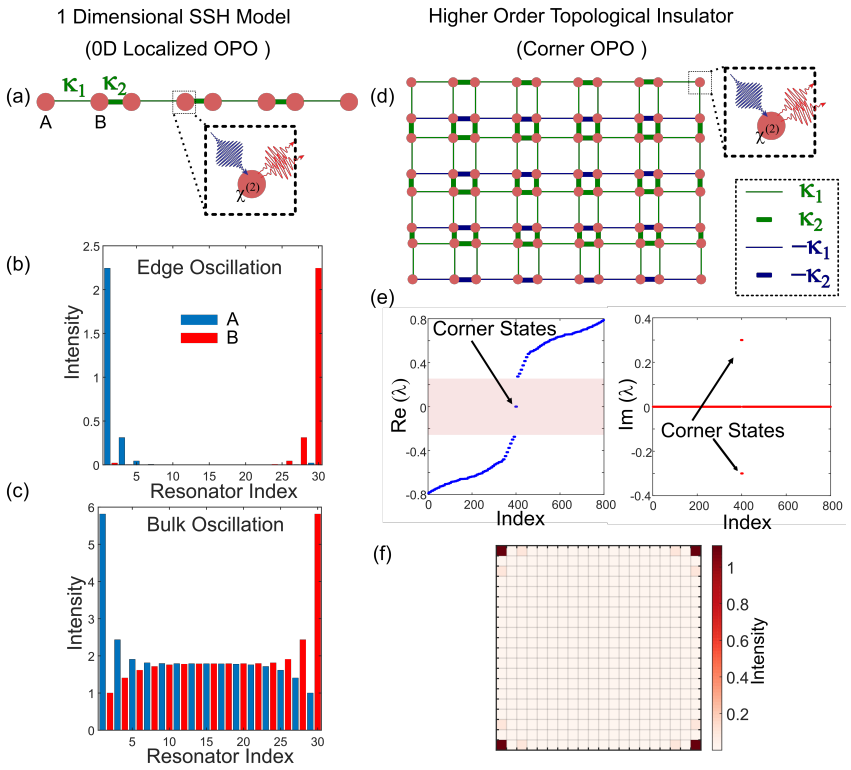

Figure 9.2: **Non-propagating topological parametric oscillation**. a) Schematic of 1D SSH model of quadratic nonlinear resonators hosting 0D localized edge modes, where the intra-cell coupling (κ_1, thin lines) is weaker than the inter-cell coupling (κ_2, thick lines). b) parametric oscillation when only the edge modes experience instability, while the bulk modes are stable. c) oscillation when the parametric gain also induces instability in the bulk modes. d) Schematic of 2D lattice of quadratic nonlinear resonators hosting corner modes. Thick and thin lines indicate strong and weak coupling, respectively, while green and blue color represents positive and negative couplings. e) Eigenvalue diagram (the real part (left) and the imaginary part (right)) showing the corner states lying within the bandgap with the non-zero imaginary part while the bulk modes are stable. f) parametric oscillation in the corner modes of the 2D lattice.

Next, we consider a 2D lattice of quadratic nonlinear resonators with quantized quadrupole moment [7, 8, 35]. The higher-order topological insulator can host localized corner states. The schematic of the 2D lattice featuring couplings with different hopping strengths and phases is shown in Fig. 9.2(d). These couplings can be realized in a photonic platform using auxiliary non-resonant coupling cavities [18]. Under uniform parametric pumping, it is possible to induce selective instability in the corner states, while the bulk modes remain stable. The eigenvalue distribution

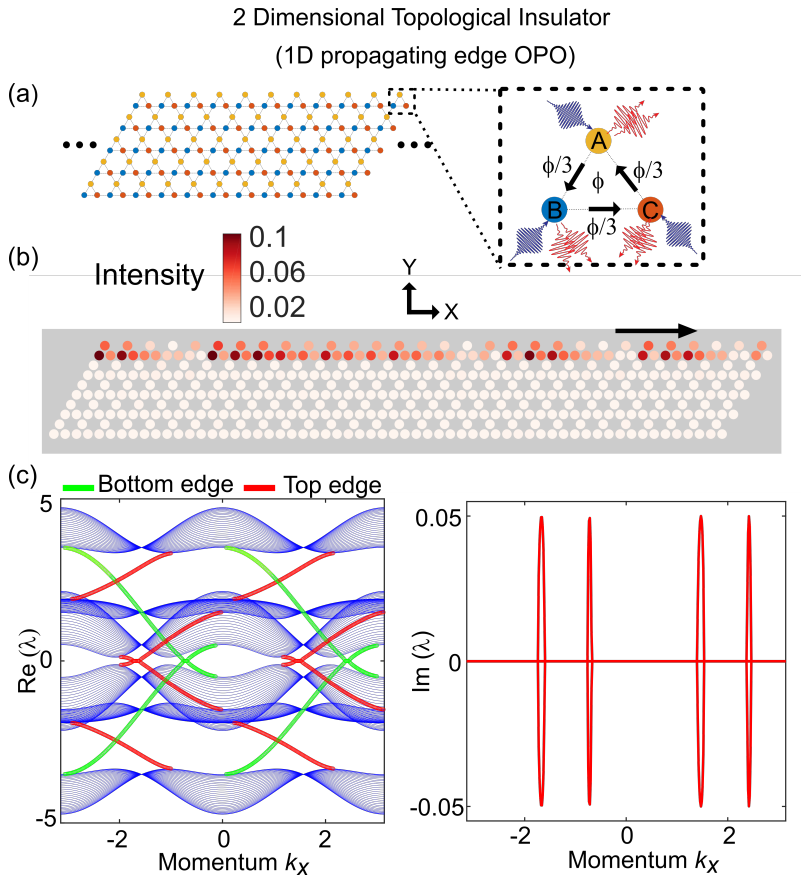

Figure 9.3: **Chiral topological parametric oscillation.** a) Schematic of an anomalous quantum Hall effect topological insulator arranged in the form of Kagome lattice. The zoomed-in view shows the nonlinear resonators with parametric gain and the gauge flux (ϕ). b) parametric oscillation in the chiral edge state of a one-dimensional strip of the 2D Kagome lattice (finite in y, and periodic boundary condition along x). c) Band diagram (the real part (left) and the imaginary part (right)) showing the edge modes experiencing gain. The edge states confined on the top and bottom edges are marked in red and green, respectively.

in such a scenario is shown in Fig. 9.2(e). When the parametric gain is above the oscillation threshold, the system can undergo parametric oscillation in the corner modes as shown by the lattice intensity distribution in Fig. 9.2(f).

So far we have considered parametric oscillation in localized topological edge states. Now we explore parametric oscillation in chiral propagating edge states. We consider an infinite strip of nonlinear resonators (finite in Y, infinite/ periodic boundary condition in X) arranged in the form of a Kagome lattice as shown in Fig. 9.3(a). A gauge flux of ϕ is enclosed in each triangular plaquette. The system corresponds to an anomalous quantum Hall topological insulator [34]. The linear

part of the Hamiltonian is given by:

$$\hat{\mathcal{H}}_L = J \sum_n \Delta \hat{a}_n^\dagger \hat{a}_n + \sum_{<n,n'>} \kappa_{n,n'} \hat{a}_n^\dagger \hat{a}_{n'} \tag{9.3}$$

where n=(n_x, n_y, s) is the vector site index, with n_x, n_y indicating the position of the unit cell in the 2D lattice, while the index $s \in (A, B, C)$ indicates the component of the sublattice. $< n, n' >$ denotes the sum of the contributions over nearest neighbours. Δ is the on-site detuning. The hopping term $\kappa_{n,n'}$ is given by $\kappa_{n,n'} = J e^{i\phi_{s,s'}}$ where $\phi_{AB} = \phi_{BC} = \phi_{CA} = \frac{\phi}{3}$. The nonlinear part of the Hamiltonian ($\hat{\mathcal{H}}_{NL}$) is the same as before. This nonlinear topological insulator is characterized by the symplectic Chern numbers [11]. With appropriate values of the detuning (Δ) and the gauge flux (ϕ) the particle and hole bands cross each other (see Supplementary Section 9.5.2). Thus, it creates a bandgap where the chiral edge states cross the zero energy. In the presence of non-zero parametric interactions, the chiral edge states can develop instability. This is displayed in the band diagram shown in Fig. 9.3(c). The parametric oscillation obtained in this case is confined along the edge as depicted in the lattice intensity distribution in Fig. 9.3(b). The corresponding edge states in the band diagram (Fig. 9.3(c)) are shown in green (bottom edge) and red (top edge). It is to be noted that the particle and hole edge states are mirror images in the band diagram. The chiral nature can be observed in the dynamic evolution of the parametric oscillation (see Supplementary Section 9.5.2).

Below the oscillation threshold, optical parametric oscillators (OPOs) can display quadrature squeezing, where the noise in one quadrature is squeezed below the shot noise limit, and the excess noise is accumulated in the orthogonal quadrature [51]. Squeezed quantum states are an important resource in sensing [1]. However, preserving the squeezing in the quadrature of interest is challenging. The occurrence of detuning or any other disorder can rotate the optimum squeezing quadrature and the squeezing in the original quadrature can be degraded due to the mixing of the anti-squeezed component. Here, we investigate the behavior of the topological quantum squeezed state in the presence of disorders. We consider the 1D SSH model (Fig. 9.2(a)), whose dynamics is modeled using the Heisenberg Langevin equations [12]. The quadrature squeezing spectrum of the topological edge mode is shown in Fig. 9.4(a). The edge mode is mostly confined to the boundary resonator. Thus the squeezing obtained in the edge/boundary OPO is close to that contained in the edge mode. Thus by accessing the boundary OPO, we can harness the benefits

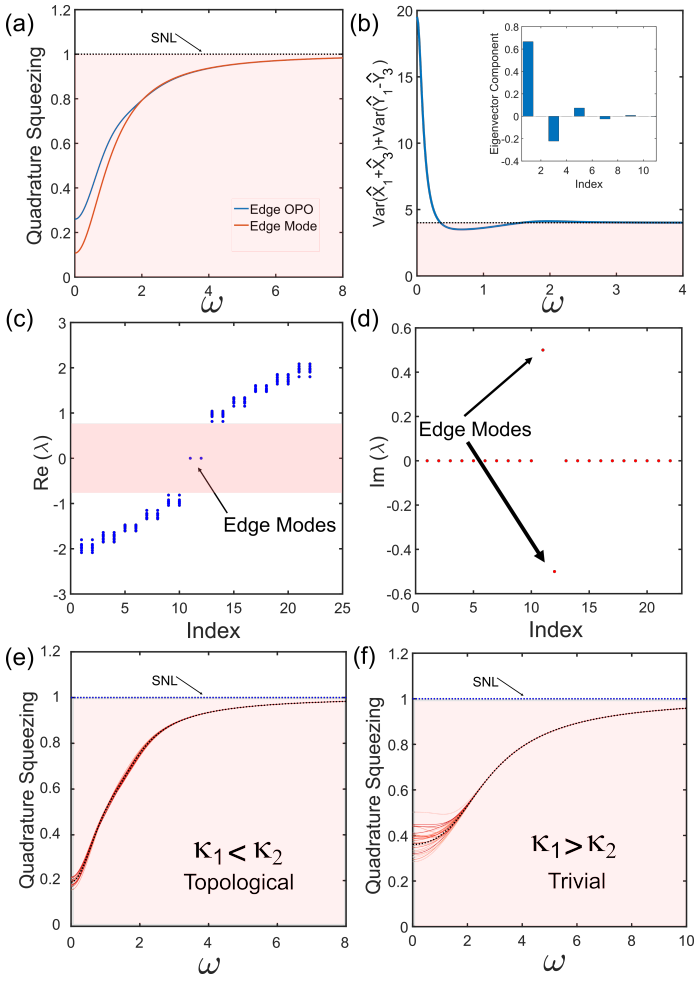

Figure 9.4: **Topological protection in the quantum regime.** a) Quadrature squeezing observed in the topological edge mode of the 1D SSH model of the quadratic nonlinear resonators when the parametric gain is below the oscillation threshold. The edge super mode spans over multiple resonators (inset of (b) showing the edge eigenvector), while the edge OPO refers to the boundary resonator only. SNL represents the shot noise limit. b) Entanglement between the first and the third resonator of the edge mode as evident from the Duan criterion, where the sum of the variances is less than 4. Eigenvalue diagram c) real part and d) imaginary part showing the robustness of the edge mode to the coupling disorders. Multiple eigenvalue diagrams corresponding to different coupling disorder realizations are overlaid together. e) Protection of the quadrature squeezing in the presence of coupling disorders in the topological case ($\kappa_1 < \kappa_2$). f) The trivial case ($\kappa_1 > \kappa_2$) is more susceptible to squeezing degradation in the presence of coupling disorders. Multiple squeezing spectra calculated in the fixed quadrature under different disorder realizations are overlaid together. The black dotted line corresponds to the squeezing spectrum in the absence of disorder. The X axis (ω) of all these sub-figures refers to the analysis frequency of the signal corresponding to the homodyne detection.

of topological protection in the quantum regime. The edge eigenvector spans over multiple resonators, with occupations in only one of the sublattices, and alternate in sign (π staggered) as shown in the inset of Fig. 9.4(b). The adjacent A sites of the edge mode, i.e., (resonators 1 and 3) are entangled as confirmed by the Duan inseparability criterion [13]. The entanglement is reflected in the sum of quadrature component variances as shown in Fig. 9.4(b).

The bulk bands are affected by the presence of random disorders in the coupling strengths, while the edge mode exhibit robustness. This is shown in the variation of the eigenvalue diagram over multiple disorder realizations in Fig. 9.4(c,d). Consequently, the quadrature squeezing is protected in the topological case (Fig. 9.4(e)). In contrast, the non-topological case is more susceptible to squeezing degradation in the presence of coupling disorders as shown in Fig. 9.4(f) (see Supplementary Section 9.5.3). The 1D SSH model cannot provide protection from detuning disorders which do not preserve the chiral symmetry (see Supplementary Section 9.5.3).

9.4 Discussion

Our proposed system consisting of a lattice of OPOs can be realized in thin-film lithium niobate on insulator platform [10, 16, 31]. In order to realize a 1D SSH lattice, the OPOs have to be coupled with each other [43] which can be executed via evanescent coupling based directional couplers.

Nanoscale OPOs can also be a promising route to realize the same [20]. Zigzag arrays comprising of $\chi^{(2)}$ dielectric nanoparticles under uniform illumination could be engineered to realize the edge-mode parametric oscillation [23, 44]. Alternatively, one can exploit synthetic dimensions to construct a lattice of OPOs in the time/ frequency domain [14, 25]. Arrays of polaritonic oscillators can potentially be designed to realize this phenomenon as well [24].

9.5 Supplementary

9.5.1 Parametric Oscillation in 1D SSH model

The SSH model consists of N-coupled quadratic nonlinear resonators where $\kappa_1 < \kappa_2$. If N is odd, there will be one edge mode, while if N is even there will be two edge modes on either side. The parametric oscillation steady state intensity distribution in both cases is shown in Fig. 9.5(a,b).

Now, we derive the condition for bulk instability. For this case, we can assume periodic boundary conditions, thereby no existence of edge modes. The linear Hamiltonian in the momentum domain (k) is given by:

$$H_L = \begin{bmatrix} 0 & \frac{\kappa_1+\kappa_2 e^{-ik}}{2} \\ \frac{\kappa_1+\kappa_2 e^{ik}}{2} & 0 \end{bmatrix} \tag{9.4}$$

where, we assume $\kappa_1 = J(1-\epsilon)$ and $\kappa_2 = J(1+\epsilon)$. We assume $J = 1$. All parameters are normalized with respect to J. The Bogoliubov- de Gennes Hamiltonian is given as:$H_{BdG} = \begin{bmatrix} H_L & H_{NL} \\ H_{NL} & H_L \end{bmatrix}$, where H_{NL} is given by:

$$H_{NL} = \begin{bmatrix} g/2 & 0 \\ 0 & g/2 \end{bmatrix}. \tag{9.5}$$

The eigenvalues determining the dynamical stability of the system are given the eigenvalues of $\sigma_z H_{BdG}$ which can be expressed as:

$$\lambda = \pm\sqrt{\frac{1+\epsilon^2}{2} + \frac{1-\epsilon^2}{2}\cos(k) - \frac{g^2}{4}}. \tag{9.6}$$

Therefore, bulk instability will occur for $g > 2\epsilon$, when the eigenvalues will be imaginary. Such a distribution of eigenvalues in such a scenario is given in Fig. 9.5(c,d).

9.5.2 Parametric oscillation in 2D Lattice

Topologically trivial case

We consider a scenario where the gauge field is zero in the 2D Kagome lattice. This is the topologically trivial case. In this case, in the presence of quadratic parametric interactions bulk instability will occur. The band diagram is shown in Fig. 9.6(a,b). The intensity distribution of the OPOs arranged in the lattice is shown in Fig. 9.6(c), showing the oscillation occurs throughout the lattice.

Topologically non-trivial case

In the presence of a gauge field, and the appropriate parameters we obtain topologically protected chiral edge states. We are considering the non-positive

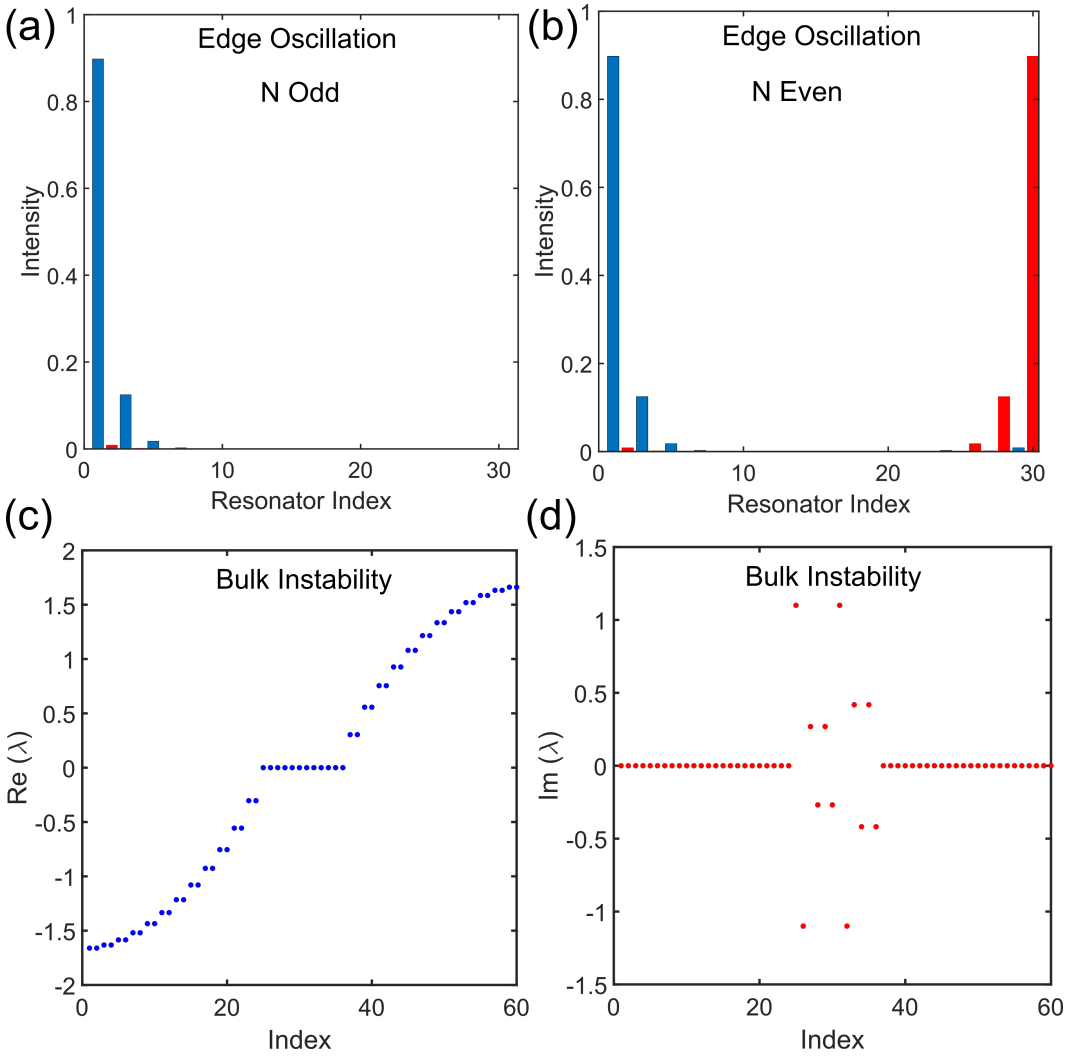

Figure 9.5: Parametric oscillation in the edge mode for 1D SSH model when a) N is odd and b) N is even. Eigenvalue diagram when bulk instability occurs c) the real part and d) the imaginary part. Parameters used in the simulation are: $J = 1, \epsilon = 0.5, g = 1.1$, and $N = 30$.

definite case of the bosonic pairing Hamiltonians [11]. Here the particle and hole bands cross each other. The particle bands are identified as: $V^{\dagger}\sigma_z V > 0$, and the hole bands as: $V^{\dagger}\sigma_z V < 0$, where V is the eigenvector. The band diagram with the particle and hole bands is shown in Fig. 9.7(a).

In the presence of a defect in the form of a missing lattice unit cell, the edge is modified around the defect, but still, the chirality is retained in the topologically non-trivial case. The intensity distribution of the OPOs arranged in the lattice is shown in Fig. 9.7(b), showing the oscillation occurring along the edge surrounding the defect.

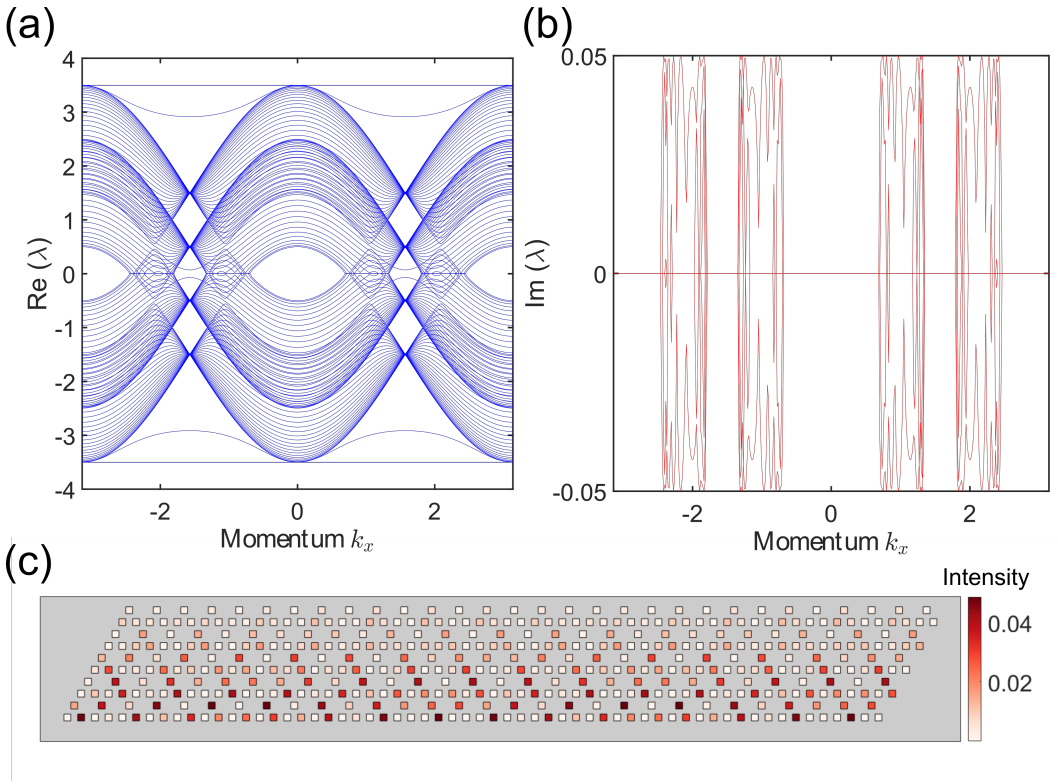

Figure 9.6: **Parametric oscillation in the topologically trivial case.** Band diagram of the Kagome lattice strip with a) showing the real and b) the imaginary part of the eigenvalues. c) The intensity distribution of the OPOs in the lattice in the topologically trivial case.

The time domain evolution of the intra-cavity intensity of an OPO lying on the edge is shown in Fig. 9.8(a,b). The spectral domain power distribution is shown in Fig. 9.8(c). The intra-cavity field of the OPOs on the edge are phase-locked with respect to each other.

9.5.3 1D SSH lattice in the quantum regime

In order to compare the protection of squeezed quantum state from coupling disorders between topologically non-trivial and trivial cases, we consider the following. We consider a topologically trivial SSH lattice where $\kappa_1 > \kappa_2$. We select the gain parameter such that one mode undergoes instability (non-zero imaginary part). This is shown in Fig. 9.9. The eigenvector is mostly localized in the Nth resonator. We compare the quadrature squeezing in this resonator with the edge OPO of the topologically non-trivial case in the main text. Both cases are taken to be equal times below the oscillation threshold, and same out-coupling efficiency.

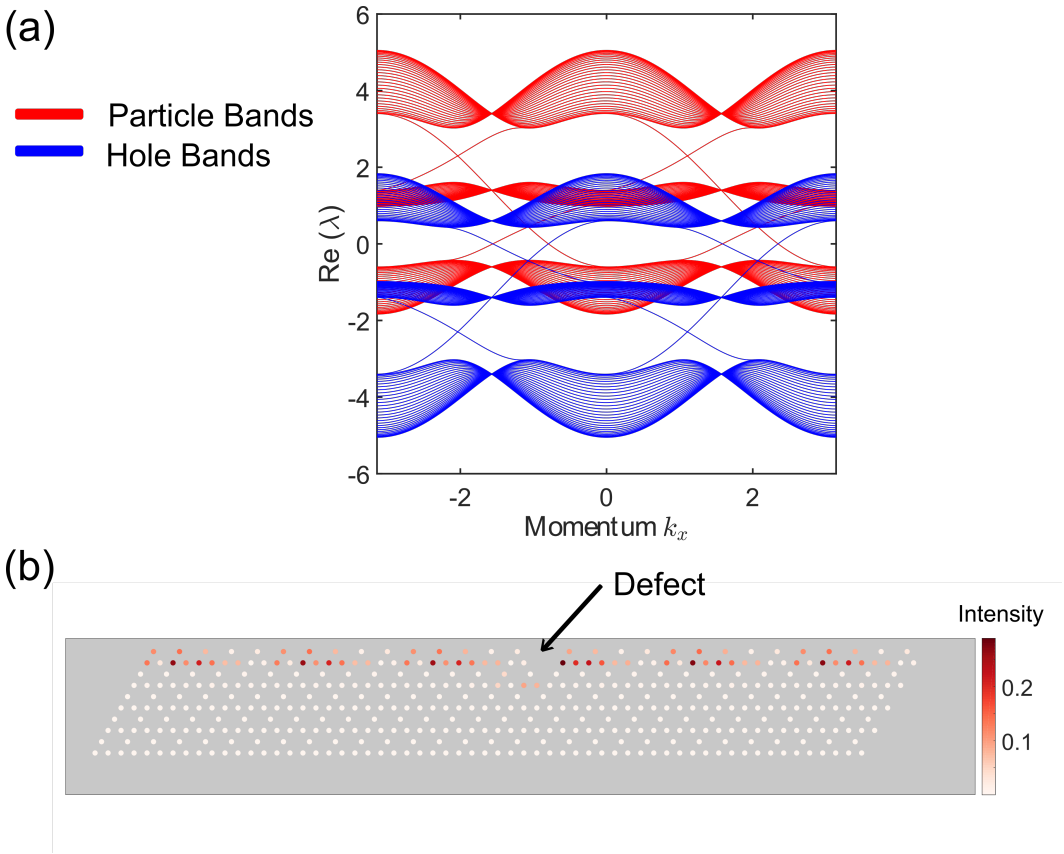

Figure 9.7: **Parametric oscillation in the topologically non-trivial case.** a) Particle and the hole bands in the band diagram. Parameters used in the simulation are $\Delta = 1.4, \phi = 0.6\pi, g = 0, J = 1$. b) The intensity distribution of the OPOs in the lattice in the topologically non-trivial case in the presence of a defect.

The squeezed quantum state in the 1D SSH model is robust to coupling disorders when the coupling disorder strength is small compared to the bandgap. However, it is not protected from detuning-induced disorder. The detuning disorder does not preserve the chiral symmetry of the SSH model. In the presence of detuning disorder, the optimum squeezed quadrature gets rotated and the squeezing is degraded due to the influence of the anti-squeezed quadrature. Fig. 9.10(a) shows that the squeezed quantum state is susceptible to the detuning-induced disorder.

When we ensure that the edge mode only experiences gain, and all other modes are stable. This causes a gap in the imaginary part of the eigenvalue spectrum. With the increasing value of the gain parameter (g), this gap increases. Increasing this gap results in the less deleterious effects of the detuning disorder. The dependence of the degradation of squeezing in the presence of detuning disorder as a function of the gain parameter is shown in Fig. 9.10(b). The error bar indicates the standard

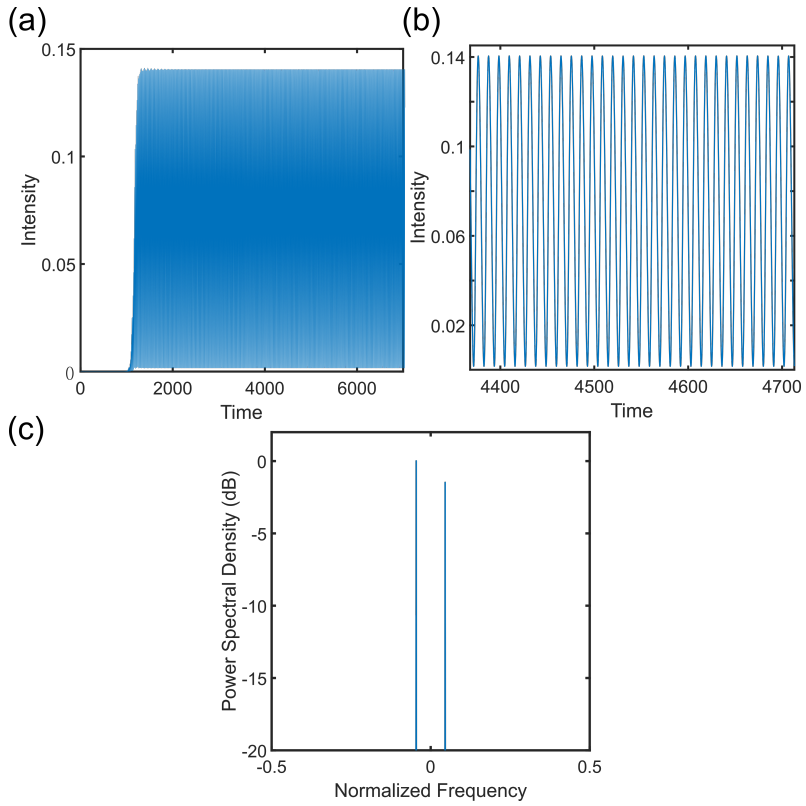

Figure 9.8: **Temporal evolution of an OPO lying on the edge in the 2D Kagome lattice.** a) Time domain evolution of the intra-cavity intensity of an OPO lying on the edge in the 2D Kagome lattice. b) The zoomed-in view of (a). c) Power spectral density. Parameters used in the simulation are: $\Delta = 1.4, \phi = 0.6\pi, g = 0.015, J = 1, \alpha = 0.002, g_s = 0.1$

deviation of the squeezing variation for each gain parameter value where 5 sets of 100 realizations of the disorder are considered. However, this is not a topological effect.

9.5.4 Model of the OPO in the classical regime

We model the OPO using a simplified governing equation that takes into account the parametric gain and the gain saturation (due to the second harmonic generation of the signal back to the pump). We assume the OPO to operate at degeneracy. The parametric oscillation occurs in a high Q cavity and is oscillating in a CW mode.

Non-resonant pump configuration

The quadratic nonlinear interaction happening in the phase-matched $\chi^{(2)}$ region is given by:

$$\frac{da}{dz} = \epsilon b a^* \tag{9.7a}$$

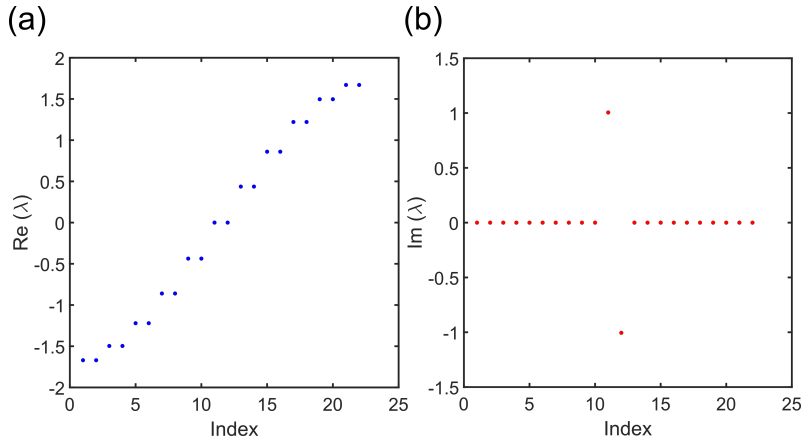

Figure 9.9: **Eigenvalue diagram for topologically trivial SSH lattice with gain experienced by a single mode.** a) the real part. b) the imaginary part. The parameters used in the simulation are : $g = 1.005, \alpha = 1.206, \rho = 0.9, \epsilon = 0.5, J = 1, N = 11$.

$$\frac{db}{dz} = -\frac{\epsilon}{2}a^2 \tag{9.7b}$$

where a and b represent the signal and pump field envelopes, respectively. ϵ is the effective nonlinear coefficient. Let, L be the length of the nonlinear interaction region. In the high Q limit, we can assume that the field does not change significantly within a round-trip. So, Eq. 9.7b can be expressed in the n^{th} round-trip as:

$$b_n = b_0 - \frac{\epsilon}{2}La_n^2 \tag{9.8}$$

where, b_0 is the input pump. We can express the evolution of the signal field on a round-trip basis as:

$$a_{n+1} = a_n + \epsilon b_0 L a_n^* - \frac{1}{2}\epsilon^2 L^2 |a_n|^2 a_n. \tag{9.9}$$

The loss in each round-trip can be included as:

$$a_{n+1} = a_n e^{-\gamma T}. \tag{9.10}$$

The detuning in each round-trip can be included as:

$$a_{n+1} = a_n e^{\mathrm{i}\Delta T} \tag{9.11}$$

where ΔT is the total detuning per round-trip. where, γ is the loss per unit time, and T is the round-trip time. In the high Q limit, we can convert the difference equation

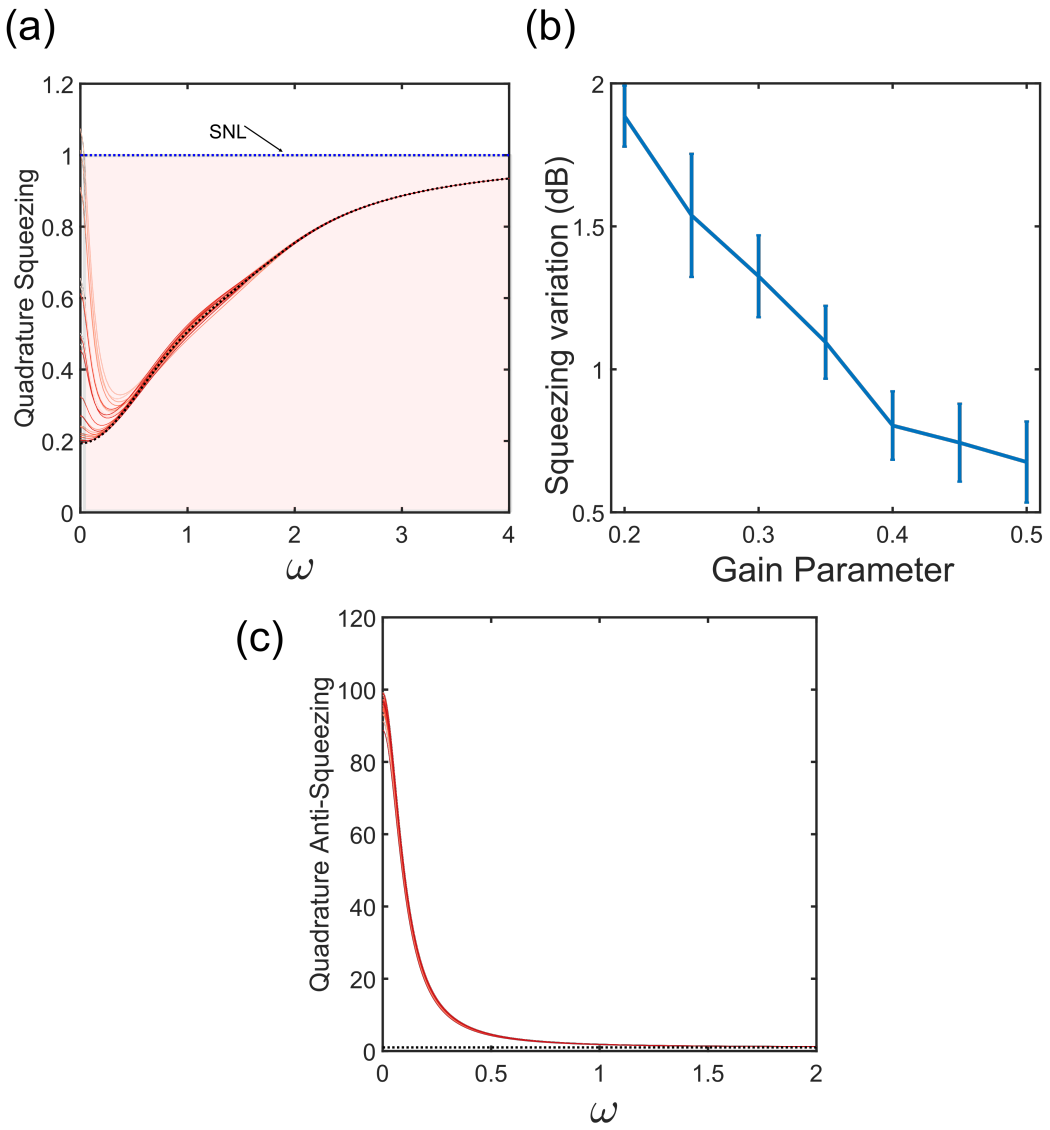

Figure 9.10: **Effect of detuning-induced disorder.** a) Absence of robustness in the quadrature squeezing for the edge OPO, in the presence of detuning disorder. Multiple squeezing spectra corresponding to different disorder realizations are overlaid on top of each other. The black dotted line refers to the squeezing in the absence of detuning and coupling disorder. SNL refers to the shot noise limit. The parameters used in the simulation are: $g = 1, \alpha = 1.2, \rho = 0.9$(out-coupling efficiency), $\epsilon = 0.5, J = 1, N = 11$. b) effect of the eigenvalue gap (in the imaginary component of the eigenvalue) on the quadrature squeezing degradation in the presence of detuning disorder. The gap is varied by changing the gain parameter (g). The disorder is assumed to be normally distributed with a standard deviation of 0.05. c) The effect of coupling disorder in the anti-squeezed quadrature.

in a differential form as:

$$T\frac{da}{dt} = -\gamma Ta + \mathrm{i}\Delta Ta + \epsilon b_0 La^* - \frac{1}{2}\epsilon^2 L^2|a|^2 a. \tag{9.12}$$

This reduces to:

$$\frac{da}{dt} = -\gamma a + \mathrm{i}\Delta a + \epsilon b_0 \frac{L}{T}a^* - \frac{1}{2T}\epsilon^2 L^2|a|^2 a. \tag{9.13}$$

Thus, we define $g = \epsilon b_0 \frac{L}{T}$ which denotes the parametric gain, and $g_s = \frac{1}{2T}\epsilon^2 L^2$ which denotes the gain saturation co-efficient.

The dynamics of a single degenerate OPO are governed by the following simplified equation:

$$\frac{da}{dt} = -\alpha a + \mathrm{i}\Delta a + ga^* - g_s|a|^2 a \tag{9.14}$$

where a is the amplitude of the intra-cavity field, α is the loss parameter (arising due to propagation loss/ out-coupling loss), Δ represents the detuning parameter (detuning between the subharmonic ω and the resonance frequency of the cavity), g represents the parametric gain that depends on the effective quadratic nonlinearity and the pump power, and g_s is the gain saturation nonlinearity co-efficient. The gain saturation arises due to pump depletion. The lattice of OPOs represents coupled OPOs, where the coupling is determined by the linear part of the Hamiltonian.

9.5.5 Model of the coupled OPO system (SSH Lattice) in the quantum regime: Langevin equations

Here we develop the input-output formalism of the coupled OPO system for analysis of the quantum behavior. This formalism has been used to obtain the results of the Quantum Regime discussion.

The signal fields $\hat{a}_i, i \in 1 \ldots N$ (where N is the number of OPOs in the finite SSH lattice) in the resonators constituting the OPOs experience a roundtrip loss (γ) consisting of two contributions: out-coupling loss (μ) and round-trip propagation loss (α). We define (ρ) as, $\rho = \frac{\mu}{\gamma}$, which is the ratio between out-coupling and total loss. The OPOs operate below the threshold. Also, the pump is non-resonant and the pumps driving the OPOs are not coupled to each other. So we can adiabatically eliminate the pump dynamics and represent the pump field with a coherent field. We assume all OPOs experience identical loss, coupling, and pump drives.

We include the loss arising from different mechanisms and the accompanying fluctuations ($\hat{V}$) using the input-output formalism of open quantum systems. We

can write the Heisenberg-Langevin equations for the intra-cavity field as [12]:

$$\dot{\hat{a}}_i = -\gamma \hat{a}_i + g\hat{a}_i^\dagger + \sum_{j \neq i} \mathrm{i}\kappa_{i,j}\hat{a}_j + \sqrt{2\alpha}\hat{V}_{\alpha,a_i} + \sqrt{2\mu}\hat{V}_{\mu,a_i} \tag{9.15a}$$

where, $\kappa_{i,j} = H_L(i,j)$ is the (i,j) the term of the linear Hamiltonian ($\hat{H}_L$) given in Eq. 9.1, expressed in the matrix (NxN) form.

The respective output field can be mapped to the intra-cavity field as:

$$\hat{A}_{i,out} = \sqrt{2\mu}\hat{a}_i - \hat{V}_{\mu,a_i}. \tag{9.15b}$$

We assume that the fluctuations have zero mean fields and are delta-correlated Gaussian noise sources. Noise from independent channels is non-correlated. These fluctuations which provide the Langevin forces follow the following commutation relations:

$$\begin{aligned} \left\langle \hat{V}_{l,j}(t)\hat{V}^\dagger_{l'j'}(t') \right\rangle &= \delta_{ll'}\delta_{jj'}\delta(t-t') \\ \left\langle \hat{V}^\dagger_{l,j}(t)\hat{V}_{l'j'}(t') \right\rangle = \left\langle \hat{V}_{l,j}(t)\hat{V}_{l'j'}(t') \right\rangle &= \left\langle \hat{V}^\dagger_{l,j}(t)\hat{V}^\dagger_{l'j'}(t') \right\rangle = 0 \end{aligned} \tag{9.16a}$$

where $l \in \{\mu, \alpha\}$ and $j \in a_i, i \in 1 \ldots N$. We define the Fourier transform as: $\tilde{V}(\omega) = \frac{1}{\sqrt{2\pi}} \int_{-\infty}^{\infty} dt \hat{V}(t) e^{i\omega t}$. Therefore in the spectral domain, the noise correlations appear as:

$$\begin{aligned} \left\langle \tilde{V}_{l,j}(\omega)\tilde{V}^\dagger_{l'j'}(\omega') \right\rangle &= \delta_{ll'}\delta_{jj'}\delta(\omega-\omega') \\ \left\langle \tilde{V}^\dagger_{l,j}(\omega)\tilde{V}_{l'j'}(\omega') \right\rangle = \left\langle \tilde{V}_{l,j}(\omega)\tilde{V}_{l'j'}(\omega') \right\rangle &= \left\langle \tilde{V}^\dagger_{l,j}(\omega)\tilde{V}^\dagger_{l'j'}(\omega') \right\rangle = 0. \end{aligned} \tag{9.16b}$$

We define the amplitude and phase quadratures as follows: $\hat{X}_i = \hat{a}_i + \hat{a}_i{}^\dagger, \hat{Y}_i = -i\left(\hat{a}_i - \hat{a}_i{}^\dagger\right)$.

Below the threshold, the mean values of the fields are zero. The fluctuations of the quadratures can be studied by analyzing the following linearized dynamics:

$$\begin{bmatrix} \dot{\hat{X}} \\ \dot{\hat{Y}} \end{bmatrix} = J \begin{bmatrix} \hat{X} \\ \hat{Y} \end{bmatrix} + \sqrt{2\alpha} \begin{bmatrix} \hat{W}^\alpha_0 \\ \hat{W}^\alpha_{\pi/2} \end{bmatrix} + \sqrt{2\mu} \begin{bmatrix} \hat{W}^\mu_0 \\ \hat{W}^\mu_{\frac{\pi}{2}} \end{bmatrix} \tag{9.17}$$

where, $\hat{X} = [\hat{X}_1 \ldots \hat{X}_N]^T$, $\hat{Y} = [\hat{Y}_1 \ldots \hat{Y}_N]^T$, $\hat{W}^j_i = [\hat{W^{j,a_1}_0} \ldots \hat{W^{j,a_N}_0}]$ for $j \in \{\mu, \alpha\}$ and $i \in \{0, \frac{\pi}{2}\}$.

$$J = -\gamma I_{2N} + g \begin{bmatrix} I_N & 0 \\ 0 & -I_N \end{bmatrix} + \begin{bmatrix} 0 & -H_L \\ H_L & 0 \end{bmatrix} \tag{9.18}$$

I_N is an identity matrix of order N. I_{2N} is an identity matrix of order 2N. J is matrix of 2N x 2N.

The other terms in Eq. 9.17 are defines as: $\hat{W}^l_{j,0} = \hat{V}_{l,j} + \hat{V}^\dagger_{l,j}$, $\hat{W}^l_{j,\pi/2} = -\mathrm{i}\left(\hat{V}_{l,j} - \hat{V}^\dagger_{l,j}\right)$, $l \in \{\mu, \alpha\}$ and $j \in \{a_1 \dots a_N\}$. The respective output field can be mapped to the intra-cavity field as:

$$\begin{bmatrix} \hat{X}_{out} \\ \hat{Y}_{out} \end{bmatrix} = \sqrt{2\mu} \begin{bmatrix} \hat{X} \\ \hat{Y} \end{bmatrix} - \begin{bmatrix} \hat{W}^\mu_0 \\ \hat{W}^\mu_{\frac{\pi}{2}} \end{bmatrix}. \tag{9.19}$$

In the spectral domain, we get,

$$\begin{bmatrix} \tilde{X}_{out}(\omega) \\ \tilde{Y}_{out}(\omega) \end{bmatrix} = -\sqrt{2\mu}\left[J + \mathrm{i}\omega I_{2N}\right]^{-1} \left(\sqrt{2\alpha} \begin{bmatrix} \hat{W}^\alpha_0(\omega) \\ \hat{W}^\alpha_{\frac{\pi}{2}}(\omega) \end{bmatrix} + \sqrt{2\mu} \begin{bmatrix} \hat{W}^\mu_0(\omega) \\ \hat{W}^\mu_{\frac{\pi}{2}}(\omega) \end{bmatrix} \right) - \begin{bmatrix} \hat{W}^\mu_0(\omega) \\ \hat{W}^\mu_{\frac{\pi}{2}}(\omega) \end{bmatrix}. \tag{9.20}$$

The output correlation matrix can be written as:

$$C^{out}(\omega) = \int_{-\infty}^{\infty} d\omega' \left\langle \begin{bmatrix} \tilde{X}_{out}(\omega) \\ \tilde{Y}_{out}(\omega) \end{bmatrix} \begin{bmatrix} \tilde{X}_{out}(\omega') \\ \tilde{Y}_{out}(\omega') \end{bmatrix}^T \right\rangle \tag{9.21}$$

where T stands for matrix transpose operation.

$$\begin{aligned} C^{out}(\omega) = \left(2\mu\left[J + \mathrm{i}\omega I_{2N}\right]^{-1} + I_{2N}\right) C^{in}(\omega) \left(2\mu\left[J - \mathrm{i}\omega I_{2N}\right]^{-1} + I_{2N}\right)^T \\ + 4\mu\alpha\left(J + \mathrm{i}\omega I_{2N}\right)^{-1} C^{in}(\omega) \left(\left(J - \mathrm{i}\omega I_{2N}\right)^{-1}\right)^T \end{aligned} \tag{9.22}$$

The input correlation matrix is:

$$C^{in}(\omega) = \begin{bmatrix} I_N & \mathrm{i}I_N \\ -\mathrm{i}I_N & I_N \end{bmatrix}. \tag{9.23}$$

9.5.6 Ring of exceptional point

We explore the 2D Kagome lattice of parametrically driven quadratic nonlinear resonators. If we vary the detuning of the resonators we can drive the bulk into the PT-broken regime. At the critical detuning, the eigenvalues become complex

conjugate pairs. The eigenstates where the PT symmetry is broken occupy a ring-like structure in the momentum space [46, 52]. At large values of detuning all the bulk modes are in the PT unbroken regime as shown in Fig. 9.11(a,b,c). At detuning values less than the critical detuning (that is characterized by the exceptional point), some of the eigenmodes undergo PT phase transition and assume imaginary eigenvalue with zero real part. This is shown in Fig. 9.11(d,e,f).

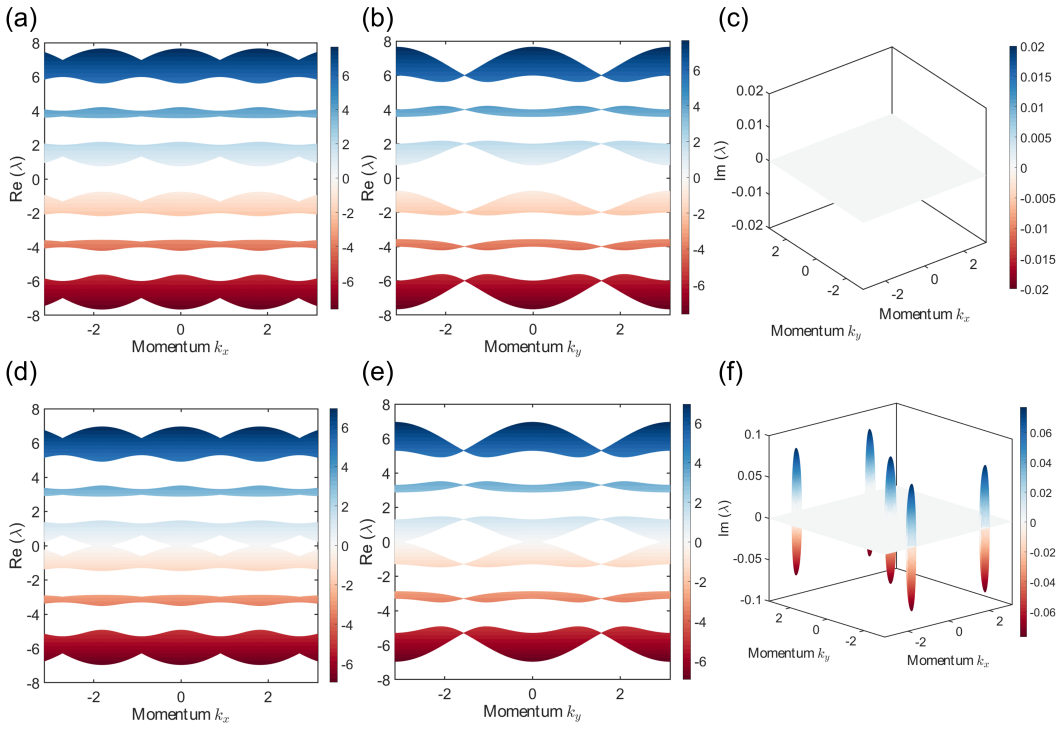

Figure 9.11: **Band structure of the 2D lattice in the PT-unbroken and PT-broken regime.** Band structure of the 2D lattice in the PT-unbroken regime. a) the real part projected in the XZ plane, b) the real part projected in the YZ plane, c) the imaginary part. Parameters used in the simulation are: $\Delta = 4, \phi = 0.6\pi, g = 0.1, J = 1$. Band structure of the 2D lattice in the PT broken regime. d) the real part projected in the XZ plane, e) the real part projected in the YZ plane, f) the imaginary part. Parameters used in the simulation are: $\Delta = 3.3, \phi = 0.6\pi, g = 0.1, J = 1$.

9.5.7 Non-Hermitian transitions from the Imaginary part of the complex Berry phase

The complex Berry phase of a non-Hermitian Hamiltonian is given by [27]:

$$\phi = \oint \left\langle L(k) | \mathrm{i} \frac{d}{dk} R(k) \right\rangle dk \tag{9.24}$$

where the integral is calculated on a close path in the momentum space $[-\pi, \pi]$. $|R(k)>$ and $|L(k)>$ are the right and left eigenvectors of σ_zH(k), respectively. We just focus on ϕ_-, which describes the Berry phase for the lower bulk band of the 1D SSH coupled system of OPOs.

$H(k)$ is given by:

$$H(k) = \begin{bmatrix} H_1(k) & H_2(k) \\ H_2(-k)^* & H_1(-k)^* \end{bmatrix}. \tag{9.25}$$

$H_1(k)$ is expressed as:

$$H_1(k) = \begin{bmatrix} \Delta & \kappa_1 + \kappa_2 e^{-ik} \\ \kappa_1 + \kappa_2 e^{ik} & \Delta \end{bmatrix} \tag{9.26}$$

where Δ is the detuning, $\kappa_1 = J(1-\epsilon)$ and $\kappa_2 = J(1+\epsilon)$.

$H_2(k)$ is expressed as:

$$H_2(k) = \begin{bmatrix} g & 0 \\ 0 & g \end{bmatrix}. \tag{9.27}$$

The right eigenvector of the lower band is given by: $|R(k)>= [-\frac{\rho}{g} + \sqrt{\frac{\rho}{\rho^*}}\frac{\Delta-\sqrt{(\Delta-|\rho|)^2-g^2}}{g}, -\frac{\Delta-|\rho|-\sqrt{(\Delta-|\rho|)^2-g^2}}{g}, -\sqrt{\frac{\rho}{\rho^*}}, 1]^T$.

where $\rho = \kappa_1 + \kappa_2 e^{-ik}$.

The left eigenvector of the lower band is given by: $|L(k)>= [\frac{\rho^*}{g} + \sqrt{\frac{\rho^*}{\rho}}\frac{-\Delta+\sqrt{(\Delta-|\rho|)^2-g^2}}{g}, -\frac{-\Delta+|\rho|+\sqrt{(\Delta-|\rho|)^2-g^2}}{g}, -\sqrt{\frac{\rho^*}{\rho}}, 1]^T$.

In Figure 9.12(a,d), we plot the imaginary part of the complex Berry phase as a function of the on-site detuning. The discontinuities in the derivative of the imaginary part of the Berry phase align with the underlying non-Hermitian phase transitions (Fig. 9.12(b,e)). This agrees with the trend of the imaginary part of the eigenvalues obtained from the numerical simulation of a finite 1D SSH lattice (Fig. 9.12(c,f)).

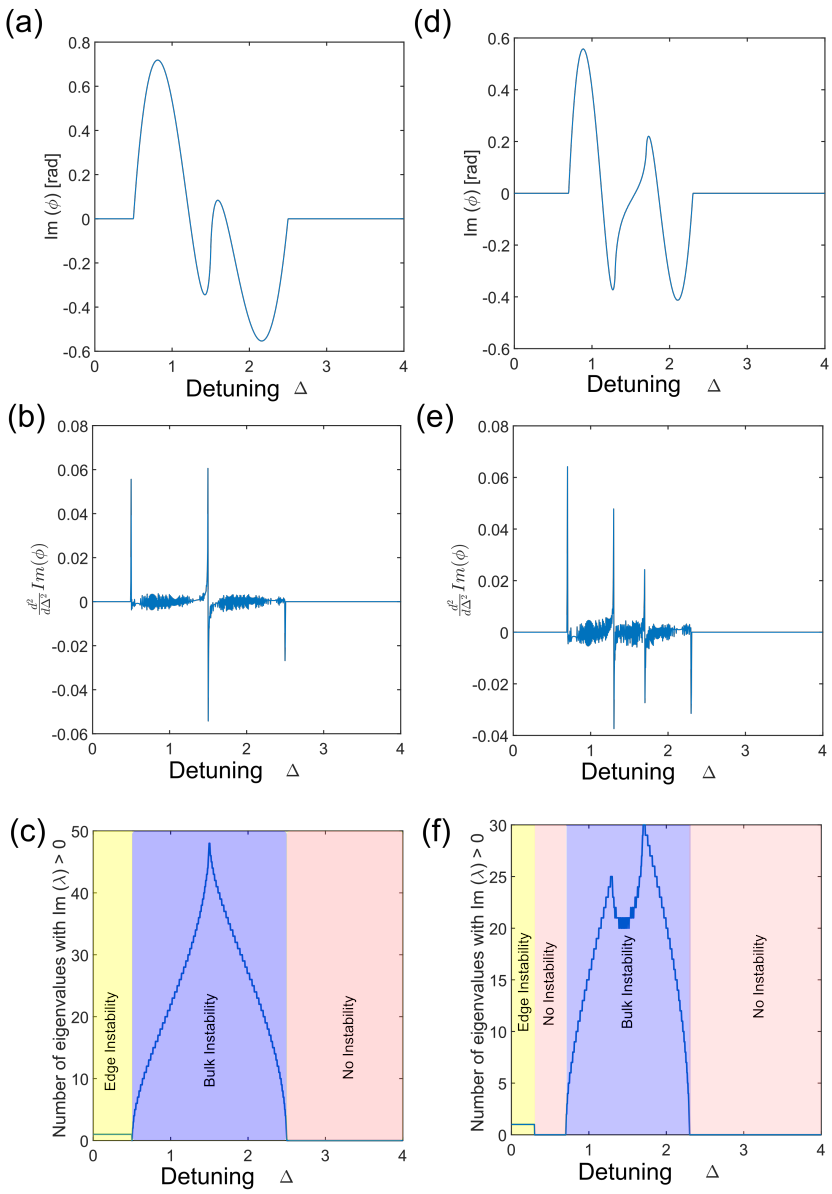

Figure 9.12: **Complex Berry phase**. For g=0.5 a) Imaginary part of the complex Berry phase b) Double derivative of the imaginary part of the Berry phase, c) Imaginary part of the Eigenvalue distribution (Im (λ) 0) obtained numerically for a finite 1D SSH lattice for N=99. For g=0.3 d) Imaginary part of the complex Berry phase e) Double derivative of the imaginary part of the Berry phase, f) Imaginary part of the Eigenvalue distribution (Im (λ) 0) obtained numerically fr a finite 1D SSH lattice for N=99. Parameters used in the simulation are: $\epsilon = 0.5, J = 1$.

9.5.8 Topological protection of the edge mode eigenvalue in the presence of symmetry protected disorder

The eigenvalue corresponding to the edge mode in the 1D SSH coupled OPO arrays is not perturbed by a small amount of symmetry-preserving disorders. Here, the

disorder is considered in the coupling co-coefficients (κ_1 and κ_2) which still preserves the chiral symmetry. The real part of the eigenvalue distribution is plotted in Fig. 9.13(a). We can see that the edge mode is not affected, while the bulk modes are affected by the introduction of the detuning disorder. The imaginary part of the eigenvalue distribution is shown in Fig. 9.13(b).

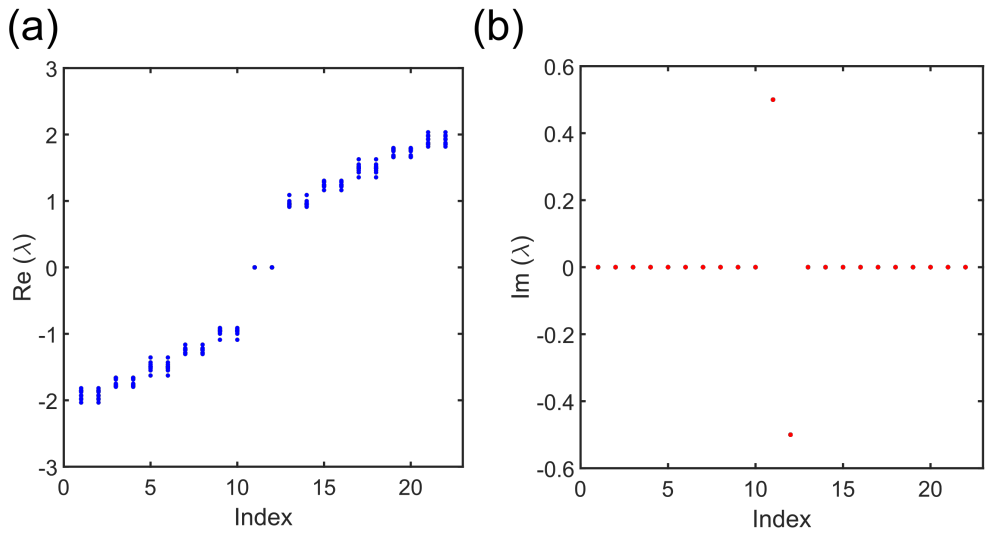

Figure 9.13: **Eigenvalue sensitivity to disorder in a 1D SSH coupled OPO arrays.** a) The real part of the eigenvalue distribution of 1D SSH coupled OPO arrays. The edge mode is unperturbed by the disorder, while the bulk modes are affected by the disorder. b) imaginary part of the eigenvalue distribution. Parameters used in the simulation are: $\epsilon = 0.5, J = 1, N = 11, g = 0.5$. The coupling disorder is assumed to be normally distributed with a standard deviation of 0.1. 10 different disorder realizations are overlaid on top of each other.

References

[1] Junaid Aasi et al. Enhanced sensitivity of the LIGO gravitational wave detector by using squeezed states of light. *Nature Photonics*, 7(8):613–619, 2013.

[2] Ivan Amelio and Iacopo Carusotto. Theory of the coherence of topological lasers. *Physical Review X*, 10(4):041060, 2020.

[3] Babak Bahari, Abdoulaye Ndao, Felipe Vallini, Abdelkrim El Amili, Yeshaiahu Fainman, and Boubacar Kanté. Nonreciprocal lasing in topological cavities of arbitrary geometries. *Science*, 358(6363):636–640, 2017.

[4] Miguel A. Bandres, Steffen Wittek, Gal Harari, Midya Parto, Jinhan Ren, Mordechai Segev, Demetrios N. Christodoulides, and Mercedeh Khajavikhan. Topological insulator laser: Experiments. *Science*, 359(6381), 2018.

[5] Charles-Edouard Bardyn, Torsten Karzig, Gil Refael, and Timothy C. H. Liew. Chiral Bogoliubov excitations in nonlinear bosonic systems. *Physical Review B*, 93(2):020502, 2016.

[6] Ryan Barnett. Edge-state instabilities of bosons in a topological band. *Physical Review A*, 88(6):063631, 2013.

[7] Wladimir A. Benalcazar, B. Andrei Bernevig, and Taylor L. Hughes. Electric multipole moments, topological multipole moment pumping, and chiral hinge states in crystalline insulators. *Physical Review B*, 96(24):245115, 2017.

[8] Wladimir A. Benalcazar, B. Andrei Bernevig, and Taylor L. Hughes. Quantized electric multipole insulators. *Science*, 357(6346):61–66, 2017.

[9] Andrea Blanco-Redondo, Bryn Bell, Dikla Oren, Benjamin J. Eggleton, and Mordechai Segev. Topological protection of biphoton states. *Science*, 362 (6414):568–571, 2018.

[10] Alexander W. Bruch, Xianwen Liu, Joshua B. Surya, Chang-Ling Zou, and Hong X. Tang. On-chip χ (2) microring optical parametric oscillator. *Optica*, 6(10):1361–1366, 2019.

[11] Gaurav Chaudhary, Michael Levin, and Aashish A Clerk. Simple approach to characterizing band topology in bosonic pairing hamiltonians. *Physical Review B*, 103(21):214306, 2021.

[12] Yanne K. Chembo. Quantum dynamics of Kerr optical frequency combs below and above threshold: Spontaneous four-wave mixing, entanglement, and squeezed states of light. *Physical Review A*, 93(3):033820, 2016.

[13] Lu-Ming Duan, Géza Giedke, Juan Ignacio Cirac, and Peter Zoller. Inseparability criterion for continuous variable systems. *Physical Review Letters*, 84(12):2722, 2000.

[14] Avik Dutt, Qian Lin, Luqi Yuan, Momchil Minkov, Meng Xiao, and Shanhui Fan. A single photonic cavity with two independent physical synthetic dimensions. *Science*, 367(6473):59–64, 2020.

[15] Bogdan Galilo, Derek K. K. Lee, and Ryan Barnett. Selective population of edge states in a 2D topological band system. *Physical review letters*, 115(24): 245302, 2015.

[16] Qiushi Guo, Ryoto Sekine, Luis Ledezma, Rajveer Nehra, Devin J. Dean, Arkadev Roy, Robert M. Gray, Saman Jahani, and Alireza Marandi. Femtojoule, femtosecond all-optical switching in lithium niobate nanophotonics. *arXiv preprint arXiv:2107.09906*, 2021.

[17] Mohammad Hafezi, Eugene A. Demler, Mikhail D. Lukin, and Jacob M. Taylor. Robust optical delay lines with topological protection. *Nature Physics*, 7(11):907–912, 2011.

[18] Mohammad Hafezi, Sunil Mittal, J. Fan, Alan Migdall, and Jacob Taylor. Imaging topological edge states in silicon photonics. *Nature Photonics*, 7(12): 1001–1005, 2013.

[19] Gal Harari, Miguel A. Bandres, Yaakov Lumer, Mikael C. Rechtsman, Yi Dong Chong, Mercedeh Khajavikhan, Demetrios N. Christodoulides, and Mordechai Segev. Topological insulator laser: Theory. *Science*, 359(6381), 2018.

[20] Saman Jahani, Arkadev Roy, and Alireza Marandi. Wavelength-scale optical parametric oscillators. *Optica*, 8(2):262–268, 2021.

[21] Alexander B. Khanikaev and Gennady Shvets. Two-dimensional topological photonics. *Nature Photonics*, 11(12):763–773, 2017.

[22] Alexander B. Khanikaev, S Hossein Mousavi, Wang-Kong Tse, Mehdi Kargarian, Allan H. MacDonald, and Gennady Shvets. Photonic topological insulators. *Nature Materials*, 12(3):233–239, 2013.

[23] Sergey Kruk, Alexander Poddubny, Daria Smirnova, Lei Wang, Alexey Slobozhanyuk, Alexander Shorokhov, Ivan Kravchenko, Barry Luther-Davies, and Yuri Kivshar. Nonlinear light generation in topological nanostructures. *Nature Nanotechnology*, 14(2):126–130, 2019.

[24] Alexander S. Kuznetsov, Galbadrakh Dagvadorj, Klaus Biermann, Marzena H. Szymanska, and Paulo V. Santos. Dynamically tuned arrays of polariton parametric oscillators. *Optica*, 7(12):1673–1681, 2020.

[25] Christian Leefmans, Avik Dutt, James Williams, Luqi Yuan, Midya Parto, Franco Nori, Shanhui Fan, and Alireza Marandi. Topological dissipation in a time-multiplexed photonic resonator network. *arXiv preprint arXiv:2104.05213*, 2021.

[26] Daniel Leykam and Yi Dong Chong. Edge solitons in nonlinear-photonic topological insulators. *Physical review letters*, 117(14):143901, 2016.

[27] Shi-Dong Liang and Guang-Yao Huang. Topological invariance and global berry phase in non-Hermitian systems. *Physical Review A*, 87(1):012118, 2013.

[28] Stefano Longhi. Non-Hermitian gauged topological laser arrays. *Annalen der Physik*, 530(7):1800023, 2018.

[29] Stefano Longhi and Liang Feng. Invited article: Mitigation of dynamical instabilities in laser arrays via non-Hermitian coupling. *APL Photonics*, 3(6): 060802, 2018.

[30] Stefano Longhi, Yannis Kominis, and Vassilios Kovanis. Presence of temporal dynamical instabilities in topological insulator lasers. *EPL (Europhysics Letters)*, 122(1):14004, 2018.

[31] Juanjuan Lu, Ayed Al Sayem, Zheng Gong, Joshua B. Surya, Chang-Ling Zou, and Hong X Tang. Ultralow-threshold thin-film lithium niobate optical parametric oscillator. *arXiv preprint arXiv:2101.04735*, 2021.

[32] Ling Lu, John D Joannopoulos, and Marin Soljačić. Topological photonics. *Nature photonics*, 8(11):821–829, 2014.

[33] Lukas J. Maczewsky, Matthias Heinrich, Mark Kremer, Sergey K. Ivanov, Max Ehrhardt, Franklin Martinez, Yaroslav V. Kartashov, Vladimir V. Konotop, Lluis Torner, Dieter Bauer, et al. Nonlinearity-induced photonic topological insulator. *Science*, 370(6517):701–704, 2020.

[34] Sunil Mittal, Venkata Vikram Orre, Daniel Leykam, Yi Dong Chong, and Mohammad Hafezi. Photonic anomalous quantum Hall effect. *Physical Review Letters*, 123(4):043201, 2019.

[35] Sunil Mittal, Venkata Vikram Orre, Guanyu Zhu, Maxim A Gorlach, Alexander Poddubny, and Mohammad Hafezi. Photonic quadrupole topological phases. *Nature Photonics*, 13(10):692–696, 2019.

[36] Tomoki Ozawa, Hannah M. Price, Alberto Amo, Nathan Goldman, Mohammad Hafezi, Ling Lu, Mikael C. Rechtsman, David Schuster, Jonathan Simon, Oded Zilberberg, et al. Topological photonics. *Reviews of Modern Physics*, 91(1):015006, 2019.

[37] Midya Parto, Steffen Wittek, Hossein Hodaei, Gal Harari, Miguel A. Bandres, Jinhan Ren, Mikael C. Rechtsman, Mordechai Segev, Demetrios N. Christodoulides, and Mercedeh Khajavikhan. Edge-mode lasing in 1D topological active arrays. *Physical Review Letters*, 120(11):113901, 2018.

[38] Vittorio Peano, Martin Houde, Christian Brendel, Florian Marquardt, and Aashish A. Clerk. Topological phase transitions and chiral inelastic transport induced by the squeezing of light. *Nature communications*, 7(1):1–8, 2016.

[39] Vittorio Peano, Martin Houde, Florian Marquardt, and Aashish A. Clerk. Topological quantum fluctuations and traveling wave amplifiers. *Physical Review X*, 6(4):041026, 2016.

[40] Mikael C. Rechtsman, Julia M. Zeuner, Yonatan Plotnik, Yaakov Lumer, Daniel Podolsky, Felix Dreisow, Stefan Nolte, Mordechai Segev, and Alexander Szameit. Photonic Floquet topological insulators. *Nature*, 496(7444):196–200, 2013.

[41] Mikael C. Rechtsman, Yaakov Lumer, Yonatan Plotnik, Armando Perez-Leija, Alexander Szameit, and Mordechai Segev. Topological protection of photonic path entanglement. *Optica*, 3(9):925–930, 2016.

[42] Arkadev Roy, Saman Jahani, Qiushi Guo, Avik Dutt, Shanhui Fan, Mohammad-Ali Miri, and Alireza Marandi. Nondissipative non-Hermitian dynamics and exceptional points in coupled optical parametric oscillators. *Optica*, 8(3):415–421, 2021.

[43] Abhi Saxena, Yueyang Chen, Zhuoran Fang, and Arka Majumdar. Photonic topological baths for quantum simulation. *ACS Photonics*.

[44] Alexey P. Slobozhanyuk, Alexander N. Poddubny, Andrey E. Miroshnichenko, Pavel A. Belov, and Yuri S. Kivshar. Subwavelength topological edge states in optically resonant dielectric structures. *Physical review letters*, 114(12): 123901, 2015.

[45] Daria Smirnova, Daniel Leykam, Yidong Chong, and Yuri Kivshar. Nonlinear topological photonics. *Applied Physics Reviews*, 7(2):021306, 2020.

[46] Alex Y. Song, Xiao-Qi Sun, Avik Dutt, Momchil Minkov, Casey Wojcik, Haiwen Wang, Ian A. D. Williamson, Meir Orenstein, and Shanhui Fan. PT-symmetric topological edge-gain effect. *Physical Review Letters*, 125(3): 033603, 2020.

[47] Philippe St-Jean, Valentin Goblot, Elisabeth Galopin, Aristide Lemaître, Tomoki Ozawa, Loic Le Gratiet, Isabelle Sagnes, Jacqueline Bloch, and Alberto Amo. Lasing in topological edge states of a one-dimensional lattice. *Nature Photonics*, 11(10):651–656, 2017.

[48] Wu-Pei Su, John R. Schrieffer, and Ao J. Heeger. Solitons in polyacetylene. *Physical Review Letters*, 42(25):1698, 1979.

[49] Jean-Luc Tambasco, Giacomo Corrielli, Robert J. Chapman, Andrea Crespi, Oded Zilberberg, Roberto Osellame, and Alberto Peruzzo. Quantum

interference of topological states of light. *Science Advances*, 4(9):eaat3187, 2018.

[50] Yu-Xin Wang and Aashish Clerk. Non-Hermitian dynamics without dissipation in quantum systems. *Physical Review A*, 99(6):063834, 2019.

[51] Ling-An Wu, Harry Jeff Kimble, John L. Hall, and Huifa Wu. Generation of squeezed states by parametric down conversion. *Physical Review Letters*, 57 (20):2520, 1986.

[52] Tsuneya Yoshida and Yasuhiro Hatsugai. Exceptional rings protected by emergent symmetry for mechanical systems. *Physical Review B*, 100(5): 054109, 2019.

[53] Han Zhao, Pei Miao, Mohammad H. Teimourpour, Simon Malzard, Ramy El-Ganainy, Henning Schomerus, and Liang Feng. Topological hybrid silicon microlasers. *Nature Communications*, 9(1):1–6, 2018.

Chapter 10

OUTLOOK

This dissertation summarized an attempt towards advancing the understanding of optical parametric oscillators and their networks in the context of applications related to sensing and computing. Nonlinear photonics is a rapidly evolving field and several improvements to the demonstrations in the present work as well as new research directions can be identified, a few of which are discussed below.

10.1 Fully-stabilized self-referenced frequency comb source

The use of frequency combs as a tool for precision metrology is crucially dependent on the stability properties of the comb. A locked comb with both its carrier-envelope-offset frequency (f_{ceo}) and repetition rate f_{rep} locked can provide a very accurate grid that can serve as a frequency ruler. One technique to achieve a locked frequency comb is the so-called f-2f based self-referencing [4, 15], where the instantaneous carrier-envelope frequency is detected via a second-harmonic generation of an octave-spanning comb followed by locking the same.

The strong nonlinearity available in the lithium niobate based integrated nanophotonics platform enables super-continuum generation at very low pulse energies ($\sim$ picoJoules) [8]. The platform also allows very efficient second-harmonic generation [18] and electro-optic modulation [19] for feedback and locking. Thus these ingredients required for full stabilization of a frequency comb can all be integrated monolithically, paving the way for disrupting several applications contingent on frequency combs with a small form factor.

Another valuable pursuit in this regard is to investigate CW-driven quadratic solitons [1, 14]. These solitons will have a much-enriched design space owing to the group-velocity mismatch parameter that is absent in their Kerr soliton counterpart. However, pulsed pump-based approaches may be more efficient, and our proposal of walk-off induced solitons (see **Chapter 2**) whereby one can generate ultrashort pulses starting with picosecond pulses can be a more practical alternative.

10.2 Mid-infrared spectroscopy

Mid-infrared spectral region is technologically very important owing to the existence of unique fingerprints of several molecules in terms of optical absorption corresponding to several rovibrational energy levels. The lithium niobate based platform provides access to a wide transparency window extending up to $4.5\mu m$. The samples under test can also be integrated with the photonics chip for compact lab-on-chip applications. This may involve bringing the samples in close proximity to the evanescent field of the waveguides. If the sample under test is interrogated within the cavity, i.e., the OPO cavity very large sensitivity enhancement is expected [5].

In these mid-infrared OPOs, the idler exists in the mid-infrared while the signal lies in the near-infrared which is easier to detect. One can deploy intriguing approaches along the lines of imaging with undetected photons, to perform spectroscopy with undetected photons by leveraging the inherent correlations between the signal and idler photons.

10.3 Further miniaturization of OPOs towards nanoscale

The ultimate miniaturization of the nonlinear devices can be achieved when the device dimensions approach the wavelength scale. However, the associated trade-offs emerge in the form of reduced quality factors and subsequently an increased threshold. Ingenuous device design approaches that optimize the field overlap [6, 7, 12] can potentially help us realize this ambitious goal [10]. Inverse-design-based approaches can also assist in informing the optimum device configuration [9]. Apart from using well-engineered Mie resonance modes, one can also deploy plasmonics-based devices as well in this regard. Materials with strong nonlinearity like aluminum gallium arsenide.

10.4 Incoherently pumped OPOs

The lasers that are used for most applications are predominantly pumped either electrically or by optical means with sources having low coherence. Lasers produce extremely coherent output with narrow linewidth which is a prerequisite for several applications. The adoption of OPOs for several photonic devices can be accelerated if we can pump the OPOs with low coherence sources and get outputs with high coherence [13, 16, 36]. The singly resonant OPOs represent a very promising route to achieve the same (see **Chapter 7**). This approach can also be extended for parametric amplifiers as well. The underlying principle relies on the convection

between the waves (pump, signal, and idler) and proper dispersion engineering (in terms of designing suitable walk-off parameters) enabled by the nanophotonics platform makes it ideal in this regard.

10.5 Investigating spectral phase transitions and parametric exceptional points in the strongly nonlinear regime

Our work has been centered around weak nonlinearities whereby the participation of a large number of photons (in the order of millions) is necessary to trigger the nonlinear interactions. Strong nonlinearity that operates at a few photons level can unveil a host of associated rich phenomena in the quantum regime. Superconducting circuit QED, trapped-ion, and cold atoms can be very promising platforms for the exploration of these phenomena. Important applications in this regard are related to enhanced sensing in the context of critical parametric sensors [2, 3], transition edge sensors, and parametric non-Hermitian sensors [11]. Getting into a deterministic strongly nonlinear regime all-optically is the holy grail [17, 20].

References

[1] Alexander W. Bruch, Xianwen Liu, Zheng Gong, Joshua B. Surya, Ming Li, Chang-Ling Zou, and Hong X. Tang. Pockels soliton microcomb. *Nature Photonics*, 15(1):21–27, 2021.

[2] Rafal Demkowicz-Dobrzański, Marcin Jarzyna, and Jan Kołodyński. Quantum limits in optical interferometry. *Progress in Optics*, 60:345–435, 2015.

[3] Roberto Di Candia, Fabrizio Minganti, Kirill Petrovnin, Gheorghe S. Paraoanu, and Simone Felicetti. Critical parametric quantum sensing. *arXiv preprint arXiv:2107.04503*, 2021.

[4] Tara Fortier and Esther Baumann. 20 years of developments in optical frequency comb technology and applications. *Communications Physics*, 2 (1):153, 2019.

[5] Robert M. Gray, Mingchen Liu, Selina Zhou, Arkadev Roy, Luis Ledezma, and Alireza Marandi. Cavity-soliton-enhanced mid-ir molecular sensing. *arXiv preprint arXiv:2301.07826*, 2023.

[6] Saman Jahani, Joong Hwan Bahng, Arkadev Roy, Nicholas Kotov, and Alireza Marandi. Confining light in all-dielectric anisotropic metamaterial particles for nano-scale nonlinear optics. *arXiv preprint arXiv:2102.13087*, 2021.

[7] Saman Jahani, Arkadev Roy, and Alireza Marandi. Wavelength-scale optical parametric oscillators. *Optica*, 8(2):262–268, 2021.

[8] Marc Jankowski, Carsten Langrock, Boris Desiatov, Alireza Marandi, Cheng Wang, Mian Zhang, Christopher R. Phillips, Marko Lončar, and Martin M. Fejer. Ultrabroadband nonlinear optics in nanophotonic periodically poled lithium niobate waveguides. *Optica*, 7(1):40–46, 2020.

[9] Zin Lin, Xiangdong Liang, Marko Lončar, Steven G. Johnson, and Alejandro W. Rodriguez. Cavity-enhanced second-harmonic generation via nonlinear-overlap optimization. *Optica*, 3(3):233–238, 2016.

[10] Giuseppe Marino, Alexander S. Solntsev, Lei Xu, Valerio F. Gili, Luca Carletti, Alexander N. Poddubny, Mohsen Rahmani, Daria A Smirnova, Haitao Chen, Aristide Lemaître, et al. Spontaneous photon-pair generation from a dielectric nanoantenna. *Optica*, 6(11):1416–1422, 2019.

[11] Alexander McDonald and Aashish A. Clerk. Exponentially-enhanced quantum sensing with non-hermitian lattice dynamics. *Nature Communications*, 11(1): 5382, 2020.

[12] Momchil Minkov, Dario Gerace, and Shanhui Fan. Doubly resonant χ (2) nonlinear photonic crystal cavity based on a bound state in the continuum. *Optica*, 6(8):1039–1045, 2019.

[13] Carlos Montes, Werner Grundkötter, Hubertus Suche, and Wolfgang Sohler. Coherent signal from incoherently cw-pumped singly resonant ti: Linbo 3 integrated optical parametric oscillators. *JOSA B*, 24(11):2796–2806, 2007.

[14] Mingming Nie and Shu-Wei Huang. Quadratic solitons in singly resonant degenerate optical parametric oscillators. *Physical Review Applied*, 13(4): 044046, 2020.

[15] Yoshitomo Okawachi, Mengjie Yu, Boris Desiatov, Bok Young Kim, Tobias Hansson, Marko Lončar, and Alexander L. Gaeta. Chip-based self-referencing using integrated lithium niobate waveguides. *Optica*, 7(6):702–707, 2020.

[16] Antonio Picozzi and Marc Haelterman. Parametric three-wave soliton generated from incoherent light. *Physical Review Letters*, 86(10):2010, 2001.

[17] Philipp Stammer, Javier Rivera-Dean, Andrew Maxwell, Theocharis Lamprou, Andrés Ordóñez, Marcelo F. Ciappina, Paraskevas Tzallas, and Maciej Lewenstein. Quantum electrodynamics of intense laser-matter interactions: A tool for quantum state engineering. *PRX Quantum*, 4(1):010201, 2023.

[18] Cheng Wang, Carsten Langrock, Alireza Marandi, Marc Jankowski, Mian Zhang, Boris Desiatov, Martin M. Fejer, and Marko Lončar. Ultrahigh-efficiency wavelength conversion in nanophotonic periodically poled lithium niobate waveguides. *Optica*, 5(11):1438–1441, 2018.

[19] Cheng Wang, Mian Zhang, Xi Chen, Maxime Bertrand, Amirhassan Shams-Ansari, Sethumadhavan Chandrasekhar, Peter Winzer, and Marko Lončar. Integrated lithium niobate electro-optic modulators operating at cmos-compatible voltages. *Nature*, 562(7725):101–104, 2018.

[20] Ryotatsu Yanagimoto, Edwin Ng, Marc Jankowski, Hideo Mabuchi, and Ryan Hamerly. Temporal trapping: A route to strong coupling and deterministic optical quantum computation. *Optica*, 9(11):1289–1296, 2022.